The Dissertation Committee for Emily Renee Adkins Certifies that this is the approved version of the following dissertation:

Silicon and Germanium Battery Materials: Exploring New Structures, Surface Treatments, and Full Cell Applications

Committee:

Brian A. Korgel, Supervisor

Charles B. Mullins

Arumugam Manthiram

Gyeong S. Hwang

Guihua Yu

Silicon and Germanium Battery Materials: Exploring New Structures, Surface Treatments, and Full Cell Applications

by

Emily Renee Adkins

Dissertation

Presented to the Faculty of the Graduate School of

The University of Texas at Austin

in Partial Fulfillment

of the Requirements

for the Degree of

Doctor of Philosophy

The University of Texas at Austin

May 2018

Dedication

For my grandfather, Dr. Orval E. Jones. He is the giant upon whose shoulders I have stood to see far.

Acknowledgements

I want to thank Dr. Korgel for the opportunities and freedom he has given me during graduate school. I got to travel and live around the world, participate in collaborations with exciting researchers, and pursue some of my non-scientific interests. His guidance and support through graduate school has meant a lot. I would also like to thank the members of my committee: Dr. Manthiram, Dr. Mullins, Dr. Hwang, and Dr. Yu. I want to thank Dr. Maynard, for whom I was a teaching assistant. I learned a lot from her about management and teaching as well as patience.

I have so many wonderful labmates to thank I will inevitably forget someone. Vikas, Dorothy, Adrien, and Cherrelle, we all entered together and supported each other. In you I always had someone to bounce ideas off, edit my papers, or just go grab some coffee. There was always someone to laugh with and talk with and it is only because of all of you that I have made it this far. I also want to thank Tim Bogart, for teaching me everything about synthesis and batteries, Xiaotang Lu, who taught me so much about *in-situ* TEM and how to analyze my data. Taizhi Jiang (TJ), has been my partner in the lab for years. He helped me through glovebox shut downs, dead batteries, and failed syntheses. Thank you for always being someone I could talk about papers and experiments with. I want to thank former Korgel group members who taught me when I first joined the group: Chris Bosoy, Taylor Harvey, Jackson Stolle, Aaron Chockla, Yixuan Yu, Philip Lu. Thank you to my current lab mates who have all been great colleagues: Dan Houck, Hyun Gyung Kim, Tim Siegler, Yangning Zhang, and Michael Abney. I want to say a special thanks to Doug Pernik and Tushti Shah, who I have sat next to in the office for years. We talked about everything under the sun and never got bored.

It takes a village to get even the tiniest piece of data, and I want to thank all the supporting scientists, students, and collaborators who helped me. Thanks to Drew Heilman, who worked with me as an undergraduate researcher. I learned a lot about planning experiments and explaining my goals through mentoring him in the lab. Thank you to Dr. Dwight Romanovicz, Dr. Karalee Jarvis, Dr. Vincent Lynch, and Dr. Hugo Celio for training me on the instruments I used. Also thank you to Dr. Chongmin Wang, my collaborator at Pacific Northwest National Labs. Jon Peck, Kate Baird, and Laura Mondino made my time in graduate school as smooth as possible and kept me on track.

I want to thank those professors at Rice University who helped me get to graduate school and guided me when I added a chemical engineering degree after my first year. Dr. Sibani Lisa Biswal taught my first ever chemical engineering class and it is all her fault that the class was so good I stayed in the major for a subsequent 8 years. Dr. Matteo Pasquali, my undergraduate research advisor, who put me on an exciting project and encouraged me while applying to graduate school. And most of all to Dr. Shannon Eichmann, who I worked with as an undergraduate. She taught me so much about how to do research, plan experiments, and be persistent even when things aren't working. The time I spent with her in the lab excited me about science and lead me to apply to graduate school. I also want to thank my homework study group at Rice. I relied on your help so much to get through school, sometimes I felt like we were working toward a single joint degree together.

I want to thank my friends who supported me and encouraged me in graduate school. They have given feedback on essays, listened to practice talks, and been there for me when I needed someone to talk to. My friends going through graduate school with me were there to share and commiserate in the process, and my friends outside of school were there when I was tired of talking about science. There are too many wonderful people to

name here, but I appreciate your love and help over the years more than you could ever know.

Finally, graduate school has not always been easy, there were many times where I thought I wouldn't be able to finish. So, I must thank my family who were there to support me in good times and in bad and always encouraged me to stick with it. I want to thank my parents, Doug and Carol, who have consistently exposed me to science throughout my life both in their own careers and in the opportunities they have given me. They supported me when I changed majors and took a fifth year in college and for that I'm eternally grateful. I must also thank my grandparents, Orval and Pauline Jones. They watched me during the day when I was growing up and taught me reading, writing, math, responsibility, and kindness. My time at their house made me into the person who I am today.

Silicon and Germanium Battery Materials: Exploring New Structures, Surface Treatments, and Full Cell Applications

Emily Renee Adkins, Ph.D.

The University of Texas at Austin, 2018

Supervisor: Brian A. Korgel

Lithium ion batteries (LIBs) with higher energy and power density are needed to meet the increasing demands of portable electronic devices, extended-range electric vehicles, and renewable energy storage. Silicon (Si) and germanium (Ge) are attractive anode materials for next generation batteries because they have significantly higher capacities compared with current graphite anodes.

One of the challenges Si and Ge face during battery cycling is high volume expansion upon lithiation, which can be accommodated by nanostructuring. LIBs made using Si and Si-Ge type II clathrates exhibited superior reversible cycling performance. This high capacity and stability is due to the type II phase purity of the samples which is a unique feature of the synthetic method used in this study.

During cycling, the anode will react with the electrolyte, forming a passivating solid electrolyte interphase (SEI) layer on the surface, which is crucial to stable battery function. The formation of this layer is influenced by the surface chemistry of the active material. Ge NWs with different surface passivations exhibited different battery performance and rate capability.

One strategy used to improve the performance of nanostructured Si, is the addition of a surface coating layer. Si nanowires coated with an SiO_x shell examined using *in situ*

transmission electron microscopy during battery cycling showed reduced volume expansion, at the expense of complete lithiation. When the nanowire is delithiated, pores are observed to form in the amorphized Si due to the SiO_x shell, which prevents the migration of vacancies formed during delithiation to the nanowire surface.

To increase the performance of the LIB, both the anode and cathode capacities must increase. Prelithiation of the Si anode was crucial to improve the capacity and stability of battery cycling for both lithium iron phosphate and sulfur cathodes, and the prelithiation process used strongly influenced battery performance. In a full cell with a sulfur cathode, no sulfides were observed in the Si SEI layer, due to the use of a carbon interlayer. Si-S batteries fully consumed the lithium nitrate electrolyte additive during cycling, resulting in high levels of electrolyte degradation that contaminated the anode and reduced battery stability.

Table of Contents

List of Tables xiii

List of Figures xiv

Chapter 1: Introduction 1

1.1 Introduction to Lithium Ion Batteries 1

1.1.1 Silicon and Germanium Battery Anodes 3

1.1.2 Anode Formulation and Materials 5

1.1.3 Electrolytes and Solid Electrolyte Interphase Layers 7

1.1.4 Cathodes and Si Anode Full Cell Batteries 8

1.2 Introduction to Nanowire Synthesis 10

1.2.1 SLFS Synthesis Growth Considerations 13

1.2.2 Nanowire Surface Passivation 15

1.3 Dissertation Overview 15

1.4 References 17

Chapter 2: High Capacity Group IV Type II Clathrates for Lithium Ion Batteries 26

2.1 Introduction 26

2.2 Experimental Details 27

2.2.1 Chemicals 27

2.2.2 Clathrate Synthesis 28

2.2.3 Electrochemical Testing 28

2.2.4 Characterization 29

2.3 Results and Discussion 29

2.4 Conclusions 36

2.5 References 37

Chapter 3: In-Situ Surface Passivated Germanium Nanowires for Lithium-Ion Batteries 40

3.1 Introduction 40

3.2 Experimental Details 42

3.2.1 Chemicals 42

3.2.2 Nanowire Synthesis 42
3.2.3 Electrochemical Testing....44
3.2.4 Characterization 44
3.3 Results and Discussion 45
3.4 Conclusions....60
3.5 References....60

Chapter 4: *In Situ* TEM of Oxide Shell-Induced Pore Formation in (De)lithiated Silicon Nanowires....64
4.1 Introduction....64
4.2 Experimental Details....65
4.2.1 Chemicals....65
4.2.2 Nanowire Synthesis 65
4.2.3 Oxide Shell Growth 66
4.2.4 *In Situ* TEM Measurements 67
4.3 Results and Discussion 67
4.4 Conclusions....77
4.5 References....78

Chapter 5: Si Anodes with Lithium Iron Phosphate and Sulfur Cathodes: Impact of Prelithiation Method and XPS Analysis 81
5.1 Introduction....81
5.2 Experimental Details....87
5.2.1 Chemicals....87
5.2.2 Silicon Nanowire Synthesis 87
5.2.3 Carbon Coated Lithium Iron Phosphate Synthesis 88
5.2.4 Sulfur Cathode and Microporous Carbon Interlayer 88
5.2.5 Electrochemical Testing....88
5.2.6 Characterization 89
5.3 Results and Discussion 90
5.3.1 Half Cell Performance 90
5.3.2 Prelithiation Method 95

5.3.3 XPS Analysis of SiNW SEI layer 101
5.4 Conclusions 105
5.5 References 106

Chapter 6: Conclusions and Future Directions 114
6.1 Conclusions 114
6.1.1 Group IV Type II Clathrate Lithium Ion Batteries 114
6.1.2 In-Situ Surface Passivated Germanium Nanowire Batteries 115
6.1.3 *In Situ* TEM of Oxide Shell Silicon Nanowires 116
6.1.4 Full Cell Batteries Using Silicon Anodes 116
6.2 Future Directions 117
6.2.1 Full Cells 117
6.2.2 Liquid *In Situ* TEM 117
6.2.3 Other Ions 118
6.3 References 120

APPENDICES 123

Appendix A 123
A.1 Supporting Figures 123
A.2 References 127

Appendix B 129
B.1 Supporting Data 129

Appendix C 132
C.1 Supporting Data 132
C.2 Supporting Videos 138

Appendix D 139
D.1 Supporting Figures 139
D.2 References 147

References 148

Vita 163

List of Tables

Table 5.1 Surface elemental composition (at. %) after extended cycling determined by XPS, of species on SiNW and Li metal electrode surfaces. 102

Table A.1 Comparison of the capacity from this work with previously reported clathrate battery results from literature. 124

Table C.1 Statistics of Observed Volume Expansion of Si Nanowires with an SiO_x Shell before and after Lithiation 132

List of Figures

Figure 1.1 Full cell capacity as a function of anode capacity using the fixed cathode capacities of $LiCoO_2$ (137 mAh/g), $LiFePO_4$ (170 mAh/g), and sulfur (1673 mAh/g). 3

Figure 1.2 Battery preparation consists of 3 main parts: slurry making, electrode preparation, and coin cell assembly. 6

Figure 1.3 Transmission electron microscope (TEM) images of Au seeded SLFS grown (a) Si and (b) Ge nanowires. Scanning electron microscope (SEM) images of Au seeded SLFS grown (c) Si and (d) Ge nanowires 11

Figure 1.4 Cartoon depiction of the SFLS growth of Au seeded Si nanowires on an Au-Si binary phase diagram.....12

Figure 2.1 Scanning electron microscope (SEM) (a, b) images of the (a) $Na_{0.5}Si_{136}$ and (b) $Na_{0.5}(Si_{0.9}Ge_{0.1})_{136}$ clathrate powders. (c) Powder XRD patterns for both clathrates. 30

Figure 2.2 Charge capacity (■) and Coulombic efficiency (□) of $Na_{0.5}Si_{136}$ (blue) and $Na_{0.5}(Si_{0.9}Ge_{0.1})_{136}$ (black) clathrate batteries cycled at (a) a current density of 0.125 A/g, (b) various current densities from 0.125 A/g to 2.5 A/g, (c) a current density of 1.25 A/g. 32

Figure 2.3 (a) Voltage profiles for Si clathrate batteries cycled at a current density of 0.125 A/g. (b) Differential capacity profiles for the same battery at different cycles. (c) Voltage profiles for $Na_{0.5}(Si_{0.9}Ge_{0.1})_{136}$ clathrate batteries cycled at a current density of 0.125 A/g. (d) Differential capacity profiles for the same battery at different cycles. 35

Figure 3.1 (a) SEM and (b) TEM of Ge NWs after synthesis, but without surface passivation.....46

Figure 3.2 (a) Chemical structures for the three passivations. (b) Reaction scheme for 1-dodecene (DDE) passivation. (c) Reaction scheme for 1-dodecanethiol (DDT) and 11-mercaptoundecanoic acid (MUA) passivation.....47

Figure 3.3 (a) ATR-FTIR spectra of Ge NWs passivated with 1-dodecene and 1-dodecanethiol. Dashed lines indicated the symmetric and asymmetric CH_2 stretching peak positions. (b) ATR-FTIR spectra of Ge NWs passivated with 11-mercaptoundecanoic acid.....48

Figure 3.4 Charge capacity (■) and Coulombic efficiency (□) of passivated Ge NWs cycled at (a) a rate of C/10, (b) a rate of 1 C and (c) various cycle rates from C/10 to 10 C for 10 cycles each, where 1 C = 1211 mAh/g. ...50

Figure 3.5 Voltage profiles for LIBs with (a) pristine Ge nanowires, (b) DDE, (c) DDT, and (d) MUA passivated Ge NWs at cycle rates ranging from C/10 to 10 C. The voltage profiles correspond to the 2^{nd} cycle data in Figure 3c with 1 C = 1211 mAh/g. The same legend shown in (a) is used for all plots. 51

Figure 3.6 Differential capacity profiles for LIBs with (a) pristine nanowires, (b) DDE passivation, (c) DDT, and (d) MUA at a cycle rate of C/10 with 1 C = 1211 mAh/g. 53

Figure 3.7 High resolution XPS elemental scans for batteries after 1 cycle (darker lines) and >80 cycles (lighter lines) (a) C 1s, (b) O 1s, (c) F 1s. 56

Figure 3.8 Elemental film compositions for batteries after (a) 1 cycle (b) >80 cycles. 58

Figure 4.1 (a) TEM images showing an 8 nm thick oxide shell grown on the Si nanowire surface. This nanowire has a twin defect along its length. (b) A magnified image of the same wire more clearly shows the SiO_x shell. (c) STEM HAADF image of a Si nanowire with an SiO_x shell with associated EDS mapping of the (d) O and (e) Si distribution. Elemental analysis shows the nanowire has a Si core and an oxide shell.....68

Figure 4.2 TEM images of a Si nanowire with an SiO_x shell taken during the first (a) lithiation and (b) delithiation cycle. The nanowire experiences 132.6% volume expansion and retains a crystalline core of 24 nm diameter at the end of lithiation. (See accompanying video file LithiationVideo_1.mp4 listed in Appendix C) (c) A cartoon of the *in situ* TEM nanobattery set up. (d) A higher magnification TEM image of pores that form in the amorphous Si region of the nanowire after delithiation.....69

Figure 4.3 TEM images of a Si nanowire with an SiO_x shell showing the formation of pores in the nanowire during the first delithiation. (See accompanying video file PoreVideo_2.mp4 listed in Appendix C.).....72

Figure 4.4 TEM images showing a Si nanowire with an SiO_x shell that bursts during the first cycle of lithiation. (See accompanying video file BurstWireVideo_3.mp4 listed in Appendix C.) This nanowire experiences a volume expansion of 273% upon lithiation and does not retain a crystalline core. 73

Figure 4.5 TEM images showing a Si nanowire with an SiO_x shell that bursts at a single point during the first lithiation. (See accompanying video file BurstWirePoresVideo_5.mp4 listed in Appendix C). A portion of the nanowire shell remains intact and pores begin to form only in this part of the nanowire during delithiation. 74

Figure 4.6 (a) TEM electron diffraction pattern of a Si nanowire with an SiO_x shell after delithiation, which shows the only crystalline species present is Li_2O. (b) A magnified TEM image of the SiO_x shell on a Si nanowire after delithiation that shows a visibly rough surface. The SiO_x shell is an active participant in the lithiation reaction and becomes rougher during the course of the battery cycle. 75

Figure 4.7 A schematic showing the pore formation mechanism in a Si nanowire with an SiO_x shell. During lithiation, the lithiation front moves first along the nanowire surface (1) and then inward toward the core (2). The nanowire reaches a point of maximum lithiation with a remaining crystalline core. Upon delithiation, vacancies form in the lithiated amorphous Si region. These vacancies are unable to migrate to the surface of the nanowire due to the SiO_x shell and nucleate into pores as more Li diffuses out of the nanowire.....77

Figure 5.1 Charge storage capacity Q_T, of LIBs fabricated using different cathode materials with capacities Q_C, plotted as a function of the capacity of the anode Q_A: $LiCoO_2$ (137 mAh/g), $LiFePO_4$ (170 mAh/g), and sulfur (1673 mAh/g).....82

Figure 5.2 Schematic describing full cell preparation. (a) Prelithiation of a Si anode by contact with Li foil prior to full cell assembly was done in the glovebox using two glass slides and paper binder clips. (b) S cathodes were used in conjunction with a carbon interlayer, which is positioned between the cathode and separator in the full cell. Full cells are made using two spacers to create even pressure within the coin cell. 83

Figure 5.3 SEM images of the (a) S cathode, (b) microporous carbon interlayer, (c) SiNWs, and (d) carbon-coated $LiFePO_4$. (e) EDS mapping of the P, C, O and Fe in the sample; scale bars represent 5µm. Elemental analysis confirms the presence of carbon. 91

Figure 5.4 Capacity (■) and Coulombic efficiency (□) of half cells and their associated voltage profiles. (a) SiNW anode half cells tested using glyme and carbonate electrolytes, (b) voltage profile for the SiNW anode using glyme electrolyte, (c-d) S cathode half cell, and (e-f) c-LFP cathode half cell. The same legend shown in (b) is used for (d, f). 94

Figure 5.5 (a) Charge capacity (■) and Coulombic efficiency (□) of SiNW-LFP full cells of different prelithiation methods. "Contact" prelithiated SiNW anodes were held in contact with Li foil for 15 minutes to lithiate them prior to full cell assembly. "Tester" anodes were prelithiated on the battery tester at an applied current density of 200 mA/g to 100 mV in a half cell, then disassembled. Full cell batteries were cycled at an applied current density of 17 mA/g_{LFP}. (b) The voltage profiles of the "Tester" prelithiated full cell. 97

Figure 5.6 (a) Charge capacity (■) and Coulombic efficiency (□) of SiNW-S full cells prelithiated by different methods. "Contact" prelithiated SiNW anodes were held in contact with Li foil for 30 minutes before assembly into a full cell. "Tester" prelithiated batteries were prelithiated using a battery tester at an applied current density of 200 mA/g to 10 mV. Full cell batteries were cycled at an applied current density of 200 mA/g_S. (b) The voltage profile of the "Tester" prelithiated full cell.....99

Figure 5.7 Charge capacity (■) and Coulombic efficiency (□) of (a) a SiNW anode prelithiated mechanically for 15 minutes and tested in a half cell with carbonate electrolyte, and (c) SiNW anodes prelithiated mechanically for different times and tested in a half cell with sulfur electrolyte. All batteries were cycled at an applied current density of 250 mA/g. ..101

Figure 5.8 High resolution XPS scans of the C 1s, S 2p, and N 1s regions, for half cell and full cell SiNW electrodes, and the Li metal anode of a S half cell.....104

Figure 6.1 Illustration of a sealed liquid cell battery.[22].....118

Figure A.1 Powder XRD pattern and Reitveld refinement for (a) $Na_{0.5}Si_{136}$ and (b) $Na_{0.5}(Si_{0.9}Ge_{0.1})_{136}$ clathrates.....123

Figure A.2 Charge capacity (closed squares) and Coulombic efficiency (open squares) of the $Si_{0.9}Ge_{0.1}$ clathrate cycled at current density of 0.025 A/g. Battery capacity had faded by over 50% by the 30th cycle.....125

Figure A.3 Charge capacity (closed squares) and Coulombic efficiency (open squares) of the $Si_{0.9}Ge_{0.1}$ clathrate cycled at current density of 0.125 A/g cycled for 200 cycles. After the first 50 cycles capacity loss occurs more slowly.....126

Figure A.4 Differential capacity profiles for the Si clathrate cycled at a current density of 0.125 A/g between cycles 10 – 50 demonstrating the gradual decrease and broadening of the peak at 450 mV. 127

Figure B.1 Charge capacity (closed squares) and Coulombic efficiency (open squares) of DDE and MUA passivated Ge NWs cycled at a rate of 1 C, where 1 C = 1211 mAh/g. Very little capacity loss occurs over 200 cycles.....129

Figure B.2 Charge capacity (closed squares) and Coulombic efficiency (open squares) of (a) pristine and (b) DDT passivated Ge NWs cycled at a rate of 1 C, where 1 C = 1211 mAh/g. Results are consistent across multiple batteries tested.....130

Figure B.3 XPS peak deconvolution of C 1s high resolution elemental scans for the batteries after 1 cycle. 131

Figure C.1 TEM images of a Si nanowire with an SiO_x shell during a second (a) lithiation and (b) delithiation cycle. (See accompanying video file LithiationVideo_1.mp4) Prior to the second lithiation, the shell was 16 nm thick. Pores are not visible as the nanowire lithiates, but reappear upon delithiation, as seen in (c) a more magnified TEM image. 134

Figure C.2 TEM images of Si nanowires after (a) the first delithiation and (b) the second. Pores are visible in each image and the diameter has increased after a second delithiation. 135

Figure C.3 TEM images of a Si nanowire with an SiO_x shell that bursts during the first lithiation. (See accompanying video file BurstWireVideo_4.mp4) The experiences 301% volume expansion at full lithiation and does not retain a crystalline Si core. Upon delithiation, the nanowire does not form pores. 136

Figure C.4 TEM images of a Si nanowire with a SiO_x shell and a twin defect lithiating. Lithiation proceeds both along the interface between the SiO_x shell and the nanowire as well as along the twin interface. The nanowire breaks into two at the gold (Au) nanoparticle defect in the center of the nanowire after 287 s. The nanowire lithiates fully and does not retain a crystalline core. 137

Figure D.1. TEM images of the c-LFP sample. The micron sized particles are made up of nanosized LFP 139

Figure D.2 Voltage profiles for SiNW anode in a half cell battery using carbonate electrolyte corresponding with the battery shown in Figure 5.4a. The battery was tested at an applied current density of 250 mA/g. 140

Figure D.3 SiNW anodes were prelithiated in contact with Li for various times for each electrolyte. 141

Figure D.4 Charge capacity (■) and Coulombic efficiency (□) of (a) SiNW-LFP full cells not prelithiated for several anode-to-cathode capacity ratios. Cycled at an applied current density of 17 mA/g_{LFP}. (b) SiNW-S full cells prelithiated in contact with Li foil for 30 minutes prior to full cell assembly for several anode-to-cathode capacity ratios. The batteries were cycled at an applied current density of 100 mA/g_S. (c) SiNW-LF full cells prelithiated on a battery tester for two anode-to-cathode capacity ratios. Cycled at an applied current density of 17 mA/g_{LFP}. (d) SiNW-S full cells prelithiated on a battery tester to 10 mV for several anode-to-cathode capacity ratios. The batteries were cycled at an applied current density of 100 mA/g_S. 143

Figure D.5 High resolution elemental XPS spectra for three electrodes after extended cycling: a SiNW-S anode, a Li metal anode from a S half cell, and a SiNW anode from a half cell. Deconvolutions for the C 1s and S 2p orbitals are shown. 145

Figure D.6 XPS survey spectrum of three electrodes zoomed in to the S 2p region: a SiNW-S anode, a Li metal anode from a S half cell, and a SiNW anode from a half cell. Polysulfides would be found between 167-162 eV, but there are none present. It appears the interlayer was successful at preventing Li polysulfides formed during cycling from migrating to the anode in all three cells. 146

Figure D.7 High resolution XPS elemental scan of the S 2p region of the S cathode from a SiNW-S full cell, after extended cycling, showing sulfur oxides and bridging sulfur. 147

Chapter 1: Introduction

1.1 Introduction to Lithium Ion Batteries

Lithium (Li) ion batteries have become ubiquitous since their first commercial production in 1991 by Sony. They are the preferred energy storage source for small electronics because Li has the highest gravimetric and volumetric density of any material, allowing for smaller, longer lasting batteries.[1] Li ion batteries (LIBs) are also gaining popularity for larger applications such as electric vehicles and grid scale energy storage.[2] American electricity demands are predicted to grow by 0.8% annually to nearly 5 trillion kilo-watt hours by 2040.[3] A significant portion of this demand will be met by intermittent renewable generation such as wind and solar energy. Energy storage is going to be crucial to this growth if it is to be done in a way that is both resilient and environmentally sustainable. LIBs have emerged as the energy storage option of choice to be paired with renewable generation. Large LIB storage facilities have already opened in Australia and California.[4,5] However, in order to meet the demands of high-power applications and improve safety, next generation LIBs require improved energy storage materials.

LIBs produce energy by shuttling Li^+ ions back and forth between anode and cathode host materials. Early battery researchers were plagued by dendrite growth on the surface of Li metal anodes during cycling which led to shorting and battery failure.[6] The dangers of using a pure metal anode can be avoided by employing intercalation materials, that hold Li^+ ions in interstitial sites of the host material, for both the cathode and anode. Because there are no structural changes to the host material during this process, there is little volume expansion, resulting in high stability over many cycles.[7] This kind of "rocking-chair" battery technology was first demonstrated in 1980.[8]

Modern LIBs have a lithium cobalt oxide ($LiCoO_2$) cathode and graphite (C_6) anode. During charging, an external voltage is applied causing Li^+ ions to dissociate from

the cathode to cross through an insulating membrane to the anode where they intercalate into graphite. Conversely, during discharge, the Li^+ ions deintercalate from the graphite sheets and spontaneously flow from the higher energy anode to the lower energy cathode. The current produced in this process can be used to power an external circuit.

The maximum theoretical capacities of $LiCoO_2$ and graphite are 274 mAh/g and 372 mAh/g, respectively. However, the practical capacity of $LiCoO_2$ is limited to 140 mAh/g due to safety concerns.[1] This low capacity limits the total storage capability of the LIB. Indeed, the total capacity of the full cell battery is determined by the equation:

$$Q_T = \frac{Q_A Q_C}{Q_A + Q_C} \qquad (1)$$

where Q_A and Q_C are the capacities of the anode and cathode, respectively. From Equation (1), a full cell using graphite and $LiCoO_2$ has a total theoretical capacity of only 102 mAh/g. Although there are modest gains to be made by increasing the anode Li^+ storage capacity alone, to realize the full benefits of a higher capacity anode, the storage capacity of the cathode must increase as well. Next generation cathodes can be broadly categorized as intercalation and conversion materials.[9] Intercalation cathodes are the most commonly used type of cathodes today, and the field of commercially used cathodes has grown significantly from only $LiCoO_2$.[2] Second generation intercalation cathodes that are commercially used today, include further transition metal oxides and polyanion compounds, such as $LiNi_{0.8}Co_{0.15}Al_{0.05}O_2$ (NCA), $LiMn_2O_4$,, $LiNi_{1-x-y}Mn_xCo_y$ (NMC), $Li_4Ti_5O_{12}$ (LTO)and $LiFePO_4$ (LFP).[2,9] The principle advantages to these materials are high structural stability, high voltage (between 3.4-4.0 V), and low cost starting materials. Intercalation cathodes still under development, but with significantly higher storage capacity are vanadium oxides (>300 mAh/g), and molybdenum oxides (>600 mAh/g).[10–12] Conversion cathode materials undergo a reaction with Li^+ ions, resulting in a change in structure and breaking of chemical bonds, as well as significantly higher battery capacity.[9]

The two subcategories within conversion cathodes are metal halides and pure metals. Metal flourides have high capacity, between 500-700 mAh/g.[13] Sulfur (S) is one of the most highly studied conversion cathode materials because it has a high theoretical capacity of 1675 mAh/g.[14–18] Another conversion metal cathode that has been studied is selenium.[19] Figure 1.1 demonstrates the potential increase in total capacity using a next generation conversion cathode compared with first and second generation intercalation cathodes and a Si anode.

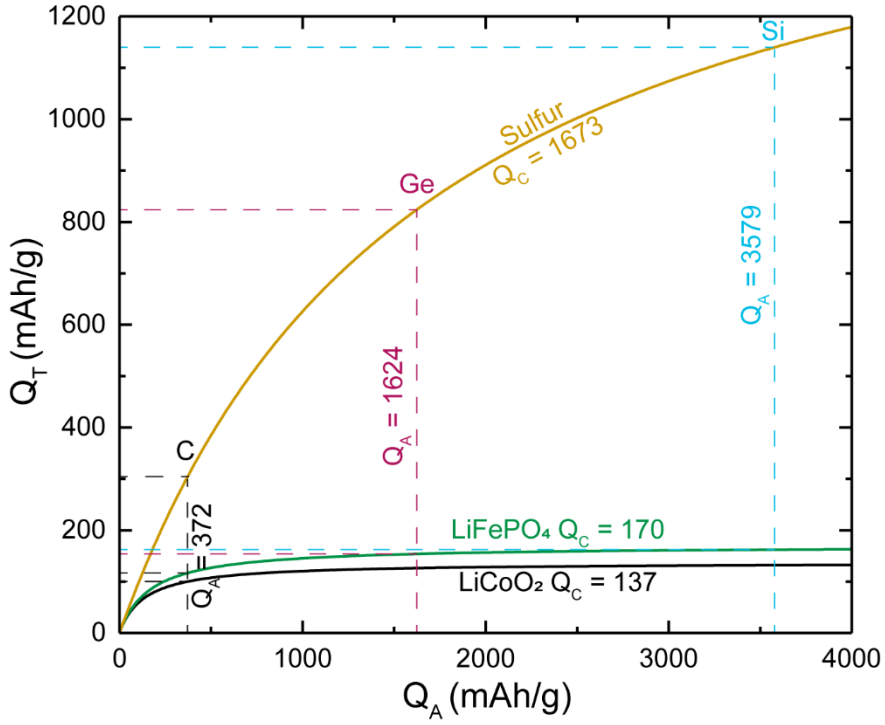

Figure 1.1 Full cell capacity as a function of anode capacity using the fixed cathode capacities of $LiCoO_2$ (137 mAh/g), $LiFePO_4$ (170 mAh/g), and sulfur (1673 mAh/g).

1.1.1 Silicon and Germanium Battery Anodes

There has been a great deal of research done on next generation anodes to improve the performance of LIBs. Current graphite anodes host Li^+ ions in interstitial sites.

Although this results in little volume expansion and thus high stability, it limits the storage capacity of the material. Alloy anode materials are of interest because they typically have significantly higher storage capacity. During cycling they alloy with Li^+, breaking the bonds of the host material. The advantage to alloy materials is that they can hold more Li than traditional intercalation anodes. Silicon (Si) and germanium (Ge) have been identified as potential Li anode materials as they have theoretical specific capacities of 3579 mAh/g and 1624 mAh/g respectively. However, this process results in significant volume change during cycling leading to mechanical fracture and poor stability.[7] Researchers have found that nanostructured materials with a diameter less than 200 nm can accommodate Li-induced volume changes during cycling without the growth of cracks.[7] Furthermore, nanostructuring allows for room temperature reaction of Si and Ge with Li with high reversibility, making them feasible next generation anode materials.[20] Many different structures of Si and Ge have been investigated for batteries, including nanowires, nanotubes, thin films, and nanospheres, and more unique structures such as egg-yoke. [21–24]

Lithiation of crystalline Si proceeds by a two-phase reaction. Crystalline Si initially forms an amorphous alloy with Li during cycling. Upon further lithiation it will form the crystalline phase of $Li_{15}Si_4$:[21]

Lithiation: $Si \underset{Li}{\rightarrow} a - Li_xSi \underset{Li}{\rightarrow} Li_{15}Si_4$ (2)

Delithiation: $Li_{15}Si_4 \underset{-Li}{\longrightarrow} a - Li_2Si \underset{-Li}{\longrightarrow} a - Si$ (3)

Subsequent cycles: $a - Si \underset{Li}{\rightarrow} a - Li_2Si \underset{Li}{\rightarrow} Li_{15}Si_4$ (4)

Here "*a"* refers to an amorphous phase. Equation (2) describes the lithiation process of the first cycle, starting with crystalline Si. Subsequent cycles are described by Equation (4), starting with amorphous Si. Although the phase $Li_{22}Si_5$ exists at high temperatures, $Li_{15}Si_4$ is the terminal phase accessible at room temperature.[7,25] This two phase mechanism has been confirmed visually using *in situ* transmission electron microscope (TEM) imaging

during battery cycling.[26,27] Upon lithiation, a shell of lithiated amorphous Si forms and then migrates into the Si core. Often a crystalline Si core will remain even after prolonged lithation.[26] This reaction process is accompanied by significant volume expansion, nearly 310% upon full lithiation.[7]

Ge lithiation takes place by a multistep process:[28]

Lithiation: $Ge \underset{Li}{\rightarrow} Li_9Ge_4 \underset{Li}{\rightarrow} Li_7Ge_2 \underset{Li}{\rightarrow} Li_{15}Ge_4 + Li_{22}Ge_5$ (5)

Germanium experiences approximately 270% volume expansion during lithiation.[24] Although Ge is more expensive than Si and has a lower capacity, there are several key areas in which it performs better. Ge has a lower band gap than Si and is thus more electrically conductive, it also has much higher rate capability due to higher Li^+ diffusion rates.[29] Ge lithiates isotropically, compared with anisotropic lithiation of Si, which lowers the stress concentration experienced in certain planar directions and improving stability.[7] When the electrode is fully charged, both the $Li_{15}Ge_4$ and $Li_{22}Ge_5$ phases are present.[28]

1.1.2 Anode Formulation and Materials

Nanowires synthesized using traditional chemical vapor deposition (CVD) techniques are grown directly attached to a current collector, which is beneficial for battery performance, but results in low mass loading.[30] Solution synthesized nanowires can be used in a battery slurry to create an electrode. Preparing a slurry cast battery samples consists of three main steps: slurry making, electrode preparation, and coin cell assembly (Figure 1.2). Variation in each step can significantly impact performance, so it is important to include sufficient detail for reproducibility. Marks *et al.* and Talaie *et al*. have published useful guides to best practices in LIB coin-cell electrode making.[31,32]

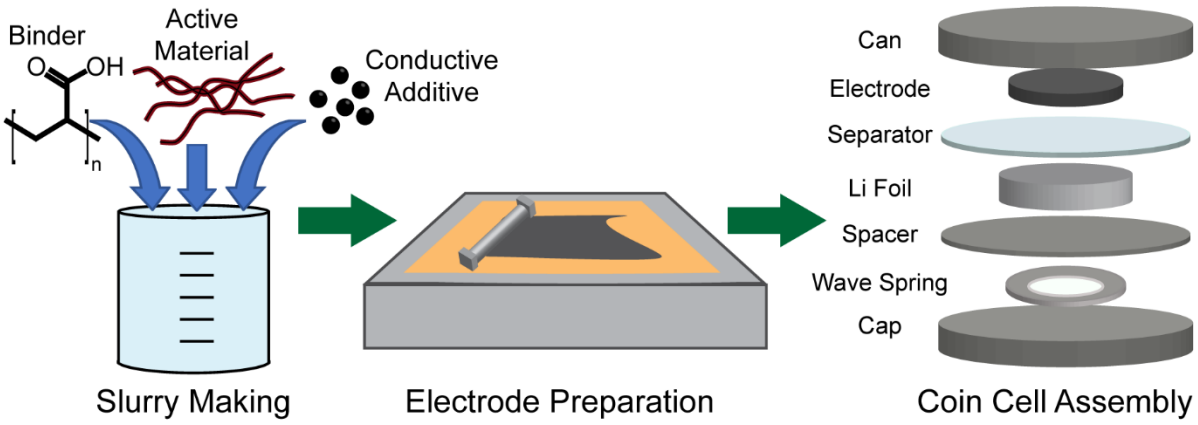

Figure 1.2 Battery preparation consists of 3 main parts: slurry making, electrode preparation, and coin cell assembly.

The slurry making step is arguably the most complicated part of the process as there are many different methods by which this can be done. A battery slurry consists of the active material, a conductive additive, and a polymeric binder all dispersed in a solvent. Because Si has low conductivity, a conductive additive such as carbon black must be included. Slurry composition can significantly impact battery performance and method sections need to clearly state the ratio of active materials and additives. Adding more conductive additive can increase surface area and thus parasitic reactions with the electrolyte, which lowers coulombic efficiency.[31,33–35] Another difficulty faced by slurry cast batteries, is the segregation of conductive and active materials during battery cycling, resulting in lower stability.[36] Modifying Si to increase the conductivity, and thus avoid using a conductive additive, through inclusion of tin or a carbon coating avoids this problem.[37–40]

Many binders have been examined for use in battery electrodes. The most common binders are poly(vinylidene) fluoride (PVdF), carboxymethyl cellulose (CMC), alginate (Alg), and poly(acrylic acid) (PAA).[21,24,35,41] The concentration of solvent added is a crucial

factor in slurry making and depends on the desired final thickness, the ratio of active material to conductive additive, and the kind of active material.[31] The slurry concentration must be thin enough to be doctor-bladed, but thick enough to ensure the slurry can adhere to the current collector and not delaminate during drying; approximately a viscosity of 1000 mPa-s (similar to maple syrup).[42]

1.1.3 Electrolytes and Solid Electrolyte Interphase Layers

Electrolyte choice is crucial for stable battery cycling. The energy separation between the Lowest Unoccupied Molecular Orbital (LUMO) and the Highest Occupied Molecular Orbital (HOMO) of the electrolyte is the window of stability in which it can operate. If the anode has a higher chemical potential than the LUMO or the cathode has a lower chemical potential than the HOMO, then the electrolyte will react with the electrodes.[43] This reactive process will proceed until a passivating solid electrolyte interphase (SEI) layer is formed on the electrode surface and prevents further reaction. For a battery to cycle stably, it is crucial to have an SEI layer that is thin and robust to protect the active material surface further direct reaction with the electrolyte.[24,43–45] The SEI layer must be thin enough to not interfere with Li^+ transport to the electrode surface, and electronically conductive. If the SEI layer is not robust, it will continually crack during electrode expansion and contraction, exposing new active material surface to the electrolyte and building a thicker SEI layer which can hinder Li^+ transport and increase electrical resistance.[24,44] The SEI layer can also trap a significant amount of Li^+, resulting in irreversible charge loss.[46] While this is unavoidable in the first cycle, upon initial SEI formation, if a stable SEI layer is formed, further electrolyte degradation will ideally be prevented.[44] In a half cell battery, with unlimited Li^+ ions, the amount of Li^+ consumed by the SEI layer will not hinder battery cycling. However, in a full cell, with a limited amount

of Li^+, this can result in battery fade upon repeat cycling.[47] To counter this effect, Si anodes can be lithiated prior to battery fabrication. There are several possible techniques to incorporate additional Li, including using a Li metal additive,[48–50] mixing Li and Si nanoparticles to make a LiSi additive,[51] controlled lithiation using a battery tester, and contact lithiation by sandwiching Li and Si.[52,53]

The composition of the SEI layer is crucial to Si anode effectiveness, and this composition is dependent on the electrolyte used. Research has been done investigating the effectiveness of electrolytes made with glyme, carbonates, or different salts.[45,54–57] The resulting SEI layer, in a battery cycled with a traditional carbonate electrolyte, consists primarily carbonate byproducts as well as LiF formed by decomposition of the salt additive.[45] An approach to SEI layer improvement is including an additive in the electrolyte. Two of the most researched additives for Si anode batteries are vinylene carbonate (VC) and fluoroethylene carbonate (FEC), which improves stability by creating a thinner, denser, SEI layer. [57–60]

1.1.4 Cathodes and Si Anode Full Cell Batteries

LFP has high thermal stability, operates at a voltage of 3.4 V, has a high thermal and structural stability, and is made from abundant and inexpensive starting materials.[43,61–65] Combined with a Si anode, a full cell using a LFP cathode would have a 155 mAh/g capacity, as calculated by Equation (1). This is a 55% increase over current $LiCoO_2$-graphite batteries. However, LFP suffers from low electronic conductivity, slow Li^+ diffusion, and a capacity of only 170 mAh/g.[9,62,65] In order to overcome these limitations, researchers have found that nanostructuring and carbon coating LFP is necessary.[61,63,65]

There have been few demonstrations of a full cell battery using Si as the anode and LFP as the cathode.[66–68] One of the primary problems these cells experience is high initial

capacity loss, and Li loss to the anode SEI, which results in poor stability.[66] This problem has previously been studied in Si-$LiCoO_2$ full cells, which found that Li^+ loss at the anode was the primary source of capacity loss.[69] Because the capacity of Si is so much higher than intercalation cathode materials, the cathode has to be very thick in order to match the anode capacity, which can hinder rate capability as Li^+ diffusion takes longer.[70] Having an anode-to-cathode capacity ratio close to 1 is important for maximizing the Li utilization within the cell.[71]

Sulfur has an extremely high capacity, of 1673 mAh/g, giving a full cell capacity with Si of 1102 mAh/g, calculated from Equation (1), nearly 10 times that of current technology. However, there are several technical difficulties to the practical use of S, as it has high electrical resistance, experiences large volume change of 80% during lithiation, and has high irreversible capacity loss.[14] During lithiation, long polysulfide chains are reduced by Li to Li_2S via intermediate lithium polysulfides. These lithium polysulfides are soluble in battery electrolytes, and experience a cycle of dissolution and deposition during battery cycling.[14] However, dissolved species can passivate the anode, which increases impedance, corrodes the Li metal anode, and reduces the amount of S that can be used for energy storage.[14] One strategy to reduce polysulfide migration to the anode is using a carbon interlayer in conjunction with a S cathode.[72–77] The interlayer can be made from a conductive material that with adsorb the dissolved polysulfides and reactivate them in subsequent cycles, which prevents them from migrating to the anode surface and increases active material utilization.[14,78] The interlayer is positioned between the cathode and the separator.

S cathodes are incompatible with traditional carbonate electrolytes because the sulfur anions will react rapidly with the carbonates.[16,79–81] Instead, glyme based electrolytes are used because they are less reactive with the S anions.[16] Lithium nitrate ($LiNO_3$) is an

important additive to glyme electrolytes for S battery function.[55,56,82–84] $LiNO_3$ can form a protective layer of Li_xNO_y on the Li metal anode, in a half cell, which prevents anode reaction with polysulfides, and it can oxidize degredation species in the electrolyte to prevent further reaction.[55,56] $LiNO_3$ is progressively consumed in the formation of a passivation coating on the anode side and is reduced irreversibly on the cathode side at voltages below 1.6 V, which ultimately leads to the total consumption of $LiNO_3$ and low battery performance.[82,84]

There has been a great deal of research interest into Si-S full cells.[47,71,79,83–89] Common problems faced by these full cell batteries were insufficient Li^+ ions due to Li^+ consumption by the SEI, S migration from the cathode to the anode, incompatibility between the Si anode and the glyme electrolyte, unbalanced anode-to-cathode capacity, and excess electrolyte, which results in diffusion of the active material away from the cathode.[71,83,84,87]

1.2 Introduction to Nanowire Synthesis*

Nanowires are a class of one-dimensional (1D), thread-like materials with a nanoscale diameter and a high aspect ratio. As shown in Figure 1.3, they are crystalline, with a diameter of 10-100 nm and a length of 1-10 μm. Nanowires exhibit different properties from the bulk material, such as diameter-dependent quantum confinement in the radial direction and improved strength and flexibility.[90–92] There are many potential applications for semiconductor nanowires, including textiles,[92,93] field-effect transistors,[94] photovoltaics,[95] chemical sensing,[96] and LIBs.[7,29,30,37,38,59] They are particularly attractive

* The work contained in this chapter is the subject of a scholarly article that is currently in preparation. Authors on this work include Emily R. Adkins, Hyun Gyung Kim, Reken N. Patel, Andrew L. Heilman, and Brian A. Korgel. Emily Adkins was responsible for writing the sections included in this dissertation, making the figures, and editing the completed document.

for battery applications because their 1D shape creates a convenient path for charge transport in the electrode.

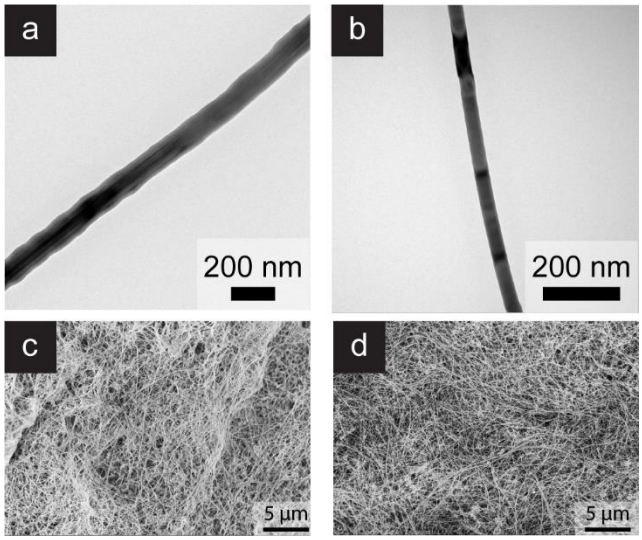

Figure 1.3 Transmission electron microscope (TEM) images of Au seeded SLFS grown (a) Si and (b) Ge nanowires. Scanning electron microscope (SEM) images of Au seeded SLFS grown (c) Si and (d) Ge nanowires

Growth of a 1D crystalline semiconductor material by vapor-liquid-solid (VLS) synthesis was first demonstrated by Wagner and Ellis in 1964.[97] They discovered the possibility of growing Si "whiskers" from a gold (Au) seed particle and a Si precursor in the vapor phase. This synthetic technique was further improved upon by Trentler et. al. in 1995 upon the discovery of solution-liquid-solid (SLS) synthesis of III-V semiconductors.[98] By using a solution phase solvent it was possible for the synthesis to be done at significantly lower temperatures. The supercritical fluid-liquid-solid (SFLS) synthesis developed by Holmes et. al. allowed for the creation of Si nanowires with a narrow diameter distribution.[99] This technique was later extended to the synthesis of Ge nanowires.[100]

In the naming scheme for reaction mechanisms, the first term (ie., vapor, solution, or supercritical fluid), refers to the state of the solvating reaction media, the second refers to the state of the metal seed particle-semiconductor alloy, and the third is the state of the resulting nanowire growth. In an SLS or SFLS reaction, a metal seed and a semiconductor precursor are introduced into a reactor in hot solvent together. The reaction temperature needs to be sufficiently high for the semiconductor precursor to decompose. This is depicted in Figure 1.4 using solution synthesized Au seeded Si nanowires as an example.[101] In region I, of the Au-Si binary phase diagram, the Si precursor decomposes and liberated Si atoms begin to alloy with the Au seed nanoparticle. In region II, the Si-Au alloy becomes a liquid droplet. As Si incorporation into the liquid Au-Si particle continues and reaches supersaturation, in region III, the Si atoms start to precipitate and crystallize. The 1D nanowire morphology develops naturally as the only crystalline growth develops at only a single interface between the alloy droplet and the semiconductor crystal.[90]

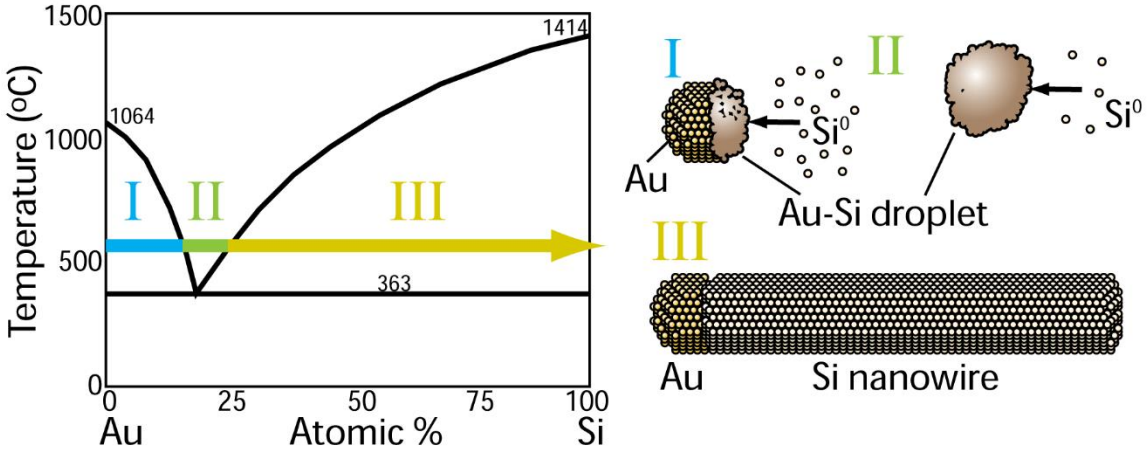

Figure 1.4 Cartoon depiction of the SFLS growth of Au seeded Si nanowires on an Au-Si binary phase diagram.

1.2.1 SLFS Synthesis Growth Considerations

SFLS reactions occur at higher temperature than SLS, above the super critical temperature for the chosen solvent. SFLS syntheses occur at temperatures of 380°C or higher and pressures of at least 6.9 MPa, which is well above the critical point of the most commonly used solvents, toluene (T_c = 319°C, P_c = 4.1 MPa), benzene (T_c = 289°C, P_c = 4.9 MPa), and hexane (T_c = 235°C, P_c = 3.0 MPa). This allows for a greater range in choice of seed metal and a high reactant diffusion coefficient, which reduces unwanted nanocrystal growth and increases nanowire yield.[99,100] If the temperature of the reaction is above the eutectic temperature, then the seed metal-semiconductor alloy is in the liquid state and the reaction mechanism is referred to as SLS or SFLS (depending on the state of the solvating media). If the temperature is below the eutectic temperature, then the synthesis mechanism is SFSS or SSS. Solid-phase seeding can occur due to two possible effects: catalytic seeds such as Ni, Co, and Fe that can help promote precursor decomposition which lowers the growth temperature, or the nanoscale diameter of the seed particles allows for easier solid-state diffusion of the precursor.[100,102]

The SFLS growth of semiconductor nanowires can be highly sensitive to changes in parameters. Through extensive study, the impact of precursor, solvent, concentration, temperature, and metal seed has been fine tuned to produce high quality nanowires.[39,99,103,104] Precursor decomposition kinetics are a determining factor in nanowire quality and yield. The precursor needs to decompose sufficiently fast to produce nanowires, but too quickly results in the formation of spherical semiconductor particles.[100] Aryl semiconductor precursors can be used to produce nanowires because they undergo a disproportionation reaction during decomposition.[104] This occurs due to the resonance effect of the benzene ring, which lowers the activation energy for disproportion. Because

there is no similar effect in alkyl precursors, they are not sufficiently reactive to produce nanowires.

Semiconductor precursor decomposition is significantly affected by the solvent in which the reaction takes place.[103] Aromatic solvents help to stabilize the disproportionation reaction and thus produce a higher yield of nanowires. Benzene has been shown to produce the highest yield and quality of nanowires, though today we use toluene out of safety considerations.[103] Although the Si/Au eutectic temperature is 363ºC, the Si nanowire reaction must be carried out at above 450ºC for sufficient precursor decomposition to produce Si nanowires. Any higher than 500ºC and there will be a high degree of carbonaceous by-products.[104] Furthermore, there is a threshold concentration of 120 mM phenylsilane (419 µL in a 30 mL injection cylinder) below which no nanowires will be formed. The growth temperature of Ge nanowires is significantly lower than for Si, 380ºC, because aryl germanes are more reactive than aryl silanes.[104]

Different metal catalyst particles can be used to seed SFLS nanowire growth. Nanowires can also be seeded using metal particles formed in-situ by the decomposition of a metal salt.[39,105] SFLS Si nanowire growth has been demonstrated with many different metal salts including gallium, tin, and indium.[106] SFSS Si nanowire growth can be accomplished using a copper metal salt. The choice in metal seed particle will affect the yield and quality of the nanowires produced and influence the molar ratio of metal to silicon necessary to produce nanowires. Au-seeded SFLS reactions require a relatively low ratio of Au-to-Si of only 1:1000 in order to produce wires.[103] In comparison, a high ratio of Sn to Si, nearly 1:22, is required.[107] Similar to Si, different metal catalysts can be used to seed Ge nanowire growth. Solution Ge nanowire growth has been demonstrated with Ni and Au nanoparticles.[100,108]

1.2.2 Nanowire Surface Passivation

SFLS grown Ge nanowires can passivated directly in the reactor in a single step by hydrogermylation or thiolation.[109,110] This technique can be used for many different passivations and functionalizations including alkenes, thiols, and polyethylene glycol.[109,111] The same process cannot be used for the SFLS grown silicon nanowires made from phenylsilane due to the polyphenyl silane shell on the surface of the nanowires. Ge nanowires are highly susceptible to oxidation and organic monolayer passivation has been shown to protect the nanowire surface.[109] Passivation can also effect nanowire performance in devices. For example, thiol passivated Ge nanowires perform better than bare Ge nanowires in batteries.[112]

1.3 Dissertation Overview

Changes in LIB electrode materials are required to meet the needs of emerging large-scale high-power applications such as extended range electric vehicles and grid storage for solar power. Si and Ge are potential options for future anodes, as they store significantly more Li^+ than graphite. However, they still face significant challenges before they are practically useful. The research in this dissertation endeavors to understand how the structure and surface chemistry of Si and Ge materials impact their performance in LIBs.

Chapter 2 studies two group IV clathrates in LIBs, $Na_{0.5}Si_{136}$ and $Na_{0.5}(Si_{0.9}Ge_{0.1})_{136}$. Both materials exhibited superior reversible cycling performance compared with previous clathrate battery studies. Analysis of differential capacity plots revealed that the clathrates amorphized during the first lithiation, resulting in high Li capacity, but degraded over repeated cycling.

Chapters 3 and 4 examine the impact surface modification has on nanowires as battery materials. In Chapter 3, Ge nanowires with different surface functionalizations were

studied in LIBs. Passivation impacted nanowire performance and stability during cycling and altered the resulting SEI layer composition. In chapter 4, SiNWs with a silicon oxide (SiO_x) shell were observed *in situ* during lithiation and delithiation using transmission electron microscopy (TEM). Pores form in the amorphized silicon upon the first delithiation. We propose that this is caused by a high barrier to vacancy migration in the SiO_x shell, which prevents vacancies formed during delithiation from transporting through the shell to the nanowire surface.

Chapter 5 examines two full cell systems using SiNW anodes and either carbon coated $LiFePO_4$ or sulfur (S) cathodes. While all materials show high capacity and stability in half cell tests, they faced significant hurdles in stable full cell performance. Specifically, we studied the impact different prelithiation methods have on SiNW anode performance, the influence of capacity matching on full cell performance, and whether species transfer from the cathode to the anode impacts SEI formation. The goal of this work was to highlight common difficulties in next generation full cell batteries with SiNW anodes, and better understand the difference between Si anode performance in a full versus half cell.

Finally, Chapter 6 summarizes the results from these studies and suggests future research directions.

1.4 REFERENCES

(1) Tarascon, J.-M.; Armand, M. Issues and Challenges Facing Rechargeable Lithium Batteries. *Nature* **2001**, *414* (6861), 359–367.

(2) Blomgren, G. E. The Development and Future of Lithium Ion Batteries. *J. Electrochem. Soc.* **2017**, *164* (1), A5019–A5025.

(3) EIA - Annual Energy Outlook 2017 https://www.eia.gov/outlooks/aeo/ (accessed Jan 25, 2018).

(4) Spector, J. California's big battery experiment: a turning point for energy storage? http://www.theguardian.com/sustainable-business/2017/sep/15/californias-big-battery-experiment-a-turning-point-for-energy-storage (accessed Jan 25, 2018).

(5) Tesla Mega-Battery in Australia Activated. *BBC News*. December 1, 2017.

(6) Armand, M.; Tarascon, J.-M. Building Better Batteries. *Nature* **2008**, *451* (7179), 652–657.

(7) McDowell, M. T.; Lee, S. W.; Nix, W. D.; Cui, Y. 25th Anniversary Article: Understanding the Lithiation of Silicon and Other Alloying Anodes for Lithium-Ion Batteries. *Adv. Mater.* **2013**, *25* (36), 4966–4985.

(8) Lazzari, M.; Scrosati, B. A Cyclable Lithium Organic Electrolyte Cell Based on Two Intercalation Electrodes. *J. Electrochem. Soc.* **1980**, *127* (3), 773–774.

(9) Nitta, N.; Wu, F.; Lee, J. T.; Yushin, G. Li-Ion Battery Materials: Present and Future. *Mater. Today* **2015**, *18* (5), 252–264.

(10) Chernova, N. A.; Roppolo, M.; Dillon, A. C.; Whittingham, M. S. Layered Vanadium and Molybdenum Oxides: Batteries and Electrochromics. *J. Mater. Chem.* **2009**, *19* (17), 2526–2552.

(11) Meduri, P.; Clark, E.; Kim, J. H.; Dayalan, E.; Sumanasekera, G. U.; Sunkara, M. K. MoO3–x Nanowire Arrays As Stable and High-Capacity Anodes for Lithium Ion Batteries. *Nano Lett.* **2012**, *12* (4), 1784–1788.

(12) Tsang, C.; Manthiram, A. Synthesis of Nanocrystalline VO 2 and Its Electrochemical Behavior in Lithium Batteries. *J. Electrochem. Soc.* **1997**, *144* (2), 520–524.

(13) Li, H.; Richter, G.; Maier, J. Reversible Formation and Decomposition of LiF Clusters Using Transition Metal Fluorides as Precursors and Their Application in Rechargeable Li Batteries. *Adv. Mater.* **2003**, *15* (9), 736–739.

(14) Manthiram, A.; Fu, Y.; Chung, S.-H.; Zu, C.; Su, Y.-S. Rechargeable Lithium–Sulfur Batteries. *Chem. Rev.* **2014**, *114* (23), 11751–11787.

(15) Peled, E.; Gorenshtein, A.; Segal, M.; Sternberg, Y. Rechargeable Lithium□sulfur Battery (Extended Abstract). *J. Power Sources* **1989**, *26* (3), 269–271.

(16) Peled, E.; Sternberg, Y.; Gorenshtein, A.; Lavi, Y. Lithium-Sulfur Battery: Evaluation of Dioxolane-Based Electrolytes. *J. Electrochem. Soc.* **1989**, *136* (6), 1621–1625.

(17) Rauh, R. D.; Abraham, K. M.; Pearson, G. F.; Surprenant, J. K.; Brummer, S. B. A Lithium/Dissolved Sulfur Battery with an Organic Electrolyte. *J. Electrochem. Soc.* **1979**, *126* (4), 523–527.

(18) Yamin, H.; Peled, E. Electrochemistry of a Nonaqueous Lithium/Sulfur Cell. *J. Power Sources* **1983**, *9* (3), 281–287.

(19) Abouimrane, A.; Dambournet, D.; Chapman, K. W.; Chupas, P. J.; Weng, W.; Amine, K. A New Class of Lithium and Sodium Rechargeable Batteries Based on Selenium and Selenium–Sulfur as a Positive Electrode. *J. Am. Chem. Soc.* **2012**, *134* (10), 4505–4508.

(20) Gao, B.; Sinha, S.; Fleming, L.; Zhou, O. Alloy Formation in Nanostructured Silicon. *Adv. Mater.* **2001**, *13* (11), 816–819.

(21) Obrovac, M. N.; Chevrier, V. L. Alloy Negative Electrodes for Li-Ion Batteries. *Chem. Rev.* **2014**, *114* (23), 11444–11502.

(22) Liu, N.; Wu, H.; McDowell, M. T.; Yao, Y.; Wang, C.; Cui, Y. A Yolk-Shell Design for Stabilized and Scalable Li-Ion Battery Alloy Anodes. *Nano Lett.* **2012**, *12* (6), 3315–3321.

(23) Zhang, Y.; Li, Y.; Wang, Z.; Zhao, K. Lithiation of SiO2 in Li-Ion Batteries: In Situ Transmission Electron Microscopy Experiments and Theoretical Studies. *Nano Lett.* **2014**, *14* (12), 7161–7170.

(24) Bogart, T. D.; Chockla, A. M.; Korgel, B. A. High Capacity Lithium Ion Battery Anodes of Silicon and Germanium. *Curr. Opin. Chem. Eng.* **2013**, *2* (3), 286–293.

(25) Obrovac, M. N.; Christensen, L. Structural Changes in Silicon Anodes during Lithium Insertion/Extraction. *Electrochem. Solid-State Lett.* **2004**, *7* (5), A93–A96.

(26) Liu, X. H.; Huang, J. Y. In Situ TEM Electrochemistry of Anode Materials in Lithium Ion Batteries. *Energy Environ. Sci.* **2011**, *4* (10), 3844–3860.

(27) Liu, X. H.; Wang, J. W.; Huang, S.; Fan, F.; Huang, X.; Liu, Y.; Krylyuk, S.; Yoo, J.; Dayeh, S. A.; Davydov, A. V.; et al. In Situ Atomic-Scale Imaging of Electrochemical Lithiation in Silicon. *Nat. Nanotechnol.* **2012**, *7* (11), 749–756.

(28) Yoon, S.; Park, C.-M.; Sohn, H.-J. Electrochemical Characterizations of Germanium and Carbon-Coated Germanium Composite Anode for Lithium-Ion Batteries. *Electrochem. Solid-State Lett.* **2008**, *11* (4), A42–A45.

(29) Chockla, A. M.; Klavetter, K. C.; Mullins, C. B.; Korgel, B. A. Solution-Grown Germanium Nanowire Anodes for Lithium-Ion Batteries. *ACS Appl. Mater. Interfaces* **2012**, *4* (9), 4658–4664.

(30) Chan, C. K.; Peng, H.; Liu, G.; McIlwrath, K.; Zhang, X. F.; Huggins, R. A.; Cui, Y. High-Performance Lithium Battery Anodes Using Silicon Nanowires. *Nat. Nanotechnol.* **2008**, *3* (1), 31–35.

(31) Marks, T.; Trussler, S.; Smith, A. J.; Xiong, D.; Dahn, J. R. A Guide to Li-Ion Coin-Cell Electrode Making for Academic Researchers. *J. Electrochem. Soc.* **2011**, *158* (1), A51–A57.

(32) Talaie, E.; Bonnick, P.; Sun, X.; Pang, Q.; Liang, X.; Nazar, L. F. Methods and Protocols for Electrochemical Energy Storage Materials Research. *Chem. Mater.* **2017**, *29* (1), 90–105.

(33) Zheng, H.; Li, J.; Song, X.; Liu, G.; Battaglia, V. S. A Comprehensive Understanding of Electrode Thickness Effects on the Electrochemical Performances of Li-Ion Battery Cathodes. *Electrochimica Acta* **2012**, *71*, 258–265.

(34) Bridel, J.-S.; Azaïs, T.; Morcrette, M.; Tarascon, J.-M.; Larcher, D. Key Parameters Governing the Reversibility of Si/Carbon/CMC Electrodes for Li-Ion Batteries. *Chem. Mater.* **2010**, *22* (3), 1229–1241.

(35) Magasinski, A.; Zdyrko, B.; Kovalenko, I.; Hertzberg, B.; Burtovyy, R.; Huebner, C. F.; Fuller, T. F.; Luzinov, I.; Yushin, G. Toward Efficient Binders for Li-Ion Battery Si-Based Anodes: Polyacrylic Acid. *ACS Appl. Mater. Interfaces* **2010**, *2* (11), 3004–3010.

(36) Ng, S. H.; Wang, J.; Wexler, D.; Chew, S. Y.; Liu, H. K. Amorphous Carbon-Coated Silicon Nanocomposites: A Low-Temperature Synthesis via Spray Pyrolysis and Their Application as High-Capacity Anodes for Lithium-Ion Batteries. *J. Phys. Chem. C* **2007**, *111* (29), 11131–11138.

(37) Bogart, T. D.; Lu, X.; Gu, M.; Wang, C.; Korgel, B. A. Enhancing the Lithiation Rate of Silicon Nanowires by the Inclusion of Tin. *RSC Adv.* **2014**, *4* (79), 42022–42028.

(38) Bogart, T. D.; Oka, D.; Lu, X.; Gu, M.; Wang, C.; Korgel, B. A. Lithium Ion Battery Peformance of Silicon Nanowires with Carbon Skin. *ACS Nano* **2014**, *8* (1), 915–922.

(39) Chockla, A. M.; Klavetter, K. C.; Mullins, C. B.; Korgel, B. A. Tin-Seeded Silicon Nanowires for High Capacity Li-Ion Batteries. *Chem. Mater.* **2012**, *24* (19), 3738–3745.

(40) Chockla, A. M.; Harris, J. T.; Akhavan, V. A.; Bogart, T. D.; Holmberg, V. C.; Steinhagen, C.; Mullins, C. B.; Stevenson, K. J.; Korgel, B. A. Silicon Nanowire

Fabric as a Lithium Ion Battery Electrode Material. *J. Am. Chem. Soc.* **2011**, *133* (51), 20914–20921.

(41) Kovalenko, I.; Zdyrko, B.; Magasinski, A.; Hertzberg, B.; Milicev, Z.; Burtovyy, R.; Luzinov, I.; Yushin, G. A Major Constituent of Brown Algae for Use in High-Capacity Li-Ion Batteries. *Science* **2011**, *334* (6052), 75–79.

(42) Ngadi, M. O.; Yu, L. J. Rheological Properties of Canadian Maple Syrup. *Can. Biosyst. Eng. Genie Biosyst. Au Can. Rev. Soc. Can. Genie Agroaliment. Biol.* **2004**.

(43) Goodenough, J. B.; Kim, Y. Challenges for Rechargeable Li Batteries. *Chem. Mater.* **2010**, *22* (3), 587–603.

(44) Verma, P.; Maire, P.; Novák, P. A Review of the Features and Analyses of the Solid Electrolyte Interphase in Li-Ion Batteries. *Electrochimica Acta* **2010**, *55* (22), 6332–6341.

(45) Chan, C. K.; Ruffo, R.; Hong, S. S.; Cui, Y. Surface Chemistry and Morphology of the Solid Electrolyte Interphase on Silicon Nanowire Lithium-Ion Battery Anodes. *J. Power Sources* **2009**, *189* (2), 1132–1140.

(46) Winter, M.; Besenhard, J. O. Electrochemical Lithiation of Tin and Tin-Based Intermetallics and Composites. *Electrochimica Acta* **1999**, *45* (1), 31–50.

(47) Yang, Y.; McDowell, M. T.; Jackson, A.; Cha, J. J.; Hong, S. S.; Cui, Y. New Nanostructured Li2S/Silicon Rechargeable Battery with High Specific Energy. *Nano Lett.* **2010**, *10* (4), 1486–1491.

(48) Forney, M. W.; Ganter, M. J.; Staub, J. W.; Ridgley, R. D.; Landi, B. J. Prelithiation of Silicon–Carbon Nanotube Anodes for Lithium Ion Batteries by Stabilized Lithium Metal Powder (SLMP). *Nano Lett.* **2013**, *13* (9), 4158–4163.

(49) Wang, Z.; Fu, Y.; Zhang, Z.; Yuan, S.; Amine, K.; Battaglia, V.; Liu, G. Application of Stabilized Lithium Metal Powder (SLMP®) in Graphite Anode – A High Efficient Prelithiation Method for Lithium-Ion Batteries. *J. Power Sources* **2014**, *260* (Supplement C), 57–61.

(50) Jarvis, C. R.; Lain, M. J.; Yakovleva, M. V.; Gao, Y. A Prelithiated Carbon Anode for Lithium-Ion Battery Applications. *J. Power Sources* **2006**, *162* (2), 800–802.

(51) Zhao, J.; Lu, Z.; Liu, N.; Lee, H.-W.; McDowell, M. T.; Cui, Y. Dry-Air-Stable Lithium Silicide–lithium Oxide Core–shell Nanoparticles as High-Capacity Prelithiation Reagents. *Nat. Commun.* **2014**, *5*, 5088.

(52) Kim, H. J.; Choi, S.; Lee, S. J.; Seo, M. W.; Lee, J. G.; Deniz, E.; Lee, Y. J.; Kim, E. K.; Choi, J. W. Controlled Prelithiation of Silicon Monoxide for High Performance Lithium-Ion Rechargeable Full Cells. *Nano Lett.* **2016**, *16* (1), 282–288.

(53) Liu, N.; Hu, L.; McDowell, M. T.; Jackson, A.; Cui, Y. Prelithiated Silicon Nanowires as an Anode for Lithium Ion Batteries. *ACS Nano* **2011**, *5* (8), 6487–6493.

(54) Aurbach, D.; Weissman, I.; Schechter, A.; Cohen, H. X-Ray Photoelectron Spectroscopy Studies of Lithium Surfaces Prepared in Several Important Electrolyte Solutions. A Comparison with Previous Studies by Fourier Transform Infrared Spectroscopy. *Langmuir* **1996**, *12* (16), 3991–4007.

(55) Etacheri, V.; Geiger, U.; Gofer, Y.; Roberts, G. A.; Stefan, I. C.; Fasching, R.; Aurbach, D. Exceptional Electrochemical Performance of Si-Nanowires in 1,3-Dioxolane Solutions: A Surface Chemical Investigation. *Langmuir* **2012**, *28* (14), 6175–6184.

(56) Jaumann, T.; Balach, J.; Klose, M.; Oswald, S.; Eckert, J.; Giebeler, L. Role of 1,3-Dioxolane and LiNO3 Addition on the Long Term Stability of Nanostructured Silicon/Carbon Anodes for Rechargeable Lithium Batteries. *J. Electrochem. Soc.* **2016**, *163* (3), A557–A564.

(57) Xu, K. Electrolytes and Interphases in Li-Ion Batteries and Beyond. *Chem. Rev.* **2014**, *114* (23), 11503–11618.

(58) Nakai, H.; Kubota, T.; Kita, A.; Kawashima, A. Investigation of the Solid Electrolyte Interphase Formed by Fluoroethylene Carbonate on Si Electrodes. *J. Electrochem. Soc.* **2011**, *158* (7), A798–A801.

(59) Chockla, A. M.; Klavetter, K. C.; Mullins, C. B.; Korgel, B. A. Tin-Seeded Silicon Nanowires for High Capacity Li-Ion Batteries. *Chem. Mater.* **2012**, *24* (19), 3738–3745.

(60) Martin, L.; Martinez, H.; Ulldemolins, M.; Pecquenard, B.; Le Cras, F. Evolution of the Si Electrode/Electrolyte Interface in Lithium Batteries Characterized by XPS and AFM Techniques: The Influence of Vinylene Carbonate Additive. *Solid State Ion.* **2012**, *215*, 36–44.

(61) Li, W.; Hwang, J.; Chang, W.; Setiadi, H.; Chung, K. Y.; Kim, J. Ultrathin and Uniform Carbon-Layer-Coated Hierarchically Porous LiFePO4 Microspheres and Their Electrochemical Performance. *J. Supercrit. Fluids* **2016**, *116* (Supplement C), 164–171.

(62) Chung, S.-Y.; Bloking, J. T.; Chiang, Y.-M. Electronically Conductive Phospho-Olivines as Lithium Storage Electrodes. *Nat. Mater.* **2002**, *1* (2), 123–128.

(63) Padhi, A. K.; Nanjundaswamy, K. S.; Goodenough, J. B. Phospho-olivines as Positive-Electrode Materials for Rechargeable Lithium Batteries. *J. Electrochem. Soc.* **1997**, *144* (4), 1188–1194.

(64) Striebel, K.; Shim, J.; Srinivasan, V.; Newman, J. Comparison of LiFePO4 from Different Sources. *J. Electrochem. Soc.* **2005**, *152* (4), A664–A670.

(65) Wang, J.; Sun, X. Understanding and Recent Development of Carbon Coating on LiFePO4 Cathode Materials for Lithium-Ion Batteries. *Energy Environ. Sci.* **2012**, *5* (1), 5163–5185.

(66) Cho, G. B.; Song, M. G.; Bae, S. H.; Kim, J. K.; Choi, Y. J.; Ahn, H. J.; Ahn, J. H.; Cho, K. K.; Kim, K. W. Surface-Modified Si Thin Film Electrode for Li Ion Batteries (LiFePO4/Si) by Cluster-Structured Ni under Layer. *J. Power Sources* **2009**, *189* (1), 738–742.

(67) Kim, J.-K.; Scheers, J.; Ryu, H.-S.; Ahn, J.-H.; Nam, T.-H.; Kim, K.-W.; Ahn, H.-J.; Cho, G.-B.; Jacobsson, P. A Layer-Built Rechargeable Lithium Ribbon-Type Battery for High Energy Density Textile Battery Applications. *J. Mater. Chem. A* **2014**, *2* (6), 1774–1780.

(68) Prosini, P. P.; Cento, C.; Rufoloni, A.; Rondino, F.; Santoni, A. A Lithium-Ion Battery Based on LiFePO4 and Silicon Nanowires. *Solid State Ion.* **2015**, *269*, 93–97.

(69) Petibon, R.; Chevrier, V. L.; Aiken, C. P.; Hall, D. S.; Hyatt, S. R.; Shunmugasundaram, R.; Dahn, J. R. Studies of the Capacity Fade Mechanisms of LiCoO2/Si-Alloy: Graphite Cells. *J. Electrochem. Soc.* **2016**, *163* (7), A1146–A1156.

(70) Eom, K.; Lee, J. T.; Oschatz, M.; Wu, F.; Kaskel, S.; Yushin, G.; Fuller, T. F. A Stable Lithiated Silicon–chalcogen Battery via Synergetic Chemical Coupling between Silicon and Selenium. *Nat. Commun.* **2017**, *8*, 13888.

(71) Piwko, M.; Kuntze, T.; Winkler, S.; Straach, S.; Härtel, P.; Althues, H.; Kaskel, S. Hierarchical Columnar Silicon Anode Structures for High Energy Density Lithium Sulfur Batteries. *J. Power Sources* **2017**, *351*, 183–191.

(72) Chung, S.-H.; Manthiram, A. A Hierarchical Carbonized Paper with Controllable Thickness as a Modulable Interlayer System for High Performance Li–S Batteries. *Chem. Commun.* **2014**, *50* (32), 4184–4187.

(73) Fu, Y.; Su, Y.-S.; Manthiram, A. Li2S-Carbon Sandwiched Electrodes with Superior Performance for Lithium-Sulfur Batteries. *Adv. Energy Mater.* **2014**, *4* (1), n/a-n/a.

(74) Su, Y.-S.; Fu, Y.; Guo, B.; Dai, S.; Manthiram, A. Fast, Reversible Lithium Storage with a Sulfur/Long-Chain-Polysulfide Redox Couple. *Chem. – Eur. J.* **2013**, *19* (26), 8621–8626.

(75) Su, Y.-S.; Manthiram, A. A New Approach to Improve Cycle Performance of Rechargeable Lithium–sulfur Batteries by Inserting a Free-Standing MWCNT Interlayer. *Chem. Commun.* **2012**, *48* (70), 8817–8819.

(76) Su, Y.-S.; Manthiram, A. Lithium–sulphur Batteries with a Microporous Carbon Paper as a Bifunctional Interlayer. *Nat. Commun.* **2012**, *3*, 1166.

(77) Zu, C.; Su, Y.-S.; Fu, Y.; Manthiram, A. Improved Lithium–sulfur Cells with a Treated Carbon Paper Interlayer. *Phys. Chem. Chem. Phys.* **2013**, *15* (7), 2291–2297.

(78) Su, Y.-S.; Manthiram, A. Lithium–sulphur Batteries with a Microporous Carbon Paper as a Bifunctional Interlayer. *Nat. Commun.* **2012**, *3*, 1166.

(79) Yim, T.; Park, M.-S.; Yu, J.-S.; Kim, K. J.; Im, K. Y.; Kim, J.-H.; Jeong, G.; Jo, Y. N.; Woo, S.-G.; Kang, K. S.; et al. Effect of Chemical Reactivity of Polysulfide toward Carbonate-Based Electrolyte on the Electrochemical Performance of Li–S Batteries. *Electrochimica Acta* **2013**, *107*, 454–460.

(80) Gao, J.; Lowe, M. A.; Kiya, Y.; Abruña, H. D. Effects of Liquid Electrolytes on the Charge–Discharge Performance of Rechargeable Lithium/Sulfur Batteries: Electrochemical and in-Situ X-Ray Absorption Spectroscopic Studies. *J. Phys. Chem. C* **2011**, *115* (50), 25132–25137.

(81) Cheon, S.-E.; Ko, K.-S.; Cho, J.-H.; Kim, S.-W.; Chin, E.-Y.; Kim, H.-T. Rechargeable Lithium Sulfur Battery I. Structural Change of Sulfur Cathode During Discharge and Charge. *J. Electrochem. Soc.* **2003**, *150* (6), A796–A799.

(82) Zhang, S. S. Role of LiNO3 in Rechargeable Lithium/Sulfur Battery. *Electrochimica Acta* **2012**, *70*, 344–348.

(83) Lee, S.-K.; Oh, S.-M.; Park, E.; Scrosati, B.; Hassoun, J.; Park, M.-S.; Kim, Y.-J.; Kim, H.; Belharouak, I.; Sun, Y.-K. Highly Cyclable Lithium–Sulfur Batteries with a Dual-Type Sulfur Cathode and a Lithiated Si/SiOx Nanosphere Anode. *Nano Lett.* **2015**, *15* (5), 2863–2868.

(84) Brückner, J.; Thieme, S.; Böttger-Hiller, F.; Bauer, I.; Grossmann, H. T.; Strubel, P.; Althues, H.; Spange, S.; Kaskel, S. Carbon-Based Anodes for Lithium Sulfur Full Cells with High Cycle Stability. *Adv. Funct. Mater.* **2014**, *24* (9), 1284–1289.

(85) Aurbach, D.; Pollak, E.; Elazari, R.; Salitra, G.; Kelley, C. S.; Affinito, J. On the Surface Chemical Aspects of Very High Energy Density, Rechargeable Li–Sulfur Batteries. *J. Electrochem. Soc.* **2009**, *156* (8), A694–A702.

(86) Choi, J.-W.; Kim, J.-K.; Cheruvally, G.; Ahn, J.-H.; Ahn, H.-J.; Kim, K.-W. Rechargeable Lithium/Sulfur Battery with Suitable Mixed Liquid Electrolytes. *Electrochimica Acta* **2007**, *52* (5), 2075–2082.

(87) Elazari, R.; Salitra, G.; Gershinsky, G.; Garsuch, A.; Panchenko, A.; Aurbach, D. Rechargeable Lithiated Silicon–sulfur (SLS) Battery Prototypes. *Electrochem. Commun.* **2012**, *14* (1), 21–24.

(88) Lee, J. T.; Kim, H.; Nitta, N.; Eom, K.; Lee, D.-C.; Wu, F.; Lin, H.-T.; Zdyrko, B.; Cho, W. I.; Yushin, G. Stabilization of Selenium Cathodes via in Situ Formation of Protective Solid Electrolyte Layer. *J. Mater. Chem. A* **2014**, *2* (44), 18898–18905.

(89) Zhou, D.; Liu, M.; Yun, Q.; Wang, X.; He, Y.-B.; Li, B.; Yang, Q.-H.; Cai, Q.; Kang, F. A Novel Lithiated Silicon–Sulfur Battery Exploiting an Optimized Solid-Like Electrolyte to Enhance Safety and Cycle Life. *Small* **2017**, *13* (3), n/a-n/a.

(90) Wang, F.; Dong, A.; Buhro, W. E. Solution–Liquid–Solid Synthesis, Properties, and Applications of One-Dimensional Colloidal Semiconductor Nanorods and Nanowires. *Chem. Rev.* **2016**, *116* (18), 10888–10933.

(91) Smith, D. A.; Holmberg, V. C.; Lee, D. C.; Korgel, B. A. Young's Modulus and Size-Dependent Mechanical Quality Factor of Nanoelectromechanical Germanium Nanowire Resonators. *J. Phys. Chem. C* **2008**, *112* (29), 10725–10729.

(92) Smith, D. A.; Holmberg, V. C.; Korgel, B. A. Flexible Germanium Nanowires: Ideal Strength, Room Temperature Plasticity, and Bendable Semiconductor Fabric. *ACS Nano* **2010**, *4* (4), 2356–2362.

(93) Holmberg, V. C.; Bogart, T. D.; Chockla, A. M.; Hessel, C. M.; Korgel, B. A. Optical Properties of Silicon and Germanium Nanowire Fabric. *J. Phys. Chem. C* **2012**, *116* (42), 22486–22491.

(94) Cui, Y.; Lieber, C. M. Functional Nanoscale Electronic Devices Assembled Using Silicon Nanowire Building Blocks. *Science* **2001**, *291* (5505), 851–853.

(95) Steinhagen, C.; Akhavan, V. A.; Goodfellow, B. W.; Panthani, M. G.; Harris, J. T.; Holmberg, V. C.; Korgel, B. A. Solution−Liquid−Solid Synthesis of CuInSe2 Nanowires and Their Implementation in Photovoltaic Devices. *ACS Appl. Mater. Interfaces* **2011**, *3* (5), 1781–1785.

(96) Cui, Y.; Wei, Q.; Park, H.; Lieber, C. M. Nanowire Nanosensors for Highly Sensitive and Selective Detection of Biological and Chemical Species. *Science* **2001**, *293* (5533), 1289–1292.

(97) Wagner, R. S.; Ellis, W. C. VAPOR-LIQUID-SOLID MECHANISM OF SINGLE CRYSTAL GROWTH. *Appl. Phys. Lett.* **1964**, *4* (5), 89–90.

(98) Trentler, T. J.; Hickman, K. M.; Goel, S. C.; Viano, A. M.; Gibbons, P. C.; Buhro, W. E. Solution-Liquid-Solid Growth of Crystalline III-V Semiconductors: An Analogy to Vapor-Liquid-Solid Growth. *Science* **1995**, *270* (5243), 1791–1794.

(99) Holmes, J. D.; Johnston, K. P.; Doty, R. C.; Korgel, B. A. Control of Thickness and Orientation of Solution-Grown Silicon Nanowires. *Science* **2000**, *287* (5457), 1471–1473.

(100) Hanrath, T.; Korgel, B. A. Nucleation and Growth of Germanium Nanowires Seeded by Organic Monolayer-Coated Gold Nanocrystals. *J. Am. Chem. Soc.* **2002**, *124* (7), 1424–1429.

(101) Chockla, A. M. *Solution Grown Silicon and Germanium Nanostructures: Characterization and Application as Lithium Ion Battery Anode Materials*; University of Texas: Austin, Tex., 2012.

(102) Tuan, H.-Y.; Lee, D. C.; Korgel, B. A. Nanocrystal-Mediated Crystallization of Silicon and Germanium Nanowires in Organic Solvents: The Role of Catalysis and Solid-Phase Seeding. *Angew. Chem.* **2006**, *118* (31), 5308–5311.

(103) Tuan, H.-Y.; Korgel, B. A. Importance of Solvent-Mediated Phenylsilane Decompositon Kinetics for High-Yield Solution-Phase Silicon Nanowire Synthesis. *Chem. Mater.* **2008**, *20* (4), 1239–1241.

(104) Lee, D. C.; Hanrath, T.; Korgel, B. A. The Role of Precursor-Decomposition Kinetics in Silicon-Nanowire Synthesis in Organic Solvents. *Angew. Chem. Int. Ed.* **2005**, *44* (23), 3573–3577.

(105) Bogart, T. D.; Lu, X.; Korgel, B. A. Precision Synthesis of Silicon Nanowires with Crystalline Core and Amorphous Shell. *Dalton Trans.* **2013**, *42* (35), 12675–12680.

(106) Bogart, T. D. Silicon Nanowires : Synthesis and Use as Lithium-Ion Battery Anodes. Thesis, 2014.

(107) Bogart, T. D.; Oka, D.; Lu, X.; Gu, M.; Wang, C.; Korgel, B. A. Lithium Ion Battery Peformance of Silicon Nanowires with Carbon Skin. *ACS Nano* **2014**, *8* (1), 915–922.

(108) Lu, X.; Harris, J. T.; Villarreal, J. E.; Chockla, A. M.; Korgel, B. A. Enhanced Nickel-Seeded Synthesis of Germanium Nanowires. *Chem. Mater.* **2013**, *25* (10), 2172–2177.

(109) Holmberg, V. C.; Korgel, B. A. Corrosion Resistance of Thiol- and Alkene-Passivated Germanium Nanowires. *Chem. Mater.* **2010**, *22* (12), 3698–3703.

(110) Hanrath, T.; Korgel, B. A. Chemical Surface Passivation of Ge Nanowires. *J. Am. Chem. Soc.* **2004**, *126* (47), 15466–15472.

(111) Holmberg, V. C.; Rasch, M. R.; Korgel, B. A. PEGylation of Carboxylic Acid-Functionalized Germanium Nanowires. *Langmuir* **2010**, *26* (17), 14241–14246.

(112) Yuan, F.-W.; Yang, H.-J.; Tuan, H.-Y. Alkanethiol-Passivated Ge Nanowires as High-Performance Anode Materials for Lithium-Ion Batteries: The Role of Chemical Surface Functionalization. *ACS Nano* **2012**, *6* (11), 9932–9942.

Chapter 2: High Capacity Group IV Type II Clathrates for Lithium Ion Batteries†

2.1 Introduction

Lithium ion batteries (LIBs) dominate the market for portable electronics because they offer the highest power density of any available battery technology. However, changes in electrode materials are required to meet the needs of emerging, large-scale, high-power, applications such as extended range electric vehicles and grid storage for solar power.[1–5] Silicon (Si) and germanium (Ge) are attractive anode materials for next generation batteries because they have significantly higher capacities, 3579 mAh/g and 1624 mAh/g, respectively, compared with current graphite anodes, 372 mAh/g.[3]

Group IV alloy clathrates are interesting potential anode materials because their electronic properties are uniquely tunable. Clathrate materials are formed at high temperature or pressure around guest atoms that serve as a template for the formation of cage-like structures.[6] Inorganic clathrates can take the form of two different crystalline structures, referred to as type I and type II. Type I has the structure A_8X_{46} and type II has the structure $A_{24}X_{136}$ where A is the guest atom and X is the Group IV element. The electronic properties of the clathrate can be tuned by changing guest atom concentration, which alters the carrier concentration of the material.[7,8] In this way clathrates can be altered to behave as insulators, semiconductors, or metals.[6,8] Removal of guest species from the type II clathrates can be achieved via heating under vacuum, resulting in an intrinsic semiconductor, that has garnered interest for photovoltaic applications.[6] The band gap can

† The work contained in this chapter is the subject of a scholarly article that is currently in preparation. Authors on this work include Emily R. Adkins, Taizhi Jiang, Andrew L. Heilman, Lakshmi Krishna, Reuben T. Collins, and Brian A. Korgel. Emily Adkins was responsible for planning the research, performing the battery experiments, with some help from Drew Heilman, analyzing the battery data, researching and writing the completed document.

further be altered by alloying two Group IV elements.[7] Group IV clathrates have previously been investigated for their unique thermoelectric and optical properties, but there has been only limited research into their application in LIBs.[6,7,9–15] Previous studies demonstrated the feasibility of reversible Si clathrate lithiation, but suffered from poor cycling stability and low capacity.[13,14,16]

Here, we report detailed electrochemical cycling data for two different type II clathrate materials. We examined a Si and an alloyed Si-Ge clathrate with $Na_{0.5}Si_{136}$ and $Na_{0.5}(Si_{0.9}Ge_{0.1})_{136}$ structures, respectively. This is the first demonstration of battery cycling capability of an alloyed clathrate. Both samples have a high phase purity, of greater than 94 wt.% type II clathrate. Clathrate battery performance was tested in half-cells and exhibited charge capacities of 3434 mAh/g and 2814 mAh/g for the $Na_{0.5}Si_{136}$ and $Na_{0.5}(Si_{0.9}Ge_{0.1})_{136}$ samples, respectively. Both materials exhibited superior reversible cycling performance, particularly compared with previous clathrate battery studies. Analysis of differential capacity plots reveals that the clathrates amorphized during the first lithiation, allowing for increased Li storage. This high capacity and stability is due to the type II phase purity of the samples which is a unique feature of the synthetic method used in this study. This research demonstrates the battery capability of Si and alloyed Si-Ge clathrates, opening the doors for future study into the impact altering the alloy ratio has on battery performance.

2.2 Experimental Details

2.2.1 Chemicals

Lithium hexafluorophosphate ($LiPF_6$, ≥99.99%), ethylene carbonate (EC, 99%), diethyl carbonate (DEC, ≥99%), poly(acrylic acid) (PAA), 1-methyl-2-pyrrolidinone (NMP, 99.5%), and ethanol (99.9%) were purchased from Sigma-Aldrich. Conductive

carbon super C65 was purchased from TIMCAL. Fluoroethylene carbonate (FEC, >98%) was purchased from TCI America. Lithium foil (1.5mm, 99.9%) was purchased from Alfa Aesar. Celgard 2400 membranes (25 μm) were purchased from Celgard. Copper foil (9 μm thick) and coin cells (2032 stainless steel) were purchased from MTI Corporation. All purchased chemicals used for battery making and testing were used as received without any further purification.

2.2.2 Clathrate Synthesis

Si and Si-Ge alloyed type II clathrates were synthesized by thermal decomposition of the precursor $Na(Si_xGe_{1-x})$ at 395ºC for 72h in a cold-wall reactor as previously published.[7] Synthesis of the precursor phases is achieved by ball milling Si and Ge precursors with NaH, then heating the resulting mixture under argon flow, also described in the same reference.

2.2.3 Electrochemical Testing

To prepare a battery slurry, clathrate powder was combined with PAA and C65 at a ratio of 70/20/10 for a total mass of ~30 mg. To this 0.12 mL of NMP and 2 mL of ethanol were added and mixed by probe sonication for 10 min. The solution was then dried in a rotovap to remove extra liquid at 700 torr and 35ºC until the slurry was more viscous, similar to the consistency of syrup. Slurries were then doctor bladed onto Cu foil (200 μm gap) and dried at 150ºC overnight under vacuum. Anodes were cut out of the foil using a 9 mm diameter hole punch. The typical mass loading was 0.40 ± 0.11 mg/cm^2 and 0.55 ± 0.08 mg/cm^2 for the Si and $Si_{0.9}Ge_{0.1}$ clathrates, respectively. Coin cells were assembled in an argon filled glovebox (<0.1 ppm O_2) using Li foil as the counter electrode. Electrolyte solution was prepared using 1 M $LiPF_6$ in 1:1 EC:DEC with 5 wt.% FEC and Celgard 2400 membranes were used as separators. Coin cells were crimped to ensure a tight seal and

removed from the glovebox for galvanostatic testing on an Arbin BT-2143 test unit. Half cells were cycled between 0.01 mV – 2.0 V vs. Li/Li^+. Capacities are reported based on the weight of the clathrate material.

2.2.4 Characterization

Scanning electron microscope (SEM) images were taken using a Zeiss Model SUPRA 40 VP SEM system operated at 2.0 kV. X-ray diffraction (XRD) was performed with a Bruker D2 diffractometer in a theta-2 theta configuration and Cu-Kα (λ = 1.54 Å) radiation.

2.3 Results and Discussion

Two type II group IV clathrates were synthesized for battery testing, SEM images shown in Figure 2.1a-b. The first clathrate had a composition of Na_xSi_{136} with $x<0.5$ and a phase purity of >94 wt.%, the balance being diamond Si. This was determined by XRD, shown in Figure 2.1c, and by Rietveld refinement, shown in Figure A.1. The second clathrate had a composition of $Na_x(Si_{0.9}Ge_{0.1})_{136}$ with $x<0.5$ and a phase purity >98.5 wt.%, the balance being crystalline SiGe.

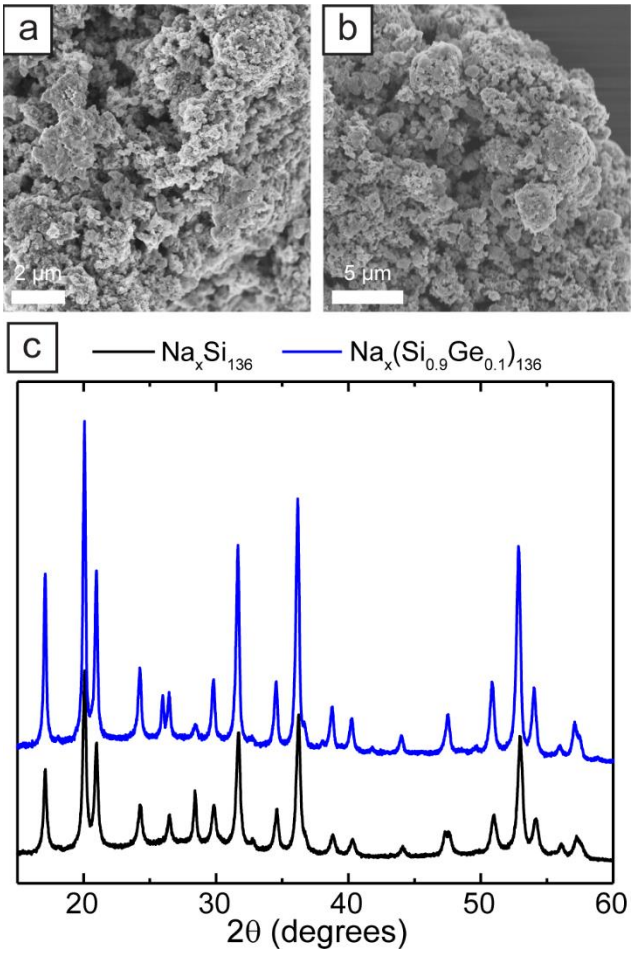

Figure 2.1 Scanning electron microscope (SEM) (a, b) images of the (a) $Na_{0.5}Si_{136}$ and (b) $Na_{0.5}(Si_{0.9}Ge_{0.1})_{136}$ clathrate powders. (c) Powder XRD patterns for both clathrates.

Both clathrate samples were tested in half cells versus Li metal. Preliminary testing of the $Na_{0.5}(Si_{0.9}Ge_{0.1})_{136}$ clathrate, shown in Figure A.2 in Appendix A, was done at an applied current density of 0.025 A/g (approximately C/50), as previously used for clathrate battery testing in literature.[13] The initial charge capacity was 2733 mAh/g, though by the 20th cycle the capacity had decreased by nearly 50% to 1392 mAh/g. This is significantly better performance than previous Si type II clathrate battery studies demonstrated at the same current density.[13,15] Table A.1 in Appendix A includes the battery performance data

of other clathrates reported in literature for the purpose of comparison. Both $Na_{0.5}Si_{136}$ and $Na_{0.5}(Si_{0.9}Ge_{0.1})_{136}$ clathrates were then tested at a higher applied current density of 0.125 A/g (approximately C/10), as shown in Figure 2.2a. Under these conditions, the $Na_{0.5}Si_{136}$ clathrate showed an initial charge capacity of 3434 mAh/g and retained 50% capacity by the 50th cycle. The $Na_{0.5}(Si_{0.9}Ge_{0.1})_{136}$ clathrate exhibited similar performance, with a lower initial charge capacity of 2814 mAh/g, and 50% capacity loss in the first 50 cycles. However, capacity loss occurs more slowly in subsequent cycles, to 893 mAh/g after 200 cycles which is 32% of initial capacity (Figure A.3 in Appendix A). The capacity decline in the early cycles is likely due to structural changes taking place in the battery as the clathrate amorphizes. The $Na_{0.5}(Si_{0.9}Ge_{0.1})_{136}$ clathrate showed significantly better Coulombic efficiency than the $Na_{0.5}Si_{136}$ clathrate, 84% for the first cycle, and greater than 97% for subsequent cycles. In comparison, the $Na_{0.5}Si_{136}$ clathrate had a first cycle capacity of 83% and only increased to 93% for subsequent cycles.

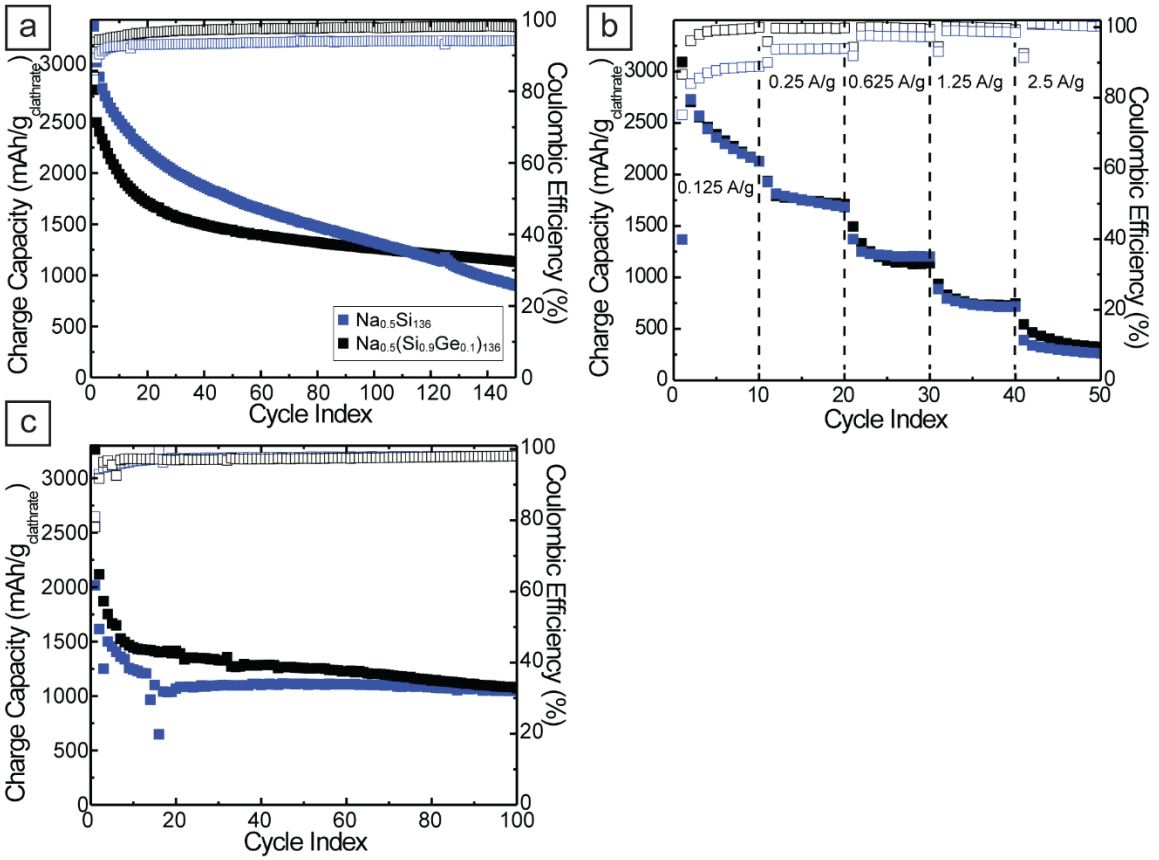

Figure 2.2 Charge capacity (■) and Coulombic efficiency (□) of $Na_{0.5}Si_{136}$ (blue) and $Na_{0.5}(Si_{0.9}Ge_{0.1})_{136}$ (black) clathrate batteries cycled at (a) a current density of 0.125 A/g, (b) various current densities from 0.125 A/g to 2.5 A/g, (c) a current density of 1.25 A/g.

To determine the rate capability of the clathrate materials, batteries were cycled at different applied current densities, as shown in Figure 2.2b. Tested at a high applied current density of 2.5 A/g, the capacity of both clathrate materials dropped to only 380 mAh/g. The $Na_{0.5}Si_{136}$ clathrate, again, had a lower Coulombic efficiency than that of the $Na_{0.5}(Si_{0.9}Ge_{0.1})_{136}$ at all applied current densities.

Both clathrates, when tested at an applied current density of 1.25 A/g, exhibited high stability and capacity, greater than 1000 mAh/g for the first 100 cycles, as shown in Figure 2.2c. The first cycle was done at a lower current density, of 0.125 A/g, to form a

stable solid electrolyte interphase (SEI) layer to passivate the active material surface to protect it from reaction with the electrolyte and improve subsequent cycling stability.[17] There was less fade than experienced at a lower applied current density, as capacity never dropped below 50% of the second cycle capacity. The $Na_{0.5}(Si_{0.9}Ge_{0.1})_{136}$ clathrate had a higher capacity, for the first 60 cycles, but after that the difference was negligible.

Figure 2.3 shows voltage profiles and differential capacity plots for the $Na_{0.5}Si_{136}$ and $Na_{0.5}(Si_{0.9}Ge_{0.1})_{136}$ clathrates cycled at an applied current density to 0.125 A/g (cycling data shown in Figure 2.2a). The voltage profiles for both clathrates, shown in Figure 2.3a and c, exhibits a lithiation plateau that from the second cycle onward shifts to lower potentials as cycling progresses. This indicates that a higher over-potential is necessary to initiate lithiation. The first delithiation plateau is found at 450 mV, corresponding to the delithiation potential of $Li_{15}Si_4$.[18]

The differential capacity plots for the same batteries are shown in Figure 2.3b and d. During the first cycle, both clathrates exhibit a sharp lithiation peak near 200 mV and a smaller, broader peak at 100 mV. Crystalline Si usually shows a single lithiation peak at 100 mV and the sharp 200 mV peak is consistent with the presence of silicon oxide on the sample.[18,19] Because the lithiation peak of silicon oxide was intense, it is possible there was a significant amount of silicon oxide present on the surface of both samples, which had been stored in air prior to battery making. Both clathrates amorphize during the first cycle. This is seen in the second cycle differential capacity plot, where the lithiation potentials move slightly higher to 300 mV and just over 100mV, characteristic of a-Si, and then shift to lower potentials with successive cycles.[20] Previous modeling has shown that further Li insertion amorphizes the Si clathrate and eventually the crystalline $Li_{15}Si_4$ (c-$Li_{15}Si_4$) phase is reached.[13] This is confirmed in the first cycle delithiation plot that exhibits a single peak at 450 mV, characteristic of the delithiation of c-$Li_{15}Si_4$.[18,21]

During subsequent cycles, the clathrates exhibit slightly different delithiation peaks. The $Na_{0.5}(Si_{0.9}Ge_{0.1})_{136}$ clathrate (Figure 2.3d) delithiation peak moves to lower potentials and broadens, more closely resembling the delithiation peaks of amorphous Si (a-Si), which occur at 300 mV and 500 mV.[18,22] The disappearance of the 450 mV peak indicates that there is capacity fade and a lower extent of lithiation in each cycle as c-$Li_{15}Si_4$ is no longer formed.

The $Na_{0.5}Si_{136}$ clathrate exhibits a single delithiation peak at 450 mV for the first 10 cycles (Figure 2.3b). This sharp peak indicates that the Si is fully lithiating to the crystalline phase of c-$Li_{15}Si_4$, which is further confirmed in Figure 2.2b by the high capacity exhibited during these cycles. Following cycle 10, as seen in Figure A.4 in Appendix A, the peak begins to broaden and shift to a lower potential. Although there is still a prominent peak at 450 mV, in cycle 20, a broad shoulder begins to develop at around 300 mV, consistent with the delithiation of a-Si.[18,20] By cycle 50, the delithiation behavior for the $Na_{0.5}Si_{136}$ and $Na_{0.5}(Si_{0.9}Ge_{0.1})_{136}$ clathrates are comparable and indicative of only a-Si.

There do not appear to be any peaks present in the differential capacity plot that can be solely attributed to Ge, of the $Na_{0.5}(Si_{0.9}Ge_{0.1})_{136}$ clathrate (Figure 2.3d). Characteristic peaks for the lithiation of Ge would be at 350 mV and a smaller yet still sharp peak at 150-200 mV.[23] The 350 mV peak is not exhibited in the differential capacity plot for the $Na_{0.5}(Si_{0.9}Ge_{0.1})_{136}$ clathrate. Delithiation of Ge occurs at 500 mV in the first cycle, but the peak shown by the clathrate is at a lower potential, closer to the discharge potential of c-$Li_{15}Si_4$.[23] This is due to the very low Ge content in the sample.

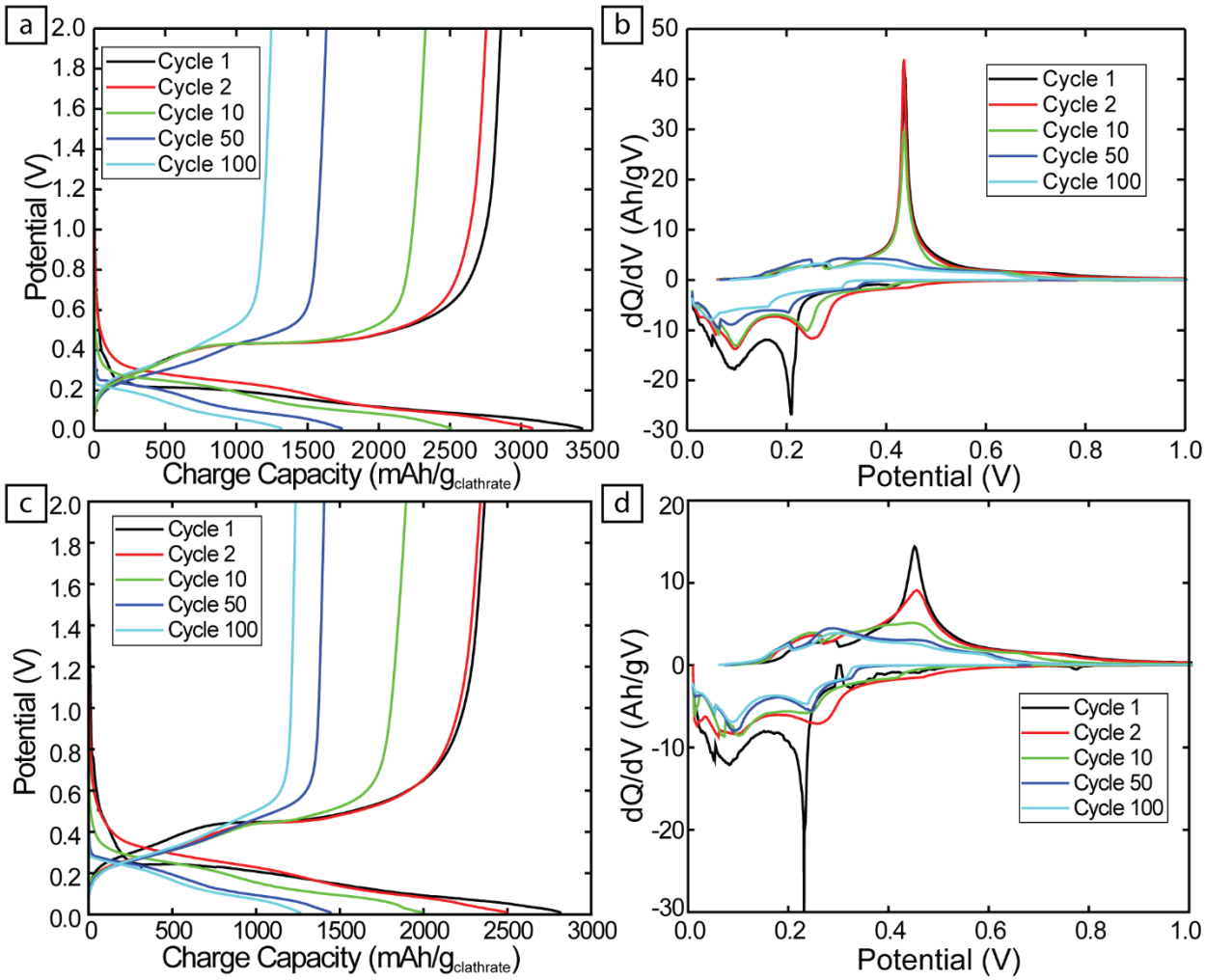

Figure 2.3 (a) Voltage profiles for Si clathrate batteries cycled at a current density of 0.125 A/g. (b) Differential capacity profiles for the same battery at different cycles. (c) Voltage profiles for $Na_{0.5}(Si_{0.9}Ge_{0.1})_{136}$ clathrate batteries cycled at a current density of 0.125 A/g. (d) Differential capacity profiles for the same battery at different cycles.

The high capacity and stability of these clathrate materials is due to the phase purity of both samples. The $Na_{0.5}Si_{136}$ clathrate had a phase purity of >94 wt.% type II and the $Na_{0.5}(Si_{0.9}Ge_{0.1})_{136}$ clathrate was >98.5 wt.% type II. Previous research has found that type I Si clathrates do not alloy with Li during battery cycling, resulting in a low capacity, as the clathrate is acting as an intercalation host.[14,16] In other experiments of type II clathrates,

the phase purity was lower, about 80 wt.% type II with the balance being type I.[13] Thus, the high concentration of type I clathrate would result in a lower total capacity for the active material. The high phase purity of the clathrate samples tested in this study is due to the synthetic procedures use to make them. The cold-wall reactor used promotes formation of type II clathrate through reducing the local Na vapor pressure in the reactor.[7] Additionally, the higher $Na_{0.5}(Si_{0.9}Ge_{0.1})_{136}$ sample phase purity is due to the presence of Ge. It has been previously suggested that type I Si-Ge clathrates may be unstable with a small guest atom like Na, thus they do not form during synthesis and a high type II phase purity is possible.[7]

Now that the reversible LIB capability of alloyed Si-Ge clathrates has been demonstrated, future research can focus on the impact altering the Si-Ge ratio has on battery performance. Ge has a higher rate capability than Si in batteries, so by increasing the Ge content it might be possible to improve the clathrate rate capability.[23] Furthermore, the $Na_{0.5}(Si_{0.9}Ge_{0.1})_{136}$ clathrate had a higher Coulombic efficiency at lower applied current densities, if the added Ge is the cause of the higher Coulombic efficiency then there might be further improvement as more is added, though this requires further study. One difficulty, however, is that the high phase purity of the clathrate samples is not achievable for all Ge concentrations. Between the region of $y = 0.15 – 0.5$ for $Na_{0.5}(Si_{1-y}Ge_y)_{136}$, there is a large amorphous content of the sample due to diffusion limitations for phase separation.[7] It is unclear how this difference would impact battery performance.

2.4 Conclusions

This work demonstrated that high capacity, reversible cycling of type II clathrates is possible. Half cell testing showed high initial charge capacities of 3434 mAh/g and 2814 mAh/g for the $Na_{0.5}Si_{136}$ and $Na_{0.5}(Si_{0.9}Ge_{0.1})_{136}$ clathrates, respectively. Both materials exhibited superior reversible cycling performance when compared with previous clathrate

battery studies. Even at a high applied current density of 1.25 A/g, both clathrates exhibited a charge capacity greater than 1000 mAh/g and were very stable. Differential capacity plots showed that both clathrates amorphized during battery cycling and formed the c-$Li_{15}Si_4$ phase after fully lithiating. The high type II phase purity of the $Na_{0.5}Si_{136}$ and $Na_{0.5}(Si_{0.9}Ge_{0.1})_{136}$ samples was critical for stable cycling. Both samples had a high phase purity, of greater than 94 wt.% type II clathrate, due to the reaction conditions under which the materials were synthesized. This research demonstrates the battery capability of Si and alloyed Si-Ge clathrates, opening the doors for future study into the impact altering the alloy ratio has on battery performance.

2.5 REFERENCES

(1) McDowell, M. T.; Lee, S. W.; Nix, W. D.; Cui, Y. 25th Anniversary Article: Understanding the Lithiation of Silicon and Other Alloying Anodes for Lithium-Ion Batteries. *Adv. Mater. Deerfield Beach Fla* **2013**, *25* (36), 4966–4985.

(2) Armand, M.; Tarascon, J.-M. Building Better Batteries. *Nature* **2008**, *451* (7179), 652–657.

(3) Bogart, T. D.; Chockla, A. M.; Korgel, B. A. High Capacity Lithium Ion Battery Anodes of Silicon and Germanium. *Curr. Opin. Chem. Eng.* **2013**, *2* (3), 286–293.

(4) Tarascon, J.-M.; Armand, M. Issues and Challenges Facing Rechargeable Lithium Batteries. *Nature* **2001**, *414* (6861), 359–367.

(5) Goodenough, J. B.; Kim, Y. Challenges for Rechargeable Li Batteries. *Chem. Mater.* **2010**, *22* (3), 587–603.

(6) Krishna, L.; Koh, C. A. Inorganic and Methane Clathrates: Versatility of Guest–host Compounds for Energy Harvesting. *MRS Energy Amp Sustain.* **2015**, *2*.

(7) L. Baranowski, L.; Krishna, L.; D. Martinez, A.; Raharjo, T.; Stevanović, V.; C. Tamboli, A.; S. Toberer, E. Synthesis and Optical Band Gaps of Alloyed Si–Ge Type II Clathrates. *J. Mater. Chem. C* **2014**, *2* (17), 3231–3237.

(8) Kovnir, K. A.; Shevelkov, A. V. Semiconducting Clathrates: Synthesis, Structure and Properties. *Russ. Chem. Rev.* **2004**, *73* (9), 923.

(9) Martinez, A. D.; Krishna, L.; Baranowski, L. L.; Lusk, M. T.; Toberer, E. S.; Tamboli, A. C. Synthesis of Group IV Clathrates for Photovoltaics. *IEEE J. Photovolt.* **2013**, *3* (4), 1305–1310.

(10) Snyder, G. J.; Toberer, E. S. Complex Thermoelectric Materials. *Nat. Mater.* **2008**, *7* (2), 105–114.

(11) Yang, J.; Tse, J. S. Silicon Clathrates as Anode Materials for Lithium Ion Batteries? *J. Mater. Chem. A* **2013**, *1* (26), 7782–7789.

(12) Warrier, P.; Koh, C. A. Silicon Clathrates for Lithium Ion Batteries: A Perspective. *Appl. Phys. Rev.* **2016**, *3* (4), 040805.

(13) Wagner, N. A.; Raghavan, R.; Zhao, R.; Wei, Q.; Peng, X.; Chan, C. K. Electrochemical Cycling of Sodium-Filled Silicon Clathrate. *ChemElectroChem* **2014**, *1* (2), 347–353.

(14) Li, Y.; Raghavan, R.; Wagner, N. A.; Davidowski, S. K.; Baggetto, L.; Zhao, R.; Cheng, Q.; Yarger, J. L.; Veith, G. M.; Ellis-Terrell, C.; et al. Type I Clathrates as Novel Silicon Anodes: An Electrochemical and Structural Investigation. *Adv. Sci.* **2015**, *2* (6), n/a-n/a.

(15) Langer, T.; Dupke, S.; Trill, H.; Passerini, S.; Eckert, H.; Pöttgen, R.; Winter, M. Electrochemical Lithiation of Silicon Clathrate-II. *J. Electrochem. Soc.* **2012**, *159* (8), A1318–A1322.

(16) Zhao, R.; Bobev, S.; Krishna, L.; Yang, T.; Weller, J. M.; Jing, H.; Chan, C. K. Anodes for Lithium-Ion Batteries Based on Type I Silicon Clathrate Ba8Al16Si30 - Role of Processing on Surface Properties and Electrochemical Behavior. *ACS Appl. Mater. Interfaces* **2017**, *9* (47), 41246–41257.

(17) Verma, P.; Maire, P.; Novák, P. A Review of the Features and Analyses of the Solid Electrolyte Interphase in Li-Ion Batteries. *Electrochimica Acta* **2010**, *55* (22), 6332–6341.

(18) Obrovac, M. N.; Krause, L. J. Reversible Cycling of Crystalline Silicon Powder. *J. Electrochem. Soc.* **2007**, *154* (2), A103–A108.

(19) Ogata, K.; Salager, E.; Kerr, C. J.; Fraser, A. E.; Ducati, C.; Morris, A. J.; Hofmann, S.; Grey, C. P. Revealing Lithium–silicide Phase Transformations in Nano-Structured Silicon-Based Lithium Ion Batteries via *in Situ* NMR Spectroscopy. *Nat. Commun.* **2014**, *5*, ncomms4217.

(20) Hatchard, T. D.; Dahn, J. R. In Situ XRD and Electrochemical Study of the Reaction of Lithium with Amorphous Silicon. *J. Electrochem. Soc.* **2004**, *151* (6), A838–A842.

(21) Cui, L.-F.; Ruffo, R.; Chan, C. K.; Peng, H.; Cui, Y. Crystalline-Amorphous Core−Shell Silicon Nanowires for High Capacity and High Current Battery Electrodes. *Nano Lett.* **2009**, *9* (1), 491–495.

(22) Bogart, T. D.; Lu, X.; Gu, M.; Wang, C.; Korgel, B. A. Enhancing the Lithiation Rate of Silicon Nanowires by the Inclusion of Tin. *RSC Adv.* **2014**, *4* (79), 42022–42028.

(23) Chockla, A. M.; Klavetter, K. C.; Mullins, C. B.; Korgel, B. A. Solution-Grown Germanium Nanowire Anodes for Lithium-Ion Batteries. *ACS Appl. Mater. Interfaces* **2012**, *4* (9), 4658–4664.

Chapter 3: In-Situ Surface Passivated Germanium Nanowires for Lithium-Ion Batteries‡

3.1 INTRODUCTION

To meet the future needs of technologies such as extended-range electric vehicles and renewable energy storage, lithium ion batteries (LIBs) with higher energy and power density will be necessary.[1–3] This will require the use of new electrode materials capable of holding more Li ions than those currently used. Traditional LIBs are made using a graphite anode, which only has a capacity of 372 mAh/g, but by upgrading to Li alloy materials such as germanium (Ge) or silicon (Si) it is possible to increase capacity to 1624 mAh/g or 3579 mAh/g, respectively.[4–6] Ge is of particular interest because it has demonstrated a high rate capability and better stability than Si.[7]

The surface chemistry of electrode materials can have an impact on battery performance in many different ways, such as improved conductivity, reduced Li^+ ion transport, and improved interaction with the binder.[8–13] The surface chemistry of the active material is important because, during cycling, the anode will react with the electrolyte, forming a passivating solid electrolyte interphase (SEI) layer on the surface.[2] This layer is crucial to stable battery function, as it protects the anode surface from further direct reaction with the electrolyte and prevents degradation of the active material.[4,9] However, if the SEI layer is not robust, it will continually crack during electrode expansion and contraction, exposing new active material surface to the electrolyte and building a thicker SEI layer, which can hinder Li^+ transport and increase electrical resistance.[4,14] The SEI layer can also trap a significant amount of Li^+, resulting in irreversible charge loss.[15] While

‡ The work contained in this chapter is the subject of a scholarly article that is currently in preparation. Authors on this work include Emily R. Adkins, Taizhi Jiang, Andrew L. Heilman, Phillip Liu, Brian A. Korgel. Emily Adkins was responsible for planning the research, synthesizing materials and performing battery experiments, with some help from Drew Heilman, analyzing the synthesis and battery data, researching and writing the completed document.

this is unavoidable in the first cycle, upon initial SEI formation, if a stable SEI layer is formed, further electrolyte degradation will ideally be prevented.[14] The composition of the SEI layer is also crucial to its effectiveness, and is dependent on the electrolyte used. The resulting SEI layer, in a battery cycled with a traditional carbonate electrolyte, consists primarily of carbonate byproducts, as well as LiF formed by decomposition of the salt additive.[16]

The surface of an active material can alter the electrochemical reaction between electrode and electrolyte, impacting the SEI composition, and ultimately the overall battery performance. One way to modify the active material from reaction with the electrolyte, is passivation. Ge nanowires (NWs) passivated with organic monolayers have improved corrosion resistance.[8,17–19] This protection would be useful in a battery environment, as electrolyte with lithium hexafluorophosphate ($LiPF_6$) often has a trace amount of hydrofluoric acid present initially due to reaction with atmospheric contaminants.[20] Furthermore, passivation can be used to alter electronic properties of the material and add functionality.[18,21] Systematic experimentation looking at the impact of several surface passivations is necessary to understand the impact the active material surface chemistry has on SEI composition and battery performance.

Here, we report the battery performance of Ge NWs with different surface passivations. The nanowires were synthesized using a supercritical-fluid-liquid-solid (SFLS) technique that allowed for in-situ passivation. Nanowire battery performance was tested in half-cells and the resulting SEI layer studied using X-ray photoelectron spectroscopy (XPS). Surface passivation was found to have an impact on initial SEI formation, which in turn affected battery performance and rate capability. Although unpassivated nanowires had higher storage capability, they experienced degradation during cycling and low rate capability. DDT passivated nanowires performed with lower capacity

at high rates and with lower stability in all tests. Adding an organic alkene monolayer improved stability, even at high cycle rates. Anodes with different surface functionalizations exhibited different first cycle SEI compositions, though after extended cycling these differences were minimal. This research shows that the interaction between the nanowire surface, polymeric binder, and SEI formation is complex and must be optimized in conjunction to achieve the best results.

3.2 Experimental Details

3.2.1 Chemicals

Diphenylgermane (>95%) and phenylsilane (>95%) were purchased from Gelest, Inc. 1-dodecene (95%), 1-dodecanethiol (>98%), 11-mercaptoundecanoic acid (>95%), lithium hexafluorophosphate ($LiPF_6$, ≥99.99%), ethylene carbonate (EC, 99%), diethyl carbonate (DEC, ≥99%), poly(acrylic acid) (PAA), 1-methyl-2-pyrrolidinone (NMP, 99.5%), anhydrous toluene (99.8%), chloroform (99.9%), and ethanol (99.9%) were purchased from Sigma-Aldrich. Conductive carbon super C65 was purchased from TIMCAL. Fluoroethylene carbonate (FEC, >98%) was purchased from TCI America. Lithium foil (1.5mm, 99.9%) was purchased from Alfa Aesar. Celgard 2400 membranes (25 μm) were purchased from Celgard. Copper foil (9 μm thick) and coin cells (2032 stainless steel) were purchased from MTI Corporation. All purchased chemicals were used as received without any further purification.

3.2.2 Nanowire Synthesis

Gold (Au) nanocrystals with an average diameter of 2 nm, capped with 1-dodecanethiol (Aldrich, >98%), were prepared using the method of Brust et al. and stored in anhydrous toluene.[22] Germanium nanowires were synthesized by the super critical fluid–liquid–solid technique which has been previously published.[23] Reactants were prepared in

an argon glovebox in order to minimize air exposure. A reaction solution of 28 mL was prepared with 0.5 mg of gold nanoparticles in a 20 mg/mL solution, 36 mM diphenylgermane, 24 mM phenylsilane and anhydrous toluene. Previous research has shown that the addition of phenylsilane as a phenyl group scavenger improves the quality and yield of the nanowires.[24] Prior to synthesis, a 10 mL titanium tubular reactor was filled with argon in the glovebox and then connected to a high pressure liquid chromatography (HPLC) pump on one end and a micrometer valve on the other. The reactor was then heated to 380ºC and pressurized to 6.9 MPa. The reactant solution was fed to the reactor at 0.5 mL/min for 40 min and the outlet pressure is maintained at 6.9 MPa.

Immediately after the synthesis the reactor was sealed and cooled for the passivation. For dodecanethiol and mercaptoundecanoic acid passivation, the temperature was set at 80ºC and for dodecene passivation to 220ºC.[17,18] An injection solution in anhydrous toluene was prepared in the glovebox. For dodecanethiol and dodecene, 4 mL of chemical were added to 8 mL of toluene, and for mercaptoundecanoic acid, 1 g of acid was added to 12 mL of toluene. After the temperature stabilized, 10 mL of passivation solution was injected into the reactor at a rate of 0.5 mL/min. The solution was injected until the pressure increased to 6.9 MPa and was held at temperature and pressure for 2 hrs. The reactor was then allowed to cool to room temperature.

After cooling, the nanowires were centrifuged at 8000 rpm for 5 minutes. The supernatant was then disposed and the nanowires were washed using chloroform, toluene, and ethanol at a 2:1:1 ratio. The nanowires were then centrifuged and washed two more times. The resulting nanowires were stored in chloroform.

3.2.3 Electrochemical Testing

To prepare a battery slurry, GeNWs were dried by rotovap at 700 torr and 30ºC. The nanowires were then combined with PAA and C65 at a ratio of 70/20/10 for a total mass of ~30 mg. To this 0.12 mL of NMP and 2.5 mL of ethanol were added and mixed by probe sonication for 30 min. The solution was then rotovapped to remove extra liquid at 700 torr and 35ºC until the slurry was more viscous. Slurries were then doctor bladed onto Cu foil (200 μm gap) and dried at 150 ºC overnight under vacuum. The typical mass loading was approximately 0.5 mg/cm^2. Anodes were cut out of the foil using a 9 mm diameter hole punch. Coin cells were assembled in an argon filled glovebox (<0.1 ppm O_2) using Li foil as the counter electrode. Electrolyte solution was prepared using 1 M $LiPF_6$ in 1:1 EC:DEC with 5 wt% FEC and Celgard 2400 membranes were used as separators. Coin cells were crimped to ensure a tight seal and removed from the glovebox for galvanostatic testing on an Arbin BT-2143 test unit. Half cells were cycled between 0.01 V – 2.0 V vs Li/Li$^+$. Capacities are reported based on the nanowire weight of the anode material and rates are reported based on C = 1211 mAh/g. This cycle rate is determined by the 70% weight fraction of the nanowires times the theoretical capacity of 1624 mAh/g plus 20% contribution from the carbon additive and binder times 372 mAh/g.

3.2.4 Characterization

Attenuated total reflectance fourier transform infrared spectroscopy (ATR-FTIR) was used to confirm the attachment of ligands in nanowire passivation. A Thermo Scientific Nicolet 6700 with a diamond ATR crystal accessory (PIKE MIRacle™) was used. The spectrometer chamber was purged with nitrogen, and IR spectra were recorded from dried nanowires. Transmission electron microscope (TEM) images were taken using a FEI Tecnai Spirit Bio Twin operated at 80 kV. Samples were prepared by depositing

them on a 200mesh lacey-carbon copper TEM grid. Scanning electron microscope (SEM) images were taken using a Zeiss Model SUPRA 40 VP SEM system operated at 2.0 kV.

Ex-situ analysis of cycled electrodes was performed using a Kratos AXIS Ultra DLD spectrometer to do x-ray photoelectron spectroscopy (XPS). Because many of the species that form on the surface of an electrode are air sensitive special care was taken to reduce oxygen exposure. Coin cells were opened in the glovebox and electrodes rinsed with DEC. They were transferred to the XPS ultra-high vacuum (UHV) chamber via a pressure-to-vacuum transfer of environmentally sensitive samples (PV-TESS) interface (designed by the Texas Materials Institute, University of Texas, Austin, U.S. Patent Application Serial No. 14/445,650 filed July 29, 2014. The resolution for the survey scan was 1 eV, and the high-resolution region data was collected every 0.1 eV. Sputtering was carried out using Argon ions with an approximate 2.5μA current measured at the sample. The spectra were analyzed using CasaXPS software (version 2.3.16, Casa Software Ltd.). Sample charging was corrected for by shifting the F1s, Li-F peak to a binding energy of 685.1 eV. A DDE anode cycled at 1C for 123 cycles, DDT and MUA at varying cycle rates for 80 cycles, and pristine anode cycled at 1C for 152 cycles were analyzed in the XPS. The differing cycle lengths does not impact the chemical species formed on the surface as seen in both the XPS spectra data and the atomic fraction data in Figures 3.7 and 3.8.

3.3 Results and Discussion

Ge nanowires would be tested both with and without surface passivation in batteries. The synthesized Ge NWs were long, straight and crystalline, as shown in Figure 3.1.

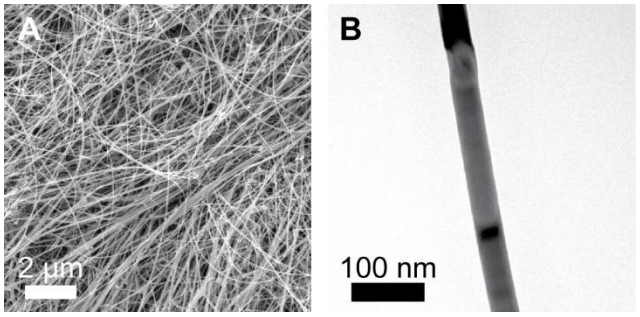

Figure 3.1 (a) SEM and (b) TEM of Ge NWs after synthesis, but without surface passivation.

Three different surface passivations were tested: 1-dodecene (DDE), 1-dodecanethiol (DDT), and 11-mercaptoundecanoic acid (MUA) (Figure 3.2a). These passivations were chosen because they had either different groups bonded to the nanowire surface (DDE and DDT) or a different terminal group (MUA and DDT), allowing for isolation of different variables and comparison. Figure 3.2b-c shows the reaction scheme for the attachment of the three passivation chemicals to the NW surface. In the thermal hydrogermylation reaction (Figure 3.2b), the double bond of 1-dodecene is cleaved and the carbon bonds with Ge on the surface.[17] In the thiolation passivations (Figure 3.2c), the sulfur will bond with the Ge on the NW surface. Surface passivation was done in-situ in the reactor immediately following synthesis to prevent formation of a surface oxide that would inhibit passivation.

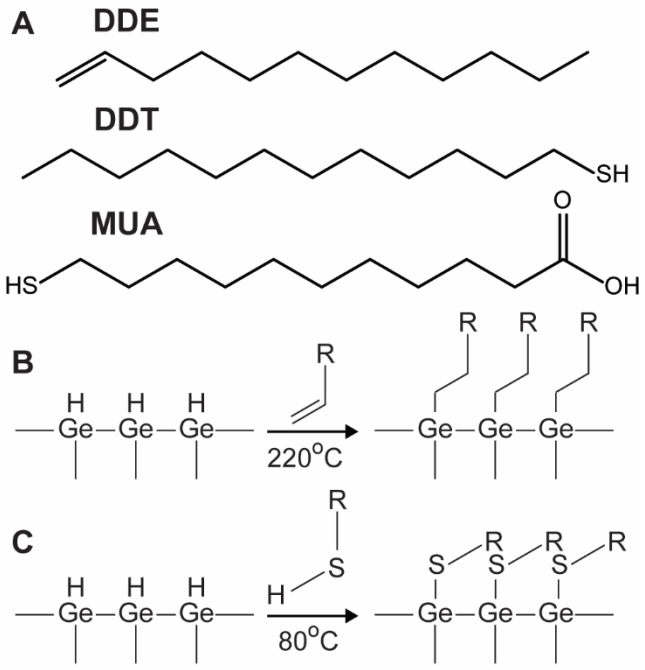

Figure 3.2 (a) Chemical structures for the three passivations. (b) Reaction scheme for 1-dodecene (DDE) passivation. (c) Reaction scheme for 1-dodecanethiol (DDT) and 11-mercaptoundecanoic acid (MUA) passivation.

Attenuated total reflectance Fourier transform infrared spectroscopy (ATR-FTIR) was used to confirm the attachment of ligands in nanowire passivation. Figure 3.3a shows the normalized transmittance spectra for the 1-dodecene and 1-dodecanethiol passivation. The dashed line indicates the asymmetric CH_2 stretching (2918 cm^{-1} and 2920 cm^{-1} for 1-dodecene and 1-dodecanethiol respectively) and the symmetric CH_2 stretching (2850 cm^{-1} for both). C-S and C-S-H stretches have weak absorption in IR spectra and were not observed.[25] Figure 3.3b shows the FTIR spectra for the NWs passivated with 11-mercaptoundecanoic acid as indicated by the presence of the carboxylic acid C=O stretch at 1710 cm^{-1}.

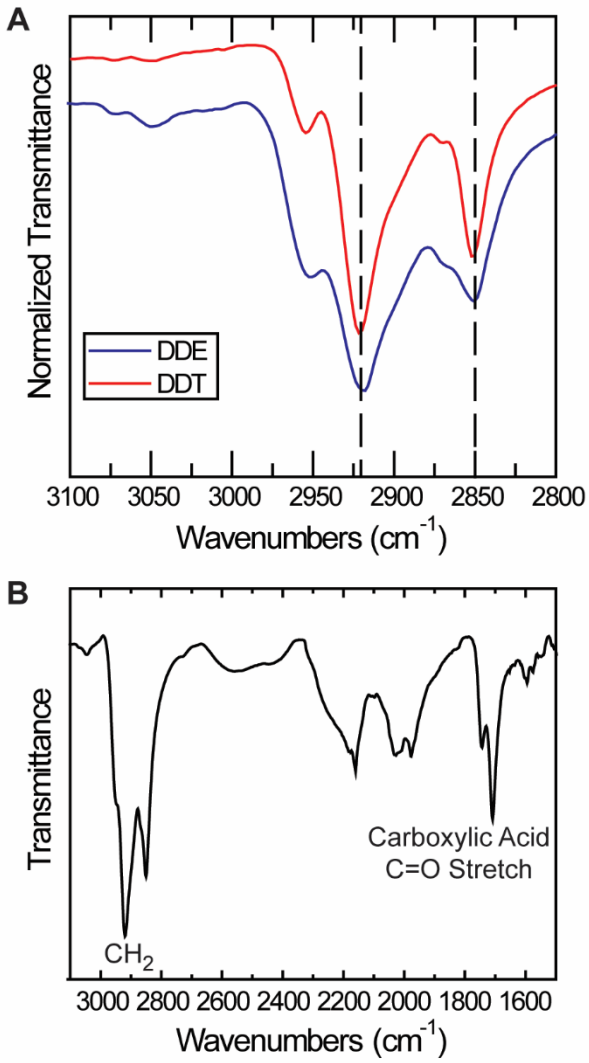

Figure 3.3 (a) ATR-FTIR spectra of Ge NWs passivated with 1-dodecene and 1-dodecanethiol. Dashed lines indicated the symmetric and asymmetric CH_2 stretching peak positions. (b) ATR-FTIR spectra of Ge NWs passivated with 11-mercaptoundecanoic acid.

Passivated and unpassivated (labeled "pristine") Ge nanowires were tested in half cells versus Li metal. Figure 3.4 shows battery data for Ge NW anodes made using PAA as a binder tested at different rates. Capacities are reported based on the weight of NWs used in the electrode. At a cycle rate of C/10 (C = 1221 mAh/g), as shown in Figure 3.4a,

all four NW anodes exhibit relatively stable cycling. Pristine nanowires exhibit the best capacity, with a capacity at 100 cycles of 1478 mAh/g, though they have the lowest Coulombic efficiency, 88.6% for the same cycle. DDT passivated nanowires exhibited the lowest capacity, with a 100^{th} cycle capacity of 1277 mAh/g. The NWs with the highest Coulombic efficiency were the MUA passivated, with a Coulombic efficiency at 100 cycles of 96.9%; these NWs also showed very stable cycling, as they retained 86.4% of capacity after the same number of cycles.

In Figure 3.4b, nanowires were tested at an increased cycle rate of 1 C, with a single first cycle done at C/10, to form a robust SEI layer. The faster cycle rate lead to lower capacities and higher Coulombic efficiencies. This occurs because at higher C-rates the Ge is not fully lithiated and delithiated, resulting in limited volumetric expansion and this better efficiency.[26] Although DDE and MUA passivated NWs exhibited lower capacities than DDT and pristine NWs, they had very stable cycling. The capacities at 100 cycles for DDE and MUA were 727 mAh/g and 636 mAh/g, respectively. Even after 200 cycles the DDE batteries still retained 96% of 2^{nd} cycle capacity, and the MUA batteries 81% of 3^{rd} cycle capacity (Figure B.1 in Appendix B). DDT and pristine GeNWs exhibited a decline in capacity during the first 100 cycles. At 100 cycles, the DDT and pristine GeNW batteries had capacities that were 75% and 79% of 2^{nd} cycle capacity, respectively. This decline in capacity was consistent across multiple DDT and pristine GeNW batteries tested at this rate, as seen in Figure B.2 in Appendix B.

Further testing was done to determine the rate capability of the nanowires. The batteries were tested at varying cycle rates from C/10 to 10 C for 10 cycles each, as shown in Figure 3.4b. All anodes demonstrated capacity even at high rates of 10 C. DDE nanowires exhibited the best performance at this cycle rate, with a capacity of 568 mAh/g. DDT and MUA passivated nanowires had the lowest capacities at the fastest cycle rates 5C

and 10 C. Pristine nanowires exhibited the best cycling performance at C/10 both before and after faster cycling, as expected from the C/10 cycle data in Figure 3.4a, though again had the lowest Coulombic efficiency.

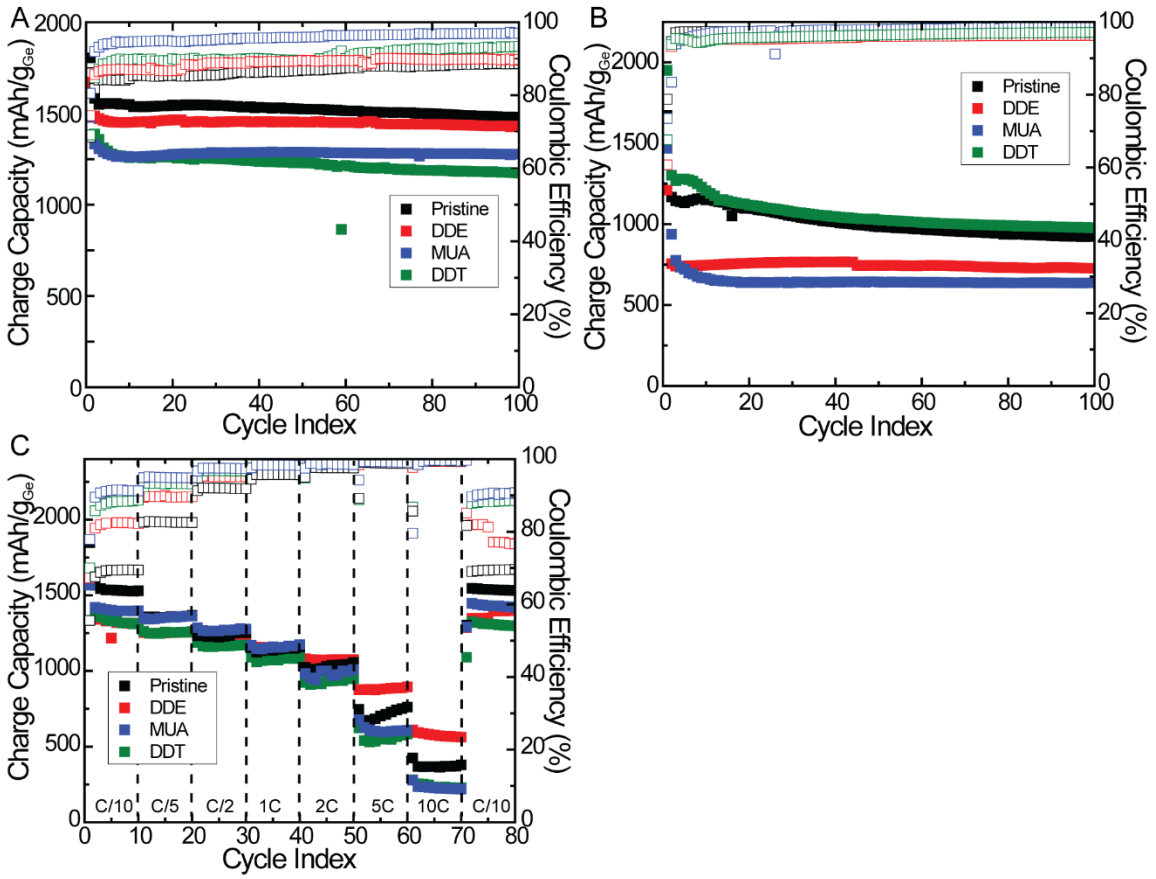

Figure 3.4 Charge capacity (■) and Coulombic efficiency (□) of passivated Ge NWs cycled at (a) a rate of C/10, (b) a rate of 1 C and (c) various cycle rates from C/10 to 10 C for 10 cycles each, where 1 C = 1211 mAh/g.

Voltage profiles for the rate test data are shown in Figure 3.5. The profile shapes are similar for all passivations and lithiation plateaus shift to lower potentials as cycle rate increases, though this is less significant for nanowires that performed better at high rate, such as DDE (Figure 3.5b). This indicates that a higher over-potential is necessary to initiate lithiation.

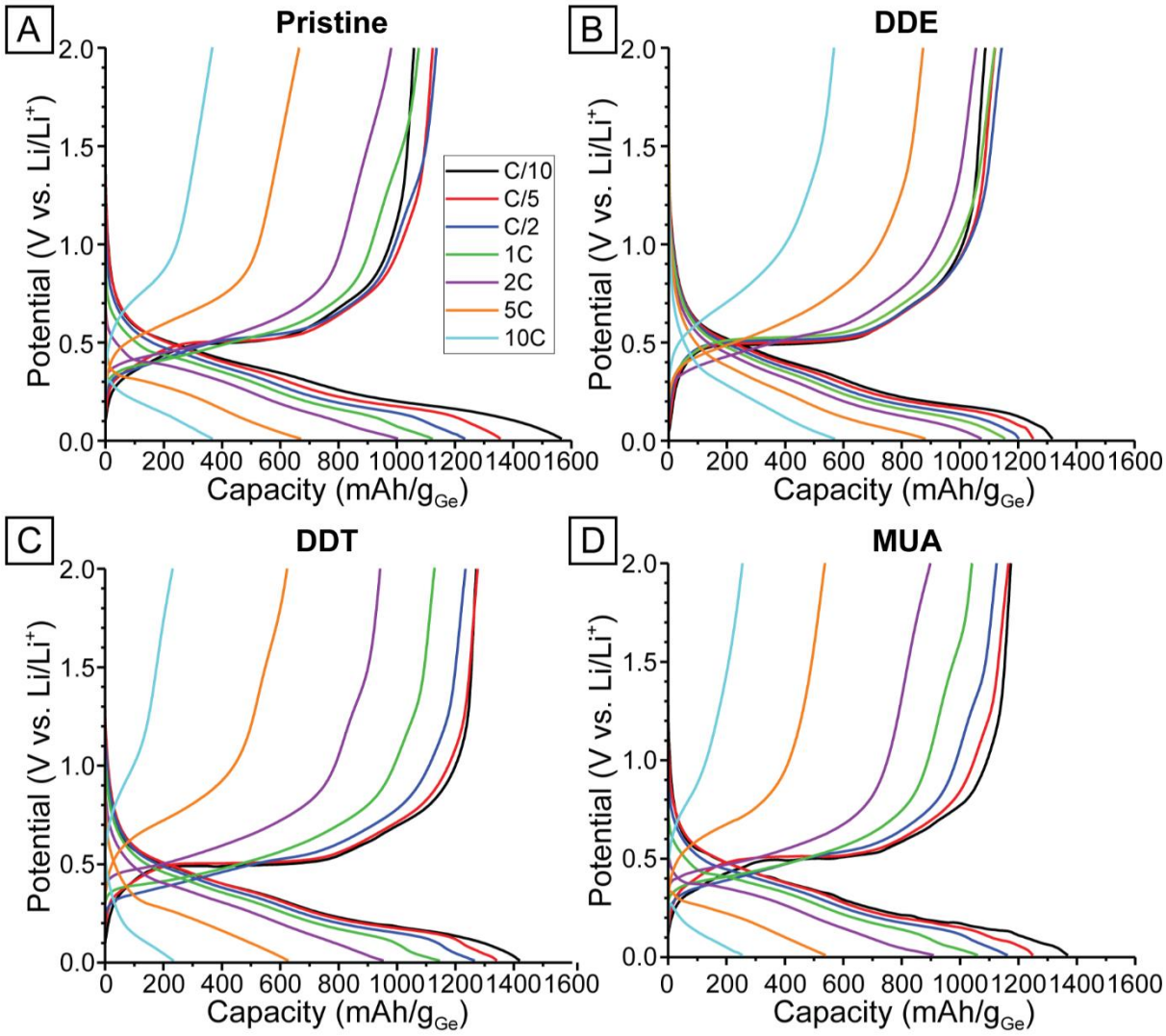

Figure 3.5 Voltage profiles for LIBs with (a) pristine Ge nanowires, (b) DDE, (c) DDT, and (d) MUA passivated Ge NWs at cycle rates ranging from C/10 to 10 C. The voltage profiles correspond to the 2nd cycle data in Figure 3c with 1 C = 1211 mAh/g. The same legend shown in (a) is used for all plots.

Figure 3.6 shows differential capacity plots for the pristine and passivated Ge NW batteries cycled at C/10 (cycle data shown in Figure 3.4a). During the first cycle, pristine, DDT and MUA Ge NW batteries exhibit a sharp lithiation peak near 250 mV. The first

cycle behavior of the DDE nanowires is slightly different, showing a large lithiation peak at 350 mV and a smaller peak at around 225 mV. This indicates a lower overpotential is necessary to induce lithiation. Both behaviors are consistent with previously reported differential capacity data for Ge nanowires.[5,7,27,28] First cycle lithiation peaks are sharper than in subsequent cycles, corresponding to the lithiation of crystalline Ge. In later cycles the Ge has amorphized and broad peaks appear, for all nanowires, at 450 mV and 200 mV.[7] Delithiation of Ge occurs at 500 mV and is indicated by a sharp peak.[7] This peak gradually decreases in size and sharpness with subsequent cycling, for all nanowires, which is indicative of capacity fade.

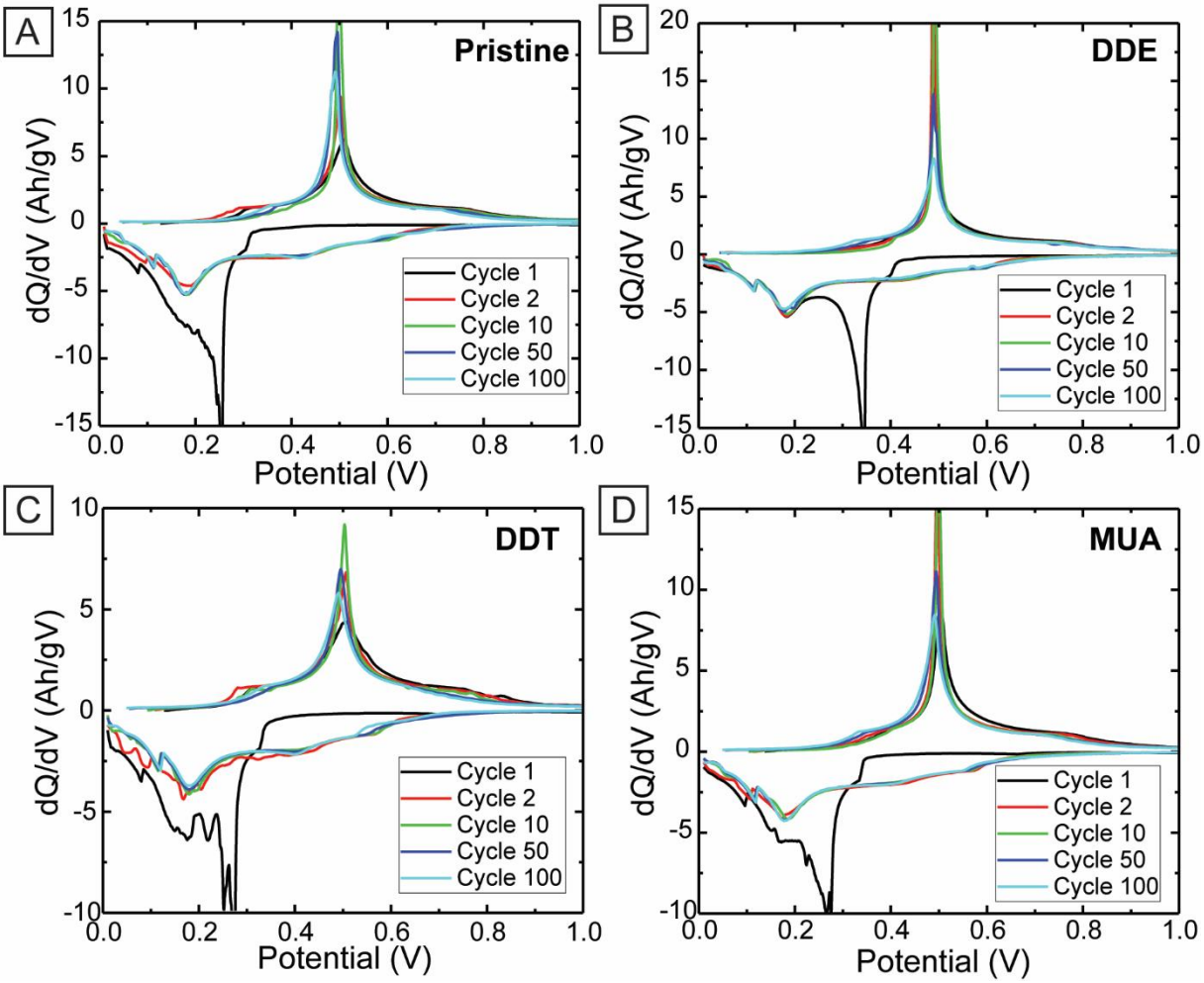

Figure 3.6 Differential capacity profiles for LIBs with (a) pristine nanowires, (b) DDE passivation, (c) DDT, and (d) MUA at a cycle rate of C/10 with 1 C = 1211 mAh/g.

To determine the impact surface passivation has on SEI layer formation, XPS was used for chemical analysis. Measurements were taken after a single cycle, and after a longer cycle time (>80 cycles). All anodes were analyzed in the delithiated state and rinsed with DEC for 15 minutes before XPS analysis to remove any Li salts from the electrode surface. Figure 3.7 compares the XPS scans for anodes after a single cycle and after a longer cycle time. The C 1s scan (Figure 3.7a) for all three passivations and the pristine nanowires

shows a strong signal at 284.9 eV, corresponding to the presence of aliphatic carbon, as expected due to the addition of conductive carbon and the passivation.[29] The second peak, present in all samples, is at 286.6 eV, attributed to carbon atoms bound to a single oxygen.[29] The final peak, again present to some degree in all samples, is at approximately 290 eV, and is due to the presence of a carbonate species.[30] These peaks arise due to the presence of decomposition products of the carbonate electrolyte. The main reduction products of EC and DEC are reduced to $ROCO_2Li$ and Li_2CO_3.[30,31]

While similar chemical species are present on the surface of the different electrodes, the relative ratio of the peaks gives us insight into the different compositions. Figure B.3 in Appendix B presents high resolution elemental XPS scans of the C 1s orbital with peak deconvolution envelopes shown for the batteries after 1 cycle. These convolutions are used to determine the relative compositions of species present in each sample. The MUA passivated electrode has a strong carbonate peak, relative to the C-C peak, indicating a higher composition of Li_2CO_3, which is a highly efficient passivating species because it is less soluble in the electrolyte solvents.[14] DDT and MUA passivated electrodes have a broader peak from 288-290 eV, which can indicate the presence of several types of carbonates.[30] The MUA passivated electrode is the only sample to show a peak at 283 eV which can be attributed to another decomposition product, $LiCH_2R$.[32] Looking at the XPS after the electrode has experienced extended cycling, we see very little difference between the four electrodes. The carbonate, ethereal, and alkoxy carbon signals have become a broad slope, due to the presence of many different species.

The O 1s scan (Figure 3.7b) is dominated by Li_2CO_3 after a single cycle showing a strong signal at 532 eV.[29] This peak is present in all samples, though the Li_2CO_3 peak in DDT has a broader shoulder at around 533 eV. This can be attributed to the presence of Li alkyl carbonates.[29] This observation is in agreement with the alkyl carbonate C 1s peak,

which is relatively larger for this. This may indicate a higher degree of carbonate electrolyte decomposition in this sample after a single cycle. This shoulder grows in all four samples after a longer cycling time. The F1s scan (Figure 3.7c) exhibits a peak for LiF at 685.1 eV for all samples.[29] A peak at 687.2 eV for both the DDE and MUA passivated samples due to the presence of remaining $LiPF_6$ salt. The presence of LiF is due to the decomposition of $LiPF_6$ during cycling.[29] All samples show a strong LiF peak after extended cycling.

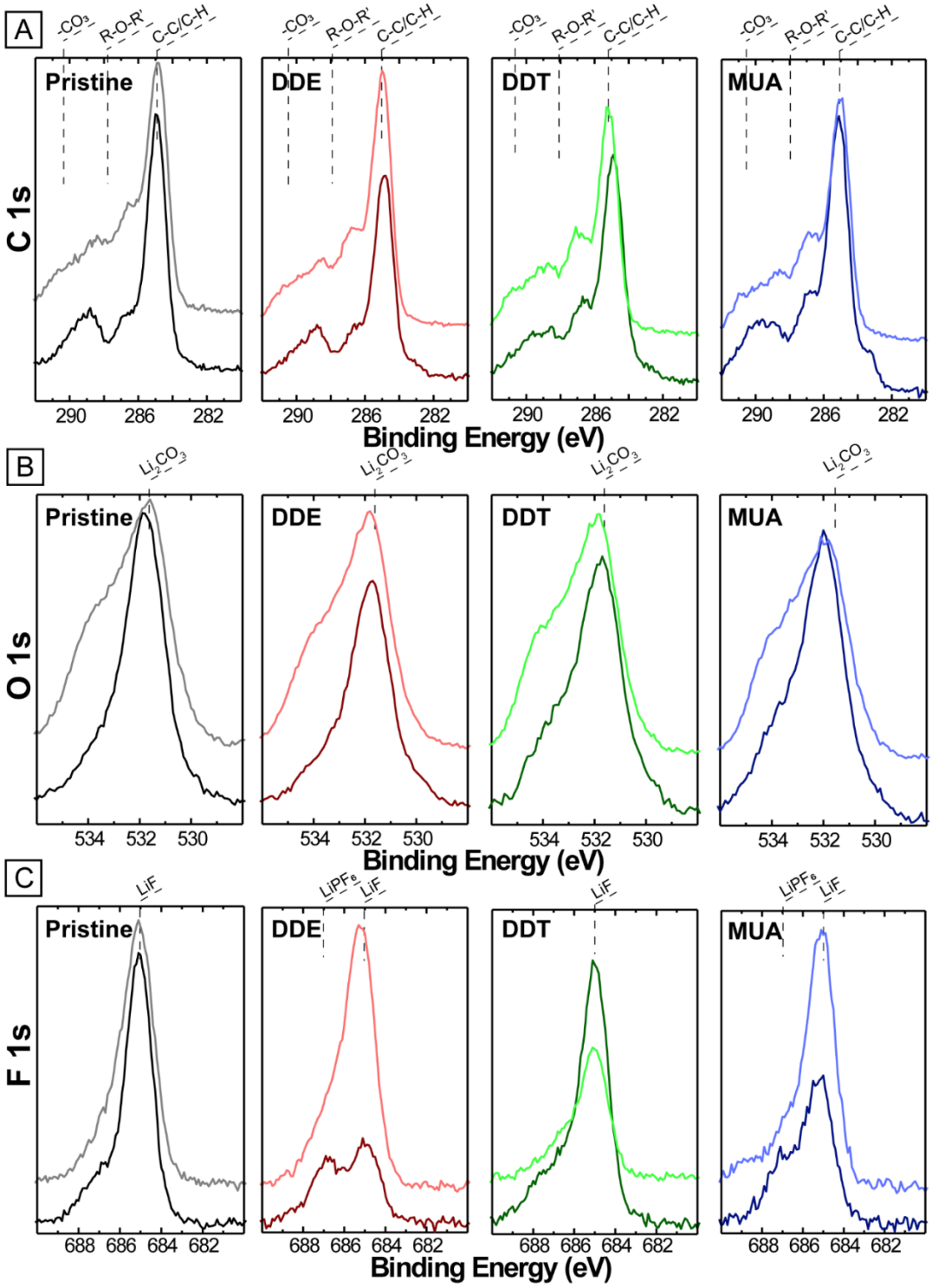

Figure 3.7 High resolution XPS elemental scans for batteries after 1 cycle (darker lines) and >80 cycles (lighter lines) (a) C 1s, (b) O 1s, (c) F 1s.

The variability in SEI composition between samples changes significantly between the 1st cycle and after a longer cycle time. First cycle SEI layer formation is crucial, since a robust SEI layer could ideally prevent further electrolyte degredation.[14,16] Surface passivation will have the most impact on this initial SEI formation since it is occurring directly on the nanowire surface. Figure 3.8a shows the atomic elemental composition of each sample after a single cycle. DDE has a high C content of 50%; by contrast MUA only has 18%. This is because the DDE sample had a significantly lower F content, 6%, than the other samples. From Figure 3.7c, this sample had a much lower LiF signal, and a comparatively higher fraction of $LiPF_6$, though the Li atom percent is low, 16%, so it is unlikely there was unreacted salt on the surface of the sample. This data indicates that the DDE sample had lower Li salt decomposition in the first cycle, compared with other samples, as LiF is one of the main decomposition products of $LiPF_6$.[16,33]

The higher Ge content of the MUA sample, 7%, may be indicative of a thinner SEI layer formed after a single cycle than the other samples, if the thickness is less than the XPS penetration depth of ~10 nm.[16] The MUA sample had a very high Li and F atomic percent, and a comparatively high ratio of $LiPF_6$ to LiF, so it is possible that there was some unreacted salt present on the surface in the XPS.

There is a high degree of variability between the atomic composition of the samples after the first cycle, but after a longer cycle time (Figure 3.8b) we see very little difference between the samples. With subsequent cycles, the electrolyte decomposition will form an SEI layer thick enough to cover that initial variability.

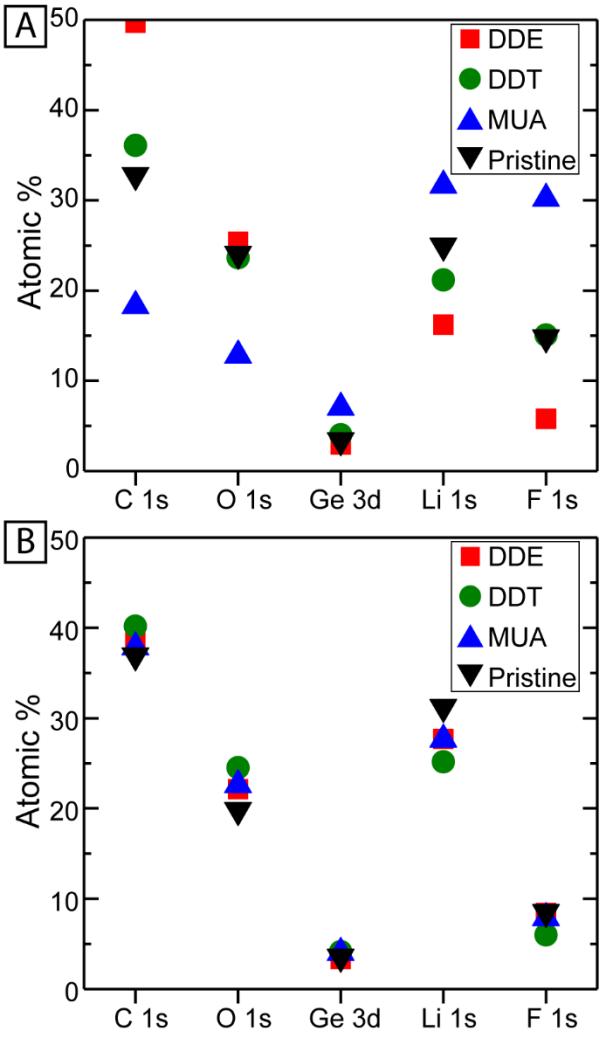

Figure 3.8 Elemental film compositions for batteries after (a) 1 cycle (b) >80 cycles.

It is difficult to definitively connect performance and passivation for each of the passivated and unpassivated GeNWs, but there are some general conclusions that can be drawn from the data. The DDT passivated nanowires performed with worse stability for every test, at all rates. For 1 C tests the DDT nanowires performed better, but with lower stability than the DDE or MUA nanowires. The higher presence of Li alkyl carbonates observed in the DDT NW XPS data following the first cycle indicates more electrolyte decomposition. A thicker SEI layer can hinder Li ion diffusion and trap Li, decreasing

storage capacity.[4,14,34] These findings differ from previously published results that found DDT passivated GeNWs performed significantly better than unpassivated GeNWs.[8] One possible reason for this difference was the use of poly(acrylic acid) (PAA) as a binder in place of polyvinylidene fluoride (PVdF). It was previously theorized that PVdF could form a stronger bond with the DDT passivation than with the oxidized nanowire surface of an unpassivated GeNW.[8] This would create an electrode with higher structural stability that could better withstand volume expansion and contraction. The same enhanced binding is not seen when PAA is used as a binder. PAA was chosen as the binder for this study because it has been proven to be a superior binder over PVdF in Si and Ge anodes.[26,35–37] PAA has strong reactions with the native surface oxide on active materials through carboxylic and hydroxyl groups which are then reduced to lithium carboxylates during cycling forming a stable SEI layer.[37]

DDE passivated GeNWs exhibited lower capacities than other passivations, but had very stable cycling, particularly at high rates of 10 C. Even though the DDE passivation would protect the NW surface from oxide formation, it does not appear that it inhibited surface functional groups of the PAA from interacting with the nanowires to create a strong network and an SEI layer that allowed for stable cyling. For applications with a need for high cycle stability at different rates, but at the expense of capacity, DDE nanowires would be best. The MUA passivated electrode had a higher composition of Li_2CO_3, following the first cycle, and may have a thinner SEI layer, as seen from the higher Ge content than other samples. While the MUA samples had lower capacities at low cycle rates, they showed very stable cycling, indicative of an effective SEI layer.

Finally, this research has shown that pristine NWs can compete with passivated NWs. The pristine NW samples had the highest capacity at low cycle rates, but at the expense of lower Coulombic efficiency and a decline in capacity throughout cycling.

However, even at high cycle rates of 10 C, the pristine NW sample still had capacity and recovered to full capacity upon a return to the C/10 rate. The added benefits of using PAA as a binder, seemed to outweigh any disadvantages higher surface oxidation might cause, and, indeed, the surface oxidation is important for strong PAA adherence to the nanowires.

3.4 CONCLUSIONS

These battery experiments examine the impact surface passivation has on battery Ge NW battery performance. Each of the nanowire passivations resulted in different cycling behavior and capability. Pristine nanowires exhibited the best capacity at slow cycle times, but consistently had the lowest Coulombic efficiency. MUA nanowires had lower capacity than unpassivated nanowires, but the highest Coulombic efficiency. DDE exhibited low capacity at 1 C, but with extremely stable cycling and the best performance at a high cycle rate 10 C. DDT passivated nanowires performed with lower capacity at high rates and with lower stability in all tests. Previous research that found that DDT had enhanced performance due to improved binding with PVdF, but the same effect was not seen with PAA. Nanowires with different passivations had very different SEI compositions in the first cycle, but were largely the same by the 100^{th} cycle. This research shows that the interaction between the nanowire surface, polymeric binder, and SEI formation is complex and must be optimized in conjunction to achieve the best results. The best surface chemistry with one binder might be different with another. Ideally, in the future, NWs with different passivations could be used for different performance needs.

3.5 REFERENCES

(1) Tarascon, J.-M.; Armand, M. Issues and Challenges Facing Rechargeable Lithium Batteries. *Nature* **2001**, *414* (6861), 359–367.

(2) Goodenough, J. B.; Kim, Y. Challenges for Rechargeable Li Batteries. *Chem. Mater.* **2010**, *22* (3), 587–603.

(3) Etacheri, V.; Marom, R.; Elazari, R.; Salitra, G.; Aurbach, D. Challenges in the Development of Advanced Li-Ion Batteries: A Review. *Energy Environ. Sci.* **2011**, *4* (9), 3243–3262.

(4) Bogart, T. D.; Chockla, A. M.; Korgel, B. A. High Capacity Lithium Ion Battery Anodes of Silicon and Germanium. *Curr. Opin. Chem. Eng.* **2013**, *2* (3), 286–293.

(5) Yoon, S.; Park, C.-M.; Sohn, H.-J. Electrochemical Characterizations of Germanium and Carbon-Coated Germanium Composite Anode for Lithium-Ion Batteries. *Electrochem. Solid-State Lett.* **2008**, *11* (4), A42–A45.

(6) McDowell, M. T.; Lee, S. W.; Nix, W. D.; Cui, Y. 25th Anniversary Article: Understanding the Lithiation of Silicon and Other Alloying Anodes for Lithium-Ion Batteries. *Adv. Mater. Deerfield Beach Fla* **2013**, *25* (36), 4966–4985.

(7) Chockla, A. M.; Klavetter, K. C.; Mullins, C. B.; Korgel, B. A. Solution-Grown Germanium Nanowire Anodes for Lithium-Ion Batteries. *ACS Appl. Mater. Interfaces* **2012**, *4* (9), 4658–4664.

(8) Yuan, F.-W.; Yang, H.-J.; Tuan, H.-Y. Alkanethiol-Passivated Ge Nanowires as High-Performance Anode Materials for Lithium-Ion Batteries: The Role of Chemical Surface Functionalization. *ACS Nano* **2012**, *6* (11), 9932–9942.

(9) McDowell, M. T.; Lee, S. W.; Ryu, I.; Wu, H.; Nix, W. D.; Choi, J. W.; Cui, Y. Novel Size and Surface Oxide Effects in Silicon Nanowires as Lithium Battery Anodes. *Nano Lett.* **2011**, *11* (9), 4018–4025.

(10) Xu, W.; Vegunta, S. S. S.; Flake, J. C. Surface-Modified Silicon Nanowire Anodes for Lithium-Ion Batteries. *J. Power Sources* **2011**, *196* (20), 8583–8589.

(11) Bogart, T. D.; Oka, D.; Lu, X.; Gu, M.; Wang, C.; Korgel, B. A. Lithium Ion Battery Peformance of Silicon Nanowires with Carbon Skin. *ACS Nano* **2014**, *8* (1), 915–922.

(12) Chan, C. K.; Patel, R. N.; O'Connell, M. J.; Korgel, B. A.; Cui, Y. Solution-Grown Silicon Nanowires for Lithium-Ion Battery Anodes. *ACS Nano* **2010**, *4* (3), 1443–1450.

(13) Chockla, A. M.; Harris, J. T.; Akhavan, V. A.; Bogart, T. D.; Holmberg, V. C.; Steinhagen, C.; Mullins, C. B.; Stevenson, K. J.; Korgel, B. A. Silicon Nanowire Fabric as a Lithium Ion Battery Electrode Material. *J. Am. Chem. Soc.* **2011**, *133* (51), 20914–20921.

(14) Verma, P.; Maire, P.; Novák, P. A Review of the Features and Analyses of the Solid Electrolyte Interphase in Li-Ion Batteries. *Electrochimica Acta* **2010**, *55* (22), 6332–6341.

(15) Winter, M.; Besenhard, J. O. Electrochemical Lithiation of Tin and Tin-Based Intermetallics and Composites. *Electrochimica Acta* **1999**, *45* (1), 31–50.

(16) Chan, C. K.; Ruffo, R.; Hong, S. S.; Cui, Y. Surface Chemistry and Morphology of the Solid Electrolyte Interphase on Silicon Nanowire Lithium-Ion Battery Anodes. *J. Power Sources* **2009**, *189* (2), 1132–1140.

(17) Holmberg, V. C.; Korgel, B. A. Corrosion Resistance of Thiol- and Alkene-Passivated Germanium Nanowires. *Chem. Mater.* **2010**, *22* (12), 3698–3703.

(18) Holmberg, V. C.; Rasch, M. R.; Korgel, B. A. PEGylation of Carboxylic Acid-Functionalized Germanium Nanowires. *Langmuir* **2010**, *26* (17), 14241–14246.

(19) Hanrath, T.; Korgel, B. A. Chemical Surface Passivation of Ge Nanowires. *J. Am. Chem. Soc.* **2004**, *126* (47), 15466–15472.

(20) Aurbach, D.; Ein-Eli, Y.; Markovsky, B.; Zaban, A.; Luski, S.; Carmeli, Y.; Yamin, H. The Study of Electrolyte Solutions Based on Ethylene and Diethyl Carbonates for Rechargeable Li Batteries II . Graphite Electrodes. *J. Electrochem. Soc.* **1995**, *142* (9), 2882–2890.

(21) Meng, A. C.; Fenrich, C. S.; Braun, M. R.; McVittie, J. P.; Marshall, A. F.; Harris, J. S.; McIntyre, P. C. Core-Shell Germanium/Germanium–Tin Nanowires Exhibiting Room-Temperature Direct- and Indirect-Gap Photoluminescence. *Nano Lett.* **2016**, *16* (12), 7521–7529.

(22) Brust, M.; Walker, M.; Bethell, D.; Schiffrin, D. J.; Whyman, R. Synthesis of Thiol-Derivatised Gold Nanoparticles in a Two-Phase Liquid–Liquid System. *J. Chem. Soc., Chem. Commun.* **1994**, No. 7, 801–802.

(23) Hanrath, T.; Korgel, B. A. Nucleation and Growth of Germanium Nanowires Seeded by Organic Monolayer-Coated Gold Nanocrystals. *J. Am. Chem. Soc.* **2002**, *124* (7), 1424–1429.

(24) Lu, X.; Harris, J. T.; Villarreal, J. E.; Chockla, A. M.; Korgel, B. A. Enhanced Nickel-Seeded Synthesis of Germanium Nanowires. *Chem. Mater.* **2013**, *25* (10), 2172–2177.

(25) Coates, J. Interpretation of Infrared Spectra: A Practical Approach. *Encyclopedia of Analytical Chemistry*; Meyers, R. A., Ed.; Wiley: Chichester, U.K., 2000; pp 10815–10837.

(26) Klavetter, K. C.; Wood, S. M.; Lin, Y.-M.; Snider, J. L.; Davy, N. C.; Chockla, A. M.; Romanovicz, D. K.; Korgel, B. A.; Lee, J.-W.; Heller, A.; et al. A High-Rate Germanium-Particle Slurry Cast Li-Ion Anode with High Coulombic Efficiency and Long Cycle Life. *J. Power Sources* **2013**, *238*, 123–136.

(27) Graetz, J.; Ahn, C. C.; Yazami, R.; Fultz, B. Nanocrystalline and Thin Film Germanium Electrodes with High Lithium Capacity and High Rate Capabilities. *J. Electrochem. Soc.* **2004**, *151* (5), A698–A702.

(28) Seo, M.-H.; Park, M.; Lee, K. T.; Kim, K.; Kim, J.; Cho, J. High Performance Ge Nanowire Anode Sheathed with Carbon for Lithium Rechargeable Batteries. *Energy Environ. Sci.* **2011**, *4* (2), 425–428.

(29) Dedryvère, R.; Laruelle, S.; Grugeon, S.; Gireaud, L.; Tarascon, J.-M.; Gonbeau, D. XPS Identification of the Organic and Inorganic Components of the Electrode/Electrolyte Interface Formed on a Metallic Cathode. *J. Electrochem. Soc.* **2005**, *152* (4), A689–A696.

(30) Andersson, A. M.; Herstedt, M.; Bishop, A. G.; Edström, K. The Influence of Lithium Salt on the Interfacial Reactions Controlling the Thermal Stability of Graphite Anodes. *Electrochimica Acta* **2002**, *47* (12), 1885–1898.

(31) Aurbach, D.; Weissman, I.; Schechter, A.; Cohen, H. X-Ray Photoelectron Spectroscopy Studies of Lithium Surfaces Prepared in Several Important Electrolyte Solutions. A Comparison with Previous Studies by Fourier Transform Infrared Spectroscopy. *Langmuir* **1996**, *12* (16), 3991–4007.

(32) Schechter, A.; Aurbach, D.; Cohen, H. X-Ray Photoelectron Spectroscopy Study of Surface Films Formed on Li Electrodes Freshly Prepared in Alkyl Carbonate Solutions. *Langmuir* **1999**, *15* (9), 3334–3342.

(33) Leroy, S.; Blanchard, F.; Dedryvère, R.; Martinez, H.; Carré, B.; Lemordant, D.; Gonbeau, D. Surface Film Formation on a Graphite Electrode in Li-Ion Batteries: AFM and XPS Study. *Surf. Interface Anal.* **2005**, *37* (10), 773–781.

(34) Nakai, H.; Kubota, T.; Kita, A.; Kawashima, A. Investigation of the Solid Electrolyte Interphase Formed by Fluoroethylene Carbonate on Si Electrodes. *J. Electrochem. Soc.* **2011**, *158* (7), A798–A801.

(35) Magasinski, A.; Zdyrko, B.; Kovalenko, I.; Hertzberg, B.; Burtovyy, R.; Huebner, C. F.; Fuller, T. F.; Luzinov, I.; Yushin, G. Toward Efficient Binders for Li-Ion Battery Si-Based Anodes: Polyacrylic Acid. *ACS Appl. Mater. Interfaces* **2010**, *2* (11), 3004–3010.

(36) Nguyen, C. C.; Yoon, T.; Seo, D. M.; Guduru, P.; Lucht, B. L. Systematic Investigation of Binders for Silicon Anodes: Interactions of Binder with Silicon Particles and Electrolytes and Effects of Binders on Solid Electrolyte Interphase Formation. *ACS Appl. Mater. Interfaces* **2016**, *8* (19), 12211–12220.

(37) Nguyen, C. C.; Seo, D. M.; Chandrasiri, K. W. D. K.; Lucht, B. L. Improved Cycling Performance of a Si Nanoparticle Anode Utilizing Citric Acid as a Surface-Modifying Agent. *Langmuir* **2017**, *33* (37), 9254–9261.

Chapter 4: *In Situ* TEM of Oxide Shell-Induced Pore Formation in (De)lithiated Silicon Nanowires[§]

4.1 Introduction

Future technologies will require improvements in the energy density, rate capability, cost, and safety of lithium ion batteries (LIBs).[1–3] Silicon (Si) is an attractive next generation anode material because it is inexpensive, abundant, and has a high theoretical gravimetric storage capacity of 3579 mAh/g, nearly ten times that of present graphite electrodes.[4] However, Si experiences massive volume expansion, of nearly 310%, when fully lithiated and suffers from low conductivity.[5] Nanostructured Si can largely withstand lithium-induced volume change without pulverization, but the continual expansion and contraction leads to loss of electrical connection between the nanowire and the conductive additive and lowers Columbic efficiency over time.[6–11]

One strategy that has been used to improve the performance of nanostructured Si, is the addition of a surface coating layer.[12–17] Coatings that have been investigated include silicon oxide (SiO_x), carbon, alucone, and TiO_2, among others.[15–18] A surface coating can increase conductivity, improve mechanical stability, and protect the active material from reaction with the electrolyte. In particular, silicon oxide is an interesting coating because it can be grown on the Si surface easily and at a controllable thickness. *Ex situ* TEM studies have found this shell limits volume expansion during lithiation, while coin cell experiments show this improves cycling stability, though reduces the capacity.[12,17] There are still questions as to exactly how the shell improves stability and the impact reduced lithiation has on structural changes during battery cycling.

[§] The work contained in this section is the subject of a scholarly article that is currently in preparation. Authors on this work include Emily R. Adkins, Taizhi Jiang, Langli Luo, Chong-Min Wang, and Brian A. Korgel. Emily Adkins was responsible for planning the research, synthesizing the materials, directing the *in-situ* TEM experiments, analyzing the data, researching and writing the completed document.

In situ TEM allows real-time direct investigation of morphology changes that occur during cycling that are not easily understood through *ex situ* techniques, such as pore formation, preferential lithiation, and self-limiting lithiation.[18–21] This technique has been used to determine the impact a surface coating has on nanowire battery cycling such as, inducing pore formation, limiting volume expansion, and increasing the lithiation rate.[14,16,22] These findings help develop a fundamental understanding of the relationship between the properties, structure, and performance of Si-based anodes.

In this paper, we examine the morphology changes that occur in Si nanowires coated with an SiO_x shell as they undergo lithiation and delithiation by *in situ* TEM. The oxide shell constrains the expansion of the nanowire and prevents complete lithiation. The nanowire retains a crystalline Si core. When the nanowire is delithiated, pores are observed to form in the amorphized Si. The SiO_x shell prevents migration of vacancies formed during delithiation to the nanowire surface. The vacancies aggregate and form pores. These *in situ* studies provide insight into the impact an SiO_x shell has on structural changes experienced by a Si nanowire during cycling.

4.2 Experimental Details

4.2.1 Chemicals

Trisilane (>99%) was purchased from Voltaix, LLC. Anhydrous toluene (99.8%), chloroform (99.9%), 1-dodecanethiol (Aldrich, >98%), and ethanol (99.9%) were purchased from Sigma-Aldrich. All purchased chemicals were used as received without any further purification.

4.2.2 Nanowire Synthesis

Si nanowires were synthesized by super critical fluid–liquid–solid (SFLS) growth following published procedures.[23] Gold (Au) nanocrystals with an average diameter of 2

nm, capped with 1-dodecanethiol, were prepared using the method of Brust et al. and stored in anhydrous toluene.[24] The nanowire synthesis was performed in a nitrogen glovebox to minimize air exposure of pyrophoric reactants. A 10 mL titanium tubular reactor was connected to a high-pressure liquid chromatography (HPLC) pump then heated to 490ºC and pressurized to 13.8 MPa. A reaction solution was prepared with 27.5 mg of gold nanoparticles in a 50 mg/mL solution, 2.01 M trisilane and anhydrous toluene. *Caution! Trisilane is pyrophoric and must be handled under inert conditions.* The reactant solution was fed to the reactor at 3 mL/min. Once the reactor has repressurized to 13.8 MPa, the inlet valve was closed and held at 490ºC for two minutes. After cooling, the nanowires were centrifuged at 8000 rpm for 5 minutes. The supernatant was then discarded and the nanowires washed using chloroform, toluene, and ethanol at a 2:1:1 ratio. The nanowires were then centrifuged and washed two more times. The resulting nanowires were stored in chloroform.

4.2.3 Oxide Shell Growth

Immediately after synthesis, nanowires have only a thin oxide shell. To examine a wider range of oxide shell thicknesses, an oxide shell was grown on the wires. This was done using a Mettler-Toledo Thermogravimetric Analyzer/DSC1 (TGA). Nanowires were prepared by depositing approximately 4 mg of nanowires into a 70 μL alumina crucible (Mettler-Toledo). In the TGA, the temperature was ramped up to 100ºC at a rate of 15ºC/min under nitrogen flow and held for 20 minutes, to allow any residual solvent to dry. The temperature was then increased to the set point of 800ºC. The gas flow was switched to air at a flowrate of 10 mL/min and the sample held at this temperature for 3 hours. After 3 hours the samples were allowed to cool.

4.2.4 *In Situ* TEM Measurements

In situ TEM measurements were made using a Nanofactory TEM holder inside a Titan 80-300 scanning/transmission electron microscope (S/TEM). Samples were dropcast by micropipette onto a platinum probe wire as a working electrode and inserted into the holder. The counter electrode was a tungsten probe mounted with lithium metal prepared in a glovebox (Figure 2c). A small amount of Li_2O was allowed to grow on the surface during transfer from the glovebox to the TEM vacuum which was used as a solid state electrolyte.[19] Inside the TEM, the nanowire probe was moved using a piezo-positioner and brought into contact with the lithium. To lithiate/delithiate the wires, a voltage was applied between -5V to 2V vs Li/Li^+. This is a larger voltage window than would be needed in a traditional lithium ion battery due to slow ion diffusion through the solid electrolyte.[19]

4.3 Results and Discussion

Figure 4.1a shows TEM images of a typical Si nanowire used in the *in situ* battery studies. The nanowire has a crystalline Si core with a thin SiO_x shell that is formed by heating the nanowires to 800ºC under constant air flow. The nanowires are several micrometers long, straight, crystalline, and have an average diameter of 42 nm with an oxide shell thickness of 11 nm. Many nanowires exhibit twins that run down the length of the nanowires, as observed in the nanowire in Figure 4.1a. The crystalline Si core of the nanowire has a higher image contrast than the SiO_x shell, making it possible to measure the shell thickness, which for the nanowire in Figure 4.1 is 8 nm thick. Figure 4.1c shows a scanning transmission electron microscopy (STEM) high-angle annular dark-field (HAADF) image of a Si nanowire with an SiO_x shell on the surface and the associated energy dispersive X-ray spectroscopy (EDS) maps (Figure 4.1d-e) which show the Si core and the oxide shell.

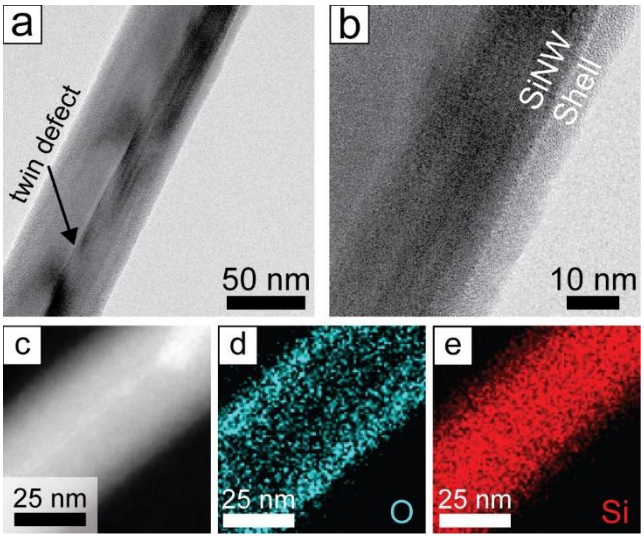

Figure 4.1 (a) TEM images showing an 8 nm thick oxide shell grown on the Si nanowire surface. This nanowire has a twin defect along its length. (b) A magnified image of the same wire more clearly shows the SiO_x shell. (c) STEM HAADF image of a Si nanowire with an SiO_x shell with associated EDS mapping of the (d) O and (e) Si distribution. Elemental analysis shows the nanowire has a Si core and an oxide shell

Si nanowires with an SiO_x surface shell were lithiated *in situ* in an all-solid nanobattery assembled in the TEM, as depicted in Figure 2.2c and described further in the Section 4.2.4. Figures 4.2 a-b show a time series of TEM images of a Si nanowire with an SiO_x shell as it undergoes lithiation and delithiation (See accompanying video file LithiationVideo_1.mp4 listed in Appendix C). Lithiation initially occurs on the surface of the nanowire and then proceeds radially into the core. This mechanism of *surface-into-core* lithiation is well-established for Si nanowires.[25,26]

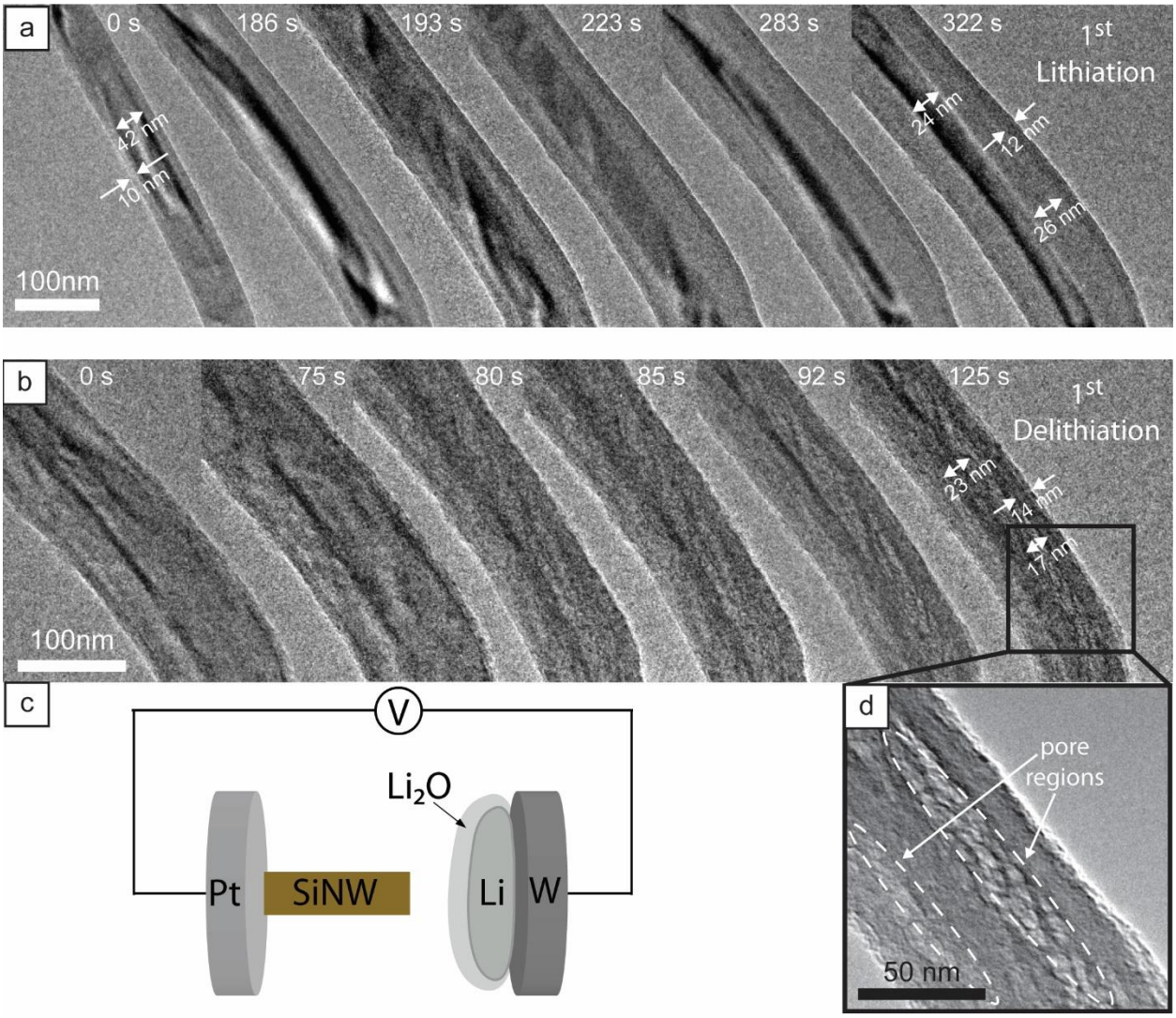

Figure 4.2 TEM images of a Si nanowire with an SiO_x shell taken during the first (a) lithiation and (b) delithiation cycle. The nanowire experiences 132.6% volume expansion and retains a crystalline core of 24 nm diameter at the end of lithiation. (See accompanying video file LithiationVideo_1.mp4 listed in Appendix C) (c) A cartoon of the *in situ* TEM nanobattery set up. (d) A higher magnification TEM image of pores that form in the amorphous Si region of the nanowire after delithiation.

Lithiation causes axial and radial expansion of the core-shell nanowire volume by an average of 130%. Volume expansion is found by measuring the diameter and length of

the nanowire before and after lithiation. Length expansion is determined by tracking two points on the nanowire during lithiation and measuring the distance as it changes. Length can be difficult to track due to bending of the nanowire out of the imaging plane. Table C.1 in Appendix C has statistics from three Si nanowires with an intact SiO_x shell. If the SiO_x shell is initially defect free, it will remain intact during cycling. In the nanowire shown in Figure 4.2a, the total diameter increases during lithiation from 60 nm to 100 nm, corresponding to a volume expansion of 132.6%. This is significantly less than the 310% volume expansion a fully lithiated Si nanowire without a shell would experience.[6]

An intact and uniform oxide shell constrains the volume expansion and prevents complete lithiation of the nanowire. This results in a thin residual crystalline Si core which remains even after prolonged applied voltage. In the nanowire shown in Figure 4.2a, the crystalline core shrinks from a pre-lithiation diameter of 42 nm to 24 nm after lithiation. This observation is consistent with coin cell data showing that Si anodes with an SiO_x surface-coating layer have reduced specific capacity during cycling.[12,17] The crystalline core is still visible after delithiation (Figure 4.2b) and during a second lithiation as well (Figure C.1 in Appendix C). During the second lithiation, the crystalline core eventually becomes no longer visible. It is not clear whether this is because it has amorphized, or due to the limited phase contrast between the core and the lithiated SiO_x shell and the increased roughness of the SiO_x shell.

Nanowires with an intact SiO_x shell exhibit pore formation upon the first delithiation. Figure 4.2d shows a magnified view of the pores that appear in the Li-Si region of the nanowire during delithiation. During delithiation, the nanowire volume begins to shrink as Li is extracted. Following a continued applied voltage, pores become visible in the part of the nanowire that has previously shrunk. These pores are small and densely packed, similar to those formed in a Si nanoparticle with an oxide shell after delithiation.[16]

The volume of the nanowire following delithiation is 43% greater than the initial volume before lithiation. This expansion is due to the pore volume remaining within the nanowires after lithium removal, as well as some degree of lithiation-induced plastic deformation.[27] During the second lithiation, the pores disappear in the nanowire and then reappear upon deltihiation (Figure C.1 in Appendix C). The volume of the nanowire following the second delithiation has expanded by 26% from the first delithiation, indicating the pores have increased in diameter more than is visible. TEM images showing nanopores after the first and second delithiations are found in Figure C.2 in appendix C. Figure 4.3 shows a time series of TEM images of an additional Si nanowire with an SiO_x shell that exhibited pore formation. (See accompanying video file PoreVideo_2.mp4 listed in Appendix C).

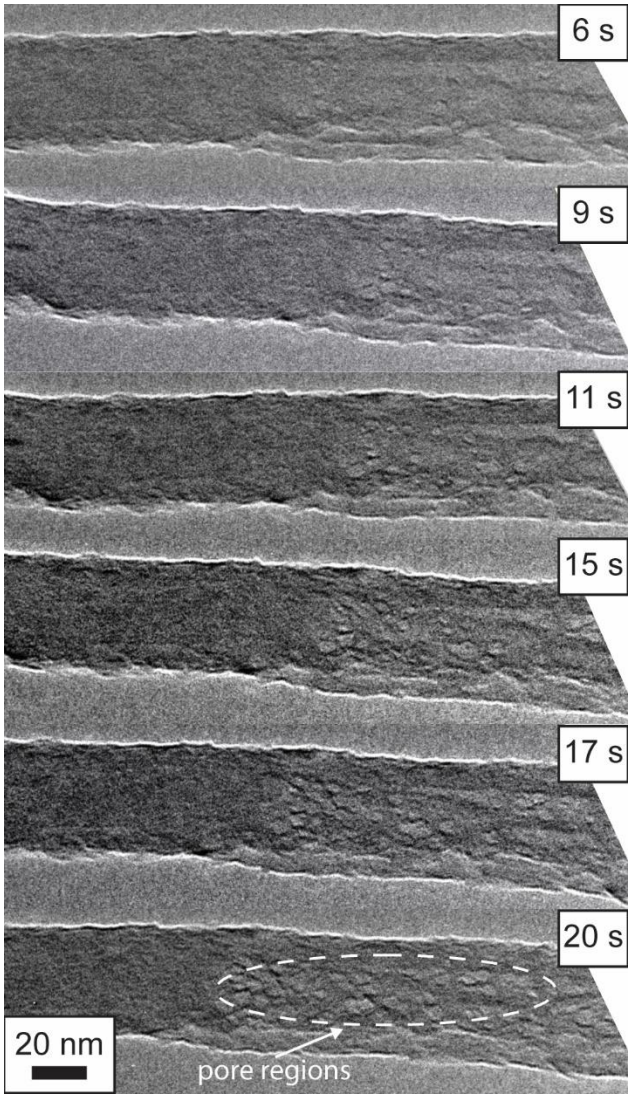

Figure 4.3 TEM images of a Si nanowire with an SiO_x shell showing the formation of pores in the nanowire during the first delithiation. (See accompanying video file PoreVideo_2.mp4 listed in Appendix C.)

The SiO_x shell of some nanowires burst during lithiation. An existing defect in the oxide shell causes the burst during lithiation. The burst SiO_x shell results in significantly more volume expansion, an average of 253%. Table C.1 in Appendix C has statistics from four Si nanowires with an SiO_x shell that burst. These nanowires did not exhibit pore formation and did not retain a crystalline core. Figure 4.4 shows a time series of TEM

images of a Si nanowire with an SiO_x shell that bursts during the first lithiation (See accompanying video file BurstWireVideo_3.mp4 listed in Appendix C). The burst occurs extremely quickly, between 110s and 111s. This nanowire experiences a volume expansion of 273% upon lithiation and does not retain a crystalline core. The burst relieves the buildup of compressive stresses created during Si lithiation and allows the nanowire to fully expand. Further time series TEM images of Si nanowires an SiO_x shell that burst during lithiation can be found in Figures C.3 and C.4 and the video file BurstWireVideo_4.mp4 listed in Appendix C.

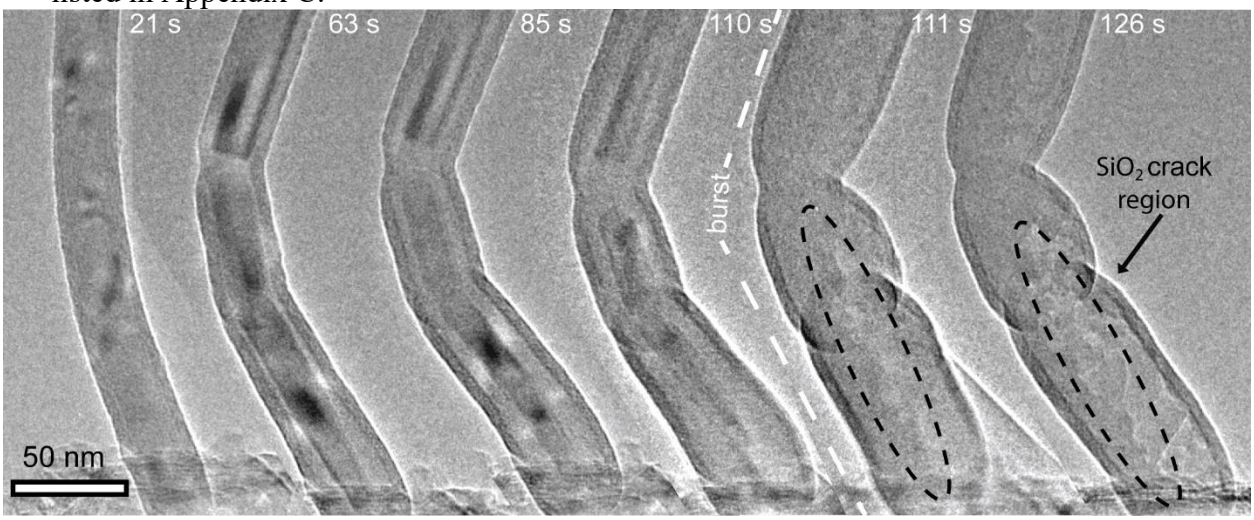

Figure 4.4 TEM images showing a Si nanowire with an SiO_x shell that bursts during the first cycle of lithiation. (See accompanying video file BurstWireVideo_3.mp4 listed in Appendix C.) This nanowire experiences a volume expansion of 273% upon lithiation and does not retain a crystalline core.

The oxide shell must be intact and present for pores to form. Nanowires with an oxide shell that burst completely did not form pores upon delithiation as shown in Figure C.3. The impact of the oxide shell is shown in the time series of TEM images in Figure 4.5 (See accompanying video file BurstWirePoresVideo_5.mp4 listed in Appendix C). This nanowire burst at a single point at 295 s and portions of the shell remained intact as the

nanowire lithiated and delithiated. In the part of the nanowire with a damaged shell no pores are seen during delithiation. In the part with a complete oxide shell, pore formation is visible.

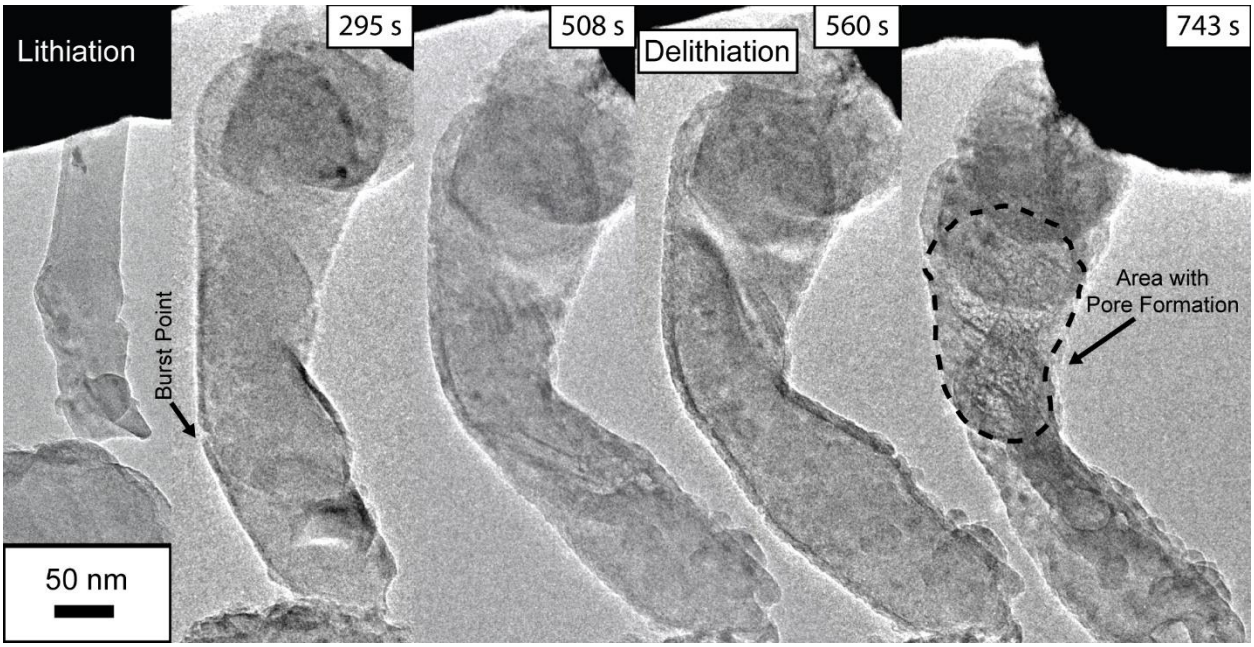

Figure 4.5 TEM images showing a Si nanowire with an SiO_x shell that bursts at a single point during the first lithiation. (See accompanying video file BurstWirePoresVideo_5.mp4 listed in Appendix C). A portion of the nanowire shell remains intact and pores begin to form only in this part of the nanowire during delithiation.

Pore formation has been observed before using *in situ* TEM.[16,20,28,29] Pore formation occurs when Li diffusion is fast and requires significantly less energy to occur than self-diffusion in the host material. This results in an accumulation of vacancies that aggregate into pores.[20,22] Pore formation is not typically seen in Si nanowires because the migration barrier for vacancies in Si, another way to describe self-diffusion, 0.45 eV, is close to the diffusion barrier for Li in amorphous lithiated Si, 0.47 eV.[22] In an uncoated Si nanowire, vacancies migrate to the surface of the nanowire during delithiation before pores can nucleate. With an SiO_x shell present, the vacancies need to migrate through the shell to the

surface, to avoid pore formation. The diffusion barrier of Li transport in lithiated SiO_x is approximately 0.72 eV.[30] The vacancy diffusion barrier for $Li_2Si_2O_5$ is 2.41 eV.[30] Theoretical modeling has shown that this barrier decreases as the SiO_x lithiates further to Li_2SiO_3 and then Li_4SiO_4, 1.19 eV and 0.91 eV respectively.[30]

To know the vacancy diffusion barrier in the lithiated oxide shell, it is helpful to know the final Li concentration. The SiO_x shell is an active participant in the lithiation reaction. The shell volume increases by 145% during lithiation and visibly roughens during subsequent cycles (Figure 4.6b). The reaction mechanism between Li and SiO_x is not fully understood, and there are many different possible products, including $Li_2Si_2O_5$, Li_4SiO_4, Li_2O, Si, and Li_xSi.[13] Previous *in situ* TEM research found Li_4SiO_4 and Li_2O to be the only crystalline phases present in a fully lithiated silicon oxide shell.[13] In the present study, the only crystalline species after lithiation, seen in the electron diffraction pattern in Figure 6a, is Li_2O. It is unclear whether this Li_2O can be attributed to reactions occurring in the shell or to diffusion of the Li_2O electrolyte along the nanowire surface from the counter electrode.

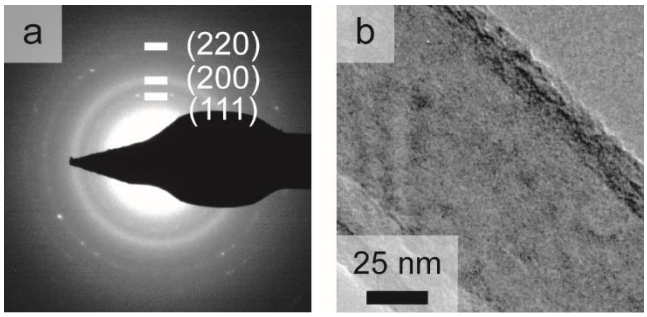

Figure 4.6 (a) TEM electron diffraction pattern of a Si nanowire with an SiO_x shell after delithiation, which shows the only crystalline species present is Li_2O. (b) A magnified TEM image of the SiO_x shell on a Si nanowire after delithiation that shows a visibly rough surface. The SiO_x shell is an active participant in the lithiation reaction and becomes rougher during the course of the battery cycle.

Even with the final lithiated composition of the shell uncertain, the vacancy diffusion barrier is still significantly higher than the energy barrier for Li transport in the Si core. Figure 4.7 illustrates the mechanism of pore formation in SiO_x shell nanowires. As Li diffuses out of the lithiated Si, vacancies form and are unable to migrate to the surface of the nanowire. These vacancies accumulate and nucleate into pores as more Li diffuses out of the nanowire. The impact a shell can have on pore formation in a nanowire during delithation has been observed before in Ge nanowires.[22] During delithiation, a denser Ge crust will form on the surface of the nanowires as vacancies close to the surface migrate out. This denser crust then creates a barrier for further vacancy migration to the surface. In contrast, pore formation is not seen in alucone coated Si nanoparticles because the surface coating has higher ionic and electrical conductivity than SiO_x.[16] Pore formation is further encouraged by the interface between the SiO_x shell and the Si core, which is a pathway for faster Li diffusion compared with in the Si bulk.[22,31,32] This creates a higher concentration of vacancies to nucleate into pores.

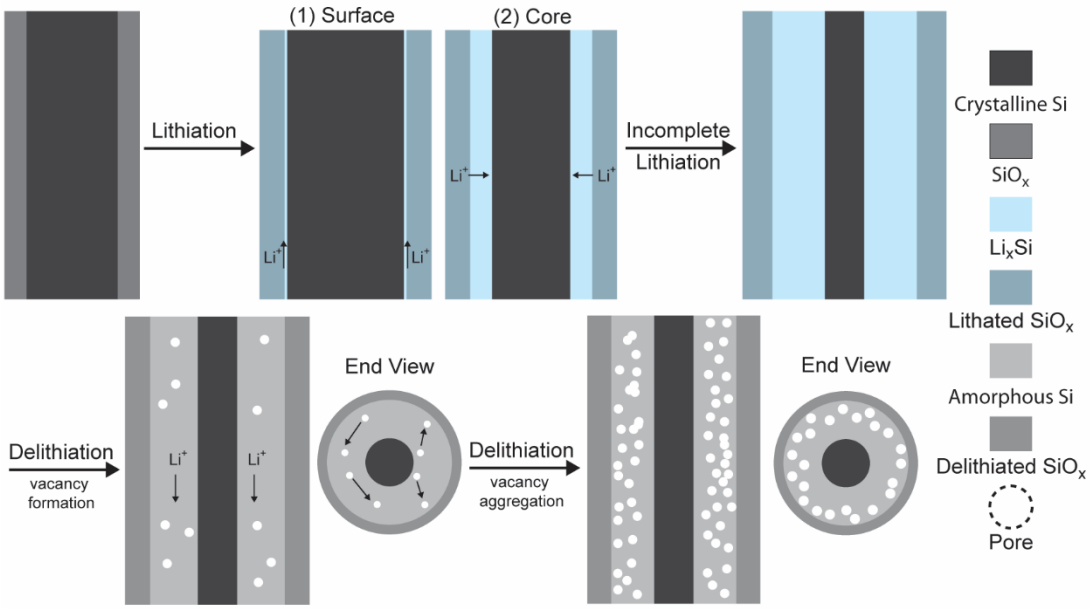

Figure 4.7 A schematic showing the pore formation mechanism in a Si nanowire with an SiO_x shell. During lithiation, the lithiation front moves first along the nanowire surface (1) and then inward toward the core (2). The nanowire reaches a point of maximum lithiation with a remaining crystalline core. Upon delithiation, vacancies form in the lithiated amorphous Si region. These vacancies are unable to migrate to the surface of the nanowire due to the SiO_x shell and nucleate into pores as more Li diffuses out of the nanowire.

4.4 CONCLUSIONS

These *in situ* TEM experiments confirmed that an intact SiO_x shell on a Si nanowire can limit the volume expansion of the Si during lithiation and cause pore formation during delithiation. The constrained volume expansion during lithiation causes incomplete lithiation of the nanowire and retention of a crystalline Si core. During delithiation, the SiO_x shell prevents vacancy migration to the surface of the nanowire, causing pore formation in the delithiated, amorphous Si region. Pore formation was not seen in nanowires with an incomplete or burst SiO_x shell. These results indicate that the interactions between a Si nanowire core and a shell are complex and can have a significant effects on changes in nanowire structure during battery cycling. *In situ* TEM observation

during cycling fully elucidates the impact an added shell has during lithiation and delithiation.

4.5 REFERENCES

(1) Tarascon, J.-M.; Armand, M. Issues and Challenges Facing Rechargeable Lithium Batteries. *Nature* **2001**, *414* (6861), 359–367.

(2) Goodenough, J. B.; Kim, Y. Challenges for Rechargeable Li Batteries. *Chem. Mater.* **2010**, *22* (3), 587–603.

(3) Etacheri, V.; Marom, R.; Elazari, R.; Salitra, G.; Aurbach, D. Challenges in the Development of Advanced Li-Ion Batteries: A Review. *Energy Environ. Sci.* **2011**, *4* (9), 3243–3262.

(4) Obrovac, M. N.; Christensen, L. Structural Changes in Silicon Anodes during Lithium Insertion/Extraction. *Electrochem. Solid-State Lett.* **2004**, *7* (5), A93–A96.

(5) Beaulieu, L. Y.; Eberman, K. W.; Turner, R. L.; Krause, L. J.; Dahn, J. R. Colossal Reversible Volume Changes in Lithium Alloys. *Electrochem. Solid-State Lett.* **2001**, *4* (9), A137–A140.

(6) Chan, C. K.; Peng, H.; Liu, G.; McIlwrath, K.; Zhang, X. F.; Huggins, R. A.; Cui, Y. High-Performance Lithium Battery Anodes Using Silicon Nanowires. *Nat. Nanotechnol.* **2008**, *3* (1), 31–35.

(7) McDowell, M. T.; Lee, S. W.; Nix, W. D.; Cui, Y. 25th Anniversary Article: Understanding the Lithiation of Silicon and Other Alloying Anodes for Lithium-Ion Batteries. *Adv. Mater. Deerfield Beach Fla* **2013**, *25* (36), 4966–4985.

(8) Chockla, A. M.; Klavetter, K. C.; Mullins, C. B.; Korgel, B. A. Tin-Seeded Silicon Nanowires for High Capacity Li-Ion Batteries. *Chem. Mater.* **2012**, *24* (19), 3738–3745.

(9) Chockla, A. M.; Klavetter, K. C.; Mullins, C. B.; Korgel, B. A. Solution-Grown Germanium Nanowire Anodes for Lithium-Ion Batteries. *ACS Appl. Mater. Interfaces* **2012**, *4* (9), 4658–4664.

(10) Chockla, A. M.; Harris, J. T.; Akhavan, V. A.; Bogart, T. D.; Holmberg, V. C.; Steinhagen, C.; Mullins, C. B.; Stevenson, K. J.; Korgel, B. A. Silicon Nanowire Fabric as a Lithium Ion Battery Electrode Material. *J. Am. Chem. Soc.* **2011**, *133* (51), 20914–20921.

(11) Chan, C. K.; Patel, R. N.; O'Connell, M. J.; Korgel, B. A.; Cui, Y. Solution-Grown Silicon Nanowires for Lithium-Ion Battery Anodes. *ACS Nano* **2010**, *4* (3), 1443–1450.

(12) Sim, S.; Oh, P.; Park, S.; Cho, J. Critical Thickness of SiO2 Coating Layer on Core@Shell Bulk@Nanowire Si Anode Materials for Li-Ion Batteries. *Adv. Mater.* **2013**, *25* (32), 4498–4503.

(13) Zhang, Y.; Li, Y.; Wang, Z.; Zhao, K. Lithiation of SiO2 in Li-Ion Batteries: In Situ Transmission Electron Microscopy Experiments and Theoretical Studies. *Nano Lett.* **2014**, *14* (12), 7161–7170.

(14) Bogart, T. D.; Oka, D.; Lu, X.; Gu, M.; Wang, C.; Korgel, B. A. Lithium Ion Battery Peformance of Silicon Nanowires with Carbon Skin. *ACS Nano* **2014**, *8* (1), 915–922.

(15) Kim, S. J.; Kargar, A.; Wang, D.; Graham, G. W.; Pan, X. Lithiation of Rutile TiO2-Coated Si NWs Observed by in Situ TEM. *Chem. Mater.* **2015**, *27* (20), 6929–6933.

(16) He, Y.; Piper, D. M.; Gu, M.; Travis, J. J.; George, S. M.; Lee, S.-H.; Genc, A.; Pullan, L.; Liu, J.; Mao, S. X.; et al. In Situ Transmission Electron Microscopy Probing of Native Oxide and Artificial Layers on Silicon Nanoparticles for Lithium Ion Batteries. *ACS Nano* **2014**, *8* (11), 11816–11823.

(17) McDowell, M. T.; Lee, S. W.; Ryu, I.; Wu, H.; Nix, W. D.; Choi, J. W.; Cui, Y. Novel Size and Surface Oxide Effects in Silicon Nanowires as Lithium Battery Anodes. *Nano Lett.* **2011**, *11* (9), 4018–4025.

(18) Liu, X. H.; Zhang, L. Q.; Zhong, L.; Liu, Y.; Zheng, H.; Wang, J. W.; Cho, J.-H.; Dayeh, S. A.; Picraux, S. T.; Sullivan, J. P.; et al. Ultrafast Electrochemical Lithiation of Individual Si Nanowire Anodes. *Nano Lett.* **2011**, *11* (6), 2251–2258.

(19) Liu, X. H.; Zheng, H.; Zhong, L.; Huang, S.; Karki, K.; Zhang, L. Q.; Liu, Y.; Kushima, A.; Liang, W. T.; Wang, J. W.; et al. Anisotropic Swelling and Fracture of Silicon Nanowires during Lithiation. *Nano Lett.* **2011**, *11* (8), 3312–3318.

(20) Liu, X. H.; Huang, S.; Picraux, S. T.; Li, J.; Zhu, T.; Huang, J. Y. Reversible Nanopore Formation in Ge Nanowires during Lithiation–Delithiation Cycling: An In Situ Transmission Electron Microscopy Study. *Nano Lett.* **2011**, *11* (9), 3991–3997.

(21) Liu, X. H.; Fan, F.; Yang, H.; Zhang, S.; Huang, J. Y.; Zhu, T. Self-Limiting Lithiation in Silicon Nanowires. *ACS Nano* **2013**, *7* (2), 1495–1503.

(22) Lu, X.; He, Y.; Mao, S. X.; Wang, C.; Korgel, B. A. Size Dependent Pore Formation in Germanium Nanowires Undergoing Reversible Delithiation Observed by In Situ TEM. *J. Phys. Chem. C* **2016**, *120* (50), 28825–28831.

(23) Heitsch, A. T.; Akhavan, V. A.; Korgel, B. A. Rapid SFLS Synthesis of Si Nanowires Using Trisilane with In Situ Alkyl-Amine Passivation. *Chem. Mater.* **2011**, *23* (11), 2697–2699.

(24) Brust, M.; Walker, M.; Bethell, D.; Schiffrin, D. J.; Whyman, R. Synthesis of Thiol-Derivatised Gold Nanoparticles in a Two-Phase Liquid–Liquid System. *J. Chem. Soc., Chem. Commun.* **1994**, No. 7, 801–802.

(25) Liu, X. H.; Wang, J. W.; Huang, S.; Fan, F.; Huang, X.; Liu, Y.; Krylyuk, S.; Yoo, J.; Dayeh, S. A.; Davydov, A. V.; et al. In Situ Atomic-Scale Imaging of Electrochemical Lithiation in Silicon. *Nat. Nanotechnol.* **2012**, *7* (11), 749–756.

(26) Gu, M.; Wang, Z.; Connell, J. G.; Perea, D. E.; Lauhon, L. J.; Gao, F.; Wang, C. Electronic Origin for the Phase Transition from Amorphous LixSi to Crystalline Li15Si4. *ACS Nano* **2013**, *7* (7), 6303–6309.

(27) Zhao, K.; Pharr, M.; Cai, S.; Vlassak, J. J.; Suo, Z. Large Plastic Deformation in High-Capacity Lithium-Ion Batteries Caused by Charge and Discharge. *J. Am. Ceram. Soc.* **2011**, *94*, s226–s235.

(28) Lu, X.; Adkins, E. R.; He, Y.; Zhong, L.; Luo, L.; Mao, S. X.; Wang, C.-M.; Korgel, B. A. Germanium as a Sodium Ion Battery Material: In Situ TEM Reveals Fast Sodiation Kinetics with High Capacity. *Chem. Mater.* **2016**, *28* (4), 1236–1242.

(29) Lu, X.; Bogart, T. D.; Gu, M.; Wang, C.; Korgel, B. A. In Situ TEM Observations of Sn-Containing Silicon Nanowires Undergoing Reversible Pore Formation Due to Fast Lithiation/Delithiation Kinetics. *J. Phys. Chem. C* **2015**, *119* (38), 21889–21895.

(30) Ostadhossein, A.; Kim, S.-Y.; Cubuk, E. D.; Qi, Y.; van Duin, A. C. T. Atomic Insight into the Lithium Storage and Diffusion Mechanism of SiO2/Al2O3 Electrodes of Lithium Ion Batteries: ReaxFF Reactive Force Field Modeling. *J. Phys. Chem. A* **2016**, *120* (13), 2114–2127.

(31) Wang, J. W.; Liu, X. H.; Zhao, K.; Palmer, A.; Patten, E.; Burton, D.; Mao, S. X.; Suo, Z.; Huang, J. Y. Sandwich-Lithiation and Longitudinal Crack in Amorphous Silicon Coated on Carbon Nanofibers. *ACS Nano* **2012**, *6* (10), 9158–9167.

(32) McDowell, M. T.; Lee, S. W.; Harris, J. T.; Korgel, B. A.; Wang, C.; Nix, W. D.; Cui, Y. In Situ TEM of Two-Phase Lithiation of Amorphous Silicon Nanospheres. *Nano Lett.* **2013**, *13* (2), 758–764.

Chapter 5: Si Anodes with Lithium Iron Phosphate and Sulfur Cathodes: Impact of Prelithiation Method and XPS Analysis**

5.1 INTRODUCTION

Lithium ion batteries (LIBs) with higher energy and power density are needed to meet the increasing demands of portable electronic devices, extended-range electric vehicles, and renewable energy storage.[1–6] An LIB operates by shuttling Li^+ ions back and forth between two electrodes, and the amount of Li^+ that these electrode materials can store determines the charge storage capacity of the battery, Q_T. To increase the performance of the LIB, both the anode and cathode capacities, Q_A and Q_C, require improvement since:

$$Q_T = \frac{Q_A Q_C}{Q_A + Q_C} \qquad (1)$$

Using common cathode and anode materials of lithium cobalt oxide ($LiCoO_2$) and graphite, with capacities of 137 mAh/g,[5,7] and 372 mAh/g,[1,5] respectively, the typical LIB capacity is ~100 mAh/g, as shown in Figure 5.1. The charge storage capacity of the anode could be increased by nearly a factor of ten by changing to silicon (Si),[5,8–14] and a number of emerging cathode materials exist with higher capacity than $LiCoO_2$, including both intercalation and conversion materials like LFP and S.

** The work contained in this chapter is the subject of a scholarly article that is currently in preparation. Authors on this work include Emily R. Adkins, Taizhi Jiang, Andrew L. Heilman, Sheng-Heng Chung, Jieun Hwang, Jaehoon Kim, Arumugam Manthiram, and Brian A. Korgel. Emily Adkins was responsible for planning the research, synthesizing Si nanowire materials, performing battery experiments using materials provided by collaborators, with some help from Drew Heilman, analyzing the battery data, researching and writing the completed document.

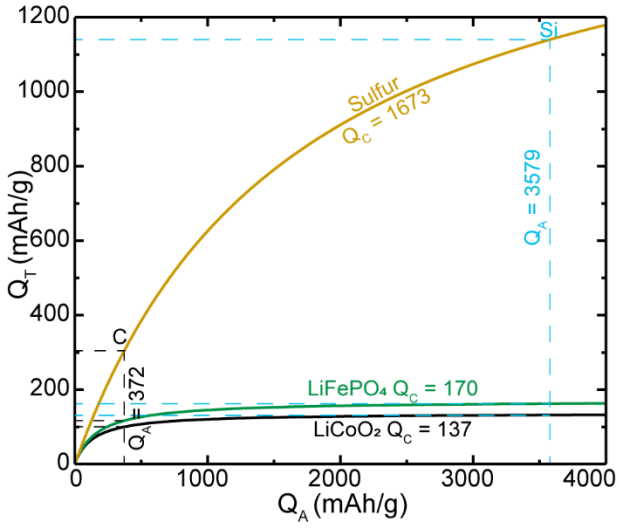

Figure 5.1 Charge storage capacity Q_T, of LIBs fabricated using different cathode materials with capacities Q_C, plotted as a function of the capacity of the anode Q_A: $LiCoO_2$ (137 mAh/g), $LiFePO_4$ (170 mAh/g), and sulfur (1673 mAh/g).

Many challenges face the use of Si in batteries,[8] including, perhaps most significantly, the large volume expansion of nearly 300% required to reach the fully lithiated state.[15] The expansion of Si reduces the volumetric charge storage capacity of the anode, but even on this basis, a Si anode has ~200% higher capacity than graphite, 2194 Ah/L and 719 Ah/L, respectively.[16] Si nanoparticles and nanowires can tolerate the expansion without significant degradation,[13,17,18] but the instability of the solid electrolyte interphase (SEI) layer has proven to be a challenge to solve. The continued accumulation of SEI during battery operation results in irreversible trapping of Li^+, which results in a gradual loss of capacity.[19] In half-cells cycled against lithium metal, both Si nanowires and nanoparticles have exhibited long-term stability,[1,3,13,20,21] but the gradual loss of Li to the SEI layer often goes unnoticed in these half-cell tests because of the nearly unlimited supply of Li in the cell, unless the battery is operated for more than a thousand cycles. The repeated expansion and contraction of the Si destabilizes the SEI layer.[3,22] While some Li^+

loss naturally occurs during the first cycle when the SEI layer forms, continued electrolyte degradation must be prevented.[23] The gradual loss of Li to the SEI layer in an LIB with a cathode material is an especially significant problem.[24] Additional Li must be incorporated into the anode during battery fabrication either by adding stabilized Li metal particles,[25–27] or lithiated Si nanoparticle additives,[28] or by pre-lithiating the nanowires, electrochemically or using direct contact with Li, as shown in Figure 5.2a.[29,30]

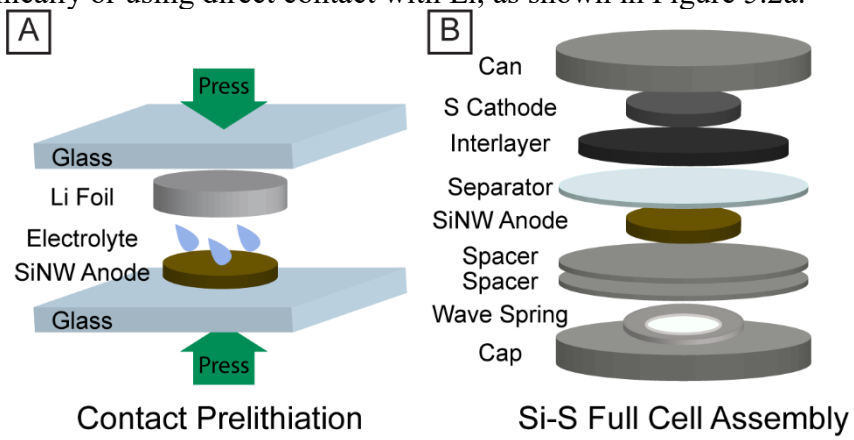

Figure 5.2 Schematic describing full cell preparation. (a) Prelithiation of a Si anode by contact with Li foil prior to full cell assembly was done in the glovebox using two glass slides and paper binder clips. (b) S cathodes were used in conjunction with a carbon interlayer, which is positioned between the cathode and separator in the full cell. Full cells are made using two spacers to create even pressure within the coin cell.

Many new types of cathodes can be combined with SiNW anodes.[31] Intercalation materials common in LIBs,[32] include commercially-used "second generation" materials like transition metal oxides and polyanion compounds, $LiNi_{0.8}Co_{0.15}Al_{0.05}O_2$ (NCA), $LiMn_2O_4$, $LiNi_{0.33}Mn_{0.33}Co_{0.33}O_2$ (NMC), $Li_4Ti_5O_{12}$ (LTO), and $LiFePO_4$ (LFP), which have theoretical capacities between ~150-280 mAh/g.[31,32] These materials exhibit high structural stability, high voltage (between 3.4-4.0 V), and are relatively inexpensive. Intercalation materials with significantly higher storage capacity that are still under

development include vanadium and molybdenum oxides with >300 mAh/g and >600 mAh/g, respectively.[33–35] Conversion materials that undergo a reaction with Li^+ offer significantly higher battery capacity, like metal flourides, with capacities between 500-700 mAh/g,[36] and selenium, which has a gravimetric capacity of 678 mAh/g.[37,38] Compared to intercalation compounds, there are added challenges to using these materials because of the changing structure and chemical bond-breaking that must be accounted for in the battery design.[31] Of the conversion cathodes, sulfur (S) has the highest known capacity, of 1,675 mAh/g.[6,39–42] Herein, we test full cell LIBs consisting of Si anodes and two different emerging cathode materials: LFP and S.

LFP has high structural and thermal stability, an operating voltage of 3.4 V, and is made from abundant and inexpensive starting materials.[5,43–47] LFP suffers from low electrical conductivity and slow Li^+ diffusion, which can be overcome, to some extent, by nanostructuring and coating with carbon.[43,45,47,48] LFP has a capacity of 170 mAh/g[31,44,47] and combined with a Si anode would provide a full cell with a capacity of 155 mAh/g.[49]

There have been a few demonstrations of a full cell battery using Si as the anode and LFP as the cathode.[50–53] Primary problems experienced by these cells include the high initial capacity loss and Li^+ loss to the anode SEI, which has resulted in poor cycle stability.[50] This problem has also been observed in Si-$LiCoO_2$ full cells, in which the irreversible loss of Li^+ to the anode SEI was the primary source of capacity loss.[54] Because the capacity of Si is so much higher than that of the intercalation cathode materials, the cathode must be very thick to match the anode capacity, which ends up hindering the rate capability due to slow Li^+ diffusion.[55] Balancing the Li capacities of the anode and cathode is needed to maximize the Li utilization within the cell.[56]

Sulfur has a much higher capacity than LFP (1673 mAh/g) and if combined with Si, could enable LIBs with an exceptionally high capacity of 1102 mAh/g.[57] There are

several significant technical challenges facing the combined use of S and Si in a LIB. First of all, S has a high electrical resistance. It experiences a large volume change (~80% upon lithiation) during cycling. It has also exhibited high irreversible capacity loss.[6] During lithiation, long polysulfide chains are reduced by Li to Li_2S via intermediate lithium polysulfides. The lithium polysulfides dissolve in the battery electrolyte and lead to a cycle of dissolution and deposition during battery cycling.[6] However, dissolved species can irreversibly passivate the anode, which increases impedance, corrodes the anode active material, and reduces the amount of S that can be used for energy storage.[6] One strategy to reduce polysulfide migration to the anode is to use a carbon interlayer in conjunction with a S cathode, as shown in Figure 2b, where it is positioned between the cathode and the separator.[58–63] The interlayer can be made from a conductive material that adsorbs the dissolved polysulfides and reutilizes them in subsequent cycles, which prevents them from migrating to the anode surface and increases capacity.[6,62]

The typical carbonate electrolyte used in LIBs cannot be used with S cathodes because sulfur anions react rapidly with carbonates.[40,64–66] Glyme-based electrolytes have a lower reactivity for S anions and can be used.[40] Lithium nitrate ($LiNO_3$) has been an important additive to glyme electrolytes for S battery function.[67–71] $LiNO_3$ forms a protective layer of Li_xNO_y on the Li metal anode (in a half cell), which prevents reaction with polysulfides, and oxidizes degradation species in the electrolyte.[69,70] $LiNO_3$ is progressively consumed in the formation of a passivating coating on the anode and is irreversibly reduced on the cathode side at voltages below 1.6 V.[67,71] This ultimately leads to the total consumption of $LiNO_3$.

Because of the potentially drastic increase in full cell capacity that Si-S full cells promise, and because of the many differences from current full cells, there has been a great deal of research on Si-S full cells.[24,55,56,68,71–78] Common problems have been identified,

including insufficient Li^+ ions due to Li^+ consumption by the SEI, S migration from the cathode to the anode, incompatibility between the Si anode and the glyme electrolyte, unbalanced anode-to-cathode capacity, and excess electrolyte, which results in diffusion of the active material away from the cathode.[56,68,71,72] However, there is still a lack of understanding as to how the anode SEI chemistry changes in a full cell with a S cathode and how it is impacted by changes in cell configuration, such the addition of an interlayer.

In this study, we reveal some common challenges in making LIBs with SiNW electrodes that occur for different cathode materials. Prelithiation of the SiNW anode was crucial to improve the capacity and stability of battery cycling for both LFP and S cathodes. The prelithiation process was also found to strongly influence battery performance and better results were achieved when SiNWs were prelithiated electrochemically at a controlled rate, compared to prelithiation of SiNWs by direct contact with Li. Prelithiation of SiNWs by direct contact with Li foil occurred very rapidly, with 60% of total lithiation taking place in 15 minutes. These prelithiated anodes showed lower capacity and less stable performance than batteries without contact prelithiation, indicating that a stable SEI layer is not formed at this high rate. In the case of the batteries made with a S cathode, no sulfides were observed in the SiNW SEI layer. This indicates that the change in cell configuration to include a carbon interlayer successfully prevented polysulfides from migrating to the anode during battery cycling. This is important because the reaction of dissolved polysulfides with a Li metal anode in half cells to form Li_2S has been shown to reduce cycle stability over time.[68] The XPS results also indicated SiNW-S and SiNW half cells in glyme electrolyte fully consumed the $LiNO_3$ additive during cycling. This results in degradation of the Li salt additive, bis(trifluoromethane) sulfonamide lithium (LiTFSI), that can contaminate the anode and reduce battery stability. SiNWs that had cycled in full cells with a S cathode had even higher levels of LiTFSI degradation than SiNW half cells.

5.2 Experimental Details

5.2.1 Chemicals

Trisilane (>99%) was purchased from Voltaix, LLC. Bis(bis(trimethylsilyl)amino) tin ($Sn(HMDS)_2$, 99.8%), anhydrous toluene (99.8%), chloroform (99.9%), ethanol (99.9%), lithium hexafluorophosphate ($LiPF_6$, ≥99.99%), ethylene carbonate (EC, 99%), diethyl carbonate (DEC, ≥99%), poly(acrylic acid) (PAA), 1-methyl-2-pyrrolidinone (NMP, 99.5%), 1,3-dioxolane (DOL, ≥99.5%), diomethoxymethane (DME, 99%), bis(trifluoromethane)sulfonimide lithium salt (LiTFSI, ≥99.95%) and were purchased from Sigma-Aldrich. Lithium nitrate ($LiNO_3$, >99%) was purchased from Acros Organics. Conductive carbon super C65 was purchased from TIMCAL. Fluoroethylene carbonate (FEC, >98%) was purchased from TCI America. Lithium foil (1.5mm, 99.9%) was purchased from Alfa Aesar. Celgard 2400 membranes (25 μm) were purchased from Celgard. Copper foil (9 μm thick) and coin cells (2032 stainless steel) were purchased from MTI Corporation. All purchased chemicals were used as received without any further purification.

5.2.2 Silicon Nanowire Synthesis

Si nanowires were synthesized by super-critical fluid–liquid–solid (SFLS) growth following published procedures.[79] The synthesis was performed in a nitrogen glovebox to minimize air exposure for pyrophoric reactants. A 10 mL titanium tubular reactor was connected to a high pressure liquid chromatography (HPLC) pump then heated to 490°C and pressurized to 13.8 MPa. A reaction solution was prepared with 27.5 mg of gold nanoparticles in a 50 mg/mL solution, 2.01 M trisilane and anhydrous toluene. *Caution! Trisilane is pyrophoric and must be handled under inert conditions.* The reactant solution was fed to the reactor at 3 mL/min. Once the reactor has repressurized to 13.8 MPa, the

inlet valve was closed and held at 490ºC for two minutes. After cooling, the nanowires were centrifuged at 8000 rpm for 5 minutes. The supernatant was then discarded and the nanowires washed using chloroform, toluene, and ethanol at a 2:1:1 ratio. The nanowires were then centrifuged and washed two more times. The resulting nanowires were stored in chloroform.

5.2.3 Carbon Coated Lithium Iron Phosphate Synthesis

Carbon coated LFP particles were synthesized using a high-pressure free-meniscus coating process.[48] A coating solution was made using liquid carbon dioxide and sucrose octaacetate (SOA). The particle synthesis technique has been previously reported.[48] The SOA-coated LFP particles were then calcined at 750ºC for 10 hr in Ar and H_2 (5%) gas to form c-LFP. To prepare a battery anode slurry, c-LFP combined with polyvinylidene fluoride binder (PVdF) and carbon black (C65) at a ratio of 70/20/10 for a total mass of ~1 g. 3 mL of *N*-methylpyrrolidinone (NMP) were added and mixed by probe sonication for 10 min. The slurry was then doctor bladed onto Al foil (200 μm gap) and dried at 80ºC overnight under vacuum.

5.2.4 Sulfur Cathode and Microporous Carbon Interlayer

Sulfur cathodes were assembled using 70 wt% precipitated sulfur, 20 wt% carbon black (Super P), and 10 wt% PVdF binder in NMP which was then slurry cast onto Al foil and dried overnight at 50ºC. The microporous carbon interlayers were prepared by combining carbon black and polytetrafluoroethylene binder (PTFE) followed by roll-pressing. Both of these processes are previously published, with further details included.[80]

5.2.5 Electrochemical Testing

To prepare a battery anode slurry, Si nanowires were combined with PAA and C65 at a ratio of 70/20/10 for a total mass of ~30 mg. To this 0.12 mL of NMP and 2 mL of

ethanol were added and mixed by probe sonication for 10 min. The solution was then rotovapped to remove extra liquid at 700 torr and 35ºC until the slurry was more viscous, similar to the consistency of syrup. Slurries were then doctor bladed onto Cu foil (200 µm gap) and dried at 150ºC overnight under vacuum. Anodes were cut out of the foil using a 9 mm diameter hole punch.

Coin cells were assembled in an argon filled glovebox (<0.7 ppm O_2) using Li foil as the counter electrode. Carbonate electrolyte solution was prepared using 1 M $LiPF_6$ in 1:1 EC:DEC with 5 wt% FEC. Sulfur cathode-compatible glyme electrolyte was prepared using 1M LiTFSI in 1:1 DOL:DME with 0.1M $LiNO_3$. Only 50µL of electrolyte is added to SiNW-S full cells. Celgard 2400 membranes were used as separators. Full cells were made using an extra spacer to ensure even pressure within the coin cell. Coin cells were crimped to ensure a tight seal and removed from the glovebox for galvanostatic testing on an Arbin BT-2143 test unit.

Silicon anode half cells were cycled between 0.01 mV – 2.0 V vs Li/Li^+. C-LFP cathode half cells were cycled between 2.5 V – 4.5 V vs Li/Li^+. Sulfur cathode half cells were cycled between 1.8 V – 2.8 V vs Li/Li^+. C-LFP cathode - SiNW anode full cells were cycled between 2.5 V – 4 V vs Li/Li^+. Sulfur cathode - SiNW anode full cells were cycled between 1.5 V – 2.8 V vs Li/Li^+. For half cells, Coulombic efficiency is defined as delithiation/lithiation of the electrode of interest. For a full cell, Coulombic efficiency is discharge/charge. Applied current densities are reported per gram of active electrode material.

5.2.6 Characterization

Scanning electron microscope (SEM) images were taken using a Zeiss Model SUPRA 40 VP SEM system operated at 2.0 kV or a FEI Quanta 650 SEM with EDS. Ex-

situ analysis of cycled electrodes was performed using a Kratos AXIS Ultra DLD spectrometer to do x-ray photoelectron spectroscopy (XPS). Because many of the species that form on the surface of an electrode are air sensitive, special care was taken to reduce oxygen exposure. Coin cells were opened in the glovebox and electrodes rinsed with electrolyte solvent. They were transferred to the XPS ultra-high vacuum (UHV) chamber via a pressure-to-vacuum transfer of environmentally sensitive samples (PV-TESS) interface (designed by the Texas Materials Institute, University of Texas, Austin, U.S. Patent Application Serial No. 14/445,650 filed July 29, 2014. The resolution for the survey scan was 1 eV, and the high-resolution region data was collected every 0.1 eV. The spectra were analyzed using CasaXPS software (version 2.3.16, Casa Software Ltd.). Sample charging was corrected for by shifting the C1s, C-C peak to a binding energy of 285.0 eV. All spectra were fitted with Gaussian-Lorentzian (30% Gausssian) functions and a Shirley-type background. The SiNW electrodes from the SiNW-S full cell and from the SiNW half cell cycled for >250 cycles before reaching a point of minimal capacity. The Li metal anode from the S half cell cycled for 140 cycles.

5.3 Results and Discussion

5.3.1 Half Cell Performance

In this study three different electrodes were studied: a SiNW anode, a carbon coated LFP cathode, and a S cathode with a microporous carbon interlayer. Figure 5.3 shows electron microscope characterization of each material. The S cathode is made using a pure sulfur powder (Figure 5.3a) combined with carbon black and polyvinylidene fluoride binder.[80] This electrode is used in conjunction with a microporous carbon interlayer (Figure 5.3b) to capture polysulfides formed during cycling.[6] SiNWs (Figure 5.3c) were synthesized via a supercritical fluid-liquid-solid (SFLS) mechanism using trisilane as the

Si precursor and tin as the metal seed.[20,81,82] Nanowires have diameters of 100 – 200 nm with lengths of approximately 10 µm, and are highly tortuous. The other cathode material investigated was carbon-coated LFP microspheres, as shown in Figure 5.3d. Carbon coating on the LFP was formed by calcinating sucrose octaacetate ligands on the LFP surface.[48] The micron-sized LFP particles are aggregates of nanosized particles, as seen in TEM images in Figure D.1. The carbon coating on each nanoparticle is extremely thin, previous studies have found it to be approximately 2 nm thick.[48] EDS mapping (Figure 5.3e) confirms the presence of carbon on the LFP particles.

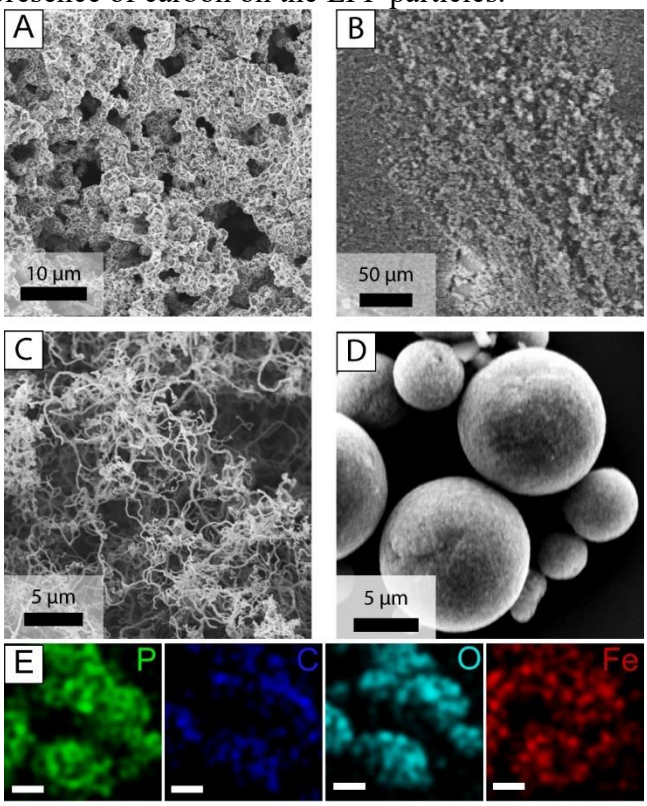

Figure 5.3 SEM images of the (a) S cathode, (b) microporous carbon interlayer, (c) SiNWs, and (d) carbon-coated $LiFePO_4$. (e) EDS mapping of the P, C, O and Fe in the sample; scale bars represent 5µm. Elemental analysis confirms the presence of carbon.

All electrodes were first tested in half cells versus Li foil to determine their individual performance. Results are shown in Figure 5.4. SiNW anodes were tested in two different electrolytes: a glyme electrolyte, compatible with a S cathode, and the traditional carbonate electrolyte used in batteries. The S compatible electrolyte used in this study is a 1:1 mixture of 1,3-dioxolane (DOL) and 1,2-dimethoxyethane (glyme) with 1 M LiTFSI and 0.1 M $LiNO_3$. Glyme based electrolytes are not typically used in full cell batteries today due to ready decomposition at high potentials, around 4.0 V, making them incompatible with traditional transition metal oxide cathodes.[83] However, because the S cathode has a lower operating voltage, of 2.1-2.3 V, they are suitable for this application.[6] The traditional electrolyte used was 1:1 EC:DEC mixture with 1 M $LiPF_6$ and 5 wt.% added FEC. Capacities are reported based on the weight of nanowires used in the electrode. Both SiNW electrodes were tested at an applied current density of 250 mA/g (~C/10), as shown in Figure 5.4a. The SiNW anode exhibited more stable performance in the carbonate electrolyte, with a capacity at 50 cycles of 2499 mAh/g compared with 1591 mAh/g in the glyme electrolyte. Anode performance in the carbonate electrolyte also had a higher Coulombic efficiency, over 97% compared with 93% in glyme electrolyte. Voltage profiles for the glyme electrolyte half cell are shown in Figure 4d. Voltage profiles for the SiNW half cell cycled in carbonate electrolyte are found in Figure D.2. Both voltage profiles show that the lithiation plateau moves to a lower potential as cycle number increases, indicating a greater overpotential is needed to initiate lithiation. Lower SiNW anode reversibility with a glyme electrolyte compared with a carbonate has been previously observed and is attributed to higher degradation of electrolyte componenets.[70]

A S cathode was tested in a half cell in conjunction with the microporous carbon interlayer and the glyme electrolyte. Capacities are reported based on the weight of S used in the electrode. Sulfur cathode half cells were tested at an applied current density of 100

mAh/g (~C/10) (Figure 5.4b). The cathode exhibits relatively stable cycling. It has a maximum discharge capacity in cycle 5 of 1462 mAh/g, which is typical behavior for a S cathode. The increase in capacity after the first cycle is due to an activation period of the active material.[84] The discharge capacity at 100 cycles was 936 mAh/g, which corresponds to a capacity retention rate of 64%. Figure 4e shows voltage profiles for the S cathode. The discharge plateaus occur at approximately 2.35 V and 2.1 V and are stable with increasing cycle number. The two plateaus are due to the conversion of octasulfur (S_8) formed during cycling to Li_2S_4 and then Li_2S_4 to Li_2S.[6]

A c-LFP cathode was tested in a half cell with carbonate electrolyte. Capacities are reported based on the weight of c-LFP used in the electrode. C-LFP half cells were tested at an applied current density of 17 mAh/g (C/10) (Figure 5.4c). The cathode exhibits very stable cycling. It has an initial discharge capacity of 135 mAh/g, with a discharge capacity at 100 cycles of 134 mAh/g. Figure 5.4f shows voltage profiles for the c-LFP cathode. The discharge plateau occurs at 3.38 V and charge plateau of 3.45 V after the first cycle. There is no change in the voltage of this plateau over repeated cycling.

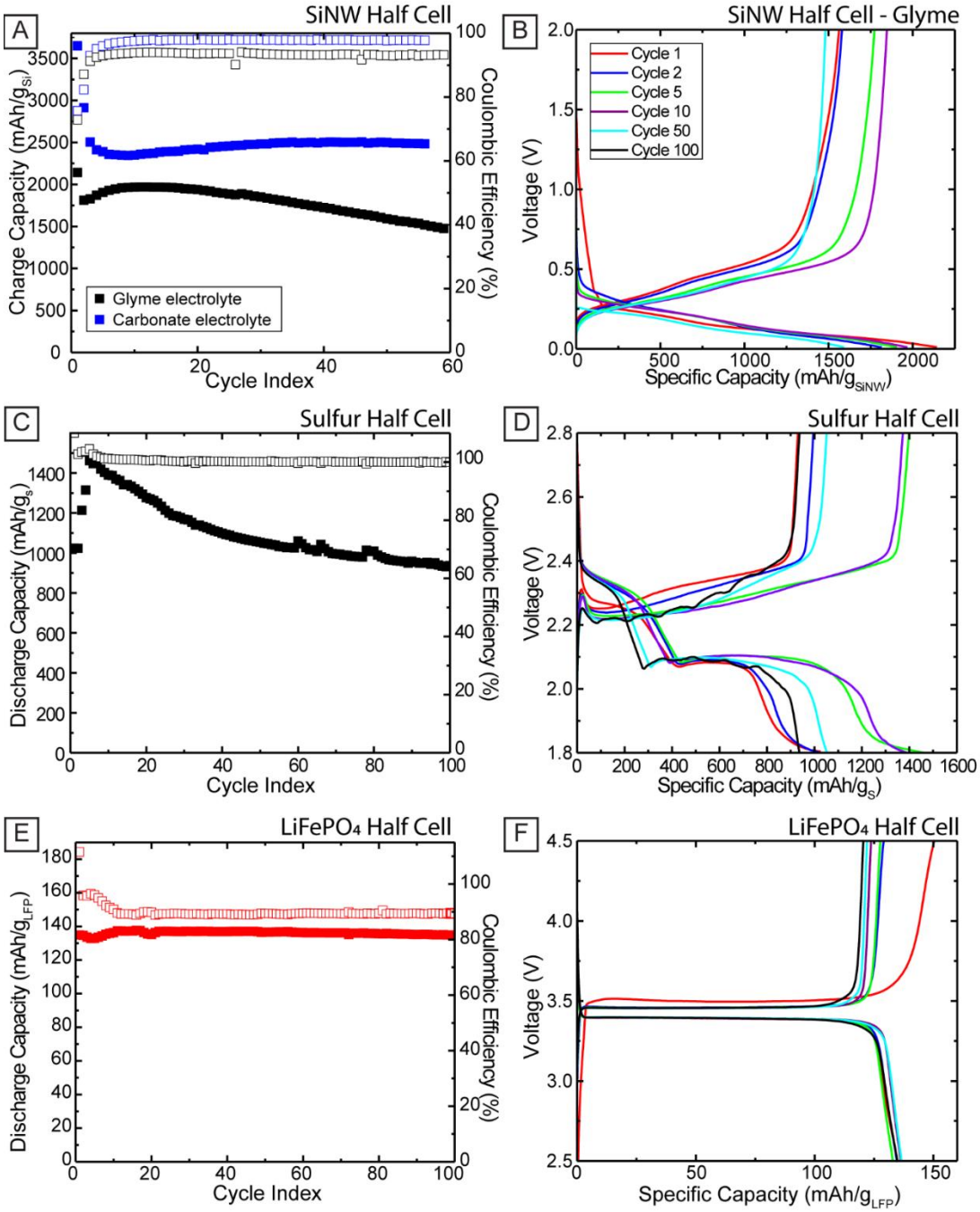

Figure 5.4 Capacity (■) and Coulombic efficiency (□) of half cells and their associated voltage profiles. (a) SiNW anode half cells tested using glyme and carbonate electrolytes, (b) voltage profile for the SiNW anode using glyme electrolyte, (c-d) S cathode half cell, and (e-f) c-LFP cathode half cell. The same legend shown in (b) is used for (d, f).

5.3.2 Prelithiation Method

In a full cell battery, the supply of Li^+ ions is limited and there are many ways to introduce additional Li^+ to the battery. Two different methods of lithiating the SiNW anode prior to fabrication were tested. Contact prelithiation is a popular method because it is a fast, easy, and potentially scalable technique that does not require changes in the existing battery electrode formulation.[29,68,71,75,76] SiNW anodes were also prelithiated on a battery tester at an applied current of 200 mA/g.

Full cells were tested at several different anode-to-cathode capacity ratios. Having a capacity ratio close to 1 is important for maximizing the Li utilization within the cell. Both systems faced hurdles in achieving a ratio close to 1. It was difficult to match SiNW anode and LFP cathode capacity, given that the maximum Si capacity is 20x greater than the maximum LFP capacity. The LFP cathodes had to be very thick in order to match the anode capacity, which can hinder Li^+ diffusion rates.[55] SiNW anodes had a lower mass loading, about 0.22 mg/cm^2, and c-LFP cathodes had a higher mass loading, on average 3.90 mg/cm^2. In contrast with LFP full cells, it was difficult to process anodes with SiNWs that were thick enough to match the S cathode capacity. The S capacity is about half that of Si and the cathodes had an average mass loading of 2.52 mg/cm^2. Si anodes were fabricated to have an average mass loading of 1.04 mg/cm^2.

The extent of contact prelithiation as a percentage was found by subtracting the first cycle lithiation capacity from the delithiation capacity divided by the delithiation capacity.[30] Figure D.3 shows the extent of lithiation as a function of time the anode is held in contact with the Li foil for both carbonate and glyme electrolytes. In as little as 15 minutes, the anodes were approximately 60% lithiated for both electrolytes. By 30 minutes, the anodes were nearly completely lithiated. A short, 15 minute, prelithiation of the SiNW anode was chosen for SiNW-LFP full cell testing and 30 minutes for SiNW-S full cell

testing. A longer time and higher extent of prelithiation was chosen for S full cells since this was the only source of Li^+ in the full cell.

The SiNW-LFP full cell was first tested without prelithiation, to determine how the limited Li^+ resource impacts cycling, seen in Figure 5.5a. The full cell showed poor stability and steep decline within the first 20 cycles. At 100 cycles, only 14% of 2nd cycle charge capacity was retained. Initial Coulombic efficiency was only 52% and 1st cycle capacity loss was over 50%. Repeating this experiment with different anode-to-cathode capacity ratios, yielded similar low capacity and stability results. (Figure D.4a). Even at the capacity ratio closest to 1, there was still a steep decline in performance to 20% capacity retention by cycle 100.

Contact prelithiated SiNW anodes paired with c-LFP cathodes demonstrated more significant capacity fade than the full cells without a prelithiated anode (Figure 5.5a), but also had rapid capacity fade. Other SiNW anodes were prelithiated on a battery tester in a half cell at an applied current of 200 mA/g to the cutoff voltage of 100 mV and then removed to put in a SiNW-LFP full cell. This significantly improved full cell battery stability, as shown in Figure 5.5a. Initial charge capacity was 152 mAh/g_{LFP} and for the first 20 cycles, capacity retention was high, 93% compared with 2nd cycle charge capacity. However, after 20 cycles, there was a steep decline in battery performance, dropping to 73% retention by cycle 50. The voltage profile of the SiNW-LFP full cell (Figure 5.5b) shows a high degree of voltage slip. In the first cycle, there is a discharge plateau at 3.11 V, and charge plateau at 3.5 V. By the second cycle the charge plateau has decreased to 3.47 V, where it remains for the rest of the cycles. The discharging plateau continually moved lower, even within the first 10 cycles, when capacity retention was still very high. This indicates the need for an overpotential to delithiate the SiNW anode.

The drop in performance after the first 20 cycles was likely due to Li^+ consumption by the SEI layer. Coulombic efficiency of the full cell was only 95%, indicating that some Li^+ was lost during each cycle. Instabilities in the SiNW electrode could also impact performance. The SiNW half cell tested with carbonate electrolyte exhibited some voltage slip to lower lithiation plateaus over extended cycling (Figure D.2) while the c-LFP half cell had extremely stable voltage profiles (Figure 5.4f). Comparing these results with another SiNW-LFP full cell, with a different anode-to-cathode ratio, shown in Figure D.4c, the full cell with a lower ratio of 1.21 performed better than the 1.87 ratio full cell.

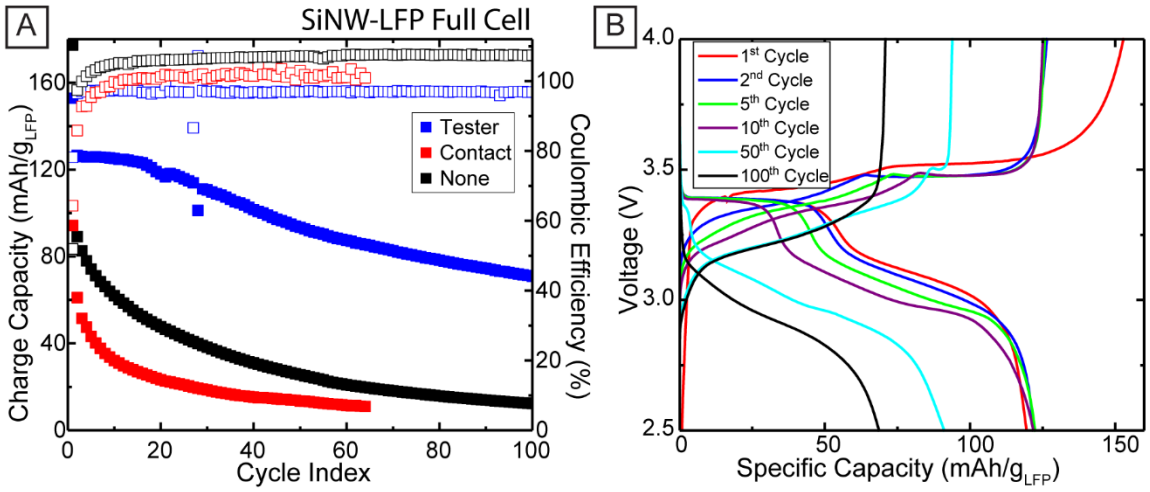

Figure 5.5 (a) Charge capacity (■) and Coulombic efficiency (□) of SiNW-LFP full cells of different prelithiation methods. "Contact" prelithiated SiNW anodes were held in contact with Li foil for 15 minutes to lithiate them prior to full cell assembly. "Tester" anodes were prelithiated on the battery tester at an applied current density of 200 mA/g to 100 mV in a half cell, then disassembled. Full cell batteries were cycled at an applied current density of 17 mA/g_{LFP}. (b) The voltage profiles of the "Tester" prelithiated full cell.

Next, the full cells using a S cathode and a SiNW anode were examined. SiNW-S batteries were cycled at an applied current density of 100 mA/g. Batteries that were prelithiated by contact with Li had low initial capacity and steep initial decline in capacity,

as seen in Figure 5.6a. Additional tests were done for several anode-to-cathode capacity ratios which showed similar performance at all ratios (Figure D.4b).

SiNW anodes were also prelithiated on a battery tester at an applied current of 200 mA/g to the cutoff voltage of 10 mV, which corresponds approximately to 100% of total capacity. These conditions greatly improved SiNW-S full cell battery capacity (Figure 5.6a). The full cell reached a maximum capacity of 792 mAh/g_S in the 4th cycle. However, there was a significant amount of fade, to 360 mAh/g_S by cycle 100, approximately 45% capacity retention. The voltage profile of the SiNW-S full cell prelithiated using the battery tester (Figure 5.6b) shows a high degree of voltage slip. In the second cycle, there are discharge plateaus at 1.76 V and 2.1 V which continually slip lower with each cycle. These results were compared with other "Tester" prelithiated SiNW-S full cell batteries of different anode-to-cathode capacity ratios. All batteries showed significant fade regardless of ratio, shown in Figure D.4d.

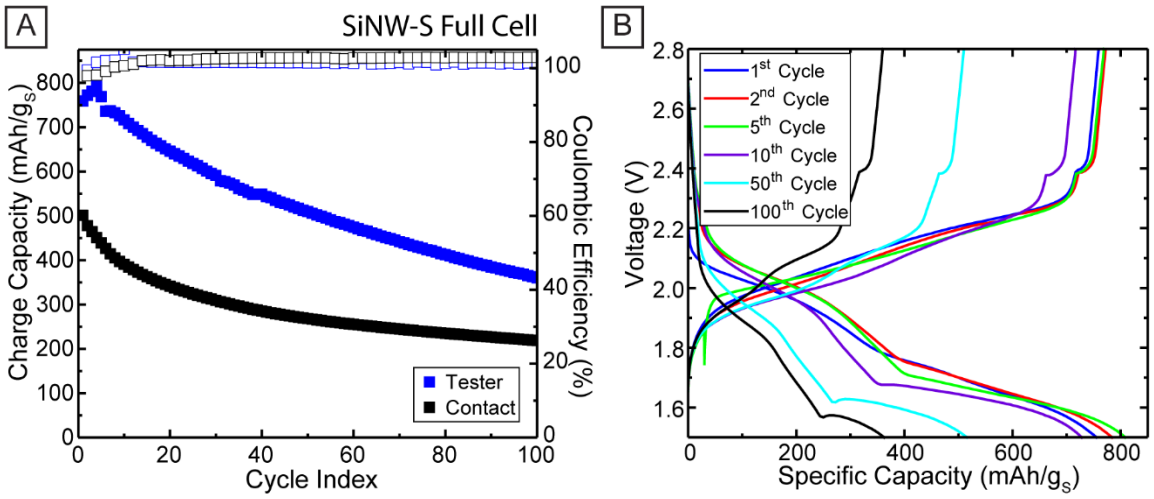

Figure 5.6 (a) Charge capacity (■) and Coulombic efficiency (□) of SiNW-S full cells prelithiated by different methods. "Contact" prelithiated SiNW anodes were held in contact with Li foil for 30 minutes before assembly into a full cell. "Tester" prelithiated batteries were prelithiated using a battery tester at an applied current density of 200 mA/g to 10 mV. Full cell batteries were cycled at an applied current density of 200 mA/g$_S$. (b) The voltage profile of the "Tester" prelithiated full cell.

The method of prelithiation has a strong impact on full cell battery performance. SiNW anodes were tested in half cells to determine how contact prelithiation affected SiNW performance. Figure 5.7a shows the charge capacity of a Si anode prelithiated by contact with Li foil, tested in a half cell with a carbonate electrolyte. After 15 minutes of prelithiation, the anode exhibits high capacity, cycling stably at 3000 mAh/g, but with a Coulombic efficiency of only 88%. This is significantly worse than performance by a SiNW anode in carbonate electrolyte half cell without prelithiation, which had a Coulombic efficiency over 97% (Figure 5.4a).

SiNW anodes tested in a half cell with the glyme electrolyte after contact prelithiation showed similar poor performance. After 30 minutes of prelithiation, the SiNW anode tested in a half cell battery with glyme electrolyte cycles stably at 1670 mAh/g till only cycle 30, then begins to decline, shown in Figure 5.7b. This is a low capacity for a

SiNW anode and poor stability, compared with SiNW anodes tested in a glyme electrolyte without prelithiation (Figure 5.4a).

Contact prelithiation alters the formation of the SEI layer in the first cycle. First cycle SEI formation is crucial to stable battery performance, as the SEI protects the electrode surface from further reaction with the electrolyte.[23] Formation of an incomplete or unstable SEI layer in the first cycles can result in further Li consumption as the SEI layer cracks and reforms in subsequent cycles.[19,85,86] For this reason, most studies do an initial conditioning cycle at a lower rate, to form a stable SEI layer, before proceeding to a higher cycle rate. Because the SiNWs were lithiated to 60% of theoretical capacity in only 15 minutes, this corresponds to an applied current density of 7.2 A/g, compared with the applied current density normally used for a conditioning cycle, which is 0.25 A/g. When SiNW anodes were prelithiated on a battery tester at a rate of 200 mA/g to 10 mV, this ensured not only a higher degree of lithiation, but formation of a more stable SEI layer, which improved full cell performance.

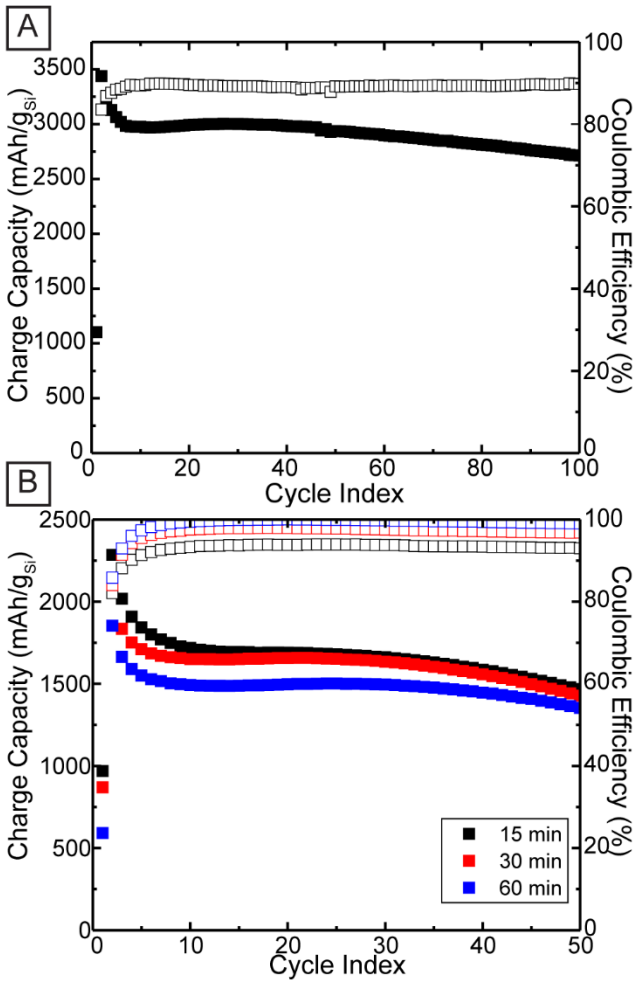

Figure 5.7 Charge capacity (■) and Coulombic efficiency (□) of (a) a SiNW anode prelithiated mechanically for 15 minutes and tested in a half cell with carbonate electrolyte, and (c) SiNW anodes prelithiated mechanically for different times and tested in a half cell with sulfur electrolyte. All batteries were cycled at an applied current density of 250 mA/g.

5.3.3 XPS Analysis of SiNW SEI layer

SiNW-S full cells suffered from high capacity loss and low stability, even when the SiNW anode was prelithiated at a controlled rate on a battery tester. XPS was used to analyze the SEI layer of a SiNW anode cycled in a SiNW-S full cell, to better understand how the cathode impacts the anode chemistry and thus performance. For comparison, two

other electrodes were examined: a Li metal anode that cycled in a S half cell, and a SiNW electrode that cycled versus Li metal. After removal from the coin cell, samples were carefully transferred in an air free environment to the XPS no ensure the samples were not exposed to oxygen. The elemental atomic composition of species in the SEI layer of each electrode are listed in Table 5.1.

Table 5.1 Surface elemental composition (at. %) after extended cycling determined by XPS, of species on SiNW and Li metal electrode surfaces.

	F 1s	**O 1s**	**N 1s**	**C 1s**	**S 2p**	**Li 1s**
SiNW Electrode, SiNW Half Cell	25.8	30.0	5.3	17.4	10.5	11.1
Li Anode, S Half Cell	22.6	20.8	4.2	25.9	7.1	19.5
SiNW Anode, SiNW-S Full Cell	31.9	21.3	4.0	27.4	9.7	4.7

Si was not detected for any samples, indicating that the SEI layer was thicker than the XPS penetration depth of ~10 nm.[86] The full cell anode has a higher concentration of fluorine (F) in the SEI layer than the SiNW and Li metal half cell electrodes, 23% and 41% higher, respectively. The only F source in the battery is the LiTFSI salt. All three electrodes were rinsed with electrolyte solvent prior to XPS analysis, so the F signal cannot be from excess salt on the surface. Thus, the concentration of F is indicative of the degree of salt decomposition.[70] The presence of salt decomposition products is corroborated by looking at XPS high resolution elemental scans. The high resolution C 1s XPS scans of all three electrodes, shown in Figure 5.8, have a peak at 293 eV, corresponding to the $-CF_3$ group.[69,70,87] The source of this peak are initial LiTFSI decomposition products, $Li_2NSO_2CF_3$ and $LiSO_2CF_3$.[88] These compounds can be reduced further to form $LiCF_3$ and Li_xCF_y which may also contribute to this peak.[70,87,88]

The shoulder on the C-C peak, present for all three electrodes, at ~287 eV, can be attributed to ethereal and alkoxy carbons that are the reduced species of DOL,

$(CH_3CH_2OCH_2O\text{-})_n$ and $(CH_2CH_2O\text{-})_n$.[69,70,88,89] In the Li metal anode and SiNW from a full cell, this peak is fairly broad indicating there are many contributing species. The O-C=O species present at 291 eV corresponds to the formation of HCO_2Li during the decomposition of DOL.[69,87,88] The Li metal anode and the SiNW anode from a SiNW-S full cell show a higher composition of oxidized carbon species than the SiNW half cell. This is indicates greater decomposition of DOL during cycling.[88] Peak deconvolutions for the C 1s spectra of all three electrodes are found in Figure D.5.

It appears the interlayer was successful at preventing Li polysulfides formed during cycling from migrating to the anode, in both the half and full cells. The S 2p spectra, shown in Figure 8 for all three electrodes, did not show sulfide or elemental sulfur, which would be found between 167-162 eV (Figure D.6 shows XPS survey spectrum of the region with no species present). The primary species in the S 2p spectra of the Li metal anode and SiNW-S full cell anodes were R_2SO_4 species, with a peak at ~169.5 eV, which are formed by the oxidation of LiTFSI decomposition products by $LiNO_3$.[69,70] The SiNW half cell electrode also showed a peak at ~168 eV which corresponds to sulfite products with some contribution from the $-NSO_2CF_3$ decomposition product of the LiTFSI.[70,90] While it is possible polysulfides were able to cross through the interlayer, only to be oxidized by the $LiNO_3$ to Li_xSO_y, this is unlikely. Previous examination of a Si anode in a Si-S full cell, found that after 50 cycles, peaks corresponding to the Li_2S phase appeared, even with a $LiNO_3$ additive.[68] Peak deconvolutions for the S 2P spectra showing the $2p_{1/2}$ and $2p_{3/2}$ contributions for each oxidative state for all three electrodes are found in Figure D.5. Bridging sulfur (-S-S-) was seen on the surface of the full cell S cathode, as expected, Figure D.7.[90]

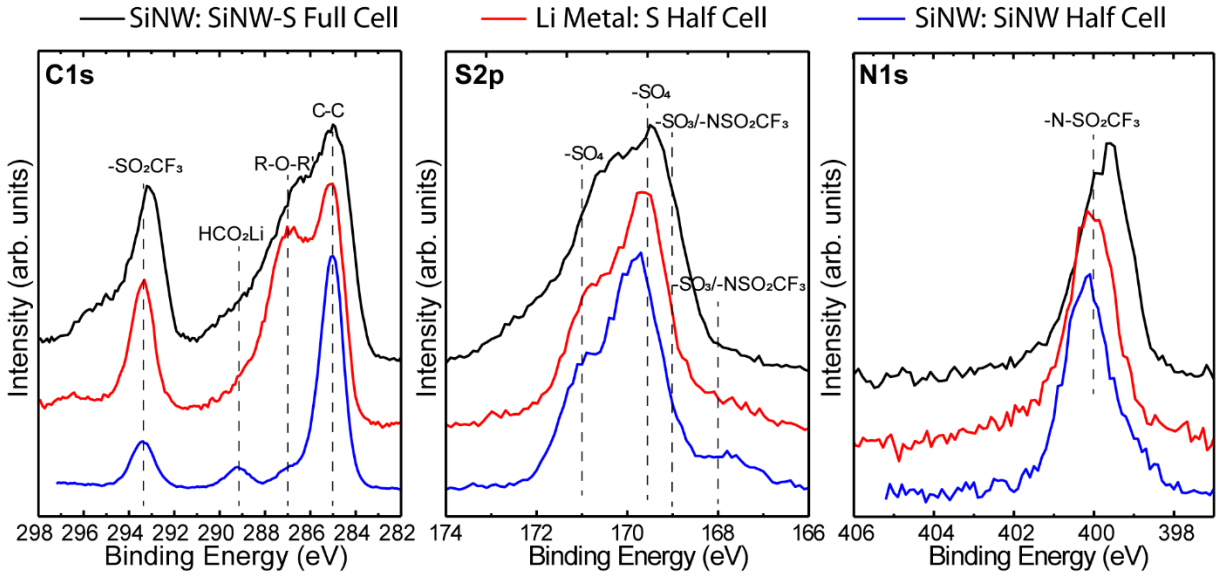

Figure 5.8 High resolution XPS scans of the C 1s, S 2p, and N 1s regions, for half cell and full cell SiNW electrodes, and the Li metal anode of a S half cell.

The N 1s spectra for all three electrodes, seen in Figure 5.8, shows a single peak at ~400 eV. This corresponds to the LiTFSI sulfone amide decomposition products such as $Li_2NSO_2CF_3$.[69,70] There is neither a peak at 407 eV, which would indicate remaining $LiNO_3$, nor a peak at ~405 eV where R-NO_2 would be found.[70]

NO_x or RNO_2 groups are the principle decomposition products of $LiNO_3$ and protect the anode surface during battery cycling, preventing reaction with polysulfides.[70,91] $LiNO_3$ also oxidizes degradation species in the electrolyte.[69,70] $LiNO_3$ is irreversibly progressively consumed during cycling. In these experiments, the lack of RNO_2 peaks indicates that after the $LiNO_3$ was consumed, further electrolyte decomposition products deposited on the anode surface and covered any RNO_2 species.[67,70] Further evidence that the $LiNO_3$ was fully consumed during cycling by all three electrodes after extended cycling, is the high F content. $LiNO_3$ prevents the decomposition of LiTFSI, but once it has been consumed during extended cycling, the LiTFSI will decompose and the F content

of the SEI will increase.[70] Previous studies found that, after electrodes in this same electrolyte had cycled more than 250 times, the F content increased from 4% after 1 cycle to 22%.[70] $LiNO_3$ consumption during battery cycling is greater in full cells than in half cells because of the wider voltage window used in experiments, here 1.5 V – 2.8 V, which results in irreversible reduction of $LiNO_3$ on the cathode side at voltages below 1.6 V.[67] $LiNO_3$ also continuously passivates the anode SEI layer, resulting in a thickening SEI layer till the $LiNO_3$ is consumed.[67] Further study is needed to determine how many battery cycles occur before the $LiNO_3$ is consumed, and what is the optimized concentration of additive.

5.4 Conclusions

In conclusion, two different full cell systems were examined that revealed common challenges to integrating SiNW anodes. Even though these two systems have several differences, notably the electrolyte, they faced the common issue of low cycle stability due to Li consumption in the SEI layer. Prelithiation of the SiNW anode was crucial to improve the capacity and stability of battery cycling for both LFP and S cathodes. Better results were achieved when SiNWs were prelithiated electrochemically at a controlled rate, compared to prelithiation of SiNWs by direct contact with Li. While lithiation on a battery tester allowed for better control of the lithiation rate and extent, future work will be needed to develop a method that is more scalable. XPS analysis was done to better understand how the SEI layer formed in SiNWs is affected by a S cathode. No sulfides were observed in the SiNW SEI layer, indicating the addition of a carbon interlayer successfully prevented polysulfides from migrating to the anode during battery cycling. XPS results showed SiNW-S full cells fully consumed the $LiNO_3$ electrolyte additive during cycling, resulting in high levels of LiTFSI degradation that can contaminate the anode and reduce battery stability. Further study is needed to determine how many battery cycles occur before the

$LiNO_3$ is consumed, and what is the optimized concentration of additive. These studies demonstrate the importance of not only testing electrodes in half cell batteries, but to optimize the full system for the best performance.

5.5 REFERENCES

(1) McDowell, M. T.; Lee, S. W.; Nix, W. D.; Cui, Y. 25th Anniversary Article: Understanding the Lithiation of Silicon and Other Alloying Anodes for Lithium-Ion Batteries. *Adv. Mater. Deerfield Beach Fla* **2013**, *25* (36), 4966–4985.

(2) Armand, M.; Tarascon, J.-M. Building Better Batteries. *Nature* **2008**, *451* (7179), 652–657.

(3) Bogart, T. D.; Chockla, A. M.; Korgel, B. A. High Capacity Lithium Ion Battery Anodes of Silicon and Germanium. *Curr. Opin. Chem. Eng.* **2013**, *2* (3), 286–293.

(4) Tarascon, J.-M.; Armand, M. Issues and Challenges Facing Rechargeable Lithium Batteries. *Nature* **2001**, *414* (6861), 359–367.

(5) Goodenough, J. B.; Kim, Y. Challenges for Rechargeable Li Batteries. *Chem. Mater.* **2010**, *22* (3), 587–603.

(6) Manthiram, A.; Fu, Y.; Chung, S.-H.; Zu, C.; Su, Y.-S. Rechargeable Lithium–Sulfur Batteries. *Chem. Rev.* **2014**, *114* (23), 11751–11787.

(7) Takahashi, Y.; Tode, S.; Kinoshita, A.; Fujimoto, H.; Nakane, I.; Fujitani, S. Development of Lithium-Ion Batteries with a LiCoO2 Cathode Toward High Capacity by Elevating Charging Potential. *J. Electrochem. Soc.* **2008**, *155* (7), A537–A541.

(8) Korgel, B. A. Nanomaterials Developments for Higher-Performance Lithium Ion Batteries. *J. Phys. Chem. Lett.* **2014**, *5* (4), 749–750.

(9) Etacheri, V.; Marom, R.; Elazari, R.; Salitra, G.; Aurbach, D. Challenges in the Development of Advanced Li-Ion Batteries: A Review. *Energy Environ. Sci.* **2011**, *4* (9), 3243–3262.

(10) Wu, H.; Cui, Y. Designing Nanostructured Si Anodes for High Energy Lithium Ion Batteries. *Nano Today* **2012**, *7* (5), 414–429.

(11) Obrovac, M. N.; Christensen, L. Structural Changes in Silicon Anodes during Lithium Insertion/Extraction. *Electrochem. Solid-State Lett.* **2004**, *7* (5), A93–A96.

(12) Li, J.; Dahn, J. R. An In Situ X-Ray Diffraction Study of the Reaction of Li with Crystalline Si. *J. Electrochem. Soc.* **2007**, *154* (3), A156–A161.

(13) Chan, C. K.; Peng, H.; Liu, G.; McIlwrath, K.; Zhang, X. F.; Huggins, R. A.; Cui, Y. High-Performance Lithium Battery Anodes Using Silicon Nanowires. *Nat. Nanotechnol.* **2008**, *3* (1), 31–35.

(14) Aside from lithium (Li) metal, Si has the highest storage capacity of any anode material, 3579 mAh/g, more than ten times that of graphite.

(15) Beaulieu, L. Y.; Eberman, K. W.; Turner, R. L.; Krause, L. J.; Dahn, J. R. Colossal Reversible Volume Changes in Lithium Alloys. *Electrochem. Solid-State Lett.* **2001**, *4* (9), A137–A140.

(16) Obrovac, M. N.; Chevrier, V. L. Alloy Negative Electrodes for Li-Ion Batteries. *Chem. Rev.* **2014**, *114* (23), 11444–11502.

(17) Ryu, I.; Choi, J. W.; Cui, Y.; Nix, W. D. Size-Dependent Fracture of Si Nanowire Battery Anodes. *J. Mech. Phys. Solids* **2011**, *59* (9), 1717–1730.

(18) Liu, X. H.; Zhong, L.; Huang, S.; Mao, S. X.; Zhu, T.; Huang, J. Y. Size-Dependent Fracture of Silicon Nanoparticles During Lithiation. *ACS Nano* **2012**, *6* (2), 1522–1531.

(19) Winter, M.; Besenhard, J. O. Electrochemical Lithiation of Tin and Tin-Based Intermetallics and Composites. *Electrochimica Acta* **1999**, *45* (1), 31–50.

(20) Bogart, T. D.; Lu, X.; Gu, M.; Wang, C.; Korgel, B. A. Enhancing the Lithiation Rate of Silicon Nanowires by the Inclusion of Tin. *RSC Adv.* **2014**, *4* (79), 42022–42028.

(21) Bogart, T. D.; Oka, D.; Lu, X.; Gu, M.; Wang, C.; Korgel, B. A. Lithium Ion Battery Peformance of Silicon Nanowires with Carbon Skin. *ACS Nano* **2014**, *8* (1), 915–922.

(22) McDowell, M. T.; Lee, S. W.; Ryu, I.; Wu, H.; Nix, W. D.; Choi, J. W.; Cui, Y. Novel Size and Surface Oxide Effects in Silicon Nanowires as Lithium Battery Anodes. *Nano Lett.* **2011**, *11* (9), 4018–4025.

(23) Verma, P.; Maire, P.; Novák, P. A Review of the Features and Analyses of the Solid Electrolyte Interphase in Li-Ion Batteries. *Electrochimica Acta* **2010**, *55* (22), 6332–6341.

(24) Yang, Y.; McDowell, M. T.; Jackson, A.; Cha, J. J.; Hong, S. S.; Cui, Y. New Nanostructured Li2S/Silicon Rechargeable Battery with High Specific Energy. *Nano Lett.* **2010**, *10* (4), 1486–1491.

(25) Forney, M. W.; Ganter, M. J.; Staub, J. W.; Ridgley, R. D.; Landi, B. J. Prelithiation of Silicon–Carbon Nanotube Anodes for Lithium Ion Batteries by Stabilized Lithium Metal Powder (SLMP). *Nano Lett.* **2013**, *13* (9), 4158–4163.

(26) Wang, Z.; Fu, Y.; Zhang, Z.; Yuan, S.; Amine, K.; Battaglia, V.; Liu, G. Application of Stabilized Lithium Metal Powder (SLMP®) in Graphite Anode – A

High Efficient Prelithiation Method for Lithium-Ion Batteries. *J. Power Sources* **2014**, *260* (Supplement C), 57–61.

(27) Jarvis, C. R.; Lain, M. J.; Yakovleva, M. V.; Gao, Y. A Prelithiated Carbon Anode for Lithium-Ion Battery Applications. *J. Power Sources* **2006**, *162* (2), 800–802.

(28) Zhao, J.; Lu, Z.; Liu, N.; Lee, H.-W.; McDowell, M. T.; Cui, Y. Dry-Air-Stable Lithium Silicide–lithium Oxide Core–shell Nanoparticles as High-Capacity Prelithiation Reagents. *Nat. Commun.* **2014**, *5*, 5088.

(29) Kim, H. J.; Choi, S.; Lee, S. J.; Seo, M. W.; Lee, J. G.; Deniz, E.; Lee, Y. J.; Kim, E. K.; Choi, J. W. Controlled Prelithiation of Silicon Monoxide for High Performance Lithium-Ion Rechargeable Full Cells. *Nano Lett.* **2016**, *16* (1), 282–288.

(30) Liu, N.; Hu, L.; McDowell, M. T.; Jackson, A.; Cui, Y. Prelithiated Silicon Nanowires as an Anode for Lithium Ion Batteries. *ACS Nano* **2011**, *5* (8), 6487–6493.

(31) Nitta, N.; Wu, F.; Lee, J. T.; Yushin, G. Li-Ion Battery Materials: Present and Future. *Mater. Today* **2015**, *18* (5), 252–264.

(32) Blomgren, G. E. The Development and Future of Lithium Ion Batteries. *J. Electrochem. Soc.* **2017**, *164* (1), A5019–A5025.

(33) Chernova, N. A.; Roppolo, M.; Dillon, A. C.; Whittingham, M. S. Layered Vanadium and Molybdenum Oxides: Batteries and Electrochromics. *J. Mater. Chem.* **2009**, *19* (17), 2526–2552.

(34) Meduri, P.; Clark, E.; Kim, J. H.; Dayalan, E.; Sumanasekera, G. U.; Sunkara, M. K. MoO3–x Nanowire Arrays As Stable and High-Capacity Anodes for Lithium Ion Batteries. *Nano Lett.* **2012**, *12* (4), 1784–1788.

(35) Tsang, C.; Manthiram, A. Synthesis of Nanocrystalline VO 2 and Its Electrochemical Behavior in Lithium Batteries. *J. Electrochem. Soc.* **1997**, *144* (2), 520–524.

(36) Li, H.; Richter, G.; Maier, J. Reversible Formation and Decomposition of LiF Clusters Using Transition Metal Fluorides as Precursors and Their Application in Rechargeable Li Batteries. *Adv. Mater.* **2003**, *15* (9), 736–739.

(37) Abouimrane, A.; Dambournet, D.; Chapman, K. W.; Chupas, P. J.; Weng, W.; Amine, K. A New Class of Lithium and Sodium Rechargeable Batteries Based on Selenium and Selenium–Sulfur as a Positive Electrode. *J. Am. Chem. Soc.* **2012**, *134* (10), 4505–4508.

(38) Luo, C.; Xu, Y.; Zhu, Y.; Liu, Y.; Zheng, S.; Liu, Y.; Langrock, A.; Wang, C. Selenium@Mesoporous Carbon Composite with Superior Lithium and Sodium Storage Capacity. *ACS Nano* **2013**, *7* (9), 8003–8010.

(39) Peled, E.; Gorenshtein, A.; Segal, M.; Sternberg, Y. Rechargeable Lithium□sulfur Battery (Extended Abstract). *J. Power Sources* **1989**, *26* (3), 269–271.

(40) Peled, E.; Sternberg, Y.; Gorenshtein, A.; Lavi, Y. Lithium-Sulfur Battery: Evaluation of Dioxolane-Based Electrolytes. *J. Electrochem. Soc.* **1989**, *136* (6), 1621–1625.

(41) Rauh, R. D.; Abraham, K. M.; Pearson, G. F.; Surprenant, J. K.; Brummer, S. B. A Lithium/Dissolved Sulfur Battery with an Organic Electrolyte. *J. Electrochem. Soc.* **1979**, *126* (4), 523–527.

(42) Yamin, H.; Peled, E. Electrochemistry of a Nonaqueous Lithium/Sulfur Cell. *J. Power Sources* **1983**, *9* (3), 281–287.

(43) Li, W.; Hwang, J.; Chang, W.; Setiadi, H.; Chung, K. Y.; Kim, J. Ultrathin and Uniform Carbon-Layer-Coated Hierarchically Porous LiFePO4 Microspheres and Their Electrochemical Performance. *J. Supercrit. Fluids* **2016**, *116* (Supplement C), 164–171.

(44) Chung, S.-Y.; Bloking, J. T.; Chiang, Y.-M. Electronically Conductive Phospho-Olivines as Lithium Storage Electrodes. *Nat. Mater.* **2002**, *1* (2), 123–128.

(45) Padhi, A. K.; Nanjundaswamy, K. S.; Goodenough, J. B. Phospho-olivines as Positive-Electrode Materials for Rechargeable Lithium Batteries. *J. Electrochem. Soc.* **1997**, *144* (4), 1188–1194.

(46) Striebel, K.; Shim, J.; Srinivasan, V.; Newman, J. Comparison of LiFePO4 from Different Sources. *J. Electrochem. Soc.* **2005**, *152* (4), A664–A670.

(47) Wang, J.; Sun, X. Understanding and Recent Development of Carbon Coating on LiFePO4 Cathode Materials for Lithium-Ion Batteries. *Energy Environ. Sci.* **2012**, *5* (1), 5163–5185.

(48) Hwang, J.; Kong, K. C.; Chang, W.; Jo, E.; Nam, K.; Kim, J. New Liquid Carbon Dioxide Based Strategy for High Energy/Power Density LiFePO4. *Nano Energy* **2017**, *36*, 398–410.

(49) Calculated by Equation (1). This is a 55% increase over current LiCoO2-graphite batteries.

(50) Cho, G. B.; Song, M. G.; Bae, S. H.; Kim, J. K.; Choi, Y. J.; Ahn, H. J.; Ahn, J. H.; Cho, K. K.; Kim, K. W. Surface-Modified Si Thin Film Electrode for Li Ion Batteries (LiFePO4/Si) by Cluster-Structured Ni under Layer. *J. Power Sources* **2009**, *189* (1), 738–742.

(51) Kim, J.-K.; Scheers, J.; Ryu, H.-S.; Ahn, J.-H.; Nam, T.-H.; Kim, K.-W.; Ahn, H.-J.; Cho, G.-B.; Jacobsson, P. A Layer-Built Rechargeable Lithium Ribbon-Type Battery for High Energy Density Textile Battery Applications. *J. Mater. Chem. A* **2014**, *2* (6), 1774–1780.

(52) Prosini, P. P.; Cento, C.; Rufoloni, A.; Rondino, F.; Santoni, A. A Lithium-Ion Battery Based on LiFePO4 and Silicon Nanowires. *Solid State Ion.* **2015**, *269*, 93–97.

(53) Song, S.; Kim, S. W.; Lee, D. J.; Lee, Y.-G.; Kim, K. M.; Kim, C.-H.; Park, J.-K.; Lee, Y. M.; Cho, K. Y. Flexible Binder-Free Metal Fibril Mat-Supported Silicon Anode for High-Performance Lithium-Ion Batteries. *ACS Appl. Mater. Interfaces* **2014**, *6* (14), 11544–11549.

(54) Petibon, R.; Chevrier, V. L.; Aiken, C. P.; Hall, D. S.; Hyatt, S. R.; Shunmugasundaram, R.; Dahn, J. R. Studies of the Capacity Fade Mechanisms of LiCoO2/Si-Alloy: Graphite Cells. *J. Electrochem. Soc.* **2016**, *163* (7), A1146–A1156.

(55) Eom, K.; Lee, J. T.; Oschatz, M.; Wu, F.; Kaskel, S.; Yushin, G.; Fuller, T. F. A Stable Lithiated Silicon–chalcogen Battery via Synergetic Chemical Coupling between Silicon and Selenium. *Nat. Commun.* **2017**, *8*, 13888.

(56) Piwko, M.; Kuntze, T.; Winkler, S.; Straach, S.; Härtel, P.; Althues, H.; Kaskel, S. Hierarchical Columnar Silicon Anode Structures for High Energy Density Lithium Sulfur Batteries. *J. Power Sources* **2017**, *351*, 183–191.

(57) Calculated from Equation (1), nearly 10 times that of current technology.

(58) Chung, S.-H.; Manthiram, A. A Hierarchical Carbonized Paper with Controllable Thickness as a Modulable Interlayer System for High Performance Li–S Batteries. *Chem. Commun.* **2014**, *50* (32), 4184–4187.

(59) Fu, Y.; Su, Y.-S.; Manthiram, A. Li2S-Carbon Sandwiched Electrodes with Superior Performance for Lithium-Sulfur Batteries. *Adv. Energy Mater.* **2014**, *4* (1), n/a-n/a.

(60) Su, Y.-S.; Fu, Y.; Guo, B.; Dai, S.; Manthiram, A. Fast, Reversible Lithium Storage with a Sulfur/Long-Chain-Polysulfide Redox Couple. *Chem. – Eur. J.* **2013**, *19* (26), 8621–8626.

(61) Su, Y.-S.; Manthiram, A. A New Approach to Improve Cycle Performance of Rechargeable Lithium–sulfur Batteries by Inserting a Free-Standing MWCNT Interlayer. *Chem. Commun.* **2012**, *48* (70), 8817–8819.

(62) Su, Y.-S.; Manthiram, A. Lithium–sulphur Batteries with a Microporous Carbon Paper as a Bifunctional Interlayer. *Nat. Commun.* **2012**, *3*, 1166.

(63) Zu, C.; Su, Y.-S.; Fu, Y.; Manthiram, A. Improved Lithium–sulfur Cells with a Treated Carbon Paper Interlayer. *Phys. Chem. Chem. Phys.* **2013**, *15* (7), 2291–2297.

(64) Yim, T.; Park, M.-S.; Yu, J.-S.; Kim, K. J.; Im, K. Y.; Kim, J.-H.; Jeong, G.; Jo, Y. N.; Woo, S.-G.; Kang, K. S.; et al. Effect of Chemical Reactivity of Polysulfide

toward Carbonate-Based Electrolyte on the Electrochemical Performance of Li–S Batteries. *Electrochimica Acta* **2013**, *107*, 454–460.

(65) Gao, J.; Lowe, M. A.; Kiya, Y.; Abruña, H. D. Effects of Liquid Electrolytes on the Charge–Discharge Performance of Rechargeable Lithium/Sulfur Batteries: Electrochemical and in-Situ X-Ray Absorption Spectroscopic Studies. *J. Phys. Chem. C* **2011**, *115* (50), 25132–25137.

(66) Cheon, S.-E.; Ko, K.-S.; Cho, J.-H.; Kim, S.-W.; Chin, E.-Y.; Kim, H.-T. Rechargeable Lithium Sulfur Battery I. Structural Change of Sulfur Cathode During Discharge and Charge. *J. Electrochem. Soc.* **2003**, *150* (6), A796–A799.

(67) Zhang, S. S. Role of LiNO3 in Rechargeable Lithium/Sulfur Battery. *Electrochimica Acta* **2012**, *70*, 344–348.

(68) Lee, S.-K.; Oh, S.-M.; Park, E.; Scrosati, B.; Hassoun, J.; Park, M.-S.; Kim, Y.-J.; Kim, H.; Belharouak, I.; Sun, Y.-K. Highly Cyclable Lithium–Sulfur Batteries with a Dual-Type Sulfur Cathode and a Lithiated Si/SiOx Nanosphere Anode. *Nano Lett.* **2015**, *15* (5), 2863–2868.

(69) Etacheri, V.; Geiger, U.; Gofer, Y.; Roberts, G. A.; Stefan, I. C.; Fasching, R.; Aurbach, D. Exceptional Electrochemical Performance of Si-Nanowires in 1,3-Dioxolane Solutions: A Surface Chemical Investigation. *Langmuir* **2012**, *28* (14), 6175–6184.

(70) Jaumann, T.; Balach, J.; Klose, M.; Oswald, S.; Eckert, J.; Giebeler, L. Role of 1,3-Dioxolane and LiNO3 Addition on the Long Term Stability of Nanostructured Silicon/Carbon Anodes for Rechargeable Lithium Batteries. *J. Electrochem. Soc.* **2016**, *163* (3), A557–A564.

(71) Brückner, J.; Thieme, S.; Böttger-Hiller, F.; Bauer, I.; Grossmann, H. T.; Strubel, P.; Althues, H.; Spange, S.; Kaskel, S. Carbon-Based Anodes for Lithium Sulfur Full Cells with High Cycle Stability. *Adv. Funct. Mater.* **2014**, *24* (9), 1284–1289.

(72) Elazari, R.; Salitra, G.; Gershinsky, G.; Garsuch, A.; Panchenko, A.; Aurbach, D. Rechargeable Lithiated Silicon–sulfur (SLS) Battery Prototypes. *Electrochem. Commun.* **2012**, *14* (1), 21–24.

(73) Hagen, M.; Quiroga-González, E.; Dörfler, S.; Fahrer, G.; Tübke, J.; Hoffmann, M. J.; Althues, H.; Speck, R.; Krampfert, M.; Kaskel, S.; et al. Studies on Preventing Li Dendrite Formation in Li–S Batteries by Using Pre-Lithiated Si Microwire Anodes. *J. Power Sources* **2014**, *248*, 1058–1066.

(74) Eom, K.; Joshi, T.; Bordes, A.; Do, I.; Fuller, T. F. The Design of a Li-Ion Full Cell Battery Using a Nano Silicon and Nano Multi-Layer Graphene Composite Anode. *J. Power Sources* **2014**, *249*, 118–124.

(75) Pu, X.; Yang, G.; Yu, C. Safe and Reliable Operation of Sulfur Batteries with Lithiated Silicon. *Nano Energy* **2014**, *9*, 318–324.

(76) Agostini, M.; Hassoun, J.; Liu, J.; Jeong, M.; Nara, H.; Momma, T.; Osaka, T.; Sun, Y.-K.; Scrosati, B. A Lithium-Ion Sulfur Battery Based on a Carbon-Coated Lithium-Sulfide Cathode and an Electrodeposited Silicon-Based Anode. *ACS Appl. Mater. Interfaces* **2014**, *6* (14), 10924–10928.

(77) Hassoun, J.; Kim, J.; Lee, D.-J.; Jung, H.-G.; Lee, S.-M.; Sun, Y.-K.; Scrosati, B. A Contribution to the Progress of High Energy Batteries: A Metal-Free, Lithium-Ion, Silicon–sulfur Battery. *J. Power Sources* **2012**, *202*, 308–313.

(78) Moreno, N.; Agostini, M.; Caballero, A.; Morales, J.; Hassoun, J. A Long-Life Lithium Ion Sulfur Battery Exploiting High Performance Electrodes. *Chem. Commun.* **2015**, *51* (77), 14540–14542.

(79) Heitsch, A. T.; Akhavan, V. A.; Korgel, B. A. Rapid SFLS Synthesis of Si Nanowires Using Trisilane with In Situ Alkyl-Amine Passivation. *Chem. Mater.* **2011**, *23* (11), 2697–2699.

(80) Su, Y.-S.; Manthiram, A. Lithium–sulphur Batteries with a Microporous Carbon Paper as a Bifunctional Interlayer. *Nat. Commun.* **2012**, *3*, 1166.

(81) Chockla, A. M.; Klavetter, K. C.; Mullins, C. B.; Korgel, B. A. Tin-Seeded Silicon Nanowires for High Capacity Li-Ion Batteries. *Chem. Mater.* **2012**, *24* (19), 3738–3745.

(82) Bogart, T. D.; Lu, X.; Korgel, B. A. Precision Synthesis of Silicon Nanowires with Crystalline Core and Amorphous Shell. *Dalton Trans.* **2013**, *42* (35), 12675–12680.

(83) Xu, K. Electrolytes and Interphases in Li-Ion Batteries and Beyond. *Chem. Rev.* **2014**, *114* (23), 11503–11618.

(84) Chung, S.-H.; Chang, C.-H.; Manthiram, A. Hierarchical Sulfur Electrodes as a Testing Platform for Understanding the High-Loading Capability of Li-S Batteries. *J. Power Sources* **2016**, *334* (Supplement C), 179–190.

(85) Nakai, H.; Kubota, T.; Kita, A.; Kawashima, A. Investigation of the Solid Electrolyte Interphase Formed by Fluoroethylene Carbonate on Si Electrodes. *J. Electrochem. Soc.* **2011**, *158* (7), A798–A801.

(86) Chan, C. K.; Ruffo, R.; Hong, S. S.; Cui, Y. Surface Chemistry and Morphology of the Solid Electrolyte Interphase on Silicon Nanowire Lithium-Ion Battery Anodes. *J. Power Sources* **2009**, *189* (2), 1132–1140.

(87) Diao, Y.; Xie, K.; Xiong, S.; Hong, X. Insights into Li-S Battery Cathode Capacity Fading Mechanisms: Irreversible Oxidation of Active Mass during Cycling. *J. Electrochem. Soc.* **2012**, *159* (11), A1816–A1821.

(88) Aurbach, D.; Pollak, E.; Elazari, R.; Salitra, G.; Kelley, C. S.; Affinito, J. On the Surface Chemical Aspects of Very High Energy Density, Rechargeable Li–Sulfur Batteries. *J. Electrochem. Soc.* **2009**, *156* (8), A694–A702.

(89) Aurbach, D.; Weissman, I.; Schechter, A.; Cohen, H. X-Ray Photoelectron Spectroscopy Studies of Lithium Surfaces Prepared in Several Important Electrolyte Solutions. A Comparison with Previous Studies by Fourier Transform Infrared Spectroscopy. *Langmuir* **1996**, *12* (16), 3991–4007.

(90) Zu, C.; Azimi, N.; Zhang, Z.; Manthiram, A. Insight into Lithium–metal Anodes in Lithium–sulfur Batteries with a Fluorinated Ether Electrolyte. *J. Mater. Chem. A* **2015**, *3* (28), 14864–14870.

(91) Xiong, S.; Xie, K.; Diao, Y.; Hong, X. Properties of Surface Film on Lithium Anode with LiNO3 as Lithium Salt in Electrolyte Solution for Lithium–sulfur Batteries. *Electrochimica Acta* **2012**, *83*, 78–86.

Chapter 6: Conclusions and Future Directions

6.1 Conclusions

Changes in lithium ion battery (LIB) electrode materials are the demands of high-power applications and improve safety, next generation LIBs require improved energy storage materials required to meet the needs of emerging large-scale high-power applications such as extended range electric vehicles and grid storage for solar power. Silicon (Si) and germanium (Ge) are potential options for future anodes, as they store significantly more Li^+ than graphite. However, they still face significant engineering challenges before they are practically useful. The alloying process results in significant volume change during cycling, leading to mechanical fracture and poor stability.[7] Strategies to improve stability and capacity include nanostructuring materials and experimenting with surface coatings or modifications.[1–7] This work builds upon these previous investigations and endeavors to understand how the structure and surface chemistry of Si and Ge materials impact their performance in LIBs.

6.1.1 Group IV Type II Clathrate Lithium Ion Batteries

Two different group IV type II clathrates were studied in Li ion batteries, $Na_{0.5}Si_{136}$ and $Na_{0.5}(Si_{0.9}Ge_{0.1})_{136}$. This work demonstrated that high capacity, reversible cycling of type II clathrates is possible. Half cell testing showed high initial charge capacities of 3434 mAh/g and 2814 mAh/g for the $Na_{0.5}Si_{136}$ and $Na_{0.5}(Si_{0.9}Ge_{0.1})_{136}$ clathrates, respectively. Both materials exhibited superior reversible cycling performance when compared with previous clathrate battery studies. Even at a high applied current density of 1.25 A/g, both clathrates exhibited a charge capacity greater than 1000 mAh/g and were very stable. Differential capacity plots showed that both clathrates amorphized during battery cycling and formed the c-$Li_{15}Si_4$ phase after fully lithiating. The high type II phase purity of the

$Na_{0.5}Si_{136}$ and $Na_{0.5}(Si_{0.9}Ge_{0.1})_{136}$ samples was critical for stable cycling. Both samples had a high phase purity, of greater than 94 wt.% type II clathrate, due to the reaction conditions under which the materials were synthesized. This research demonstrates the battery capability of Si and alloyed Si-Ge clathrates, opening the doors for future study into the impact altering the alloy ratio has on battery performance.

6.1.2 In-Situ Surface Passivated Germanium Nanowire Batteries

Battery performance of germanium (Ge) nanowires (NWs) with different surface passivations was tested. The nanowires were synthesized using a supercritical-fluid-liquid-solid technique that allowed for easy in-situ passivation. Three different functionalizations were tested in comparison with pristine nanowires: dodecene (DDE), dodecanethiol (DDT), and mercaptoundecanoic acid (MUA). Each of the nanowire passivations resulted in different cycling behavior and capability. Pristine nanowires exhibited the best capacity at slow cycle times, but consistently had the lowest Coulombic efficiency. MUA nanowires had lower capacity than unpassivated nanowires, but the highest Coulombic efficiency. DDE exhibited low capacity at 1 C, but with extremely stable cycling and the best performance at a high cycle rate 10 C. DDT passivated nanowires performed with lower capacity at high rates and with lower stability in all tests. Previous research that found that DDT had enhanced performance due to improved binding with PVdF, but the same effect was not seen with PAA. Nanowires with different passivations had very different SEI compositions in the first cycle, but were largely the same by the 100th cycle. This research shows that the interaction between the nanowire surface, polymeric binder, and SEI formation is complex and must be optimized in conjunction to achieve the best results. The best surface chemistry with one binder might be different with another. Ideally, in the future, NWs with different passivations could be used for different performance needs.

6.1.3 *In Situ* TEM of Oxide Shell Silicon Nanowires

In situ transmission electron microscope (TEM) experiments confirmed that an intact silicon oxide (SiO_x) shell on a Si nanowire can limit volume expansion of the Si during lithiation and cause pore formation during delithiation. The constrained volume expansion during lithiation causes incomplete lithiation of the nanowire, retaining a crystalline Si core. The SiO_x shell prevents vacancy migration to the surface of the nanowire during delithiation, causing pore formation in the delithiated, amorphous, Si region. Pore formation was not seen in nanowires with an incomplete or burst SiO_x shell. *In situ* TEM observation during cycling fully elucidates the impact an added shell has during lithiation and delithiation.

6.1.4 Full Cell Batteries Using Silicon Anodes

Two different full cell systems were examined that revealed common challenges to integrating SiNW anodes. Even though these two systems have several differences, notably the electrolyte, they faced the common issue of low cycle stability due to Li consumption in the SEI layer. Prelithiation of the SiNW anode was crucial to improve the capacity and stability of battery cycling for both LFP and S cathodes. Better results were achieved when SiNWs were prelithiated electrochemically at a controlled rate, compared to prelithiation of SiNWs by direct contact with Li. While, lithiation on a battery tester allowed for better control of the lithiation rate and extent, future work will be needed to develop a method that is more scalable. XPS analysis was done to better understand how the SEI layer formed in SiNWs is affected by a S cathode. No sulfides were observed in the SINW SEI layer indicating the addition of a carbon interlayer successfully prevented polysulfides from migrating to the anode during battery cycling. XPS results also indicated SiNW-S full cells fully consumed the $LiNO_3$ electrolyte additive during cycling resulting in high levels of LiTFSI degradation that can contaminate the anode and reduce battery stability. Further

study is needed to determine how many battery cycles occur before the $LiNO_3$ is consumed, and what is the optimized concentration of additive. These studies demonstrate the importance of not only testing electrodes in half cell batteries, but to optimize the full system for the best performance.

6.2 Future Directions

6.2.1 Full Cells

To realize the full benefits of a higher capacity anode the storage capacity of the cathode must increase as well. While there are many different next generation cathodes that are being explored, there are some universal problems that must be addressed for Si anodes to be used in a full cell system. Irreversible consumption of Li by the SEI layer formed on the SiNW surface results in poor cycling stability and loss of capacity.[8–12] To counter this effect, SiNW anodes must be prelithiated. There are several possible prelithiation techniques, including using a Li metal additive,[13–15] mixing Li and Si nanoparticles to make a LiSi additive,[16] prelithiation using a battery tester, and mechanical prelithiation.[17,18] For SiNW anodes to be widely adopted, there must be a prelithiation method that is fast, easy, and potentially scalable and that does not require changes in the existing battery electrode formulation.

6.2.2 Liquid *In Situ* TEM

In situ TEM studies are traditionally done in an open cell, either with a drop of ionic liquid electrolyte on the counter electrode, or using solid Li_2O as the electrolyte.[19] In particular, the all-solid battery has the advantage of high contrast and resolution of the active material during lithiation. Over time, the electron bean will cause the ionic liquid electrolyte to degrade.[19] However, there are several drawbacks to using an open cell. It is impossible, using this configuration, to learn more about the interaction between the active

material and the electrolyte as well as the formation of the SEI layer in real time. Furthermore, in this technique, the electrolyte is only in contact with a single point of the active material, not along the length of the nanowire like in a real battery. This might alter the structural changes that take place in the material during lithiation.

Researchers have developed a sealed liquid cell that can be used inside the TEM to examine active materials in more realistic conditions, shown in Figure 7.1.[20–23] In this configuration, silicon nitride (Si_3N_4) membranes supported on Si chips create a sealed cell that can enclose any liquid electrolyte inside the TEM. The Si_3N_4 is very thin, ~50 nm thick, and allows transmission of the electron beam.[23] Using this set up it is possible to better understand SEI formation and growth during battery cycling. This technique could be used in the future to better understand the impact surface functionalization of NWs and electrolyte additives have on SEI formation.

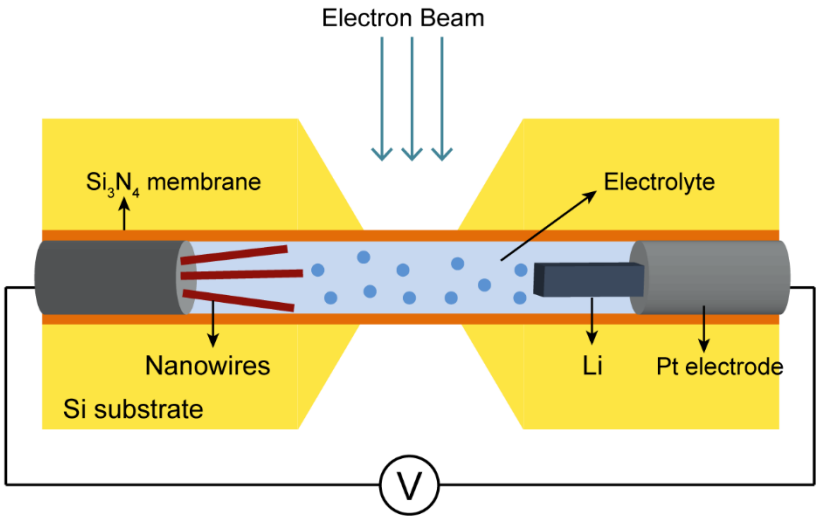

Figure 6.1 Illustration of a sealed liquid cell battery.[22]

6.2.3 Other Ions

Li has relatively low abundance in the Earth's crust and the rate which Li demand has increased over recent years has raised concerns that the world Li supply will run out in

the next century.[24] Researchers have already begun to investigate sodium (Na) and magnesium (Mg) as replacement active materials.[25,26]

Na is more abundant than Li, comprising nearly two percent of the Earth's crust, and significantly less expensive to produce. Graphite does not reversibly host Na ions, leading researchers to investigate alloy materials from group IV.[26] However, because Na^+ ions have a larger ionic radius than Li^+ ions, the accompanying volume expansion is more than twice as large as that experienced in LIBs.[26] Accommodating this volume change and overcoming poor solid-state Na^+ ion diffusion are two key issues that researchers have to consider when studying new negative electrode materials. Room temperature Ge anodes for NIBs have been experimentally demonstrated and studied using *in situ* TEM, but further work can be done to improve their capacity and stability.[27–30] A few reports have been made of room temperature sodiation of Si, but the capacity was extremely low and unstable.[31–33]

Magnesium is an attractive replacement material for Li because it is significantly more abundant and less air sensitive.[34] It has a smaller ionic radius and higher theoretical capacity than Na. Additionally, because Mg is divalent, it can undergo two-electron reduction and has a volumetric capacity that is close to twice as high as that of Li, 2062 and 3837 mAh/cm^3 for Li and Mg respectively. Previous research has already found that MIBs can be made using Sn, antimony, and bismuth.[35,36] However, they suffered from poor stability and low rate capability. Theoretical has suggested Ge is a potentially attractive anode material has a theoretical capacity in MIBs of 1476 mAh/g and a low dopant Mg migration barrier of Ge is around 0.7 eV.[37]

6.3 REFERENCES

(1) McDowell, M. T.; Lee, S. W.; Nix, W. D.; Cui, Y. 25th Anniversary Article: Understanding the Lithiation of Silicon and Other Alloying Anodes for Lithium-Ion Batteries. *Adv. Mater. Deerfield Beach Fla* **2013**, *25* (36), 4966–4985.

(2) Sim, S.; Oh, P.; Park, S.; Cho, J. Critical Thickness of SiO2 Coating Layer on Core@Shell Bulk@Nanowire Si Anode Materials for Li-Ion Batteries. *Adv. Mater.* **2013**, *25* (32), 4498–4503.

(3) Zhang, Y.; Li, Y.; Wang, Z.; Zhao, K. Lithiation of SiO2 in Li-Ion Batteries: In Situ Transmission Electron Microscopy Experiments and Theoretical Studies. *Nano Lett.* **2014**, *14* (12), 7161–7170.

(4) Bogart, T. D.; Oka, D.; Lu, X.; Gu, M.; Wang, C.; Korgel, B. A. Lithium Ion Battery Peformance of Silicon Nanowires with Carbon Skin. *ACS Nano* **2014**, *8* (1), 915–922.

(5) Kim, S. J.; Kargar, A.; Wang, D.; Graham, G. W.; Pan, X. Lithiation of Rutile TiO2-Coated Si NWs Observed by in Situ TEM. *Chem. Mater.* **2015**, *27* (20), 6929–6933.

(6) He, Y.; Piper, D. M.; Gu, M.; Travis, J. J.; George, S. M.; Lee, S.-H.; Genc, A.; Pullan, L.; Liu, J.; Mao, S. X.; et al. In Situ Transmission Electron Microscopy Probing of Native Oxide and Artificial Layers on Silicon Nanoparticles for Lithium Ion Batteries. *ACS Nano* **2014**, *8* (11), 11816–11823.

(7) McDowell, M. T.; Lee, S. W.; Ryu, I.; Wu, H.; Nix, W. D.; Choi, J. W.; Cui, Y. Novel Size and Surface Oxide Effects in Silicon Nanowires as Lithium Battery Anodes. *Nano Lett.* **2011**, *11* (9), 4018–4025.

(8) Nakai, H.; Kubota, T.; Kita, A.; Kawashima, A. Investigation of the Solid Electrolyte Interphase Formed by Fluoroethylene Carbonate on Si Electrodes. *J. Electrochem. Soc.* **2011**, *158* (7), A798–A801.

(9) Bogart, T. D.; Chockla, A. M.; Korgel, B. A. High Capacity Lithium Ion Battery Anodes of Silicon and Germanium. *Curr. Opin. Chem. Eng.* **2013**, *2* (3), 286–293.

(10) Winter, M.; Besenhard, J. O. Electrochemical Lithiation of Tin and Tin-Based Intermetallics and Composites. *Electrochimica Acta* **1999**, *45* (1), 31–50.

(11) Verma, P.; Maire, P.; Novák, P. A Review of the Features and Analyses of the Solid Electrolyte Interphase in Li-Ion Batteries. *Electrochimica Acta* **2010**, *55* (22), 6332–6341.

(12) Goodenough, J. B.; Kim, Y. Challenges for Rechargeable Li Batteries. *Chem. Mater.* **2010**, *22* (3), 587–603.

(13) Forney, M. W.; Ganter, M. J.; Staub, J. W.; Ridgley, R. D.; Landi, B. J. Prelithiation of Silicon–Carbon Nanotube Anodes for Lithium Ion Batteries by Stabilized Lithium Metal Powder (SLMP). *Nano Lett.* **2013**, *13* (9), 4158–4163.

(14) Wang, Z.; Fu, Y.; Zhang, Z.; Yuan, S.; Amine, K.; Battaglia, V.; Liu, G. Application of Stabilized Lithium Metal Powder (SLMP®) in Graphite Anode – A High Efficient Prelithiation Method for Lithium-Ion Batteries. *J. Power Sources* **2014**, *260* (Supplement C), 57–61.

(15) Jarvis, C. R.; Lain, M. J.; Yakovleva, M. V.; Gao, Y. A Prelithiated Carbon Anode for Lithium-Ion Battery Applications. *J. Power Sources* **2006**, *162* (2), 800–802.

(16) Zhao, J.; Lu, Z.; Liu, N.; Lee, H.-W.; McDowell, M. T.; Cui, Y. Dry-Air-Stable Lithium Silicide–lithium Oxide Core–shell Nanoparticles as High-Capacity Prelithiation Reagents. *Nat. Commun.* **2014**, *5*, 5088.

(17) Kim, H. J.; Choi, S.; Lee, S. J.; Seo, M. W.; Lee, J. G.; Deniz, E.; Lee, Y. J.; Kim, E. K.; Choi, J. W. Controlled Prelithiation of Silicon Monoxide for High Performance Lithium-Ion Rechargeable Full Cells. *Nano Lett.* **2016**, *16* (1), 282–288.

(18) Liu, N.; Hu, L.; McDowell, M. T.; Jackson, A.; Cui, Y. Prelithiated Silicon Nanowires as an Anode for Lithium Ion Batteries. *ACS Nano* **2011**, *5* (8), 6487–6493.

(19) Liu, X. H.; Huang, J. Y. In Situ TEM Electrochemistry of Anode Materials in Lithium Ion Batteries. *Energy Environ. Sci.* **2011**, *4* (10), 3844–3860.

(20) Zeng, Z.; Liang, W.-I.; Liao, H.-G.; Xin, H. L.; Chu, Y.-H.; Zheng, H. Visualization of Electrode–Electrolyte Interfaces in LiPF6/EC/DEC Electrolyte for Lithium Ion Batteries via in Situ TEM. *Nano Lett.* **2014**, *14* (4), 1745–1750.

(21) Wu, F.; Yao, N. Advances in Sealed Liquid Cells for In-Situ TEM Electrochemial Investigation of Lithium-Ion Battery. *Nano Energy* **2015**, *11*, 196–210.

(22) Lu, X. Silicon and Germanium Nanostructures : Synthesis and in Situ TEM Study. Thesis, 2015.

(23) Gu, M.; Parent, L. R.; Mehdi, B. L.; Unocic, R. R.; McDowell, M. T.; Sacci, R. L.; Xu, W.; Connell, J. G.; Xu, P.; Abellan, P.; et al. Demonstration of an Electrochemical Liquid Cell for Operando Transmission Electron Microscopy Observation of the Lithiation/Delithiation Behavior of Si Nanowire Battery Anodes. *Nano Lett.* **2013**, *13* (12), 6106–6112.

(24) *Lithium*; Mineral Commodity Summaries 2015; U.S. Geological Survey: Reston, VA, 2015.

(25) Gregory, T. D.; Hoffman, R. J.; Winterton, R. C. Nonaqueous Electrochemistry of Magnesium Applications to Energy Storage. *J. Electrochem. Soc.* **1990**, *137* (3), 775–780.

(26) Yabuuchi, N.; Kubota, K.; Dahbi, M.; Komaba, S. Research Development on Sodium-Ion Batteries. *Chem. Rev.* **2014**, *114* (23), 11636–11682.

(27) Kohandehghan, A.; Cui, K.; Kupsta, M.; Ding, J.; Memarzadeh Lotfabad, E.; Kalisvaart, W. P.; Mitlin, D. Activation with Li Enables Facile Sodium Storage in Germanium. *Nano Lett.* **2014**, *14* (10), 5873–5882.

(28) Abel, P. R.; Lin, Y.-M.; de Souza, T.; Chou, C.-Y.; Gupta, A.; Goodenough, J. B.; Hwang, G. S.; Heller, A.; Mullins, C. B. Nanocolumnar Germanium Thin Films as a High-Rate Sodium-Ion Battery Anode Material. *J. Phys. Chem. C* **2013**, *117* (37), 18885–18890.

(29) Baggetto, L.; Keum, J. K.; Browning, J. F.; Veith, G. M. Germanium as Negative Electrode Material for Sodium-Ion Batteries. *Electrochem. Commun.* **2013**, *34*, 41–44.

(30) Lu, X.; Adkins, E. R.; He, Y.; Zhong, L.; Luo, L.; Mao, S. X.; Wang, C.-M.; Korgel, B. A. Germanium as a Sodium Ion Battery Material: In Situ TEM Reveals Fast Sodiation Kinetics with High Capacity. *Chem. Mater.* **2016**, *28* (4), 1236–1242.

(31) Jangid, M. K.; Lakhnot, A. S.; Vemulapally, A.; Sonia, F. J.; Sinha, S.; Dusane, R. O.; Mukhopadhyay, A. Crystalline Core/Amorphous Shell Structured Silicon Nanowires Offer Size and Structure Dependent Reversible Na-Storage. *J. Mater. Chem. A* **2018**, *6* (8), 3422–3434.

(32) Xu, Y.; Swaans, E.; Basak, S.; Zandbergen, H. W.; Borsa, D. M.; Mulder, F. M. Reversible Na-Ion Uptake in Si Nanoparticles. *Adv. Energy Mater.* **2016**, *6* (2), n/a-n/a.

(33) Han, Y.; Lin, N.; Xu, T.; Li, T.; Tian, J.; Zhu, Y.; Qian, Y. An Amorphous Si Material with a Sponge-like Structure as an Anode for Li-Ion and Na-Ion Batteries. *Nanoscale* **2018**, *10* (7), 3153–3158.

(34) John Muldoon, C. B. B. Quest for Nonaqueous Multivalent Secondary Batteries: Magnesium and Beyond. *Chem. Rev.* **2014**.

(35) Arthur, T. S.; Singh, N.; Matsui, M. Electrodeposited Bi, Sb and Bi1-XSbx Alloys as Anodes for Mg-Ion Batteries. *Electrochem. Commun.* **2012**, *16* (1), 103–106.

(36) Singh, N.; Arthur, T. S.; Ling, C.; Matsui, M.; Mizuno, F. A High Energy-Density Tin Anode for Rechargeable Magnesium-Ion Batteries. *Chem. Commun.* **2012**, *49* (2), 149–151.

(37) Malyi, O. I.; Tan, T. L.; Manzhos, S. In Search of High Performance Anode Materials for Mg Batteries: Computational Studies of Mg in Ge, Si, and Sn. *J. Power Sources* **2013**, *233*, 341–345.

APPENDICES

Appendix A††

A.1 SUPPORTING FIGURES

Reitveld refinement results. Figure A.1 shows the powder XRD pattern and Reitveld refinement for (a) $Na_{0.5}Si_{136}$ and (b) Na0.5(Si0.9Ge0.1)136 clathrates. The material in (a) was NaxSi136 with x<0.5 and a phase purity of >94 wt.%, the balance being diamond Si. The second clathrate in (b) had a composition of Nax(Si0.9Ge0.1)136 with x<0.5 and a phase purity >98.5 wt.%, the balance being crystalline SiGe.

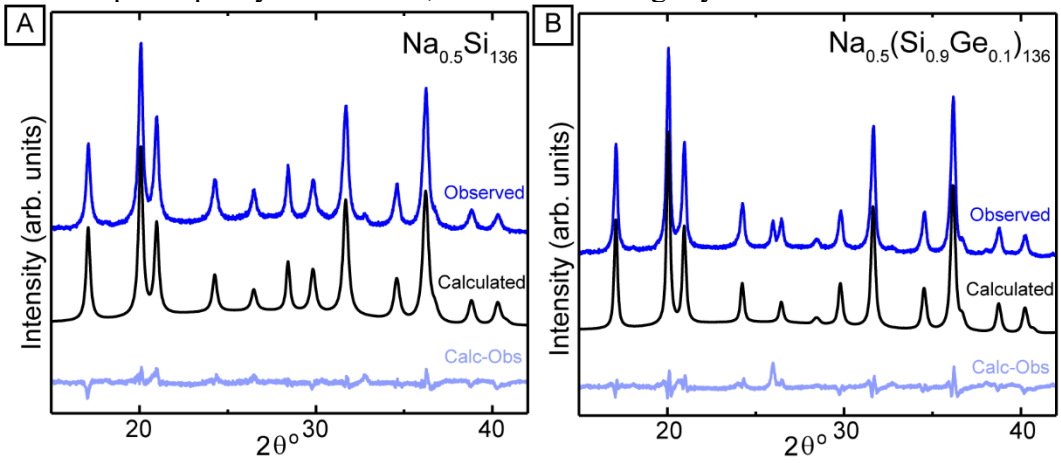

Figure A.1 Powder XRD pattern and Reitveld refinement for (a) $Na_{0.5}Si_{136}$ and (b) $Na_{0.5}(Si_{0.9}Ge_{0.1})_{136}$ clathrates.

Battery results from literature. Table A.1 compares the battery performance of other clathrates reported in literature. Most studies focused exclusively on one type of clathrate, with Ref. 4 being the exception. To the best of our knowledge, this paper reports

†† The work contained in this chapter is the subject of a scholarly article that is currently in preparation. Authors on this work include Emily R. Adkins, Taizhi Jiang, Andrew L. Heilman, Lakshmi Krishna, Reuben T. Collins, and Brian A. Korgel. Emily Adkins was responsible for planning the research, performing the battery experiments, with some help from Drew Heilman, analyzing the battery data, researching and writing the completed document.

significantly better battery performance than has previously been observed with clathrate batteries. Capacities were estimated as best possible from graph data included in papers.

Table A.1 Comparison of the capacity from this work with previously reported clathrate battery results from literature.

Clathrate	Type		Current Density (mA/g)	Cycles	Initial Capacity (mA/g)	Final Capacity (mAh/g)	Year	Ref
	I	II						
$Ba_8Al_{8.54}Si_{37.46}$	100%	-	50	20	400 *	260 *	2015	[1]
$Ba_8Al_{16}Si_{30}$	100%	-	25	100	410 *	150 *	2017	[2]
$Na_{\sim 1.3}Si_{136}$	2%	98%	2	1	1550	-	2012	[3]
$Na_8Si_{46}/Na_{24}Si_{136}$	20%	80%	25	5	2500	171	2013	[4]
$Na_{0.5}(Si_{0.9}Ge_{0.1})_{136}$	-	98.5%	25	30	2750 *	1100 *	**2018**	**This study**
			50	150	2815 *	1131 *		
$Na_{0.5}Si_{136}$	-	94%	50	150	3435 *	901 *		

* These papers reported capacity in $mA/g_{clathrate}$. The other papers did not specifically mention their reporting basis.

Additional battery data. Figure A.2 shows battery results for the $Si_{0.9}Ge_{0.1}$ clathrate tested at an applied current density of 0.025 A/g (approximately C/50). This initial test was done for comparison with previous literature results that used the same applied current density.[4] Initial charge capacity was 2733 mAh/g, though by the 20th cycle the capacity had decreased by nearly 50% to 1392 mAh/g.

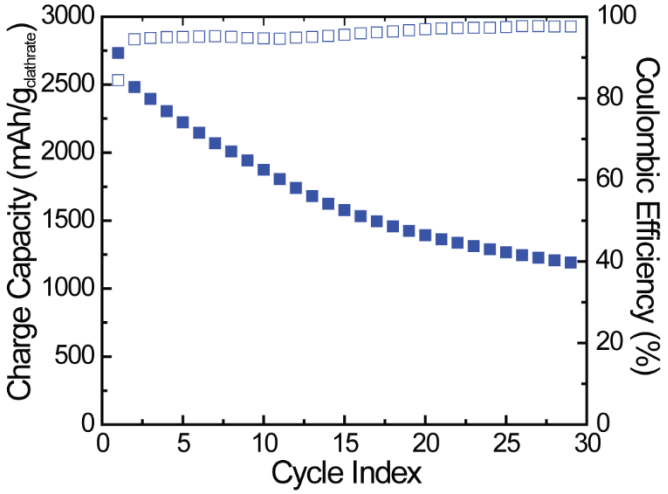

Figure A.2 Charge capacity (closed squares) and Coulombic efficiency (open squares) of the $Si_{0.9}Ge_{0.1}$ clathrate cycled at current density of 0.025 A/g. Battery capacity had faded by over 50% by the 30th cycle.

Figure A.3 shows extended battery cycling data for the $Si_{0.9}Ge_{0.1}$ clathrate tested at the applied current density of 0.125 A/g (approximately C/10). While 50% of total capacity is lost in the first 50 cycles, capacity loss occurs more slowly in subsequent cycles, to 893 mAh/g after 200 cycles which is 32% of initial capacity.

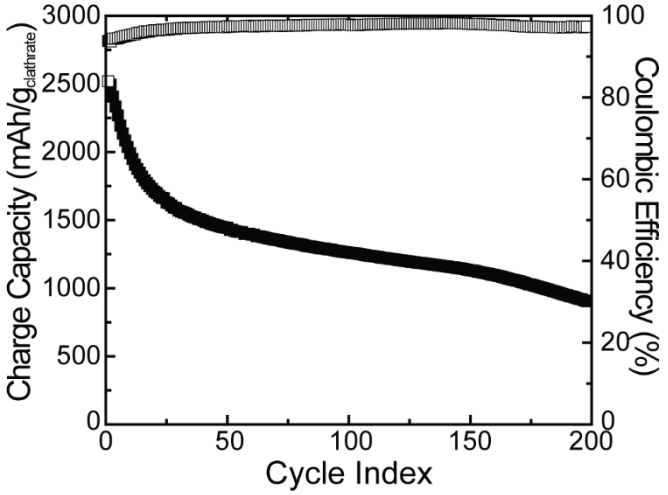

Figure A.3 Charge capacity (closed squares) and Coulombic efficiency (open squares) of the $Si_{0.9}Ge_{0.1}$ clathrate cycled at current density of 0.125 A/g cycled for 200 cycles. After the first 50 cycles capacity loss occurs more slowly.

Additional differential capacity data. Figure A.4 shows additional differential capacity data for the Si clathrate cycled at an applied current density of 0.125 A/g between cycles 10 – 50. Following cycle 10, the peak at 450 mV begins to broaden and shift to a lower potential. Although there is still a prominent peak at 450 mV in cycle 20, a broad shoulder begins to develop at around 300 mV, consistent with the delithiation of a-Si.[5,6] By cycle 50 the delithiation behavior for the Si and $Si_{0.9}Ge_{0.1}$ clathrates are comparable.

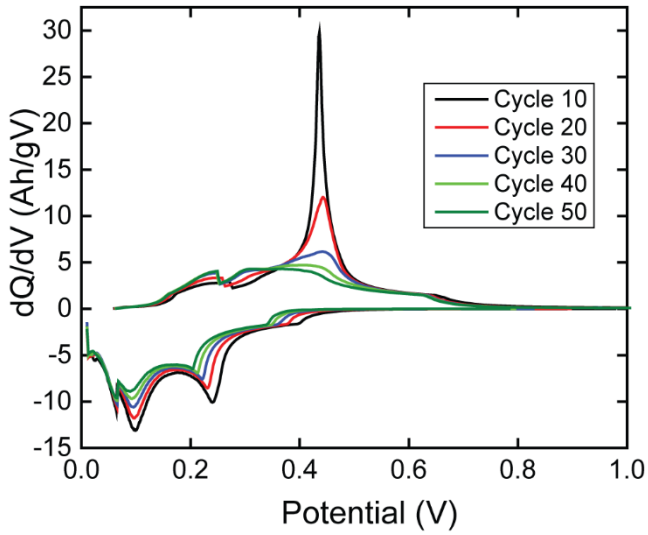

Figure A.4 Differential capacity profiles for the Si clathrate cycled at a current density of 0.125 A/g between cycles 10 – 50 demonstrating the gradual decrease and broadening of the peak at 450 mV.

A.2 REFERENCES

(1) Li, Y.; Raghavan, R.; Wagner, N. A.; Davidowski, S. K.; Baggetto, L.; Zhao, R.; Cheng, Q.; Yarger, J. L.; Veith, G. M.; Ellis-Terrell, C.; et al. Type I Clathrates as Novel Silicon Anodes: An Electrochemical and Structural Investigation. *Adv. Sci.* **2015**, *2* (6), n/a-n/a.

(2) Zhao, R.; Bobev, S.; Krishna, L.; Yang, T.; Weller, J. M.; Jing, H.; Chan, C. K. Anodes for Lithium-Ion Batteries Based on Type I Silicon Clathrate Ba8Al16Si30 - Role of Processing on Surface Properties and Electrochemical Behavior. *ACS Appl. Mater. Interfaces* **2017**, *9* (47), 41246–41257.

(3) Langer, T.; Dupke, S.; Trill, H.; Passerini, S.; Eckert, H.; Pöttgen, R.; Winter, M. Electrochemical Lithiation of Silicon Clathrate-II. *J. Electrochem. Soc.* **2012**, *159* (8), A1318–A1322.

(4) Wagner, N. A.; Raghavan, R.; Zhao, R.; Wei, Q.; Peng, X.; Chan, C. K. Electrochemical Cycling of Sodium-Filled Silicon Clathrate. *ChemElectroChem* **2014**, *1* (2), 347–353.

(5) Obrovac, M. N.; Krause, L. J. Reversible Cycling of Crystalline Silicon Powder. *J. Electrochem. Soc.* **2007**, *154* (2), A103–A108.

(6) Hatchard, T. D.; Dahn, J. R. In Situ XRD and Electrochemical Study of the Reaction of Lithium with Amorphous Silicon. *J. Electrochem. Soc.* **2004**, *151* (6), A838–A842.

Appendix B‡‡

B.1 Supporting Data

Extended 1 C battery cycling data for DDE and MUA passivated GeNWs. Figure B.1 shows extended battery cycling data for DDE and MUA passivated GeNWs at a 1 C cycle rate. DDE and MUA passivated Ge nanowires exhibited extremely stable cycling behavior. Even after 200 cycles the DDE batteries still retained 96% of 2nd cycle capacity, and the MUA batteries 81% of 3rd cycle capacity.

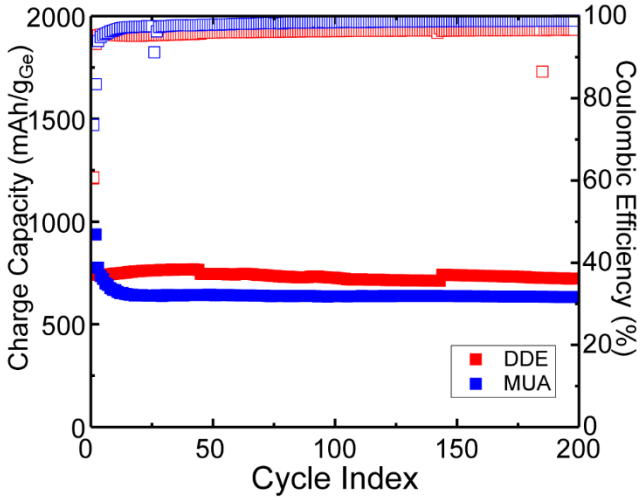

Figure B.1 Charge capacity (closed squares) and Coulombic efficiency (open squares) of DDE and MUA passivated Ge NWs cycled at a rate of 1 C, where 1 C = 1211 mAh/g. Very little capacity loss occurs over 200 cycles.

‡‡ The work contained in this chapter is the subject of a scholarly article that is currently in preparation. Authors on this work include Emily R. Adkins, Taizhi Jiang, Andrew L. Heilman, Phillip Liu, Brian A. Korgel. Emily Adkins was responsible for planning the research, synthesizing materials and performing battery experiments, with some help from Drew Heilman, analyzing the synthesis and battery data, researching and writing the completed document.

Additional 1 C pristine and DDT passivated GeNW battery data. Figure B.2 shows additional (a) pristine and (b) DDT passivated GeNWs cycled at 1C. Consistently, these batteries experienced a decline in capacity during the first 100 cycles.

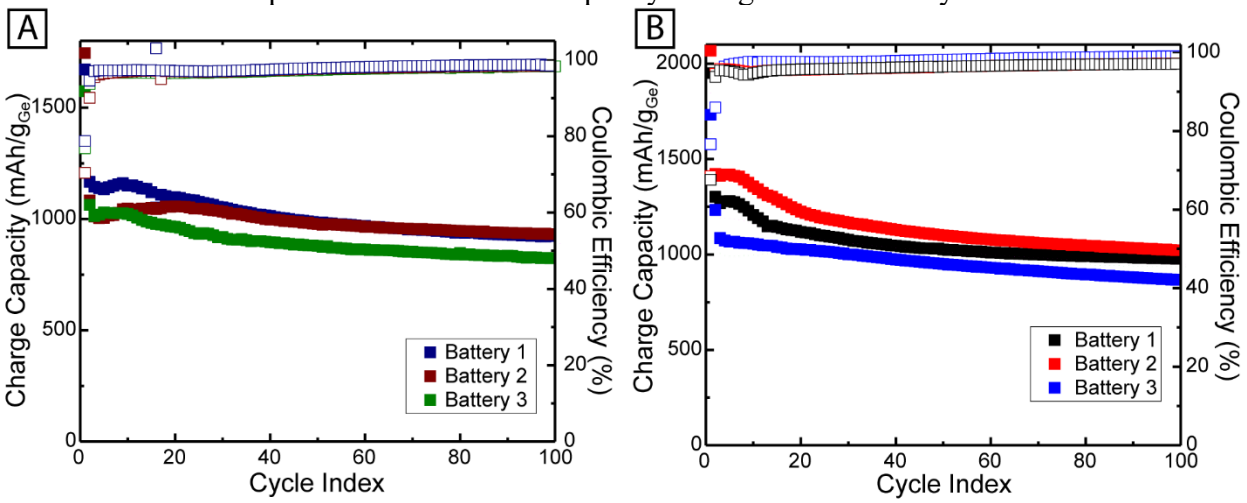

Figure B.2 Charge capacity (closed squares) and Coulombic efficiency (open squares) of (a) pristine and (b) DDT passivated Ge NWs cycled at a rate of 1 C, where 1 C = 1211 mAh/g. Results are consistent across multiple batteries tested.

XPS peak deconvolution of C 1s high resolution elemental scans. Figure B.3 presents high resolution elemental XPS scans of the C 1s orbital with peak deconvolution envelopes shown for the batteries after 1 cycle. These convolutions are used to determine the relative compositions of carbonate species present in each sample.

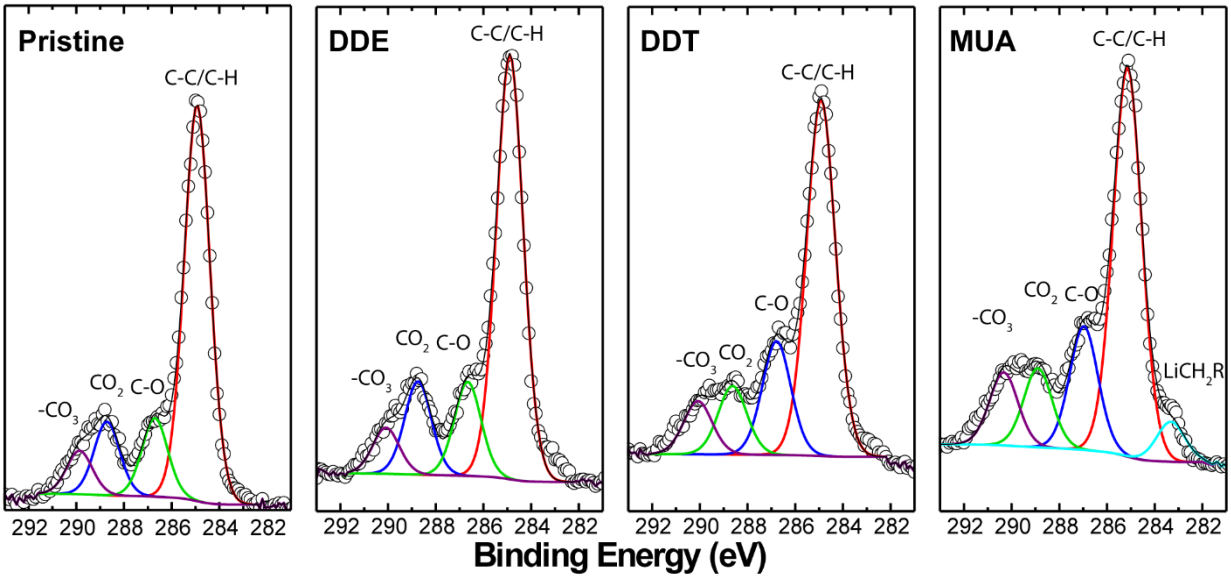

Figure B.3 XPS peak deconvolution of C 1s high resolution elemental scans for the batteries after 1 cycle.

Appendix C[§§]

C.1 Supporting Data

Volume expansion data. Table S1 describes the volume expansion of several Si nanowires with SiO_x shells following lithiation. This volume expansion is found by measuring the diameter and length of the nanowire after lithiation. Length is determined by tracking two points on the nanowire during lithiation and delithiation and measuring the distance as it changes. Length can be difficult to track due to bending of the nanowire out of the imaging plane. For this reason, a couple nanowires have a shorter measured length after lithiation. Nanowires with an SiO_x shell that burst during lithiation are marked.

Table C.1 Statistics of Observed Volume Expansion of Si Nanowires with an SiO_x Shell before and after Lithiation

Nanowire	Original Diameter (nm)	Original Length (nm)	Diameter after Lithiation (nm)	Length after Lithiation (nm)	% Expansion	Burst (y/n)
1	59.5	227.4	100.0	186.3	132.6	n
2	96.1	105.2	130.3	143.2	150.2	n
3	130.0	400.0	184.3	439.8	121.0	n
4	31.1	115.9	55.0	138.5	273.2	y
5	29.0	103.4	50.3	81.2	137.6	y
6	62.2	141.6	105.8	196.1	300.2	y
7	113.0	80.5	194.2	109.7	302.0	y

[§§] The work contained in this section is the subject of a scholarly article that is currently in preparation. Authors on this work include Emily R. Adkins, Taizhi Jiang, Langli Luo, Chong-Min Wang, and Brian A. Korgel. Emily Adkins was responsible for planning the research, synthesizing the materials, directing the *in-situ* TEM experiments, analyzing the data, researching and writing the completed document.

Additional TEM images of a Si nanowire with a SiO_x shell exhibiting pore formation upon delithiation. Figure C.1 shows TEM images of the Si nanowire from Figure 4.2 undergoing a second lithiation and delithiation cycle (See accompanying video file LithiationVideo_1.mp4). During lithiation, (Figure C.1a) the diameter increased from 83 nm to 119 nm. As the nanowire lithiates the pores are no longer visible. A thin crystalline core, which is darker than the surrounding lithiated Si, can be seen clearly through the first 200s of lithiation. It is not clear whether this is because it has amorphized, or due to the limited phase contrast between the core and the lithiated SiO_x shell and the increased roughness of the SiO_x shell. Pores again form after the second delithiation (Figure C.1b, and a more magnified view in Figure C.1c).

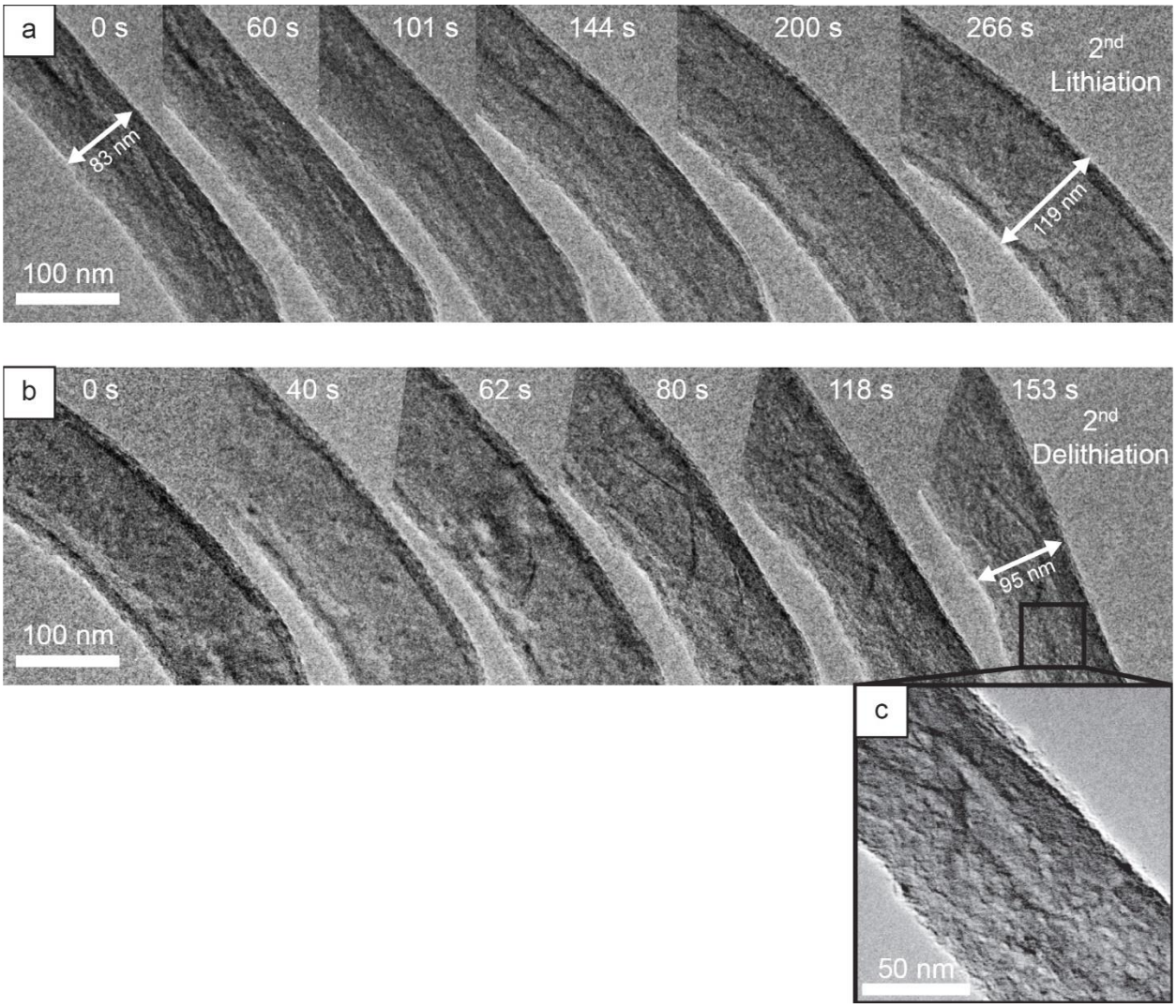

Figure C.1 TEM images of a Si nanowire with an SiO_x shell during a second (a) lithiation and (b) delithiation cycle. (See accompanying video file LithiationVideo_1.mp4) Prior to the second lithiation, the shell was 16 nm thick. Pores are not visible as the nanowire lithiates, but reappear upon delithiation, as seen in (c) a more magnified TEM image.

Figure C.2 shows TEM images of the pores formed in the same Si nanowire after the first and second delithiation cycles. The volume of the nanowire following the second delithiation has expanded by 26% from the first delithiation, indicating the pores have increased in diameter more than is visible. This volume expansion is found by measuring the diameter and length of the nanowire after each delithiation.

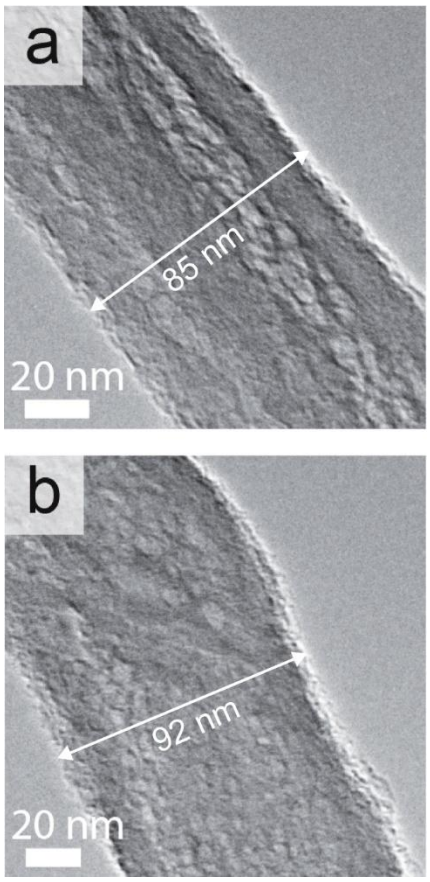

Figure C.2 TEM images of Si nanowires after (a) the first delithiation and (b) the second. Pores are visible in each image and the diameter has increased after a second delithiation.

Additional TEM images of Si nanowires with an SiO_x shell that burst during lithiation. Figure C.3 shows TEM images of a Si nanowire with an SiO_x shell that formed a lengthwise crack (See accompanying video file BurstWireVideo_4.mp4). The crack initiates at 181 seconds and propagates along the nanowire. The nanowire experiences 301% volume expansion upon total lithiation. The nanowire does not retain a crystalline core. Upon delithiation it does not form pores.

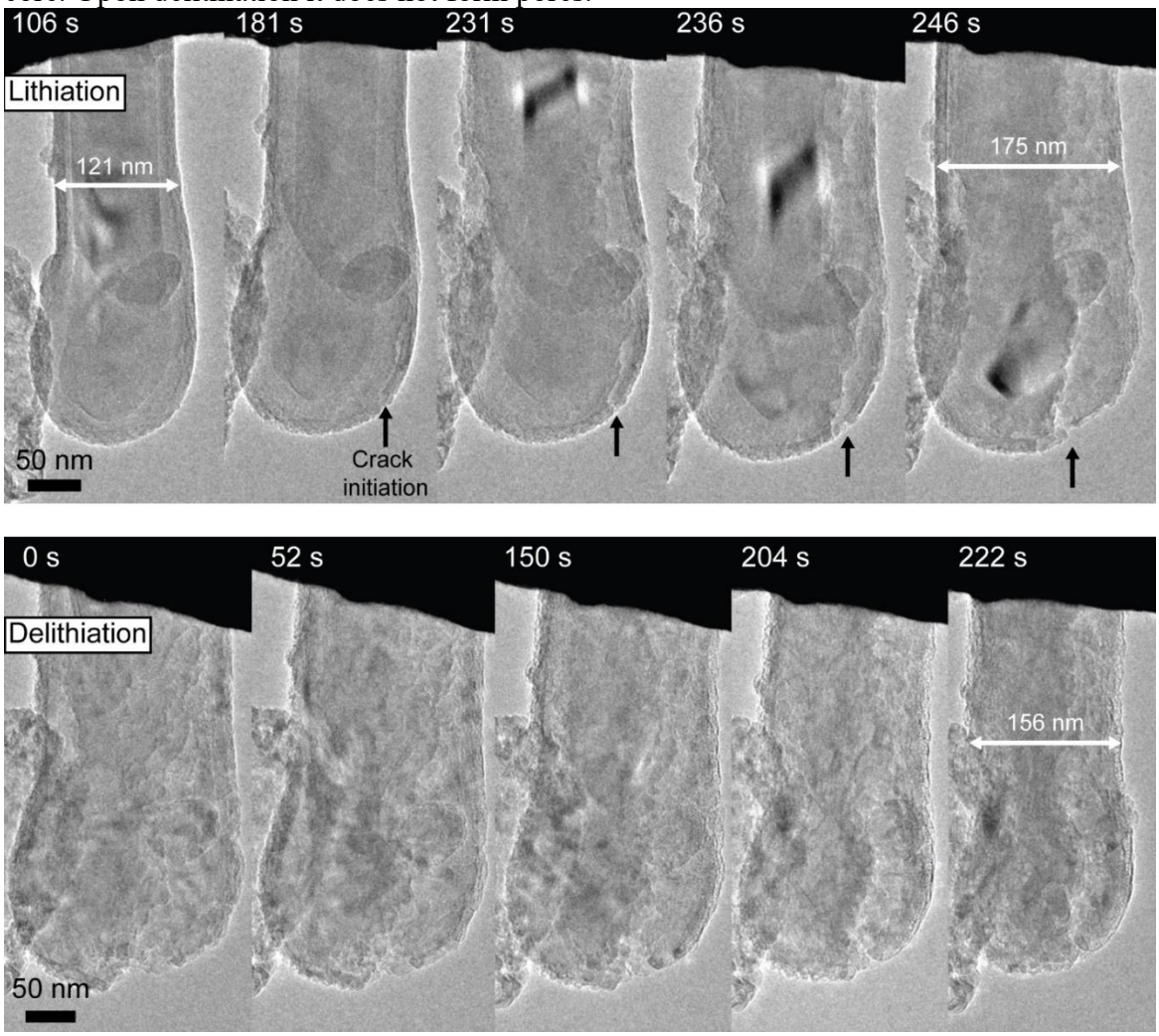

Figure C.3 TEM images of a Si nanowire with an SiO_x shell that bursts during the first lithiation. (See accompanying video file BurstWireVideo_4.mp4) The experiences 301% volume expansion at full lithiation and does not retain a crystalline Si core. Upon delithiation, the nanowire does not form pores.

Figure C.4 shows TEM images of a Si nanowire with a SiO_x shell and a twin defect during the first lithiation. Lithiation proceeds both along the interface between the SiO_x shell and the nanowire as well as along the twin interface. A burst occurs at the gold nanoparticle defect in the center of the nanowire.

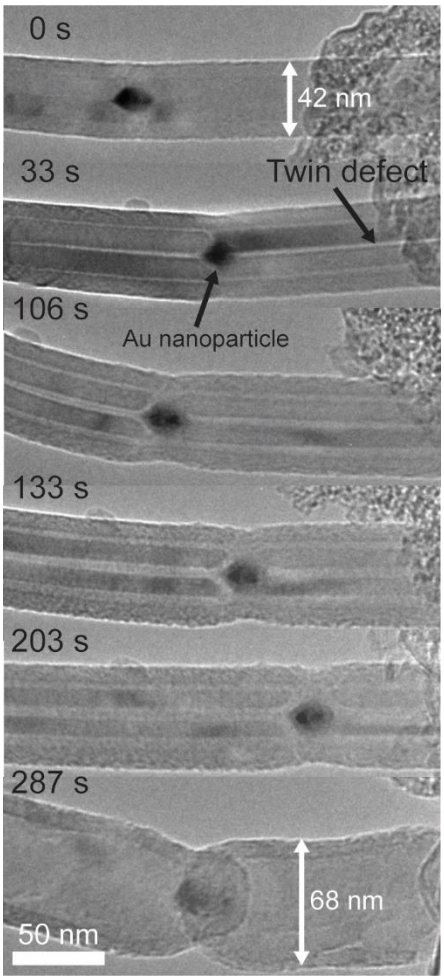

Figure C.4 TEM images of a Si nanowire with a SiO_x shell and a twin defect lithiating. Lithiation proceeds both along the interface between the SiO_x shell and the nanowire as well as along the twin interface. The nanowire breaks into two at the gold (Au) nanoparticle defect in the center of the nanowire after 287 s. The nanowire lithiates fully and does not retain a crystalline core.

C.2 SUPPORTING VIDEOS

LithiationVideo_1.mp4: Video of in situ TEM experiment showing a nanowire with an intact SiO_x shell undergoing two cycles of lithiation and delithiation

PoreVideo_2.mp4: Video of in situ TEM experiment showing a nanowire undergoing delithiation and the pore formation in the wire

BurstWireVideo_3.mp4: Video of in situ TEM experiment showing a nanowire that bursts upon lithiation

BurstWireVideo_4.mp4: Video of in situ TEM experiment showing a nanowire that bursts upon lithiation

BurstWiresPoresVideos_5.mp4: Video of in situ TEM experiment showing a nanowire that bursts at a single point upon lithiation and then forms pores upon delithiation

Appendix D[***]

D.1 Supporting Figures

TEM images of LFP. Figure D.1 shows TEM images of the c-LFP particles, that are several hundred nanometers in diameter are aggregates of nanosized particles.

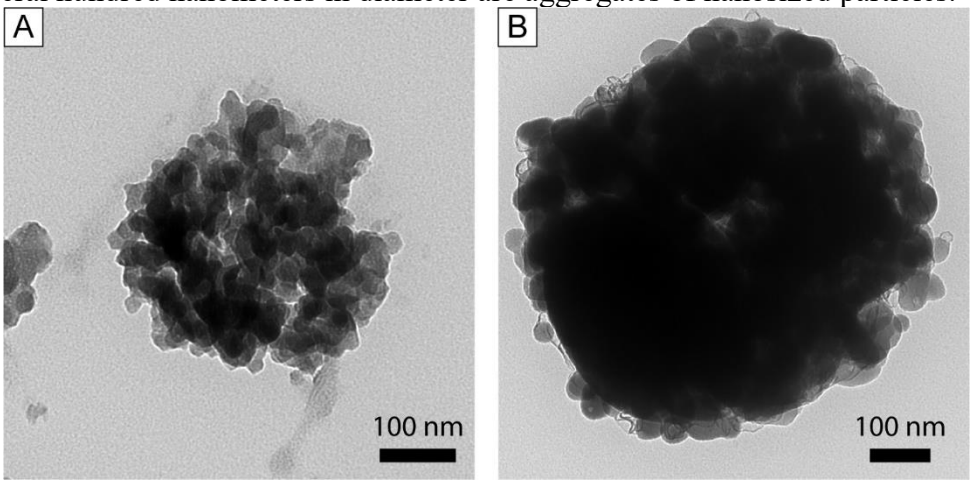

Figure D.1. TEM images of the c-LFP sample. The micron sized particles are made up of nanosized LFP

[***] The work contained in this chapter is the subject of a scholarly article that is currently in preparation. Authors on this work include Emily R. Adkins, Taizhi Jiang, Andrew L. Heilman, Sheng-Heng Chung, Jieun Hwang, Jaehoon Kim, Arumugam Manthiram, and Brian A. Korgel. Emily Adkins was responsible for planning the research, synthesizing Si nanowire materials, performing battery experiments using materials provided by collaborators, with some help from Drew Heilman, analyzing the battery data, researching and writing the completed document.

Additional SiNW half cell battery data. Figure D.2 shows a SiNW electrode tested in a half cell with carbonate electrolyte at an applied current density of 250 mA/g (C/10). The SiNW anode exhibited relatively stable performance, with a capacity at 50 cycles of 2499 mAh/g and a high Coulombic efficiency, over 97%. However, the lithiation plateau moves to a lower potential between cycles 2 – 50 indicating a greater over potential is needed to initiate lithiation.

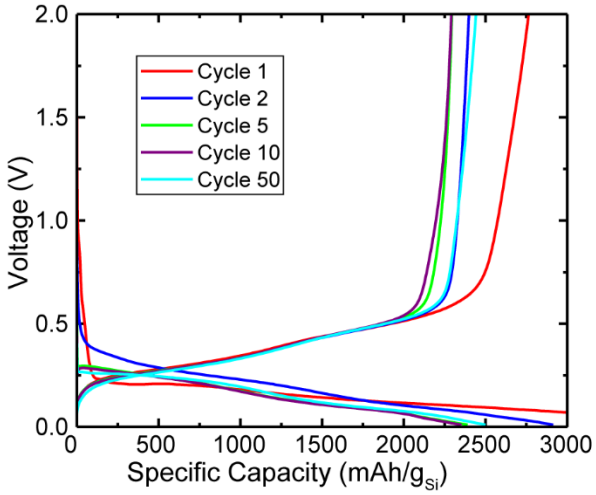

Figure D.2 Voltage profiles for SiNW anode in a half cell battery using carbonate electrolyte corresponding with the battery shown in Figure 5.4a. The battery was tested at an applied current density of 250 mA/g.

Additional SiNW contact prelithiation data. Figure D.3 shows the extent of SiNW lithiation as a function of the time the electrode is prelithiated in contact with Li foil in the presence of both glyme and carbonate electrolytes. Lithiation percentage was found by subtracting the first cycle lithiation capacity from the delithiation capacity divided by the delithiation capacity. Even at only 15 minutes of prelithiation the anodes were over 60% lithiated, though there was a large degree of variability at each time.

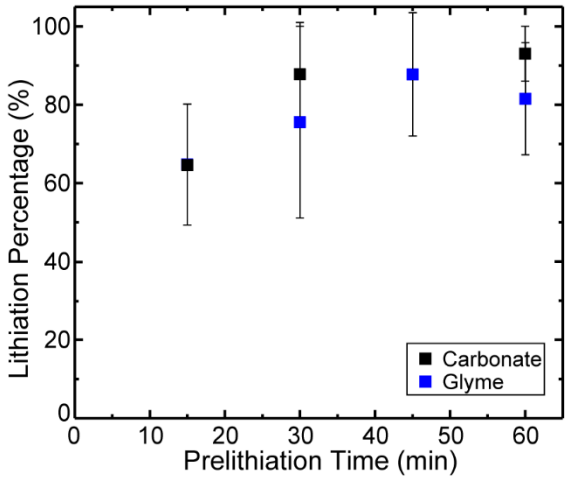

Figure D.3 SiNW anodes were prelithiated in contact with Li for various times for each electrolyte.

Anode-to-cathode capacity ratio. Figure D.4 shows the impact of anode-to-cathode capacity ratio for (a,c) SiNW-LFP and (b,d) SiNW-S full cells that were (a) not prelithiated, (b) prelithiated contact with Li foil or (c,d) on a battery tester. Figure D.4a shows the battery results for SiNW-LFP full cells for a variety of different anode-to-cathode ratios. The SiNWs were not prelithiated for these batteries. All batteries showed a high degree of fade and low capacity.

Figure D.4b shows the battery results for SiNW-S full cells for a variety of different anode-to-cathode capacity ratios. The SiNW anodes for these full cells were held in contact with Li foil for 30 minutes prior to full cell assembly. While the batteries did cycle stably after the first 20 cycles, they exhibited low capacity, regardless of the anode-to-cathode capacity ratio.

Figure D.4c shows the battery results for SiNW-LFP full cells prelithiated on a battery tester to 100 mV for a variety of different anode-to-cathode ratios. The full cell with a lower ratio of 1.21 performed better than the 1.87 ratio full cell. The higher ratio full cell had a Coulombic efficiency of 110% for all cycles after the first.

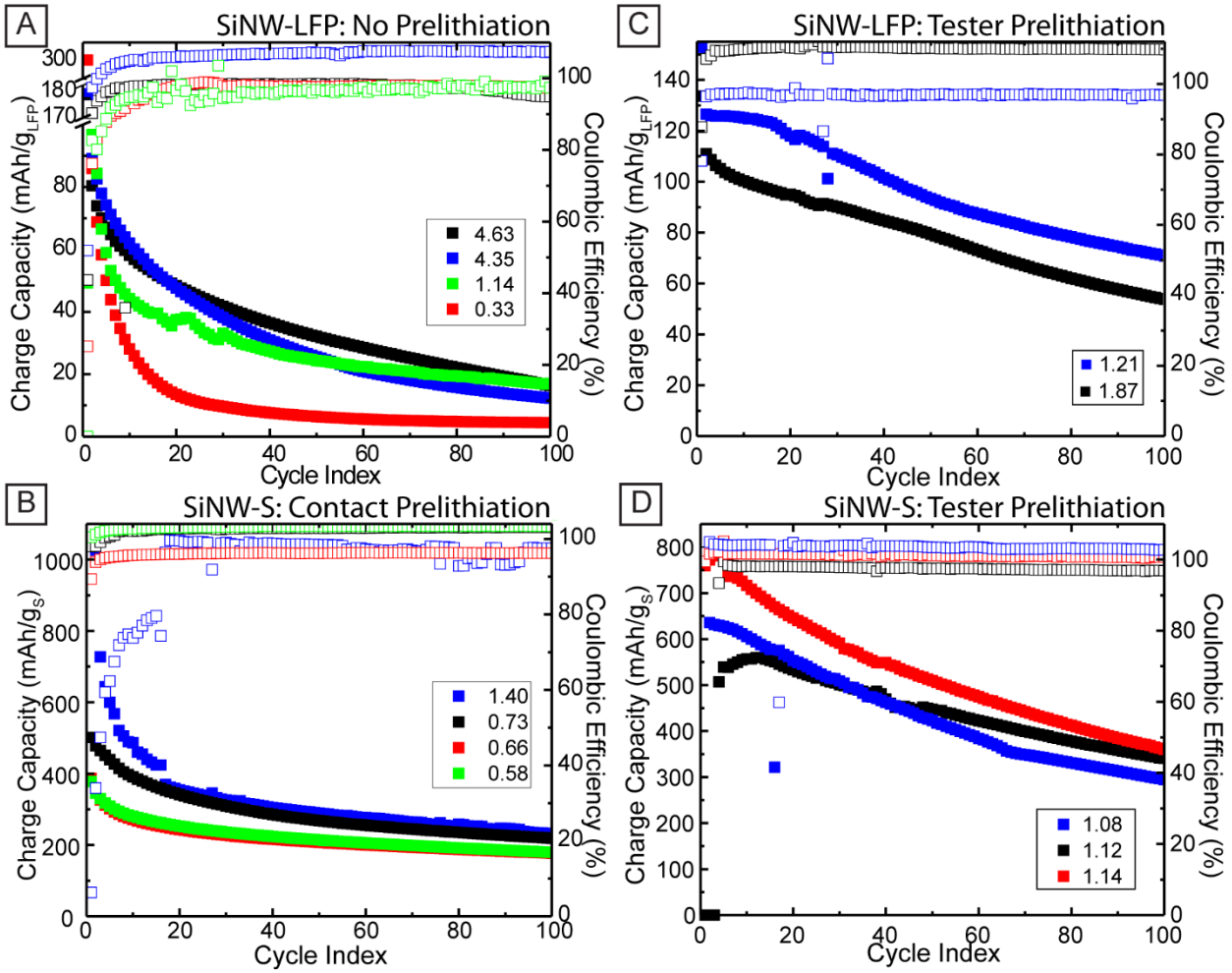

Figure D.4 Charge capacity (■) and Coulombic efficiency (□) of (a) SiNW-LFP full cells not prelithiated for several anode-to-cathode capacity ratios. Cycled at an applied current density of 17 mA/g_{LFP}. (b) SiNW-S full cells prelithiated in contact with Li foil for 30 minutes prior to full cell assembly for several anode-to-cathode capacity ratios. The batteries were cycled at an applied current density of 100 mA/g_S. (c) SiNW-LF full cells prelithiated on a battery tester for two anode-to-cathode capacity ratios. Cycled at an applied current density of 17 mA/g_{LFP}. (d) SiNW-S full cells prelithiated on a battery tester to 10 mV for several anode-to-cathode capacity ratios. The batteries were cycled at an applied current density of 100 mA/g_S.

XPS characterization of cycled battery electrodes. Figure D.5 shows the high resolution elemental XPS spectra for three electrodes after extended cycling: a SiNW-S anode, a Li metal anode from a S half cell, and a SiNW anode from a half cell. Deconvolutions for the C 1s and S 2p orbitals are shown. In analyzing the spectra, three constraints were applied: the peak spacing (1.16 eV between S $2p_{3/2}$ and S $2p_{1/2}$) peaks, the peak intensity ratio (0.511), and equal full width half max.[1]

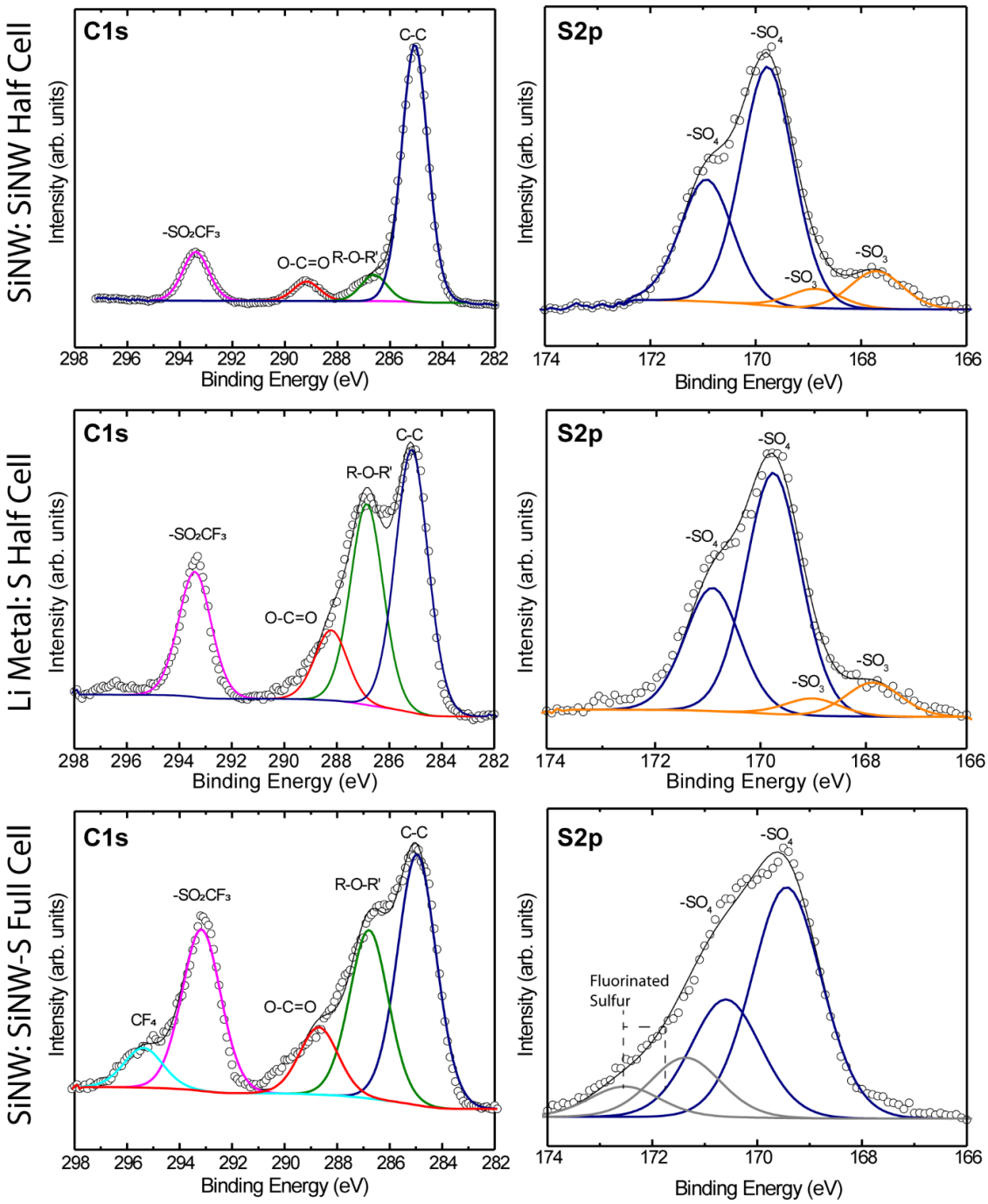

Figure D.5 High resolution elemental XPS spectra for three electrodes after extended cycling: a SiNW-S anode, a Li metal anode from a S half cell, and a SiNW anode from a half cell. Deconvolutions for the C 1s and S 2p orbitals are shown.

XPS S 2p results from the SiNW-S full cell. Figures D.6 and D.7 show the XPS analysis of the S 2p region of the SiNW anode and the S cathode that cycled in a SiNW-S full cell, and the Li metal anode from a S half cell, and a SiNW anode from a half cell.

Figure D.6 shows the XPS survey spectrum of three electrodes zoomed in to the S 2p region: a SiNW-S anode, a Li metal anode from a S half cell, and a SiNW anode from a half cell. Polysulfides would be found between 167-162 eV, but there are none present. It appears the interlayer was successful at preventing Li polysulfides formed during cycling from migrating to the anode in all three cells.

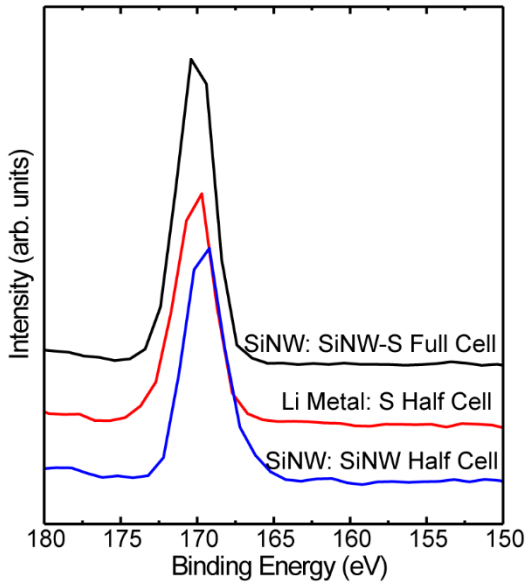

Figure D.6 XPS survey spectrum of three electrodes zoomed in to the S 2p region: a SiNW-S anode, a Li metal anode from a S half cell, and a SiNW anode from a half cell. Polysulfides would be found between 167-162 eV, but there are none present. It appears the interlayer was successful at preventing Li polysulfides formed during cycling from migrating to the anode in all three cells.

Figure D.7 shows the high resolution XPS elemental scan of the S 2p region of the S cathode from a SiNW-S full cell, after extended cycling. Sulfur oxides and -S-S- (bridging sulfur) are present. The sulfur oxides are predominately decomposition products of the LiTFSI salt.

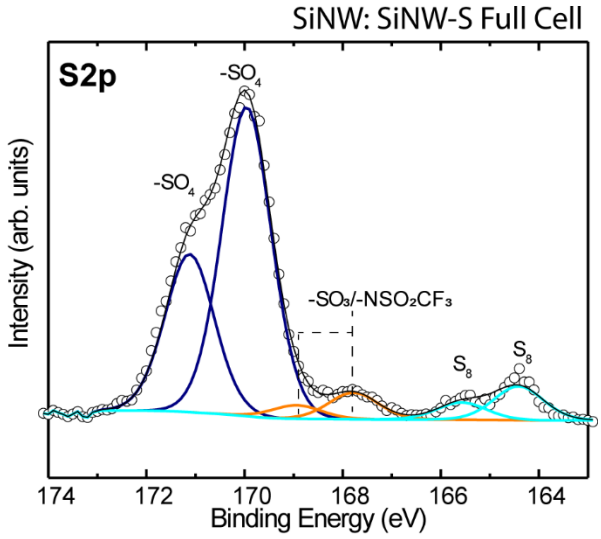

Figure D.7 High resolution XPS elemental scan of the S 2p region of the S cathode from a SiNW-S full cell, after extended cycling, showing sulfur oxides and bridging sulfur.

D.2 REFERENCES

(1) Su, Y.-S.; Fu, Y.; Cochell, T.; Manthiram, A. A Strategic Approach to Recharging Lithium-Sulphur Batteries for Long Cycle Life. *Nat. Commun.* **2013**, *4*, 2985.

References

Abel, P. R.; Lin, Y.-M.; de Souza, T.; Chou, C.-Y.; Gupta, A.; Goodenough, J. B.; Hwang, G. S.; Heller, A.; Mullins, C. B. Nanocolumnar Germanium Thin Films as a High-Rate Sodium-Ion Battery Anode Material. J. Phys. Chem. C 2013, 117 (37), 18885–18890.

Abouimrane, A.; Dambournet, D.; Chapman, K. W.; Chupas, P. J.; Weng, W.; Amine, K. A New Class of Lithium and Sodium Rechargeable Batteries Based on Selenium and Selenium–Sulfur as a Positive Electrode. J. Am. Chem. Soc. 2012, 134 (10), 4505–4508.

Agostini, M.; Hassoun, J.; Liu, J.; Jeong, M.; Nara, H.; Momma, T.; Osaka, T.; Sun, Y.-K.; Scrosati, B. A Lithium-Ion Sulfur Battery Based on a Carbon-Coated Lithium-Sulfide Cathode and an Electrodeposited Silicon-Based Anode. ACS Appl. Mater. Interfaces 2014, 6 (14), 10924–10928.

Andersson, A. M.; Herstedt, M.; Bishop, A. G.; Edström, K. The Influence of Lithium Salt on the Interfacial Reactions Controlling the Thermal Stability of Graphite Anodes. Electrochimica Acta 2002, 47 (12), 1885–1898.

Armand, M.; Tarascon, J.-M. Building Better Batteries. Nature 2008, 451 (7179), 652–657.

Arthur, T. S.; Singh, N.; Matsui, M. Electrodeposited Bi, Sb and Bi1-XSbx Alloys as Anodes for Mg-Ion Batteries. Electrochem. Commun. 2012, 16 (1), 103–106.

Aside from lithium (Li) metal, Si has the highest storage capacity of any anode material, 3579 mAh/g, more than ten times that of graphite.

Aurbach, D.; Ein-Eli, Y.; Markovsky, B.; Zaban, A.; Luski, S.; Carmeli, Y.; Yamin, H. The Study of Electrolyte Solutions Based on Ethylene and Diethyl Carbonates for Rechargeable Li Batteries II . Graphite Electrodes. J. Electrochem. Soc. 1995, 142 (9), 2882–2890.

Aurbach, D.; Pollak, E.; Elazari, R.; Salitra, G.; Kelley, C. S.; Affinito, J. On the Surface Chemical Aspects of Very High Energy Density, Rechargeable Li–Sulfur Batteries. J. Electrochem. Soc. 2009, 156 (8), A694–A702.

Aurbach, D.; Weissman, I.; Schechter, A.; Cohen, H. X-Ray Photoelectron Spectroscopy Studies of Lithium Surfaces Prepared in Several Important Electrolyte Solutions. A Comparison with Previous Studies by Fourier Transform Infrared Spectroscopy. Langmuir 1996, 12 (16), 3991–4007.

Baggetto, L.; Keum, J. K.; Browning, J. F.; Veith, G. M. Germanium as Negative Electrode Material for Sodium-Ion Batteries. Electrochem. Commun. 2013, 34, 41–44.

Beaulieu, L. Y.; Eberman, K. W.; Turner, R. L.; Krause, L. J.; Dahn, J. R. Colossal Reversible Volume Changes in Lithium Alloys. Electrochem. Solid-State Lett. 2001, 4 (9), A137–A140.

Blomgren, G. E. The Development and Future of Lithium Ion Batteries. J. Electrochem. Soc. 2017, 164 (1), A5019–A5025.

Bogart, T. D. Silicon Nanowires: Synthesis and Use as Lithium-Ion Battery Anodes. Thesis, 2014.

Bogart, T. D.; Chockla, A. M.; Korgel, B. A. High Capacity Lithium Ion Battery Anodes of Silicon and Germanium. Curr. Opin. Chem. Eng. 2013, 2 (3), 286–293.

Bogart, T. D.; Lu, X.; Gu, M.; Wang, C.; Korgel, B. A. Enhancing the Lithiation Rate of Silicon Nanowires by the Inclusion of Tin. RSC Adv. 2014, 4 (79), 42022–42028.

Bogart, T. D.; Lu, X.; Korgel, B. A. Precision Synthesis of Silicon Nanowires with Crystalline Core and Amorphous Shell. Dalton Trans. 2013, 42 (35), 12675–12680.

Bogart, T. D.; Oka, D.; Lu, X.; Gu, M.; Wang, C.; Korgel, B. A. Lithium Ion Battery Peformance of Silicon Nanowires with Carbon Skin. ACS Nano 2014, 8 (1), 915–922.

Bridel, J.-S.; Azaïs, T.; Morcrette, M.; Tarascon, J.-M.; Larcher, D. Key Parameters Governing the Reversibility of Si/Carbon/CMC Electrodes for Li-Ion Batteries. Chem. Mater. 2010, 22 (3), 1229–1241.

Brückner, J.; Thieme, S.; Böttger-Hiller, F.; Bauer, I.; Grossmann, H. T.; Strubel, P.; Althues, H.; Spange, S.; Kaskel, S. Carbon-Based Anodes for Lithium Sulfur Full Cells with High Cycle Stability. Adv. Funct. Mater. 2014, 24 (9), 1284–1289.

Brust, M.; Walker, M.; Bethell, D.; Schiffrin, D. J.; Whyman, R. Synthesis of Thiol-Derivatised Gold Nanoparticles in a Two-Phase Liquid–Liquid System. J. Chem. Soc., Chem. Commun. 1994, No. 7, 801–802.

Chan, C. K.; Patel, R. N.; O'Connell, M. J.; Korgel, B. A.; Cui, Y. Solution-Grown Silicon Nanowires for Lithium-Ion Battery Anodes. ACS Nano 2010, 4 (3), 1443–1450.

Chan, C. K.; Peng, H.; Liu, G.; McIlwrath, K.; Zhang, X. F.; Huggins, R. A.; Cui, Y. High-Performance Lithium Battery Anodes Using Silicon Nanowires. Nat. Nanotechnol. 2008, 3 (1), 31–35.

Chan, C. K.; Ruffo, R.; Hong, S. S.; Cui, Y. Surface Chemistry and Morphology of the Solid Electrolyte Interphase on Silicon Nanowire Lithium-Ion Battery Anodes. J. Power Sources 2009, 189 (2), 1132–1140.

Cheon, S.-E.; Ko, K.-S.; Cho, J.-H.; Kim, S.-W.; Chin, E.-Y.; Kim, H.-T. Rechargeable Lithium Sulfur Battery I. Structural Change of Sulfur Cathode During Discharge and Charge. J. Electrochem. Soc. 2003, 150 (6), A796–A799.

Chernova, N. A.; Roppolo, M.; Dillon, A. C.; Whittingham, M. S. Layered Vanadium and Molybdenum Oxides: Batteries and Electrochromics. J. Mater. Chem. 2009, 19 (17), 2526–2552.

Cho, G. B.; Song, M. G.; Bae, S. H.; Kim, J. K.; Choi, Y. J.; Ahn, H. J.; Ahn, J. H.; Cho, K. K.; Kim, K. W. Surface-Modified Si Thin Film Electrode for Li Ion Batteries (LiFePO4/Si) by Cluster-Structured Ni under Layer. J. Power Sources 2009, 189 (1), 738–742.

Chockla, A. M. Solution Grown Silicon and Germanium Nanostructures: Characterization and Application as Lithium Ion Battery Anode Materials; University of Texas: Austin, Tex., 2012.

Chockla, A. M.; Harris, J. T.; Akhavan, V. A.; Bogart, T. D.; Holmberg, V. C.; Steinhagen, C.; Mullins, C. B.; Stevenson, K. J.; Korgel, B. A. Silicon Nanowire Fabric as a Lithium Ion Battery Electrode Material. J. Am. Chem. Soc. 2011, 133 (51), 20914–20921.

Chockla, A. M.; Klavetter, K. C.; Mullins, C. B.; Korgel, B. A. Solution-Grown Germanium Nanowire Anodes for Lithium-Ion Batteries. ACS Appl. Mater. Interfaces 2012, 4 (9), 4658–4664.

Chockla, A. M.; Klavetter, K. C.; Mullins, C. B.; Korgel, B. A. Tin-Seeded Silicon Nanowires for High Capacity Li-Ion Batteries. Chem. Mater. 2012, 24 (19), 3738–3745.

Choi, J.-W.; Kim, J.-K.; Cheruvally, G.; Ahn, J.-H.; Ahn, H.-J.; Kim, K.-W. Rechargeable Lithium/Sulfur Battery with Suitable Mixed Liquid Electrolytes. Electrochimica Acta 2007, 52 (5), 2075–2082.

Chung, S.-H.; Chang, C.-H.; Manthiram, A. Hierarchical Sulfur Electrodes as a Testing Platform for Understanding the High-Loading Capability of Li-S Batteries. J. Power Sources 2016, 334 (Supplement C), 179–190.

Chung, S.-H.; Manthiram, A. A Hierarchical Carbonized Paper with Controllable Thickness as a Modulable Interlayer System for High Performance Li–S Batteries. Chem. Commun. 2014, 50 (32), 4184–4187.

Chung, S.-Y.; Bloking, J. T.; Chiang, Y.-M. Electronically Conductive Phospho-Olivines as Lithium Storage Electrodes. Nat. Mater. 2002, 1 (2), 123–128.

Coates, J. Interpretation of Infrared Spectra: A Practical Approach. Encyclopedia of Analytical Chemistry; Meyers, R. A., Ed.; Wiley: Chichester, U.K., 2000; pp 10815–10837.

Cui, L.-F.; Ruffo, R.; Chan, C. K.; Peng, H.; Cui, Y. Crystalline-Amorphous Core-Shell Silicon Nanowires for High Capacity and High Current Battery Electrodes. Nano Lett. 2009, 9 (1), 491–495.

Cui, Y.; Lieber, C. M. Functional Nanoscale Electronic Devices Assembled Using Silicon Nanowire Building Blocks. Science 2001, 291 (5505), 851–853.

Cui, Y.; Wei, Q.; Park, H.; Lieber, C. M. Nanowire Nanosensors for Highly Sensitive and Selective Detection of Biological and Chemical Species. Science 2001, 293 (5533), 1289–1292.

Dedryvère, R.; Laruelle, S.; Grugeon, S.; Gireaud, L.; Tarascon, J.-M.; Gonbeau, D. XPS Identification of the Organic and Inorganic Components of the Electrode/Electrolyte Interface Formed on a Metallic Cathode. J. Electrochem. Soc. 2005, 152 (4), A689–A696.

Diao, Y.; Xie, K.; Xiong, S.; Hong, X. Insights into Li-S Battery Cathode Capacity Fading Mechanisms: Irreversible Oxidation of Active Mass during Cycling. J. Electrochem. Soc. 2012, 159 (11), A1816–A1821.

EIA - Annual Energy Outlook 2017 https://www.eia.gov/outlooks/aeo/ (accessed Jan 25, 2018).

Elazari, R.; Salitra, G.; Gershinsky, G.; Garsuch, A.; Panchenko, A.; Aurbach, D. Rechargeable Lithiated Silicon–sulfur (SLS) Battery Prototypes. Electrochem. Commun. 2012, 14 (1), 21–24.

Eom, K.; Joshi, T.; Bordes, A.; Do, I.; Fuller, T. F. The Design of a Li-Ion Full Cell Battery Using a Nano Silicon and Nano Multi-Layer Graphene Composite Anode. J. Power Sources 2014, 249, 118–124.

Etacheri, V.; Geiger, U.; Gofer, Y.; Roberts, G. A.; Stefan, I. C.; Fasching, R.; Aurbach, D. Exceptional Electrochemical Performance of Si-Nanowires in 1,3-Dioxolane Solutions: A Surface Chemical Investigation. Langmuir 2012, 28 (14), 6175–6184.

Etacheri, V.; Marom, R.; Elazari, R.; Salitra, G.; Aurbach, D. Challenges in the Development of Advanced Li-Ion Batteries: A Review. Energy Environ. Sci. 2011, 4 (9), 3243–3262.

Forney, M. W.; Ganter, M. J.; Staub, J. W.; Ridgley, R. D.; Landi, B. J. Prelithiation of Silicon–Carbon Nanotube Anodes for Lithium Ion Batteries by Stabilized Lithium Metal Powder (SLMP). Nano Lett. 2013, 13 (9), 4158–4163.

Fu, Y.; Su, Y.-S.; Manthiram, A. Li2S-Carbon Sandwiched Electrodes with Superior Performance for Lithium-Sulfur Batteries. Adv. Energy Mater. 2014, 4 (1), n/a-n/a.

Gao, B.; Sinha, S.; Fleming, L.; Zhou, O. Alloy Formation in Nanostructured Silicon. Adv. Mater. 2001, 13 (11), 816–819.

Gao, J.; Lowe, M. A.; Kiya, Y.; Abruña, H. D. Effects of Liquid Electrolytes on the Charge–Discharge Performance of Rechargeable Lithium/Sulfur Batteries: Electrochemical and in-Situ X-Ray Absorption Spectroscopic Studies. J. Phys. Chem. C 2011, 115 (50), 25132–25137.

Goodenough, J. B.; Kim, Y. Challenges for Rechargeable Li Batteries. Chem. Mater. 2010, 22 (3), 587–603.

Graetz, J.; Ahn, C. C.; Yazami, R.; Fultz, B. Nanocrystalline and Thin Film Germanium Electrodes with High Lithium Capacity and High Rate Capabilities. J. Electrochem. Soc. 2004, 151 (5), A698–A702.

Gregory, T. D.; Hoffman, R. J.; Winterton, R. C. Nonaqueous Electrochemistry of Magnesium Applications to Energy Storage. J. Electrochem. Soc. 1990, 137 (3), 775–780.

Gu, M.; Parent, L. R.; Mehdi, B. L.; Unocic, R. R.; McDowell, M. T.; Sacci, R. L.; Xu, W.; Connell, J. G.; Xu, P.; Abellan, P.; et al. Demonstration of an Electrochemical Liquid Cell for Operando Transmission Electron Microscopy Observation of the Lithiation/Delithiation Behavior of Si Nanowire Battery Anodes. Nano Lett. 2013, 13 (12), 6106–6112.

Gu, M.; Wang, Z.; Connell, J. G.; Perea, D. E.; Lauhon, L. J.; Gao, F.; Wang, C. Electronic Origin for the Phase Transition from Amorphous LixSi to Crystalline Li15Si4. ACS Nano 2013, 7 (7), 6303–6309.

Hagen, M.; Quiroga-González, E.; Dörfler, S.; Fahrer, G.; Tübke, J.; Hoffmann, M. J.; Althues, H.; Speck, R.; Krampfert, M.; Kaskel, S.; et al. Studies on Preventing Li Dendrite Formation in Li–S Batteries by Using Pre-Lithiated Si Microwire Anodes. J. Power Sources 2014, 248, 1058–1066.

Han, Y.; Lin, N.; Xu, T.; Li, T.; Tian, J.; Zhu, Y.; Qian, Y. An Amorphous Si Material with a Sponge-like Structure as an Anode for Li-Ion and Na-Ion Batteries. Nanoscale 2018, 10 (7), 3153–3158.

Hanrath, T.; Korgel, B. A. Chemical Surface Passivation of Ge Nanowires. J. Am. Chem. Soc. 2004, 126 (47), 15466–15472.

Hanrath, T.; Korgel, B. A. Nucleation and Growth of Germanium Nanowires Seeded by Organic Monolayer-Coated Gold Nanocrystals. J. Am. Chem. Soc. 2002, 124 (7), 1424–1429.

Hassoun, J.; Kim, J.; Lee, D.-J.; Jung, H.-G.; Lee, S.-M.; Sun, Y.-K.; Scrosati, B. A Contribution to the Progress of High Energy Batteries: A Metal-Free, Lithium-Ion, Silicon–sulfur Battery. J. Power Sources 2012, 202, 308–313.

Hatchard, T. D.; Dahn, J. R. In Situ XRD and Electrochemical Study of the Reaction of Lithium with Amorphous Silicon. J. Electrochem. Soc. 2004, 151 (6), A838–A842.

He, Y.; Piper, D. M.; Gu, M.; Travis, J. J.; George, S. M.; Lee, S.-H.; Genc, A.; Pullan, L.; Liu, J.; Mao, S. X.; et al. In Situ Transmission Electron Microscopy Probing of Native Oxide and Artificial Layers on Silicon Nanoparticles for Lithium Ion Batteries. ACS Nano 2014, 8 (11), 11816–11823.

Heitsch, A. T.; Akhavan, V. A.; Korgel, B. A. Rapid SFLS Synthesis of Si Nanowires Using Trisilane with In Situ Alkyl-Amine Passivation. Chem. Mater. 2011, 23 (11), 2697–2699.

Holmberg, V. C.; Bogart, T. D.; Chockla, A. M.; Hessel, C. M.; Korgel, B. A. Optical Properties of Silicon and Germanium Nanowire Fabric. J. Phys. Chem. C 2012, 116 (42), 22486–22491.

Holmberg, V. C.; Korgel, B. A. Corrosion Resistance of Thiol- and Alkene-Passivated Germanium Nanowires. Chem. Mater. 2010, 22 (12), 3698–3703.

Holmberg, V. C.; Rasch, M. R.; Korgel, B. A. PEGylation of Carboxylic Acid-Functionalized Germanium Nanowires. Langmuir 2010, 26 (17), 14241–14246.

Holmes, J. D.; Johnston, K. P.; Doty, R. C.; Korgel, B. A. Control of Thickness and Orientation of Solution-Grown Silicon Nanowires. Science 2000, 287 (5457), 1471–1473.

Hwang, J.; Kong, K. C.; Chang, W.; Jo, E.; Nam, K.; Kim, J. New Liquid Carbon Dioxide Based Strategy for High Energy/Power Density LiFePO4. Nano Energy 2017, 36, 398–410.

Jangid, M. K.; Lakhnot, A. S.; Vemulapally, A.; Sonia, F. J.; Sinha, S.; Dusane, R. O.; Mukhopadhyay, A. Crystalline Core/Amorphous Shell Structured Silicon Nanowires Offer Size and Structure Dependent Reversible Na-Storage. J. Mater. Chem. A 2018, 6 (8), 3422–3434.

Jarvis, C. R.; Lain, M. J.; Yakovleva, M. V.; Gao, Y. A Prelithiated Carbon Anode for Lithium-Ion Battery Applications. J. Power Sources 2006, 162 (2), 800–802.

Jaumann, T.; Balach, J.; Klose, M.; Oswald, S.; Eckert, J.; Giebeler, L. Role of 1,3-Dioxolane and LiNO3 Addition on the Long Term Stability of Nanostructured Silicon/Carbon Anodes for Rechargeable Lithium Batteries. J. Electrochem. Soc. 2016, 163 (3), A557–A564.

John Muldoon, C. B. B. Quest for Nonaqueous Multivalent Secondary Batteries: Magnesium and Beyond. Chem. Rev. 2014.

Kim, H. J.; Choi, S.; Lee, S. J.; Seo, M. W.; Lee, J. G.; Deniz, E.; Lee, Y. J.; Kim, E. K.; Choi, J. W. Controlled Prelithiation of Silicon Monoxide for High Performance Lithium-Ion Rechargeable Full Cells. Nano Lett. 2016, 16 (1), 282–288.

Kim, J.-K.; Scheers, J.; Ryu, H.-S.; Ahn, J.-H.; Nam, T.-H.; Kim, K.-W.; Ahn, H.-J.; Cho, G.-B.; Jacobsson, P. A Layer-Built Rechargeable Lithium Ribbon-Type Battery for High Energy Density Textile Battery Applications. J. Mater. Chem. A 2014, 2 (6), 1774–1780.

Kim, S. J.; Kargar, A.; Wang, D.; Graham, G. W.; Pan, X. Lithiation of Rutile TiO2-Coated Si NWs Observed by in Situ TEM. Chem. Mater. 2015, 27 (20), 6929–6933.

Klavetter, K. C.; Wood, S. M.; Lin, Y.-M.; Snider, J. L.; Davy, N. C.; Chockla, A. M.; Romanovicz, D. K.; Korgel, B. A.; Lee, J.-W.; Heller, A.; et al. A High-Rate Germanium-Particle Slurry Cast Li-Ion Anode with High Coulombic Efficiency and Long Cycle Life. J. Power Sources 2013, 238, 123–136.

Kohandehghan, A.; Cui, K.; Kupsta, M.; Ding, J.; Memarzadeh Lotfabad, E.; Kalisvaart, W. P.; Mitlin, D. Activation with Li Enables Facile Sodium Storage in Germanium. Nano Lett. 2014, 14 (10), 5873–5882.

Korgel, B. A. Nanomaterials Developments for Higher-Performance Lithium Ion Batteries. J. Phys. Chem. Lett. 2014, 5 (4), 749–750.

Kovalenko, I.; Zdyrko, B.; Magasinski, A.; Hertzberg, B.; Milicev, Z.; Burtovyy, R.; Luzinov, I.; Yushin, G. A Major Constituent of Brown Algae for Use in High-Capacity Li-Ion Batteries. Science 2011, 334 (6052), 75–79.

Kovnir, K. A.; Shevelkov, A. V. Semiconducting Clathrates: Synthesis, Structure and Properties. Russ. Chem. Rev. 2004, 73 (9), 923.

Krishna, L.; Koh, C. A. Inorganic and Methane Clathrates: Versatility of Guest–host Compounds for Energy Harvesting. MRS Energy Amp Sustain. 2015, 2.

L. Baranowski, L.; Krishna, L.; D. Martinez, A.; Raharjo, T.; Stevanovic, V.; C. Tamboli, A.; S. Toberer, E. Synthesis and Optical Band Gaps of Alloyed Si–Ge Type II Clathrates. J. Mater. Chem. C 2014, 2 (17), 3231–3237.

Langer, T.; Dupke, S.; Trill, H.; Passerini, S.; Eckert, H.; Pöttgen, R.; Winter, M. Electrochemical Lithiation of Silicon Clathrate-II. J. Electrochem. Soc. 2012, 159 (8), A1318–A1322.

Lazzari, M.; Scrosati, B. A Cyclable Lithium Organic Electrolyte Cell Based on Two Intercalation Electrodes. J. Electrochem. Soc. 1980, 127 (3), 773–774.

Lee, D. C.; Hanrath, T.; Korgel, B. A. The Role of Precursor-Decomposition Kinetics in Silicon-Nanowire Synthesis in Organic Solvents. Angew. Chem. Int. Ed. 2005, 44 (23), 3573–3577.

Lee, J. T.; Kim, H.; Nitta, N.; Eom, K.; Lee, D.-C.; Wu, F.; Lin, H.-T.; Zdyrko, B.; Cho, W. I.; Yushin, G. Stabilization of Selenium Cathodes via in Situ Formation of Protective Solid Electrolyte Layer. J. Mater. Chem. A 2014, 2 (44), 18898–18905.

Lee, S.-K.; Oh, S.-M.; Park, E.; Scrosati, B.; Hassoun, J.; Park, M.-S.; Kim, Y.-J.; Kim, H.; Belharouak, I.; Sun, Y.-K. Highly Cyclable Lithium–Sulfur Batteries with a Dual-Type Sulfur Cathode and a Lithiated Si/SiOx Nanosphere Anode. Nano Lett. 2015, 15 (5), 2863–2868.

Leroy, S.; Blanchard, F.; Dedryvère, R.; Martinez, H.; Carré, B.; Lemordant, D.; Gonbeau, D. Surface Film Formation on a Graphite Electrode in Li-Ion Batteries: AFM and XPS Study. Surf. Interface Anal. 2005, 37 (10), 773–781.

Li, H.; Richter, G.; Maier, J. Reversible Formation and Decomposition of LiF Clusters Using Transition Metal Fluorides as Precursors and Their Application in Rechargeable Li Batteries. Adv. Mater. 2003, 15 (9), 736–739.

Li, J.; Dahn, J. R. An In Situ X-Ray Diffraction Study of the Reaction of Li with Crystalline Si. J. Electrochem. Soc. 2007, 154 (3), A156–A161.

Li, W.; Hwang, J.; Chang, W.; Setiadi, H.; Chung, K. Y.; Kim, J. Ultrathin and Uniform Carbon-Layer-Coated Hierarchically Porous LiFePO4 Microspheres and Their Electrochemical Performance. J. Supercrit. Fluids 2016, 116 (Supplement C), 164–171.

Li, Y.; Raghavan, R.; Wagner, N. A.; Davidowski, S. K.; Baggetto, L.; Zhao, R.; Cheng, Q.; Yarger, J. L.; Veith, G. M.; Ellis-Terrell, C.; et al. Type I Clathrates as Novel Silicon Anodes: An Electrochemical and Structural Investigation. Adv. Sci. 2015, 2 (6), n/a-n/a.

Lithium; Mineral Commodity Summaries 2015; U.S. Geological Survey: Reston, VA, 2015.

Liu, N.; Hu, L.; McDowell, M. T.; Jackson, A.; Cui, Y. Prelithiated Silicon Nanowires as an Anode for Lithium Ion Batteries. ACS Nano 2011, 5 (8), 6487–6493.

Liu, N.; Wu, H.; McDowell, M. T.; Yao, Y.; Wang, C.; Cui, Y. A Yolk-Shell Design for Stabilized and Scalable Li-Ion Battery Alloy Anodes. Nano Lett. 2012, 12 (6), 3315–3321.

Liu, X. H.; Fan, F.; Yang, H.; Zhang, S.; Huang, J. Y.; Zhu, T. Self-Limiting Lithiation in Silicon Nanowires. ACS Nano 2013, 7 (2), 1495–1503.

Liu, X. H.; Huang, J. Y. In Situ TEM Electrochemistry of Anode Materials in Lithium Ion Batteries. Energy Environ. Sci. 2011, 4 (10), 3844–3860.

Liu, X. H.; Huang, S.; Picraux, S. T.; Li, J.; Zhu, T.; Huang, J. Y. Reversible Nanopore Formation in Ge Nanowires during Lithiation–Delithiation Cycling: An In Situ Transmission Electron Microscopy Study. Nano Lett. 2011, 11 (9), 3991–3997.

Liu, X. H.; Wang, J. W.; Huang, S.; Fan, F.; Huang, X.; Liu, Y.; Krylyuk, S.; Yoo, J.; Dayeh, S. A.; Davydov, A. V.; et al. In Situ Atomic-Scale Imaging of Electrochemical Lithiation in Silicon. Nat. Nanotechnol. 2012, 7 (11), 749–756.

Liu, X. H.; Zhang, L. Q.; Zhong, L.; Liu, Y.; Zheng, H.; Wang, J. W.; Cho, J.-H.; Dayeh, S. A.; Picraux, S. T.; Sullivan, J. P.; et al. Ultrafast Electrochemical Lithiation of Individual Si Nanowire Anodes. Nano Lett. 2011, 11 (6), 2251–2258.

Liu, X. H.; Zheng, H.; Zhong, L.; Huang, S.; Karki, K.; Zhang, L. Q.; Liu, Y.; Kushima, A.; Liang, W. T.; Wang, J. W.; et al. Anisotropic Swelling and Fracture of Silicon Nanowires during Lithiation. Nano Lett. 2011, 11 (8), 3312–3318.

Liu, X. H.; Zhong, L.; Huang, S.; Mao, S. X.; Zhu, T.; Huang, J. Y. Size-Dependent Fracture of Silicon Nanoparticles During Lithiation. ACS Nano 2012, 6 (2), 1522–1531.

Lu, X. Silicon and Germanium Nanostructures: Synthesis and in Situ TEM Study. Thesis, 2015.

Lu, X.; Adkins, E. R.; He, Y.; Zhong, L.; Luo, L.; Mao, S. X.; Wang, C.-M.; Korgel, B. A. Germanium as a Sodium Ion Battery Material: In Situ TEM Reveals Fast Sodiation Kinetics with High Capacity. Chem. Mater. 2016, 28 (4), 1236–1242.

Lu, X.; Bogart, T. D.; Gu, M.; Wang, C.; Korgel, B. A. In Situ TEM Observations of Sn-Containing Silicon Nanowires Undergoing Reversible Pore Formation Due to Fast Lithiation/Delithiation Kinetics. J. Phys. Chem. C 2015, 119 (38), 21889–21895.

Lu, X.; Harris, J. T.; Villarreal, J. E.; Chockla, A. M.; Korgel, B. A. Enhanced Nickel-Seeded Synthesis of Germanium Nanowires. Chem. Mater. 2013, 25 (10), 2172–2177.

Lu, X.; He, Y.; Mao, S. X.; Wang, C.; Korgel, B. A. Size Dependent Pore Formation in Germanium Nanowires Undergoing Reversible Delithiation Observed by In Situ TEM. J. Phys. Chem. C 2016, 120 (50), 28825–28831.

Luo, C.; Xu, Y.; Zhu, Y.; Liu, Y.; Zheng, S.; Liu, Y.; Langrock, A.; Wang, C. Selenium@Mesoporous Carbon Composite with Superior Lithium and Sodium Storage Capacity. ACS Nano 2013, 7 (9), 8003–8010.

Magasinski, A.; Zdyrko, B.; Kovalenko, I.; Hertzberg, B.; Burtovyy, R.; Huebner, C. F.; Fuller, T. F.; Luzinov, I.; Yushin, G. Toward Efficient Binders for Li-Ion Battery Si-Based Anodes: Polyacrylic Acid. ACS Appl. Mater. Interfaces 2010, 2 (11), 3004–3010.

Malyi, O. I.; Tan, T. L.; Manzhos, S. In Search of High Performance Anode Materials for Mg Batteries: Computational Studies of Mg in Ge, Si, and Sn. J. Power Sources 2013, 233, 341–345.

Manthiram, A.; Fu, Y.; Chung, S.-H.; Zu, C.; Su, Y.-S. Rechargeable Lithium–Sulfur Batteries. Chem. Rev. 2014, 114 (23), 11751–11787.

Marks, T.; Trussler, S.; Smith, A. J.; Xiong, D.; Dahn, J. R. A Guide to Li-Ion Coin-Cell Electrode Making for Academic Researchers. J. Electrochem. Soc. 2011, 158 (1), A51–A57.

Martin, L.; Martinez, H.; Ulldemolins, M.; Pecquenard, B.; Le Cras, F. Evolution of the Si Electrode/Electrolyte Interface in Lithium Batteries Characterized by XPS and AFM Techniques: The Influence of Vinylene Carbonate Additive. Solid State Ion. 2012, 215, 36–44.

Martinez, A. D.; Krishna, L.; Baranowski, L. L.; Lusk, M. T.; Toberer, E. S.; Tamboli, A. C. Synthesis of Group IV Clathrates for Photovoltaics. IEEE J. Photovolt. 2013, 3 (4), 1305–1310.

McDowell, M. T.; Lee, S. W.; Harris, J. T.; Korgel, B. A.; Wang, C.; Nix, W. D.; Cui, Y. In Situ TEM of Two-Phase Lithiation of Amorphous Silicon Nanospheres. Nano Lett. 2013, 13 (2), 758–764.

McDowell, M. T.; Lee, S. W.; Nix, W. D.; Cui, Y. 25th Anniversary Article: Understanding the Lithiation of Silicon and Other Alloying Anodes for Lithium-Ion Batteries. Adv. Mater. 2013, 25 (36), 4966–4985.

McDowell, M. T.; Lee, S. W.; Ryu, I.; Wu, H.; Nix, W. D.; Choi, J. W.; Cui, Y. Novel Size and Surface Oxide Effects in Silicon Nanowires as Lithium Battery Anodes. Nano Lett. 2011, 11 (9), 4018–4025.

Meduri, P.; Clark, E.; Kim, J. H.; Dayalan, E.; Sumanasekera, G. U.; Sunkara, M. K. MoO3–x Nanowire Arrays As Stable and High-Capacity Anodes for Lithium Ion Batteries. Nano Lett. 2012, 12 (4), 1784–1788.

Meng, A. C.; Fenrich, C. S.; Braun, M. R.; McVittie, J. P.; Marshall, A. F.; Harris, J. S.; McIntyre, P. C. Core-Shell Germanium/Germanium–Tin Nanowires Exhibiting Room-Temperature Direct- and Indirect-Gap Photoluminescence. Nano Lett. 2016, 16 (12), 7521–7529.

Moreno, N.; Agostini, M.; Caballero, A.; Morales, J.; Hassoun, J. A Long-Life Lithium Ion Sulfur Battery Exploiting High Performance Electrodes. Chem. Commun. 2015, 51 (77), 14540–14542.

Nakai, H.; Kubota, T.; Kita, A.; Kawashima, A. Investigation of the Solid Electrolyte Interphase Formed by Fluoroethylene Carbonate on Si Electrodes. J. Electrochem. Soc. 2011, 158 (7), A798–A801.

Ng, S. H.; Wang, J.; Wexler, D.; Chew, S. Y.; Liu, H. K. Amorphous Carbon-Coated Silicon Nanocomposites:? A Low-Temperature Synthesis via Spray Pyrolysis and Their Application as High-Capacity Anodes for Lithium-Ion Batteries. J. Phys. Chem. C 2007, 111 (29), 11131–11138.

Ngadi, M. O.; Yu, L. J. Rheological Properties of Canadian Maple Syrup. Can. Biosyst. Eng. Genie Biosyst. Au Can. Rev. Soc. Can. Genie Agroaliment. Biol. 2004.

Nguyen, C. C.; Seo, D. M.; Chandrasiri, K. W. D. K.; Lucht, B. L. Improved Cycling Performance of a Si Nanoparticle Anode Utilizing Citric Acid as a Surface-Modifying Agent. Langmuir 2017, 33 (37), 9254–9261.

Nguyen, C. C.; Yoon, T.; Seo, D. M.; Guduru, P.; Lucht, B. L. Systematic Investigation of Binders for Silicon Anodes: Interactions of Binder with Silicon Particles and Electrolytes and Effects of Binders on Solid Electrolyte Interphase Formation. ACS Appl. Mater. Interfaces 2016, 8 (19), 12211–12220.

Nitta, N.; Wu, F.; Lee, J. T.; Yushin, G. Li-Ion Battery Materials: Present and Future. Mater. Today 2015, 18 (5), 252–264.

Obrovac, M. N.; Chevrier, V. L. Alloy Negative Electrodes for Li-Ion Batteries. Chem. Rev. 2014, 114 (23), 11444–11502.

Obrovac, M. N.; Christensen, L. Structural Changes in Silicon Anodes during Lithium Insertion/Extraction. Electrochem. Solid-State Lett. 2004, 7 (5), A93–A96.

Obrovac, M. N.; Krause, L. J. Reversible Cycling of Crystalline Silicon Powder. J. Electrochem. Soc. 2007, 154 (2), A103–A108.

Ogata, K.; Salager, E.; Kerr, C. J.; Fraser, A. E.; Ducati, C.; Morris, A. J.; Hofmann, S.; Grey, C. P. Revealing Lithium–silicide Phase Transformations in Nano-Structured Silicon-Based Lithium Ion Batteries via in Situ NMR Spectroscopy. Nat. Commun. 2014, 5, ncomms4217.

Ostadhossein, A.; Kim, S.-Y.; Cubuk, E. D.; Qi, Y.; van Duin, A. C. T. Atomic Insight into the Lithium Storage and Diffusion Mechanism of SiO2/Al2O3 Electrodes of Lithium Ion Batteries: ReaxFF Reactive Force Field Modeling. J. Phys. Chem. A 2016, 120 (13), 2114–2127.

Padhi, A. K.; Nanjundaswamy, K. S.; Goodenough, J. B. Phospho-olivines as Positive-Electrode Materials for Rechargeable Lithium Batteries. J. Electrochem. Soc. 1997, 144 (4), 1188–1194.

Peled, E.; Gorenshtein, A.; Segal, M.; Sternberg, Y. Rechargeable Lithium sulfur Battery (Extended Abstract). J. Power Sources 1989, 26 (3), 269–271.

Peled, E.; Sternberg, Y.; Gorenshtein, A.; Lavi, Y. Lithium-Sulfur Battery: Evaluation of Dioxolane-Based Electrolytes. J. Electrochem. Soc. 1989, 136 (6), 1621–1625.

Petibon, R.; Chevrier, V. L.; Aiken, C. P.; Hall, D. S.; Hyatt, S. R.; Shunmugasundaram, R.; Dahn, J. R. Studies of the Capacity Fade Mechanisms of LiCoO2/Si-Alloy: Graphite Cells. J. Electrochem. Soc. 2016, 163 (7), A1146–A1156.

Piwko, M.; Kuntze, T.; Winkler, S.; Straach, S.; Härtel, P.; Althues, H.; Kaskel, S. Hierarchical Columnar Silicon Anode Structures for High Energy Density Lithium Sulfur Batteries. J. Power Sources 2017, 351, 183–191.

Prosini, P. P.; Cento, C.; Rufoloni, A.; Rondino, F.; Santoni, A. A Lithium-Ion Battery Based on LiFePO4 and Silicon Nanowires. Solid State Ion. 2015, 269, 93–97.

Pu, X.; Yang, G.; Yu, C. Safe and Reliable Operation of Sulfur Batteries with Lithiated Silicon. Nano Energy 2014, 9, 318–324.

Rauh, R. D.; Abraham, K. M.; Pearson, G. F.; Surprenant, J. K.; Brummer, S. B. A Lithium/Dissolved Sulfur Battery with an Organic Electrolyte. J. Electrochem. Soc. 1979, 126 (4), 523–527.

Ryu, I.; Choi, J. W.; Cui, Y.; Nix, W. D. Size-Dependent Fracture of Si Nanowire Battery Anodes. J. Mech. Phys. Solids 2011, 59 (9), 1717–1730.

Schechter, A.; Aurbach, D.; Cohen, H. X-Ray Photoelectron Spectroscopy Study of Surface Films Formed on Li Electrodes Freshly Prepared in Alkyl Carbonate Solutions. Langmuir 1999, 15 (9), 3334–3342.

Seo, M.-H.; Park, M.; Lee, K. T.; Kim, K.; Kim, J.; Cho, J. High Performance Ge Nanowire Anode Sheathed with Carbon for Lithium Rechargeable Batteries. Energy Environ. Sci. 2011, 4 (2), 425–428.

Sim, S.; Oh, P.; Park, S.; Cho, J. Critical Thickness of SiO2 Coating Layer on Core@Shell Bulk@Nanowire Si Anode Materials for Li-Ion Batteries. Adv. Mater. 2013, 25 (32), 4498–4503.

Singh, N.; Arthur, T. S.; Ling, C.; Matsui, M.; Mizuno, F. A High Energy-Density Tin Anode for Rechargeable Magnesium-Ion Batteries. Chem. Commun. 2012, 49 (2), 149–151.

Smith, D. A.; Holmberg, V. C.; Korgel, B. A. Flexible Germanium Nanowires: Ideal Strength, Room Temperature Plasticity, and Bendable Semiconductor Fabric. ACS Nano 2010, 4 (4), 2356–2362.

Snyder, G. J.; Toberer, E. S. Complex Thermoelectric Materials. Nat. Mater. 2008, 7 (2), 105–114.

Song, S.; Kim, S. W.; Lee, D. J.; Lee, Y.-G.; Kim, K. M.; Kim, C.-H.; Park, J.-K.; Lee, Y. M.; Cho, K. Y. Flexible Binder-Free Metal Fibril Mat-Supported Silicon Anode for High-Performance Lithium-Ion Batteries. ACS Appl. Mater. Interfaces 2014, 6 (14), 11544–11549.

Spector, J. California's big battery experiment: a turning point for energy storage? http://www.theguardian.com/sustainable-business/2017/sep/15/californias-big-battery-experiment-a-turning-point-for-energy-storage (accessed Jan 25, 2018).

Steinhagen, C.; Akhavan, V. A.; Goodfellow, B. W.; Panthani, M. G.; Harris, J. T.; Holmberg, V. C.; Korgel, B. A. Solution-Liquid-Solid Synthesis of CuInSe2 Nanowires and Their Implementation in Photovoltaic Devices. ACS Appl. Mater. Interfaces 2011, 3 (5), 1781–1785.

Striebel, K.; Shim, J.; Srinivasan, V.; Newman, J. Comparison of LiFePO4 from Different Sources. J. Electrochem. Soc. 2005, 152 (4), A664–A670.

Su, Y.-S.; Fu, Y.; Cochell, T.; Manthiram, A. A Strategic Approach to Recharging Lithium-Sulphur Batteries for Long Cycle Life. Nat. Commun. 2013, 4, 2985.

Su, Y.-S.; Fu, Y.; Guo, B.; Dai, S.; Manthiram, A. Fast, Reversible Lithium Storage with a Sulfur/Long-Chain-Polysulfide Redox Couple. Chem. – Eur. J. 2013, 19 (26), 8621–8626.

Su, Y.-S.; Manthiram, A. A New Approach to Improve Cycle Performance of Rechargeable Lithium–sulfur Batteries by Inserting a Free-Standing MWCNT Interlayer. Chem. Commun. 2012, 48 (70), 8817–8819.

Su, Y.-S.; Manthiram, A. Lithium–sulphur Batteries with a Microporous Carbon Paper as a Bifunctional Interlayer. Nat. Commun. 2012, 3, 1166.

Takahashi, Y.; Tode, S.; Kinoshita, A.; Fujimoto, H.; Nakane, I.; Fujitani, S. Development of Lithium-Ion Batteries with a LiCoO2 Cathode Toward High Capacity by Elevating Charging Potential. J. Electrochem. Soc. 2008, 155 (7), A537–A541.

Talaie, E.; Bonnick, P.; Sun, X.; Pang, Q.; Liang, X.; Nazar, L. F. Methods and Protocols for Electrochemical Energy Storage Materials Research. Chem. Mater. 2017, 29 (1), 90–105.

Tarascon, J.-M.; Armand, M. Issues and Challenges Facing Rechargeable Lithium Batteries. Nature 2001, 414 (6861), 359–367.

Tesla Mega-Battery in Australia Activated. BBC News. December 1, 2017.

Trentler, T. J.; Hickman, K. M.; Goel, S. C.; Viano, A. M.; Gibbons, P. C.; Buhro, W. E. Solution-Liquid-Solid Growth of Crystalline III-V Semiconductors: An Analogy to Vapor-Liquid-Solid Growth. Science 1995, 270 (5243), 1791–1794.

Tsang, C.; Manthiram, A. Synthesis of Nanocrystalline VO 2 and Its Electrochemical Behavior in Lithium Batteries. J. Electrochem. Soc. 1997, 144 (2), 520–524.

Tuan, H.-Y.; Korgel, B. A. Importance of Solvent-Mediated Phenylsilane Decompositon Kinetics for High-Yield Solution-Phase Silicon Nanowire Synthesis. Chem. Mater. 2008, 20 (4), 1239–1241.

Verma, P.; Maire, P.; Novák, P. A Review of the Features and Analyses of the Solid Electrolyte Interphase in Li-Ion Batteries. Electrochimica Acta 2010, 55 (22), 6332–6341.

Wagner, N. A.; Raghavan, R.; Zhao, R.; Wei, Q.; Peng, X.; Chan, C. K. Electrochemical Cycling of Sodium-Filled Silicon Clathrate. ChemElectroChem 2014, 1 (2), 347–353.

Wagner, R. S.; Ellis, W. C. VAPOR-LIQUID-SOLID MECHANISM OF SINGLE CRYSTAL GROWTH. Appl. Phys. Lett. 1964, 4 (5), 89–90.

Wang, F.; Dong, A.; Buhro, W. E. Solution–Liquid–Solid Synthesis, Properties, and Applications of One-Dimensional Colloidal Semiconductor Nanorods and Nanowires. Chem. Rev. 2016, 116 (18), 10888–10933.

Wang, J. W.; Liu, X. H.; Zhao, K.; Palmer, A.; Patten, E.; Burton, D.; Mao, S. X.; Suo, Z.; Huang, J. Y. Sandwich-Lithiation and Longitudinal Crack in Amorphous Silicon Coated on Carbon Nanofibers. ACS Nano 2012, 6 (10), 9158–9167.

Wang, J.; Sun, X. Understanding and Recent Development of Carbon Coating on LiFePO4 Cathode Materials for Lithium-Ion Batteries. Energy Environ. Sci. 2012, 5 (1), 5163–5185.

Wang, Z.; Fu, Y.; Zhang, Z.; Yuan, S.; Amine, K.; Battaglia, V.; Liu, G. Application of Stabilized Lithium Metal Powder (SLMP®) in Graphite Anode – A High Efficient Prelithiation Method for Lithium-Ion Batteries. J. Power Sources 2014, 260 (Supplement C), 57–61.

Warrier, P.; Koh, C. A. Silicon Clathrates for Lithium Ion Batteries: A Perspective. Appl. Phys. Rev. 2016, 3 (4), 040805.

Winter, M.; Besenhard J. O. Electrochemical Lithiation of Tin and Tin-Based Intermetallics and Composites. Electrochimica Acta 1999, 45 (1), 31–50.

Wu, F.; Yao, N. Advances in Sealed Liquid Cells for In-Situ TEM Electrochemial Investigation of Lithium-Ion Battery. Nano Energy 2015, 11, 196–210.

Wu, H.; Cui, Y. Designing Nanostructured Si Anodes for High Energy Lithium Ion Batteries. Nano Today 2012, 7 (5), 414–429.

Xiong, S.; Xie, K.; Diao, Y.; Hong, X. Properties of Surface Film on Lithium Anode with LiNO3 as Lithium Salt in Electrolyte Solution for Lithium–sulfur Batteries. Electrochimica Acta 2012, 83, 78–86.

Xu, K. Electrolytes and Interphases in Li-Ion Batteries and Beyond. Chem. Rev. 2014, 114 (23), 11503–11618.

Xu, W.; Vegunta, S. S. S.; Flake, J. C. Surface-Modified Silicon Nanowire Anodes for Lithium-Ion Batteries. J. Power Sources 2011, 196 (20), 8583–8589.

Xu, Y.; Swaans, E.; Basak, S.; Zandbergen, H. W.; Borsa, D. M.; Mulder, F. M. Reversible Na-Ion Uptake in Si Nanoparticles. Adv. Energy Mater. 2016, 6 (2), n/a-n/a.

Yabuuchi, N.; Kubota, K.; Dahbi, M.; Komaba, S. Research Development on Sodium-Ion Batteries. Chem. Rev. 2014, 114 (23), 11636–11682.

Yamin, H.; Peled, E. Electrochemistry of a Nonaqueous Lithium/Sulfur Cell. J. Power Sources 1983, 9 (3), 281–287.

Yang, J.; Tse, J. S. Silicon Clathrates as Anode Materials for Lithium Ion Batteries? J. Mater. Chem. A 2013, 1 (26), 7782–7789.

Yang, Y.; McDowell, M. T.; Jackson, A.; Cha, J. J.; Hong, S. S.; Cui, Y. New Nanostructured Li2S/Silicon Rechargeable Battery with High Specific Energy. Nano Lett. 2010, 10 (4), 1486–1491.

Yim, T.; Park, M.-S.; Yu, J.-S.; Kim, K. J.; Im, K. Y.; Kim, J.-H.; Jeong, G.; Jo, Y. N.; Woo, S.-G.; Kang, K. S.; et al. Effect of Chemical Reactivity of Polysulfide toward Carbonate-Based Electrolyte on the Electrochemical Performance of Li–S Batteries. Electrochimica Acta 2013, 107, 454–460.

Yoon, S.; Park, C.-M.; Sohn, H.-J. Electrochemical Characterizations of Germanium and Carbon-Coated Germanium Composite Anode for Lithium-Ion Batteries. Electrochem. Solid-State Lett. 2008, 11 (4), A42–A45.

Yuan, F.-W.; Yang, H.-J.; Tuan, H.-Y. Alkanethiol-Passivated Ge Nanowires as High-Performance Anode Materials for Lithium-Ion Batteries: The Role of Chemical Surface Functionalization. ACS Nano 2012, 6 (11), 9932–9942.

Zeng, Z.; Liang, W.-I.; Liao, H.-G.; Xin, H. L.; Chu, Y.-H.; Zheng, H. Visualization of Electrode–Electrolyte Interfaces in LiPF6/EC/DEC Electrolyte for Lithium Ion Batteries via in Situ TEM. Nano Lett. 2014, 14 (4), 1745–1750.

Zhang, S. S. Role of LiNO3 in Rechargeable Lithium/Sulfur Battery. Electrochimica Acta 2012, 70, 344–348.

Zhang, Y.; Li, Y.; Wang, Z.; Zhao, K. Lithiation of SiO2 in Li-Ion Batteries: In Situ Transmission Electron Microscopy Experiments and Theoretical Studies. Nano Lett. 2014, 14 (12), 7161–7170.

Zhao, J.; Lu, Z.; Liu, N.; Lee, H.-W.; McDowell, M. T.; Cui, Y. Dry-Air-Stable Lithium Silicide–lithium Oxide Core–shell Nanoparticles as High-Capacity Prelithiation Reagents. Nat. Commun. 2014, 5, 5088.

Zhao, K.; Pharr, M.; Cai, S.; Vlassak, J. J.; Suo, Z. Large Plastic Deformation in High-Capacity Lithium-Ion Batteries Caused by Charge and Discharge. J. Am. Ceram. Soc. 2011, 94, s226–s235.

Zhao, R.; Bobev, S.; Krishna, L.; Yang, T.; Weller, J. M.; Jing, H.; Chan, C. K. Anodes for Lithium-Ion Batteries Based on Type I Silicon Clathrate Ba8Al16Si30 - Role of Processing on Surface Properties and Electrochemical Behavior. ACS Appl. Mater. Interfaces 2017, 9 (47), 41246–41257.

Zheng, H.; Li, J.; Song, X.; Liu, G.; Battaglia, V. S. A Comprehensive Understanding of Electrode Thickness Effects on the Electrochemical Performances of Li-Ion Battery Cathodes. Electrochimica Acta 2012, 71, 258–265.

Zhou, D.; Liu, M.; Yun, Q.; Wang, X.; He, Y.-B.; Li, B.; Yang, Q.-H.; Cai, Q.; Kang, F. A Novel Lithiated Silicon–Sulfur Battery Exploiting an Optimized Solid-Like Electrolyte to Enhance Safety and Cycle Life. Small 2017, 13 (3), n/a-n/a.

Zu, C.; Azimi, N.; Zhang, Z.; Manthiram, A. Insight into Lithium–metal Anodes in Lithium–sulfur Batteries with a Fluorinated Ether Electrolyte. J. Mater. Chem. A 2015, 3 (28), 14864–14870.

Zu, C.; Su, Y.-S.; Fu, Y.; Manthiram, A. Improved Lithium–sulfur Cells with a Treated Carbon Paper Interlayer. Phys. Chem. Chem. Phys. 2013, 15 (7), 2291–2297.

Vita

Emily Renee Adkins was born in Albuquerque, New Mexico and lived with her parents and younger brother. She graduated *cum laude* from Albuquerque Academy and went on to attend Rice University where she graduated *cum laude* with a Bachelor of Science in Chemical Engineering and a Bachelor of Art in Political Science in 2013. Upon graduation she enrolled at The University of Texas at Austin. She earned a Master of Science in Engineering in the fall of 2016 and completed her Ph.D. in Chemical Engineering in the spring of 2018. She performed her graduate studies on semiconductor nanowires under the supervision of Dr. Brian A. Korgel.

The author can be reached at emily.adkins@gmail.com

This dissertation was typed by the author.